CORA Cork Open Research Archive
Cartlann Taighde Oscailte Chorcaí

Title	Computational studies of the transverse structure of AGN jets
Authors	Murphy, Eoin Gerard
Publication date	2014
Original Citation	Murphy, E. G. 2014. Computational studies of the transverse structure of AGN jets. PhD Thesis, University College Cork.
Type of publication	Doctoral thesis
Rights	© 2014, Eoin G. Murphy - http://creativecommons.org/licenses/by-nc-nd/3.0/
Download date	2024-04-19 08:54:25
Item downloaded from	https://hdl.handle.net/10468/1671

UCC
University College Cork, Ireland
Coláiste na hOllscoile Corcaigh

Computational Studies of the Transverse Structure of AGN Jets

Eoin Murphy
BSC
105642248

NATIONAL UNIVERSITY OF IRELAND, CORK

Faculty of Science

Department of Physics

Thesis submitted for the degree of Doctor of Philosophy

16th January 2014

Supervisor: Dr. Denise Gabuzda
Head of Department/School: Prof. John Mc Inerney

Contents

List of Figures . . . iii
List of Tables . . . vii
Acknowledgements . . . x
Abstract . . . xi

1 Introduction **1**
1.1 History of Radio Astronomy . . . 1
1.2 Active Galactic Nuclei . . . 4
1.2.1 Energy Production in AGN . . . 5
1.2.2 Constituent Components . . . 6
1.2.2.1 Central Engine . . . 7
1.2.2.2 Circumnuclear Medium . . . 8
1.2.2.3 Jet Outflows . . . 9
1.2.3 Taxonomy of AGN . . . 10
1.2.4 AGN Unification . . . 14
1.3 AGN Jets . . . 17
1.3.1 Jet Launching . . . 17
1.3.2 Structure of an AGN Jet . . . 17
1.3.3 Superluminal Motion . . . 18
1.3.4 Jet Matter Content . . . 20
1.3.5 Jet Magnetic Field . . . 21
1.4 Synchrotron Radiation . . . 22
1.4.1 Synchrotron Emission . . . 22
1.4.2 Synchrotron Spectrum . . . 24
1.4.3 Synchrotron Polarization . . . 27
1.5 Radio Astronomy . . . 31
1.5.1 Radio Interferometry . . . 33
1.5.2 The CLEAN Algorithm . . . 37
1.5.3 Polarization Observations using Interferometry . . . 41
1.5.3.1 Polarization Calibration . . . 46

2 Helical Magnetic Fields and AGN Jets **48**
2.1 Observational Evidence for Helical Magnetic Fields . . . 48
2.2 Faraday Rotation . . . 53
2.2.1 Faraday Rotation in Plasma . . . 53
2.2.2 Faraday Rotation in a Helical Magnetic field. . . . 57
2.3 Poynting Robertson Battery . . . 57
2.4 Thesis Summary . . . 59

3 Simple Helical Magnetic field Model **61**
3.0.1 Simple Helical Field Model . . . 61
3.0.2 Model Predictions . . . 65

4 Analysis of Transverse Polarized Structure **71**
4.1 Fitting Procedure . . . 71

4.2 Markarian 501 74
4.2.1 Fitting Results 77
4.2.2 Markarian 501 Spectral Index 85
4.2.3 Derivation of δ and $\beta = v/c$ in the Observer's Frame . . . 86
4.2.4 Agreement with Faraday Rotation Results 89
4.3 M87 91
4.3.1 Fitting Results 93
4.3.1.1 Knot A Diffuse & Knot B 94
4.3.1.2 Knot A & Knot C 98
4.3.2 Agreement with Faraday Rotation Results 100

5 Rotation Measure Resolution Requirements 101
5.1 Monte Carlo Analysis Procedure 102
5.2 Monte Carlo Results 103
5.2.1 Monte Carlo Results for 18 – 22 cm Simulations source at declination +42° 103
5.2.2 Monte Carlo Results for 1.9 – 3.8 cm Simulations, Source at Declination +32° 115
5.2.3 Monte Carlo Results for 1.9 – 3.8 cm Simulations, Source at Declination −7° 127
5.2.4 Faraday Depolarization 138
5.3 RM Gradient Reversal 138
5.3.1 Monte Carlo Results 142

6 Occurrence of Spurious Gradients 147
6.1 Monte Carlo Statistics for Spurious Gradients 148
6.2 Additional Frequencies 149
6.3 Comparison to Hovatta et al. & Algaba 151

7 Conclusions 156

Bibliography 168

A CASA Code 169
A.0.1 Code Verification 169
A.1 Visibility Replacer 170
A.2 Mapper 178
A.3 RM 183
A.4 Sigma Checker 199

List of Figures

1.1 Jansky's "merry-go-round". 2
1.2 Grote Reber's reflector 3
1.3 Reber's detection of radio emission from the Milky Way. 4
1.4 Constituent Components of an AGN 7
1.5 AGN Classifications 11
1.6 FRI and FRII morphology 12
1.7 AGN Unification 14
1.8 Sketch of the various sites of emission in an active galactic nucleus with a relativistic jet. 18
1.9 The geometry assumed to explain apparent superluminal motion in the jets of AGN. 19
1.10 Plot of F(x) vs x 28
1.11 Log plot of F(x) vs x 28
1.12 Generic synchrotron spectrum 29
1.13 Electromagnetic opacity of the Earth's atmosphere. 31
1.14 Arecibo Radio Telescope 32
1.15 Radio Interferometry with 2 telescope array. 33
1.16 Response of an interferometer to an extended source. 34
1.17 The VLBA 35
1.18 The (u, v) and (l, m) coordinate system 37
1.19 Figure describing what is meant by Sampled Visibility 39
1.20 The CLEAN algorithm 40
1.21 Definitions of orthogonal modes for Stokes parameters and definition for the direction of RCP radiation. 41
1.22 The Stokes Parameters 43

2.1 Distribution of the electric vector offsets in MOJAVE sample . . 49
2.2 Rotation Measure Map of SOURCE 50
2.3 Asymmetric Total Intensity and Polarized Intensity Profiles . . . 51
2.4 RM maps produced by the canonical GRMHD model of Broderick & McKinney (2010) 52
2.5 Helical magnetic field schematic 56
2.6 Poynting Robertson Battery schematic 58

3.1 Effect of tangled magnetic field component on the observed transverse structures. 65
3.2 Transverse structure predicted by simple helical magnetic field model. 66
3.3 The effects of finite resolution on observed transverse profiles. . . 68

4.1 4 cm Polarization Map of Markarian 501 75
4.2 6 cm Polarization Map of Markarian 501 76
4.3 13 cm Polarization Map of Markarian 501 77
4.4 18 cm Polarization Map of Markarian 501 78
4.5 6 cm Polarization Map of Markarian 501 with slice locations . . . 79

4.6 Observed 6 cm Markarian 501 I, Q & U transverse profiles. . . . 80
4.7 Observed and best-fit 6 cm Markarian 501 I & Q transverse profiles. 81
4.8 Observed and best-fit 4 cm, 13 cm & 18 cm Markarian 501 I and Q transverse profiles. 83
4.9 Markarian 501 Spectral Index map. 87
4.10 Analytical v. Numerical transverse profile example. 88
4.11 Magnetic-field configuration maps for different spectral indices. . 88
4.12 Figure highlighting how line of sight influences observed RM and percentage polarization. 90
4.13 3.75 cm Intensity Map of M87 92
4.14 1.36 cm Polarization Map of M87 93
4.15 2.00 cm Polarization Map of M87 94
4.16 3.75cm Polarization Map of M87 95
4.17 Observed I, Q and U profiles for the slices analysed from M87 Knot A Diffuse and Knot B 96
4.18 Plots of observed and best-fit model I and Q profiles for M87 Knot A Diffuse and Knot B 97
4.19 Observed I, Q and U profile for slice transverse to M87 Knot A and observed and best-fit model I and Q profiles for M87 Knot A 99
4.20 Observed I, Q and U profile for a slice transverse to M87 Knot C. 99

5.1 UV distribution for 22 cm visibility data for model source at +42° used in this analysis, based on existing VLBA snapshot observations. 104
5.2 Model and Observed 18 – 22 cm Total Intensity Maps 105
5.3 First & Second sets of 18 – 22 cm Monte Carlo simulations. . . . 106
5.4 Third & Fourth sets of 18 – 22 cm Monte Carlo simulations. . . . 107
5.5 Fifth & Sixth sets of 18 – 22 cm Monte Carlo simulations. 108
5.6 Seventh & Eighth sets of 18 – 22 cm Monte Carlo simulations. . 109
5.7 Ninth set of 18 – 22 cm Monte Carlo simulations. 110
5.8 MC results for first set of 18 – 22 cm simulations. 111
5.9 MC results for second set of 18 – 22 cm simulations. 111
5.10 MC results for third set of 18 – 22 cm simulations. 112
5.11 MC results for fourth set of 18 – 22 cm simulations. 112
5.12 MC results for fifth set of 18 – 22 cm simulations. 113
5.13 MC results for sixth set of 18 – 22 cm simulations. 113
5.14 MC results for seventh set of 18 – 22 cm simulations. 114
5.15 MC results for eighth set of 18 – 22 cm simulations. 114
5.16 MC results for ninth set of 18 – 22 cm simulations. 115
5.17 UV distribution for 3.8 cm visibility data for model source at +32° used in this analysis, based on existing VLBA snapshot observations. 116
5.18 First & Second sets of +32° declination 1.9 – 3.8 cm Monte Carlo simulations. 118
5.19 Third & Fourth sets of +32° declination 1.9 – 3.8 cm Monte Carlo simulations. 119

5.20 Fifth & Sixth sets of +32° declination 1.9 – 3.8 cm Monte Carlo simulations. 120
5.21 Seventh & Eighth sets of +32° declination 1.9 – 3.8 cm Monte Carlo simulations. 121
5.22 Ninth set of +32° declination 1.9 – 3.8 cm Monte Carlo simulations. 122
5.23 MC Results for Model Jet with 25% Polarized Flux and RM Range -1000 to 1000 rad m^{-2} 122
5.24 MC results for second set of 1.9 – 3.8 cm simulations at +32° declination. 123
5.25 MC results for third set of 1.9 – 3.8 cm simulations at +32° declination. 123
5.26 MC results for fourth set of 1.9 – 3.8 cm simulations at +32° declination. 124
5.27 MC results for fifth set of 1.9 – 3.8 cm simulations at +32° declination. 124
5.28 MC results for sixth set of 1.9 – 3.8 cm simulations at +32° declination. 125
5.29 MC results for seventh set of 1.9 – 3.8 cm simulations at +32° declination. 125
5.30 MC results for eighth set of 1.9 – 3.8 cm simulations at +32° declination. 126
5.31 MC results for ninth set of 1.9 – 3.8 cm simulations at +32° declination. 126
5.32 UV distribution for 3.8 cm visibility data for model source at −7° used in this analysis, based on existing VLBA snapshot observations. 128
5.33 First & Second sets of −7° declination 1.9 – 3.8 cm Monte Carlo simulations. 129
5.34 Third & Fourth sets of −7° declination 1.9 – 3.8 cm Monte Carlo simulations. 130
5.35 Fifth & Sixth sets of −7° declination 1.9 – 3.8 cm Monte Carlo simulations. 131
5.36 Seventh & Eighth sets of −7° declination 1.9 – 3.8 cm Monte Carlo simulations. 132
5.37 Ninth set of −7° declination 1.9 – 3.8 cm Monte Carlo simulations. 133
5.38 MC results for first set of 1.9 – 3.8 cm simulations at −7° declination. 133
5.39 MC results for second set of 1.9 – 3.8 cm simulations at −7° declination. 134
5.40 MC results for third set of 1.9 – 3.8 cm simulations at −7° declination. 134
5.41 MC results for fourth set of 1.9 – 3.8 cm simulations at −7° declination. 135
5.42 MC results for fifth set of 1.9 – 3.8 cm simulations at −7° declination. 135
5.43 MC results for sixth set of 1.9 – 3.8 cm simulations at −7° declination. 136

5.44 MC results for seventh set of 1.9 – 3.8 cm simulations at −7° declination. 136
5.45 MC results for eighth set of 1.9 – 3.8 cm simulations at −7° declination. 137
5.46 MC results for ninth set of 1.9 – 3.8 cm simulations at −7° declination. 137
5.47 The effects of Faraday depolarization. 139
5.48 RM distribution of 0716 + 714. 140
5.49 Intrinsic total intensity image of the model source and observed total intensity of single MC instance. 141
5.50 Monte Carlo results using model core–jet sources with uniformly directed monotonic transverse RM gradients for intrinsics widths of 0.35 and 0.20 mas. 143
5.51 Monte Carlo results using model core–jet sources with uniformly directed monotonic transverse RM gradients for intrinsics widths of 0.10 and 0.05 mas. 144
5.52 Monte Carlo results using model core–jet sources with oppositely directed transverse RM gradients for intrinsics widths of 0.35 and 0.20 mas. 145
5.53 Monte Carlo results using model core–jet sources with oppositely directed transverse RM gradients for intrinsics widths of 0.10 and 0.05 mas. 146

6.1 Fraction of spuriously detected RM gradients vs. observed jet width after convolution for 18 – 22 cm simulations (source at +42° declination). 149
6.2 Fraction of spuriously detected RM gradients vs. observed jet width after convolution for 1.9 – 3.8 cm simulations (source at +32° declination). 150
6.3 Fraction of spuriously detected RM gradients vs. observed jet width after convolution for 1.9 – 3.8 cm simulations (source at −7° declination). 151
6.4 Results for Monte Carlo simulations to evaluate the reduction in observed spurious RM gradients when wavelength range is increased. 152
6.5 Fraction of total gradients vs. slice width from the Monte Carlo simulations of Hovatta et al. (2012) 154
6.6 Fraction of total gradients vs. slice width from the Monte Carlo simulations of Algaba (2013) 155

List of Tables

1.1 Expected degrees of polarization (m), for both optical thin and thick regions 30

4.1 Best fit Parameters for 6 cm Markarian 501 Slices (Epoch February 1997) 82
4.2 Best fit Parameters for Markarian 501 Slice 2 for 4 different wavelengths 84
4.3 Best fit Parameters for 13 cm Markarian 501 Slice for three values of α 86
4.4 Best fit Parameters for M87 Knot A Diffuse & Knot B Slices . . 95
4.5 Best fit Parameters for M87 Knot A Slices 98

5.1 Parameters used for Monte Carlo Analysis for 18 – 22 cm wavelength 104
5.2 Parameters used for Monte Carlo Analysis for 1.9 – 3.8 cm wavelength, source at declination +32° 116
5.3 Parameters used for Monte Carlo Analysis for 1.9 – 3.8 cm wavelength source at declination −7°. 127

I, Eoin Murphy, certify that this thesis is my own work and I have not obtained a degree in this university or elsewhere on the basis of the work submitted in this thesis.

Eoin Murphy

To my parents, Sean and Betty Murphy

Acknowledgements

First and foremost, I would like to thank Denise Gabuzda for the excellent supervision that she provided over the duration of my PhD. Denise has been always there to provide support, encouragement and advice on any issues that arose over the past four years. I could not have imagined having a better supervisor and mentor for my Ph.D study.

I would like to thank Tim Cawthorne for his encouragement, insightful comments, immense knowledge and for giving me the opportunity to spend two wonderful summers working with him at the University of Central Lancashire. A special thanks to Juan Carlos Algaba who provided me the data required to carry out research on the jet of M87.

Thanks to my supportive lab mates, Colm, Fiona, Mark, Andrea and all the summer students who graced our lab over the past 4 years. The lab was never boring and I'm going to miss our Monday evening expeditions!

I would like to thank my friends, especially Stephen, Mark, Steve, James, Killian, Karen, Sarah, Saorlaith, Noirin, Cliodhna and Anna. Having friends to come home to after long and, sometimes, stressful days in UCC made all the difference. The many lunches were also wonderful. I would also like to thank the UCC Wargaming and Roleplaying Society. For the past eight years I have been able to play games and relax in the company of friends every Thursday. It has always been a highpoint of my week.

Many thanks the Irish Research Council for Science Engineering and Technology for their financial support.

I would like to thank my examiners, Philip Hughes and Stephen Fahy, for comments and suggestions which I believe helped make this thesis more complete and clear.

Finally, a special thanks to my family, especially my mother and father, for always believing in me and for their continuous support. Without them I would not have made it here. I dedicate this thesis to them.

Abstract

Both the emission properties and the evolution of the radio jets of Active Galactic Nuclei are dependent on the magnetic (B) fields that thread them. A number of observations of AGN jets suggest that the B fields they carry have a significant helical component, at least on parsec scales. This thesis uses a model, first proposed by Laing and then developed by Papageorgiou, to explore how well the observed properties of AGN jets can be reproduced by assuming a helical B field with three parameters; pitch angle, viewing angle and degree of entanglement. This model has been applied to multifrequency Very Long Baseline Interferometry (VLBI) observations of the AGN jets of Markarian 501 and M87, making it possible to derive values for the helical pitch angle, the viewing angle and the degree of entanglement for these jets.

Faraday rotation measurements are another important tool for investigating the B fields of AGN jets. A helical B field component should result in a systematic gradient in the observed Faraday rotation across the jet. Real observed radio images have finite resolution; typical beam sizes for cm-wavelength VLBI observations are often comparable to or larger than the intrinsic jet widths, raising questions about how well resolved a jet must be in the transverse direction in order to reliably detect transverse Faraday-rotation structure. This thesis presents results of Monte Carlo simulations of Faraday rotation images designed to directly investigate this question, together with a detailed investigation into the probabilities of observing spurious Faraday Rotation gradients as a result of random noise and finite resolution. These simulations clearly demonstrate the possibility of detecting transverse Faraday-rotation structures even when the intrinsic jet widths are appreciably smaller than the beam width.

Astronomy?
Impossible to understand and madness to investigate.

Sophocles, c. 420 BCE

Chapter 1

Introduction

The chapter gives an overview of the history of Radio Astronomy in addition to an overview of synchrotron radiation, Active Galactic Nuclei (AGN) and the tools required to observe and study them.

1.1 History of Radio Astronomy

While astronomy is considered by many to be the oldest of the natural sciences it wasn't until the 1600s when Galileo Galilei began using a telescope to observe the heavens that astronomy began to evolve into the modern science we know today. Since then astronomers have used optical observation to help further our understanding of the universe.

The use of non optical wavelengths in astronomy only began during the twentieth century, mostly due to the huge advancements in technology which occurred during the course of the second World War. Using a combination of ground based and air based telescopes (mostly carried in balloons and aircraft before finally being placed in satellites) the parts of the electromagnetic (EM) spectrum available to astronomers quickly transitioned from just the optical spectrum to almost the entire electromagnetic spectrum.

In 1888 Heinrich Hertz successfully produced radio waves in his laboratory at the University of Karlsruhe. Soon after this discovery many astronomers proposed observing celestial objects using radio waves. One of the more famous of such experiments was conducted in 1894 by Sir Oliver Lodge who attempted to observe radio emission from the Sun at University College Liverpool. Unfortunately, the

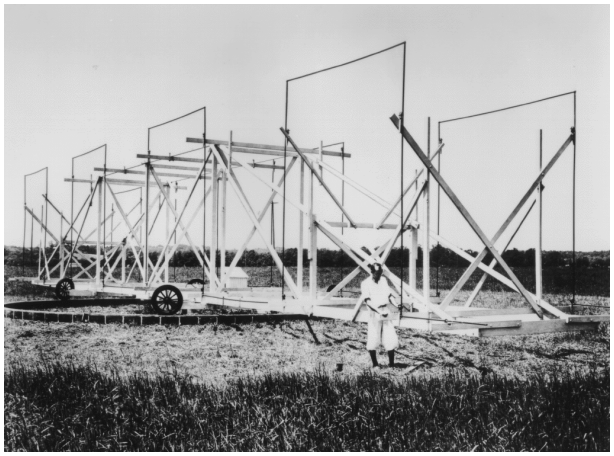

Figure 1.1: Jansky's "merry-go-round", an antenna designed to receive radio waves at a frequency of 20.5 MHz (wavelength about 14.5 meters) mounted on a turntable that allowed it to rotate in any direction (Image from NRAO website http://www.nrao.edu).

apparatus he used was not sensitive enough to reliably detect solar radio emission due to the large amounts of electromagnetic interference being produced by the nearby city of Liverpool. It would be another 40 years before extra-terrestrial radio emission was observed by an American named Karl Jansky.

Jansky was working as a electrical engineer at Bell Telephone Laboratories (Bell Labs) in Holmdel, New Jersey when Bell Labs began to investigate the possibility of using "short radio waves" (wavelengths varying between 10m and 20m) for transatlantic telecommunications. Jansky was asked by Bell Labs to investigate static which was interfering with their endeavours. He did so by building a radio antenna (Fig. 1.1) and recording signals from all directions for several months. He was able to identify what he first believed to be the three main sources of this static

- Nearby thunderstorms
- Distant thunderstorms
- The Sun

However, upon further investigation Jansky observed that the source of this third source of static moved away from the Sun's position and that it was periodic with a period of a sidereal day (23 hours 56 minutes). He soon realised that the radiation was coming from our own galaxy and was strongest in the direction of its centre, in the constellation of Sagittarius. The discovery was widely publicised, appearing in the New York Times of May 5, 1933. Unfortunately, Bell Labs was

not interested in continuing research into the source of this radiation and Jansky was unable to contribute more to the field that was to become known as Radio Astronomy. To honour the importance of his discovery, the unit of flux density in radio observations, the Jansky (Jy), was named after him.

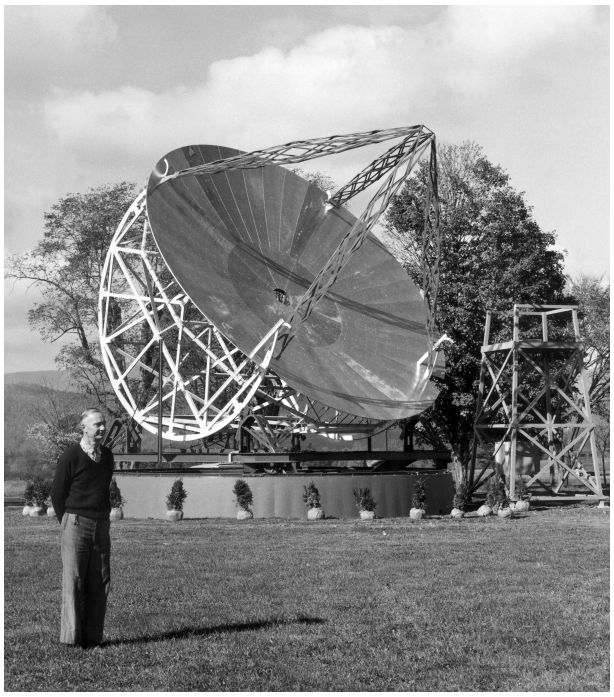

Figure 1.2: Grote Reber and his 9.5m parabolic reflector in Illinois, Chicago (Image from NRAO website http://www.nrao.edu).

Inspired by Jansky's discovery, an American radio engineer named Grote Reber decided to construct his own radio telescope in his back yard (in Wheaton, Illinois) at his own expense. Reber chose to build a parabolic dish (Fig. 1.2) rather than an antenna of the style Jansky had used. He guessed that it would be important to observe a wide range of wavelengths of extraterrestrial radiation in order to understand how it was being produced; a parabolic dish would focus all the emission received at a single focus. While still working as a radio engineer by day Reber began to scan the skies at night using his telescope. After multiple failed attempts he was finally successful in observing radio emission from the Milky Way at 160MHz (Fig. 1.3).

In 1942 J.S. Hey and G.C. Southworth both detected radio emission from the Sun while working at two different laboratories. Hey successfully discovered intense radio emission associated with solar activity (a large sunspot) while, 6 months later, Southworth was able to observe the thermal radio emission of the quiet Sun. However, circulation of both discoveries was severely limited due to the

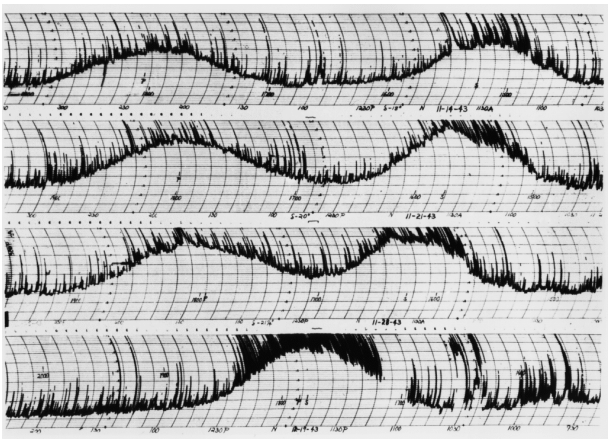

Figure 1.3: Reber's detection of radio emission from the Milky Way. The multiple spikes are due to interference from automobile engine sparks (Image from NRAO website http://www.nrao.edu).

confidential nature of the work both were carrying out. Nevertheless, it was this work that ultimately formed the foundation of solar radio astronomy. In 1944, Oort and Van de Hulst predicted that neutral atomic hydrogen should be detectable at 21 cm wavelength. It was successfully observed 7 years later.

In the early 1950s more and more astronomers were getting interested in the new results being discovered using radio astronomy. Due to this the first Cambridge Catalogue of Radio Sources was published. This first Catalogue (C1) contained 50 difference radio sources. However, many of these were discovered to be not real. It wasn't until the second and third Cambridge Catalogues (2C and 3C) that the first detailed survey of the radio sky was made available to astronomers.

The radio source 3C 48, discovered in the 1960s, was the first radio source which had an optical counterpart, which was thought to be a faint blue star. Further analysis of the spectrum of this star was unable to identify several broad emission lines. In 1962, another radio source, 3C 273 showed the same strange spectrum and its discoverer, Maarten Schmidt, realised that the spectral lines were actually redshifted hydrogen lines at a very high redshift. These new objects, first named 'quasi-stellar radio sources', were later named 'quasars' by Hong-Yee Chui.

1.2 Active Galactic Nuclei

The primary reference for material in this section was 'An Introduction to Active Galactic Nuclei' by Bradley M. Peterson (1997).

Active Galactic Nuclei (AGN) are galaxies in which a huge amount of radiation is observed to emanate from their nucleus (or central region). The levels of radiation observed are too high to be explained by nuclear fusion occurring in the centres of stars. The bolometric luminosities inferred for AGN range from about 10^{38} W to more than 10^{41} W, with 5×10^{39} W being a typical value. This implies that the most luminous AGN are of the order of 10^5 more energetic than a normal galaxy like our own Milky Way.

1.2.1 Energy Production in AGN

The enormously high energy output of AGN leads to the question of what sort of physical process could continuously generate such large amount of energy. Currently the astrophysics community believes that supermassive black holes reside at the centre of AGN, which are surrounded by a hot accretion disks. The gravitational infall of material from these hot disks onto the black holes results in the unusually high levels of energy output observed.

Any source of radiation has an associated radiation pressure which exerts a force on any particles in its emitting region. If this force is larger than the gravitational force attracting these particles to the system the system will begin to lose mass as the particles move away from the source of radiation. This mass loss allows us to put an upper limit on the luminosity of any object in hydrostatic equilibrium (where this radiation pressure is exactly equal to the gravitational force). This upper limit is known as the Eddington Luminosity. For a spherically symmetric, fully ionised object (a reasonable assumption as we are dealing with such highly energetic objects) this limit is given by

$$L_{Ed} \simeq 1.5 \times 10^{31} \ \frac{M}{M_\odot} \ W$$

where $M_\odot$ is the mass of the Sun. Using a typical AGN luminosity it is possible to determine a lower limit on the mass of its central object

$$L < L_{Ed}$$
$$5 \times 10^{39} \ W < 1.5 \times 10^{31} \ \frac{M}{M_\odot} \ W$$
$$M > 3 \times 10^8 M_\odot$$

AGN are often observed to be variable. The timescales of these variations range from as long as several months to as short as only a few hours. These variations put a limit on the size of the active core regions of AGN. In order to vary coherently, the size of the source must be comparable to the distance light can travel in that time. For a typical AGN this puts a limit on the scale of the core AGN region of only a few light days. Combining this information with the lower mass limit requires several hundred million solar masses to be contained in a region not that much larger than our own solar system. A supermassive black hole is the only object that can achieve the required density.

For an AGN, the luminosity observed can be explained by the infall of matter onto its central supermassive black hole. This matter is transformed into energy (what we observe) with some efficiency η. This efficiency is believed to be close to 0.1.

$$\begin{aligned} L &= \frac{dE}{dt} = \eta \dot{M} c^2 \\ \dot{M} &= \frac{L}{\eta c^2} \\ &= \frac{5 \times 10^{39}\ W}{\eta c^2} \\ &= 5.6 \times 10^{23}\ kg\ s^{-1} \\ &\simeq 8.8\ M_{\odot}\ yr^{-1} \end{aligned}$$

Thus, a black hole accreting only a few solar masses per year is capable of producing the large luminosities observed in AGN.

1.2.2 Constituent Components

The constituent components of all AGN can be, roughly, divided into 3 main components

- Central Engine
- Gas Clouds & Obscuring Torus
- Jet Outflows

The approximate location of these components can be seen in Fig. 1.4.

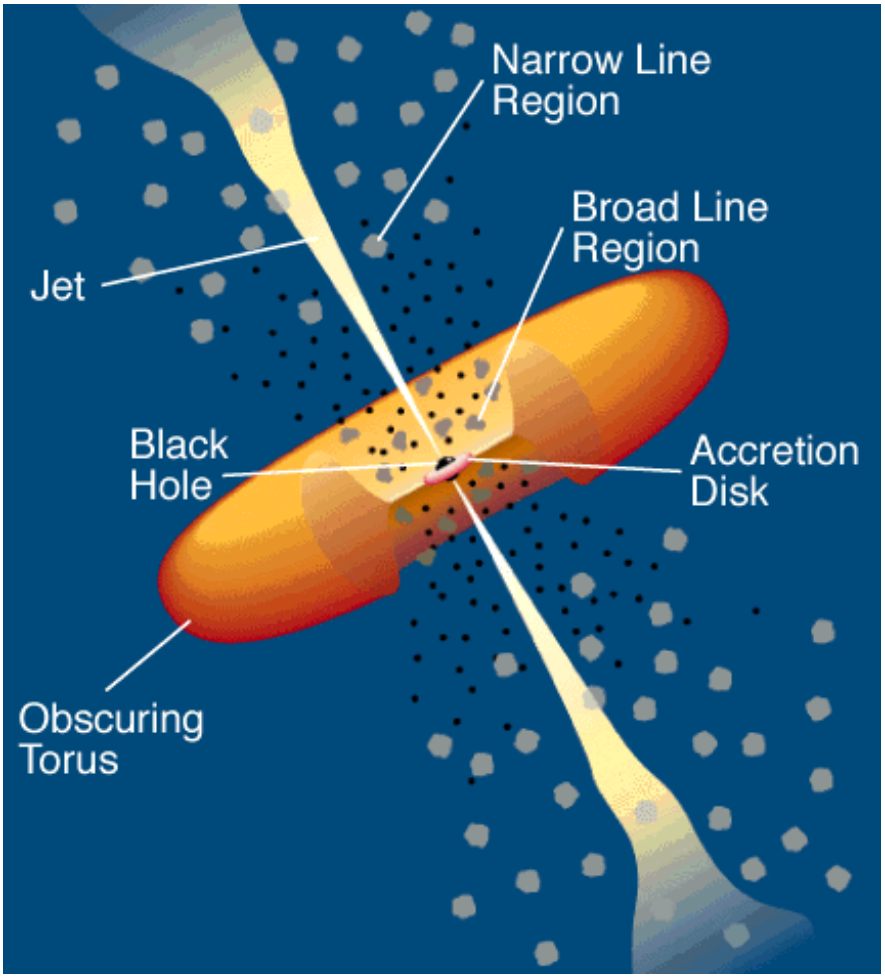

Figure 1.4: Constituent Components of an AGN (not to scale) (Urry 2003)

1.2.2.1 Central Engine

The central engine of an AGN is comprised of a supermassive black hole (as discussed in Section 1.2.1) surrounded by a hot accretion disk.

One of the fundamental questions raised by this model is how angular momentum is conserved in the system. Balbus & Hawley (1998) discovered the mechanism which allows for angular momentum to be transported out through the disk. This mechanism is known as magneto-rotational instability (MRI) or Balbus-Hawley instability. In MRI, magnetic tension between fluid elements results in a retarding torque on the fluid element closer to the centre of motion. This retarding torque results in the inner fluid element moving into a lower orbit. Conservation of angular momentum then requires that the outer fluid element moves into a higher orbit. This further increases the magnetic tension between the two fluid elements and the process continues, resulting in angular momentum being transferred out

along the disk.

AGN are believed to have 2 main classes of accretion disk; optically thick accretion disks and optically thin accretions disks.

Optically thick accretions disks are believed to be geometrically thin. This type of disk absorbs high energy photons which results in a highly luminous thermal spectrum. Many AGN optical spectra exhibit a feature called the "big blue bump". This is thought to be due to contribution of the hot accretion disk's blackbody spectrum to the overall synchrotron spectrum of the AGN.

An optically thin but geometrically thick accretion disk can be generated in the case where cooling is mainly due to advection rather than radiation. This is known as advection dominated accretion flow (ADAF). Here, much of the energy gained from accretion is not radiated away but is instead transported with the flow inside the event horizon of the supermassive black hole. This results in a much lower luminosity than that of an AGN with an optically thick accretion disk.

1.2.2.2 Circumnuclear Medium

It is believed that the central engine of an AGN is surrounded by clouds of gas and dust. There are 3 main components (as seen in Fig. 1.4) of the circumnuclear medium.

- Broad-line Region
- Narrow-line Region
- Dusty Torus

The broad emission lines observed in the spectrum of many AGN (see Section 1.2.3) are formed in a broad-line region that is relatively close to the central engine. The broad-line region is clumpy, containing partially ionized clouds of gas. The optically thick clouds that produce the emission lines occupy only about 1% of the available volume and probably have a flattened distribution. Studies of the broad Fe II emission lines indicate that the temperature of the broad-line region is $\sim 10^4$ K and other lines indicate an electron number density of $\sim 10^{16}\text{m}^{-3}$. Such high densities will result in a high frequency of collisions between the electrons, resulting in forbidden emission lines not being emitted, as the long lived states required to give rise to these lines are de-excited by the

collisions.

The electron number density of the narrow-line region is $\sim 10^{10}$ m^{-3}, significantly less than that of the broad line region and low enough to allow for the formation of forbidden emission lines. This value is comparable to the values found in planetary nebulae and dense H II regions. Studies of these emission lines also indicate a temperature of $\sim 10^4$ K. Like the broad-line region, the narrow-line region is clumpy and is believed to consist of a spherical distribution of clouds. These clouds are at a lower velocity than the gas clouds the broad-line region. While the broad-line region is very compact, the narrow-line region is believed to be diffuse. The narrow-line regions of some AGN have been successfully imaged with the Hubble space telescope. (Falcke et al. 1998)

The spectra of most AGN have a small bump in the infra-red part of the spectrum that cannot be explained by synchrotron emission. This suggests a large, optically thick torus of warm dust surrounds the clouds of the broad-line region. This torus plays a very important role in the Unified Model of AGNs (Section 1.2.4).

1.2.2.3 Jet Outflows

The radio lobes of AGN are produced by jets of charged particles ejected from the central engine at highly relativistic velocities. The particles are accelerated away from the central engine powered by either the energy of accretion or by the extraction of rotational kinetic energy from the supermassive black hole via a process known as the Blandford-Znajek mechanism. (Blandford & Znajek 1977)

Every AGN is believed to produce twin jets which emanate perpendicular to the accretion disk. These jets are believed to be present intermittently. They are electrically neutral but it is unknown if they are comprised of electrons and ions or an electron-positron plasma. They penetrate both the broad-line and narrow-line emission regions. Most of these jets terminate in a pair of diffuse, extended structures called lobes. It is unclear if these represent a backflow of jet material or if they are the residue of the jet from an earlier epoch. Some of the most powerful jets instead terminate in a compact region of very high luminosity called “hot spots”. These “hot spots” are the result of shocks between the highly relativistic jets and the plasma which fill the lobes in which the jets are embedded.

In general, radio observations of AGN probe these jet outflows only. Even though only $\sim 10\%$ of observed AGN are radio loud, these radio observations offer one of

the few ways to directly study AGN from sub-pc to Mpc scales. They are crucial in the efforts of astronomers worldwide to understand AGN.

1.2.3 Taxonomy of AGN

The 13th edition of *The Catalog of Quasars and Active Galactic Nuclei* by Veron-Cetty and Veron contains a grand total of 168941 AGN. This is the largest catalogue of AGN to date and shows that AGN make up around 7% of all observed galaxies.(Véron-Cetty & Véron, 2010)

In order to help understand the various physical properties of observed AGN they are classified as different classes and subclasses. Distinguishing between different classes of AGN can sometimes be difficult as there is no simple rule that can be evoked to do so. There are 5 main classes of AGN and most observed AGN can be classified as one of these classes. They are

- Radio Galaxies
- Quasars
- Blazars
- Seyfert Galaxies
- LINERS

Radio Galaxies

Radio galaxies are normally elliptical galaxies with levels of radio emission far in excess of that emitted by normal galaxies. Radio galaxies are further subdivided into broad line radio galaxies (BLRG) or narrow line radio galaxies (NLRG) based on the presence (or absence) of broad optical lines in their spectrum. Radio galaxies tend to show radio structure on kiloparsec (kpc) scales which generally feature a double structure consisting of two lobes of radio emission located on both sides of the core. Many radio galaxies also feature jets that get launched at the core and lead out to the extended lobes. If a radio galaxy does have an observable jet it is normally one sided; Doppler beaming beams one side of the jet towards the observer, greatly enhancing the brightness of the jet approaching the observer while diminishing the jet moving away from the observer.

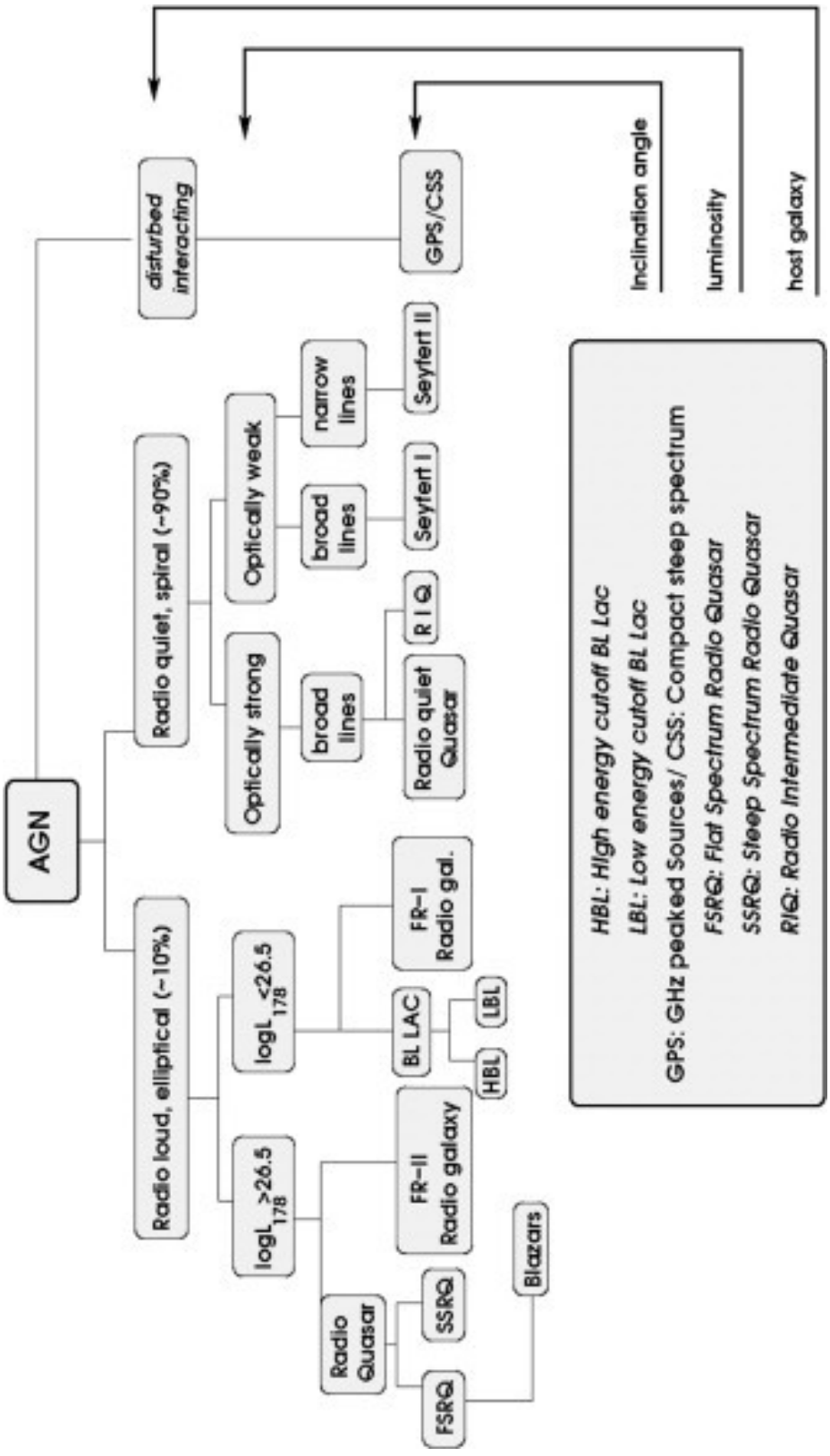

Figure 1.5: AGN Classifications (Achterberg et al. 2006)

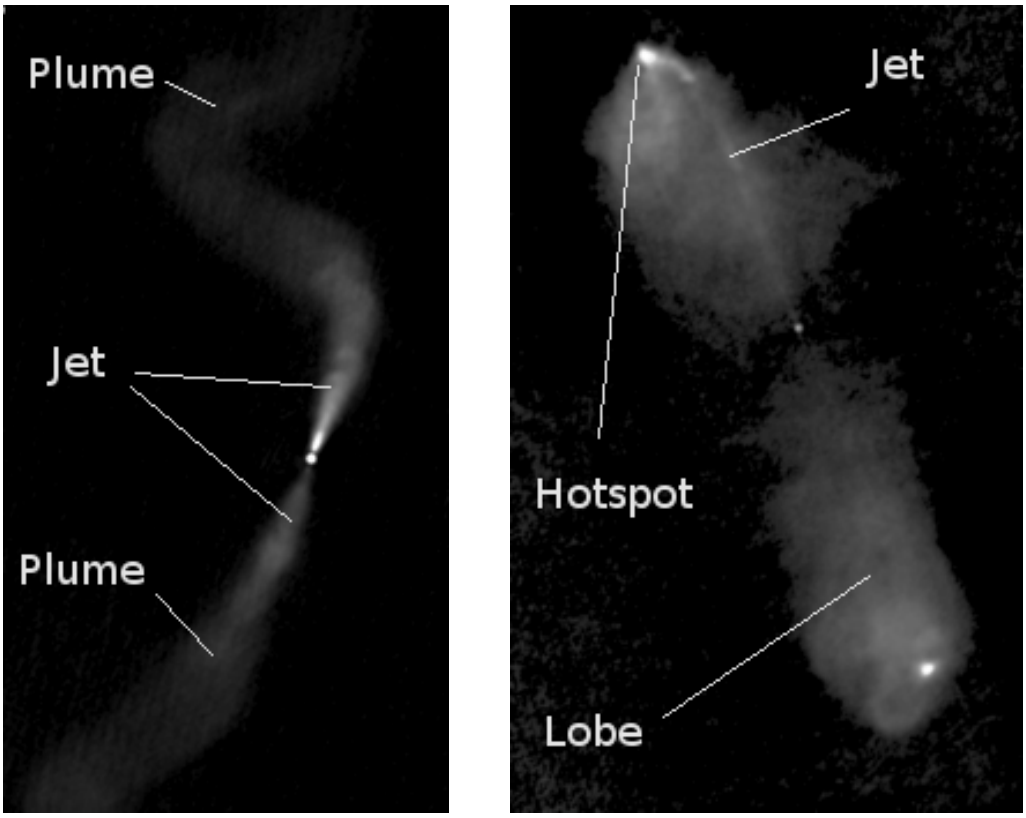

(a) FRI Radio Galaxy 3C31 (b) FRI Radio Galaxy 3C98

Figure 1.6: Figure demonstrating difference between FRI and FRII morphology (Hardcastle et al. 2003).

In 1974, Fanaroff and Riley proposed two further radio galaxy subclasses based on luminosity structure of their extended radio structure. FRI sources are most luminous near the core while FRII are most luminous near the edges. Fanaroff and Riley observed that there is a reasonably sharp divide in luminosity between the two classes: FRIs are low-luminosity, FRIIs are high luminosity. FRI objects typically have bright jets in the centre, while FRIIs have faint jets but bright hotspots at the ends of the lobes. A key difference between both types is the efficiency of energy transport, FRIIs are able to transport energy efficiently to the ends of the lobes resulting in the observed hotspots while FRI beams are inefficient in the sense that they radiate a significant amount of their energy away as they travel, which results in the high luminosity observed near their cores. Fig. 1.6 shows both a FRI radio galaxy and a FRII radio galaxy for quick comparison.

Radio galaxies represent a small subset of all AGNs with only $\approx 10\%$ of all AGN being radio loud.

Quasars

A quasi-stellar radio source (quasar) is an AGN with broad emission lines at high redshift. Only 5% - 10% of quasars are strong radio sources. Quasars tend to have radio structures consisting of jets and lobes similar to what is observed in radio galaxies. 3C 273 was the first quasar to be discovered in 1963 by Matthews & Sandage. At first it was believed to be a variable star until Schmidt (1963), found it had a very high redshift of z=0.158, requiring it to have a luminosity of over 4 trillion solar luminosities. Quasars are the most luminous persistent objects in the observable Universe with over 10^5 found to date. The highest redshift quasar known (as of June 2011) is J1120+0641, with a redshift of 7.085, which corresponds to a proper distance of approximately 9 Gpc from Earth.

Blazars

Blazars are a subset of AGN that are highly variable at all wavelengths and feature comparable high and variable polarization. Every known blazar is also radio loud. The class is divided into 2 subclasses: BL Lac objects and optically violently variable (OVV) quasars. BL Lac objects are named for their prototype, BL Lacertae, an object once believed to be a variable star. Unlike OVVs, BL Lac objects have very weak emission and absorption lines. OVV quasars are also observed to have higher superluminal speeds than BL Lac objects in addition to different jet magnetic field structures. This suggests there are intrinsic physical differences between BL Lacs and OVV quasars. All blazars are believed to be AGN with a very strong relativistically beamed jet very close to our line of sight.

Seyfert Galaxies

Seyfert galaxies are normally spiral galaxies. They have a lower luminosity than quasars and, while having quasar like core, their host galaxy is clearly detectable. They are the most common type of nearby AGN and were the first type of AGN to be discovered by Seyfert in 1943. While radio quiet their radio emission is still believed to be due to synchrotron emission from a jet. Seyfert galaxies can be divided into 2 subclasses. Seyfert 1 galaxies have both broad and narrow emission lines in addition to strong ultraviolet (UV) and X-Ray emission. Seyfert 2 galaxies have only narrow emission lines and in addition to strong infra-red (IR) emission and weak UV and X-Ray emission. This IR emission is believed

to be due to dust near the nucleus absorbing radiation at other wavelengths and emitting IR radiation.

LINERS

Low Ionization Nuclear Emission Line Region galaxies (LINERS) are very common, found in nearly one half of all the observed spiral galaxies. They are spectroscopically similar to Seyfert 2 galaxies but have strong low-ionization lines. They can be divided into 2 subclasses. LINER 1 galaxies show broad line emission while LINER 2 galaxies do not. LINER galaxies are also sometimes referred to as low luminosity AGN (LLAGN) due to their relatively low luminosity.

1.2.4 AGN Unification

As demonstrated in Section 1.2.3 there are many different types of AGN which, while having many similarities, also demonstrate various different emission properties. This results in a very important question. Are the different types of AGN

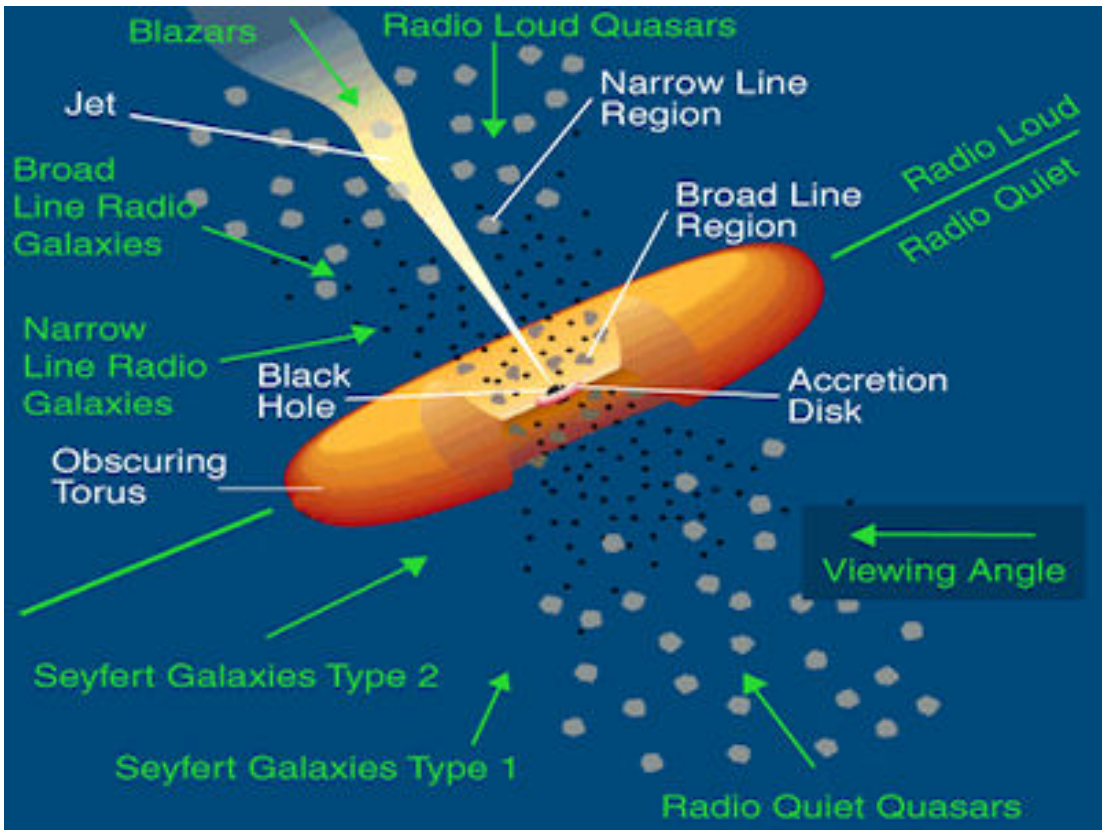

Figure 1.7: AGN Unification (Urry 2003)

fundamentally different or fundamentally the same?

It is now believed that all AGN consist of the 3 main components discussed in Section 1.4. Therefore, the observational differences in AGN are due to different central engine properties (black hole masses, accretion rates, etc) and, more importantly, different orientations of AGNs as viewed from Earth. This theory of a unified scheme of AGN was proposed by Antonucci (1993) and further developed by Urry & Padovani (1995). Fig. 1.7 demonstrates the different line of sight angles which correspond to different AGN types for this unified scheme.

The fundamental difference between radio loud and radio quiet objects is still not well understood. Currently, the most believed theory comes from the "spin paradigm" in which the power of the jet (and therefore, observed radio luminosity) is related to the spin of the central supermassive black hole. The most massive black holes reside in elliptical galaxies which are believed to have higher spin than lower mass black holes. This is believed to be due to the hierarchical growth structure of such galaxies, in which the most massive elliptical galaxies are the result of major mergers. These mergers trigger large amounts of accretion (with the same angular momentum direction) onto the central supermassive black hole resulting in the back hole spin increasing. In contrast to this, spiral galaxies are believed to have relatively low black hole spin due to the minor mergers with random angular momentum direction which occur during their growth.

It is important to note that the "spin paradigm" is not the only theory regarding the difference between radio loud and radio quiet AGN. For example, Fender et al (2004) demonstrated how the physical state of the accretion disk can have a direct influence on the generation of a strong radio jet.

Radio Galaxies

Both broad line radio galaxies (BLRG) and narrow line radio galaxies (NLRG) are observed in cases where the AGN synchrotron emission is being slightly beamed towards to the observer. Broad-line emission can be explained by the broad-line region being directly visible. A viewing angle roughly perpendicular to the plane of the torus will result in a BLRG while one roughly parallel will result in a NLRG as the optically thick dust torus obscures the broad-line region of the AGN. The difference between FRI and FRII radio galaxies is believed to be due to different central engine properties rather than different orientations. Specifically, Baum et al. (1995) suggest that FR I sources are AGN with low mass accretion rates

while FR II sources are AGN with high mass accretion rates. The higher mass accretion rate then accounts for the higher luminosity observed in FR II sources.

Quasars

Quasars are AGN which have viewing angles which are closer to being perpendicular to plane of the obscuring torus than BLRG. This results in a higher observed luminosity due to relativistic beaming.

Blazars

Blazars are AGN which have viewing angles which are almost perfectly perpendicular to the plane of the obscuring torus. As such, Blazars are very strongly relativistically beamed towards us. The difference between BL Lacs and OVVs is believed to be due to different central engine properties. Similarly to FRI and FRII radio galaxies, BL Lac objects are believed to be AGN with low mass accretion rates while OVVs are believed to be AGN with high mass accretion rates.

Seyfert Galaxies

The difference between Seyfert 1 and Seyfert 2 galaxies is identical to the difference between broad-line and narrow-line radio galaxies. However, unlike radio galaxies, Seyfert galaxies are usually found in radio quiet spiral galaxies. Seyfert galaxies are additionally important as they offered the first observational evidence for the unified scheme of AGNs when Antonucci (1982) detected weak "hidden" broad line emission in the polarized radio emission of many Seyfert 2 galaxies. This diminished Seyfert 1 spectrum, while normally overwhelmed by the direct Seyfert 2 spectrum, is believed to come from light that reaches us indirectly by reflection from the interstellar medium outside the nucleus. This reflection results in the Seyfert 1 spectrum being polarized.

LINERs

LINERS are not normally discussed when describing a unified scheme of AGN. This is because there is still great debate as to whether LINERs really do represent low luminosity AGN or if they are something else. For example, the low-ionization

lines observed in LINERs are also observed in both starburst galaxies and in H II regions.

1.3 AGN Jets

As discussed previously, the radio lobes of AGN are produced by jets of charged particles ejected from the central engine at highly relativistic velocities. Figure 1.8 describes more than half of an AGN; the other half is presumed to be essentially identical. The geometry of the accretion flow within a few tens of gravitational radii ($R_S = \frac{2GM}{c^2}$) is unknown.

1.3.1 Jet Launching

Magnetic launching is considered to be the driving force behind most relativistic jets in AGN. The differential rotation of the ergosphere (the region around a rotating black hole from which it is possible to extract energy and mass) of a rotating black hole and/or accretion disk causes the component of the magnetic field lines of the accreting matter to wind up into a helix. The toroidal component of this magnetic field, provides a pinching force directed toward the jet axis. The magnetic field expands with distance from the black hole, lowering the magnetic pressure. This creates a strong pressure gradient along the axis, which accelerates the plasma flow and produces the jet. The magnetic acceleration essentially stops when the kinetic energy density of the particles reaches equipartition with the magnetic energy density.

1.3.2 Structure of an AGN Jet

The standard structure of an AGN jet consists of an unresolved or barely resolved "core" from which a jet protrudes. Such jets come in a range of different shapes, long or short, straight or very sharply curved. Many jets are smooth while others are dominated by strong knots. The majority of such knots move at apparent superluminal velocities (see Section 1.3.3).

Projection effects shorten the jets pointing within several degrees to the line of sight so that they appear broader, shorter and more sharply bent. Images of FR I and FR II radio galaxies (Fig. 1.6) which are believed to be AGNs observed at

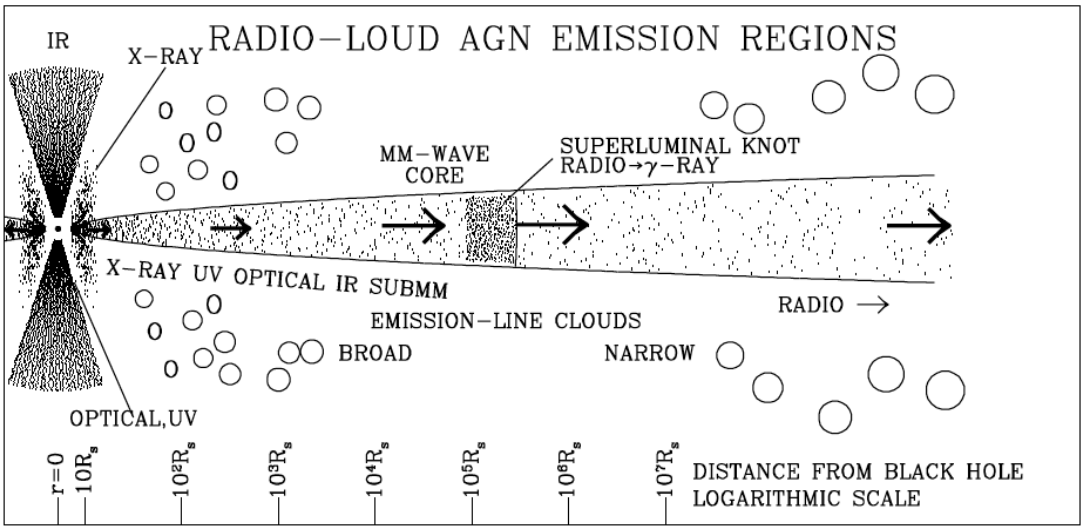

Figure 1.8: Sketch of the various sites of emission in an active galactic nucleus with a relativistic jet. The density of the dots signifies in a qualitative way the intensity of emission. The radiation produced in the jet is relativistically beamed, while the emission from outside the jet is not. The length of the arrows indicates the Lorentz factor of the flow. The logarithmic scale of approximate distance from the black hole is measured in Schwarzschild radii. (Marscher 2006)

large angle to the line of sight feature predominantly straight jets. Therefore, the jets of all AGN jets are believed to be bent by less than a few degrees in three dimensions.

1.3.3 Superluminal Motion

VLBI observations have established the presence of multiple bright components or 'knots' in the relativistic jets of AGN. Repeated observations of these AGN often show proper motions for these components with observed velocities in excess of the speed of light. The most likely explanation for this apparent 'superluminal' motion is that these velocities are attributable to bulk relativistic motion along the line of sight to the source (Blandford, McKee and Rees 1977).

Fig. 1.9 shows the geometry of this model. An observer at A initially observes two components at point B at time t'_1 after the light has transversed the distance $|AB|$. At a later time $t_2 = t_1 + \delta t$ one of the two components has moved some distance $v\delta t$. The observer retakes observations of both components at time t'_2. The angular separation between the two components at the second observation is

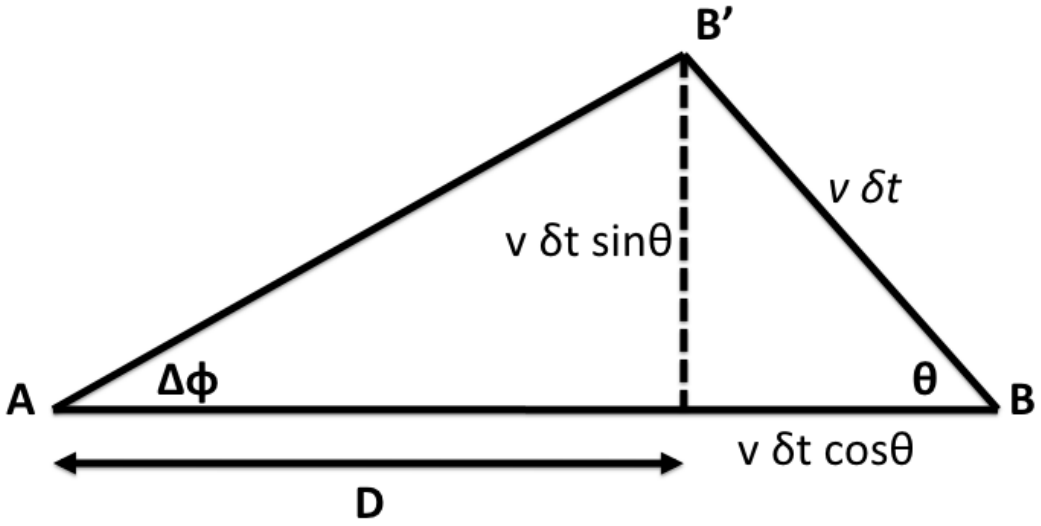

Figure 1.9: The geometry assumed to explain apparent superluminal motion in the jets of AGN. The observer at A sees the radio emitting component move from B to B' at a speed apparently exceeding the speed of light.

$$\Delta\phi = \frac{v\delta t \sin\theta}{D} \tag{1.1}$$

The times that the observer measures between the two observations are given by

$$t_1' = t_1 + \frac{D + v\delta t \cos\theta}{c} \tag{1.2}$$

$$t_2' = t_2 + \frac{D}{c} \tag{1.3}$$

Therefore the observer at A measures a time interval Δt of

$$\Delta t = t_2' - t_1' \tag{1.4}$$
$$= t_2 - t_1 - \frac{v\delta t \cos\theta}{c} \tag{1.5}$$
$$= \delta t(1 - \beta\cos\theta) \tag{1.6}$$

where $\beta = \frac{v}{c}$. The transverse velocity (v_T) inferred by the observer is then given by

$$\beta_T = \frac{v_T}{c} = \frac{D}{c}\frac{\Delta\phi}{\Delta t} = \frac{v\sin\theta}{c(1-\beta\cos\theta)} = \frac{\beta\sin\theta}{1-\beta\cos\theta} \tag{1.7}$$

Simple differentiation yields that the maximum value of β_T is given by

$$\beta_T^{max} = \beta\gamma \tag{1.8}$$

Accordingly as $\beta \to 1$, $\beta_T^{max} \simeq \gamma$ where γ can be arbitrarily high. Therefore, for relativistic bulk, motion superluminal motions far in excess of the speed of light can be observed.

1.3.4 Jet Matter Content

The particles which comprise the jets of AGN are not well understood. It is unclear if the jets are comprised of electrons and protons, electrons and positrons or some combination of both. Originally it was believed that ~ 80% of the positive particles in AGN jets were positrons. This was due to the relatively high levels of circularly polarized emission observed in the core of 3C 279. This polarization was believed to be due to Faraday conversion, in which some of the linearly polarized synchrotron emission was converted to circularly polarized emission by jet electrons and positrons in the presence of a magnetic field (Wardle et al. 1998) However, Ruszkowski & Begelmann (2002) showed that a turbulent magnetic field in a plasma consisting of only electrons and protons could also produce the high levels of observed circularly polarization observed .

The detection of the 511 keV electron positron annihilation line would provide definitive evidence for the existence of positrons in AGN jets. In the jet itself, the line would be broadened beyond recognition due to Doppler line broadening.

However, it has been theorised that if an AGN jet was to mix with the interstellar medium of its host galaxy, its electrons and positrons would thermalise which would result in a narrowly peaked annihilation line. Such mixing has been detected in the radio galaxy 3C120. However, to date, any experiment to detect the redshifted 511 keV line has failed to do so. Accordingly, Marscher et al. (2007) suggests that positrons can compose no more than 10% of the positive particles in the jets of AGN.

The number density of a typical AGN jet is estimated to be 1 cm^{-3} (for a pure electron-proton jet) to 10^2 cm^{-3} (for a pure electron-positron jet).

1.3.5 Jet Magnetic Field

As discussed in Section 1.3.1, the magnetic field threading the jets of AGN are expected to have a tight helical geometry close to the black hole. At the end of this acceleration and collimation zone, current driven instabilities mix the field into a more chaotic configuration.

As in any spherical or conical flow in which magnetic flux is conserved, the longitudinal component of the magnetic field decreases as R^2 while the transverse component of the magnetic field decreases as R^1. There are numerous examples of extended jets in which the expected transition from longitudinal to transverse magnetic field is evident in the linear polarization (Bridle 1984). However, comparison of simulated and observed polarization indicates that, while the toroidal to longitudinal magnetic field ratio does increase with distance down the jet, the gradient in the ratio is not as steep as predicted in the case of a magnetic field that is frozen into the plasma (Laing et al. 2006). There is instead a substantial component of disordered field that has a more complex behaviour.

The magnetic field strength of a typical magnetic field threading an AGN jet is estimated to be ~ 1 Gauss at sub parsec scales. This magnetic field strength then decreases with distance from the jet launching region as described in the previous paragraph.

1.4 Synchrotron Radiation

1.4.1 Synchrotron Emission

The primary reference for material in this section was 'Radiative Processes in Astrophysics' by George B. Rybicki and Alan P. Lightman (1985).

AGN emit over most of the electromagnetic spectrum. As such, they are unable to be modelled by a blackbody at a single temperature. In order to correctly model AGN, non-thermal processes must be taken into account. Originally the continuum emission from AGN was believed to be a power law in frequency described by

$$F_\nu \propto \nu^{-\alpha} \tag{1.9}$$

where F_ν is the monochromatic flux at the frequency ν and α is known as the spectral index. Relativistic electrons spiralling around a magnetic $\mathbf{B}$ field can produce such a continuum (with constant α) through a non-thermal process in which these electrons lose energy via synchrotron radiation.

The motion of a relativistic charged particle moving through a electromagnetic field is governed by the following equations:

$$\frac{d}{dt}(\gamma m\mathbf{v}) = q\mathbf{v}\times\mathbf{B} \tag{1.10}$$

$$\frac{d}{dt}(\gamma mc^2) = q\mathbf{v}\cdot\mathbf{E} \tag{1.11}$$

where γ is the Lorentz factor, m is the mass, q is the charge and $\mathbf{B}$ is the magnetic field. It is widely believed that a magnetic field is formed in AGN as a result of the rotation of the hot accretion disk surrounding the central black hole. The forces due to this magnetic field dominate the forces due to the electric field. For this reason we can make the assumption that

$$\frac{d}{dt}(\gamma mc^2) = q\mathbf{v}\cdot\mathbf{E} = 0 \tag{1.12}$$

This implies that γ is a constant and, as γ is a function of v^2, $|\mathbf{v}|$ must also be a constant. The equations of motion for the components of the velocity parallel

and perpendicular to the magnetic field are given by

$$\frac{d\mathbf{v}_{\parallel}}{dt} = 0 \tag{1.13}$$

$$\frac{d\mathbf{v}_{\perp}}{dt} = \frac{q}{\gamma mc}\,\mathbf{v}_{\perp} \times \mathbf{B} \tag{1.14}$$

As both $|\mathbf{v}|$ and $\mathbf{v}_{\parallel}$ have been shown to be constant, $\mathbf{v}_{\perp}$ must also be constant. Therefore, Equation 1.6 describes uniform circular motions in the plane normal to $\mathbf{B}$. As $\mathbf{v}_{\parallel}$ is constant the particles follow a helical path about the magnetic field lines with a gyration frequency given by

$$\omega_B = \frac{qB}{\gamma m} \tag{1.15}$$

where ω_B is the gyration frequency and $B = |\mathbf{B}|$ is the magnetic field strength.

The Larmor formula describes the power radiated by a charged particle in its rest frame. It is given by

$$P = \frac{2e^2}{3c^3}\mathbf{a} \cdot \mathbf{a} \tag{1.16}$$

where P is the magnitude of the radiated power and $\mathbf{a}$ is the acceleration in the rest frame of the particle. This may be rewritten using Equation 1.6 as

$$P = \frac{2e^2 a_{\perp}^2}{3c^3} = \frac{2e^2}{3c^3}\left(\frac{eB}{\gamma mc} v_{\perp}\right)^2 \tag{1.17}$$

If we define the pitch angle (ϕ) to be the direction between the magnetic field and the electron velocity this can be written as

$$P = \sigma_T \beta_{\perp}^2 \gamma^2 c U_B \sin^2\theta \tag{1.18}$$

where σ_T is the Thompson cross section of the particle, $\beta_{\perp} = v_{\perp}/c$ and the magnetic field energy density, $U_B = B^2/8\pi$. The estimated lifetimes of the relativistic electrons in AGN producing this synchrotron radiation are of the order of a million years. Therefore, the distribution of their pitch angles, θ, is expected to gradually become random as they are repeatedly scattered by other charged particles in their environment in addition to random magnetic field fluctuations.

The average synchrotron power per electron is thus dependant on a group of electrons with the same Lorentz factor, γ, but different, random, pitch angles, θ. Therefore

$$\langle P \rangle = \sigma_T \beta_\perp^2 \gamma^2 c U_B \ \langle \sin^2 \theta \rangle \tag{1.19}$$

$$\langle \sin \phi^2 \rangle = \frac{\int \sin \phi^2 d\Omega}{\int d\Omega} = \frac{1}{4\pi} \int_0^{2\pi} \int_0^{\pi} \sin^3 \theta \ \mathrm{d}\theta \ \mathrm{d}\phi = \frac{2}{3} \tag{1.20}$$

$$\langle P \rangle = \frac{4}{3} \sigma_T \beta_\perp^2 \gamma^2 c U_B \tag{1.21}$$

Relativistic effects result in the emitted synchrotron radiation being beamed sharply in the direction of motion as β approaches 1. The angular distribution of power in the observer's frame of reference is given by

$$\frac{dP}{d\Omega} = \frac{e^2 a_\perp^2}{4\pi c^3} \frac{1}{1 - \beta \cos \theta} \left(1 - \frac{\sin \theta^2 \cos \phi^2}{\gamma^2 (1 - \beta \cos \theta)^2} \right) \tag{1.22}$$

Here θ is the angle between the emitted photon and the direction of motion of the particle and ϕ is the azimuthal angle. For highly relativistic motion ($\gamma >> 1$) this equation can be approximated to

$$\frac{dP}{d\Omega} = \frac{4e^2 a_\perp^2}{\pi c^3} \gamma^8 \left(\frac{1 - 2\gamma^2 \theta^2 \cos 2\phi + \gamma^4 \theta^4}{(1 + \gamma^2 \theta^2)^6} \right) \tag{1.23}$$

The full derivation of this expression can be found in Rybiki & Lightman (1979), Chapter 4. This expression depends on θ solely through the combination of $\gamma\theta$. It can be shown that the peak of this relativistic beaming occurs for $\theta = 1/\gamma$. The synchrotron radiation is therefore sharply beamed in the forward direction.

1.4.2 Synchrotron Spectrum

Rybiki & Lightman (1979) gives the synchrotron power spectrum of a single electron as

$$P(\nu) = \frac{\sqrt{3} e^3 B \sin \phi}{mc^2} \frac{\nu}{\nu_c} \int_{\frac{\nu}{\nu_c}}^{\infty} K_{5/3}(\xi) \ \mathrm{d}\xi \tag{1.24}$$

where $K_{5/3}(\xi)$ is a Bessel function and ν_c is the critical frequency given by

$$\nu_c = \frac{3\gamma^2 eB\sin\phi}{2mc} \tag{1.25}$$

A synchrotron source is said to be optically thick if the optical depth, τ_ν (the negative natural logarithm of the fraction of radiation that is not scattered or absorbed on a path) is greater than 1 and optically thin if τ_ν is less than 1. The low frequency spectrum of an optically thin synchrotron source is the superposition of the spectra from individual electrons (Fig. 1.11). This part of the spectrum is unable to rise more steeply than the frequency to the $\frac{1}{3}$ power.

Observed AGN display power law energy distributions given by

$$N(E)\ \mathrm{d}E = CE^{-p}\ \mathrm{d}E \tag{1.26}$$

where C is some constant that can vary with pitch angle and p is the particle distribution index. Using this with Eqn. 1.16 gives the total power radiated per unit volume per unit frequency by integrating over all the energies of the above power law distribution multiplied by the single particle emission.

$$P_{total}(\nu) = C\int_{E_1}^{E_2} P(\nu)E^{-p}\ \mathrm{d}E \tag{1.27}$$

Ginzburg & Syrovatskii (1965) give the following expression for synchrotron energy

$$\gamma = \frac{E}{mc^2} = \left(\frac{2mc}{3eB\sin\phi}\right)^{\frac{1}{2}} \nu^{\frac{1}{2}} \left(\frac{\nu}{\nu_c}\right)^{\frac{1}{2}} \tag{1.28}$$

This equation demonstrates that the majority of the synchrotron emission from a single electron is emitted at a specific frequency, the critical frequency, ν_c given in Eqn. 1.25. This is clearly demonstrated in Fig. 1.10 which shows that the function $F(x)$, which is defined below and directly proportional to the energy of emitted synchrotron emission, is very sharply peaked at this critical frequency. This results in

$$E^{-p}\ dE = -\frac{1}{2}\left(\frac{2m^3c^5}{3eB\sin\phi}\right)^{\frac{1-p}{2}} \nu^{\frac{1-p}{2}} \left(\frac{\nu}{\nu_c}\right)^{\frac{p-3}{2}} \nu_c\ \ \mathrm{d}\nu \tag{1.29}$$

Writing ν/ν_c as x and using $F(x) \equiv x\int_x^\infty K_{5/3}(\xi)d\xi$ (see Fig. 1.10 and Fig. 1.11) we can now write Eqn. 1.19 as

$$P_{total}(\nu) = \left(\frac{2m^3c^5}{3eB\sin\phi}\right)^{\frac{1-p}{2}} \frac{\sqrt{3}e^3B\sin\phi}{mc^2}\nu^{\frac{1-p}{2}} \int_{x_1}^{x_2} x^{\frac{p-3}{2}}F(x)\ \mathrm{d}x \tag{1.30}$$

The limits of the integral present in the above equation can be approximated to $x_1 \approx 0$ and $x_2 \approx \infty$. Equation 11.4.22 of Abramowitz and Stegun (1965) gives the solution of an integral of this type. Using this gives

$$P_{total}(\nu) = \left(\frac{2m^3c^5}{3eB\sin\phi}\right)^{\frac{1-p}{2}} \frac{\sqrt{3}e^3B\sin\phi}{mc^2}\nu^{\frac{1-p}{2}}\ \Gamma\left(\frac{3p+19}{12}\right)\ \Gamma\left(\frac{3p-1}{12}\right) \tag{1.31}$$

where $\Gamma(z)$ is the Gamma function of argument z and is a constant. Writing (1-p)/2 as the spectral index α we obtain

$$P_{total}(\nu) \propto F_\nu \propto \nu^{-\alpha} \tag{1.32}$$

as described in Eqn. 1.1.

If the intensity of synchrotron radiation within a source becomes sufficiently high, then re-absorption of the radiation by the synchrotron emitting electrons becomes important. This re-absorption of radiation is termed as "synchrotron self absorption". Synchrotron self-absorption will drastically modify the spectrum of the source at low frequencies.

The radiative transfer equation taking re-absorption into account is given by

$$\frac{dI_\nu}{ds} = j_\nu - k_\nu I_\nu \tag{1.33}$$

where I_ν is the specific intensity at frequency ν. The emission coefficient, j_ν and the absorption coefficient, k_ν are given by

$$j_\nu = 4\pi P_{total}(\nu) \tag{1.34}$$

$$k_\nu = \frac{(p+2)c^2}{8\pi\nu^2}\int P(\nu)N(E)E^{-1}\ \mathrm{d}E \tag{1.35}$$

Repeating the same analysis procedure used in deriving Eqn. 1.23 gives the following

$$k_\nu = \frac{\sqrt{3}e^3}{8\pi m}\left(\frac{3e}{2\pi m^3 c^5}\right)^{\frac{p}{2}} C(B\sin\phi)^{\frac{p+2}{2}}\ \Gamma\left(\frac{3p+2}{12}\right)\Gamma\left(\frac{3p+22}{12}\right)\nu^{-\frac{p+4}{2}} \tag{1.36}$$

As optical depth increases so does the probability of synchrotron self-absorption occurring. For a large enough optical depth $\frac{dI_\nu}{ds} = 0$ and so $I_\nu = \frac{j_\nu}{k_\nu}$. In this case the frequency dependance of the synchrotron spectrum in the optically thick region becomes

$$\frac{\nu^{\frac{1-p}{2}}}{\nu^{-\frac{p+4}{2}}} = \nu^{\frac{5}{2}} \tag{1.37}$$

The synchrotron spectrum is therefore independent of the particle distribution index, p, in the optically thick part of the spectrum. The optically thick region occurs at low frequencies while the optically thin region occurs at higher frequencies. At a frequency known as the turnover frequency the spectrum transitions from optically thick to optically thin (Fig. 1.12). Knowledge of the value of this turnover frequency allows for the determination of many important physical parameters such a magnetic field strength (eg. Lobanov 1998)

1.4.3 Synchrotron Polarization

Synchrotron Radiation is also highly polarized. For a completely uniform magnetic field at a frequency at which the emission was optically thin the observed linear polarization would be 100% as every emitting electron would be moving in circles in planes perpendicular to the magnetic field. However, in nature, this "perfect case" will never be observed as, due to scattering, the emitting electrons will never all be moving uniformly in planes perpendicular to the magnetic field. In order to investigate the degree of linear polarization for synchrotron radiation we must investigate the case of a uniform magnetic field present in a region of relativistic electrons with a random distribution of pitch angles. In such a case, the degree of polarization (m) is given by

$$m = \frac{P_\perp - P_\parallel}{P_\perp + P_\parallel} \tag{1.38}$$

where $P_\perp$ and $P_\parallel$ are the synchrotron radiation powers perpendicular and parallel

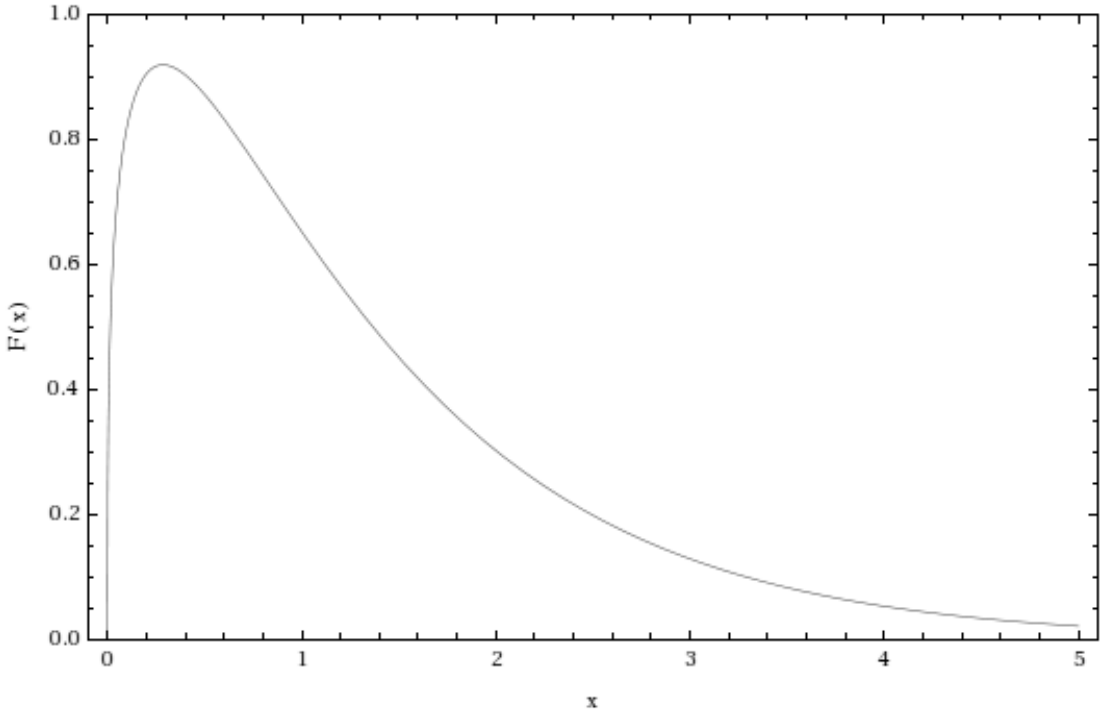

Figure 1.10: Plot of F(x) vs x where $x = \nu/\nu_c$. The majority of the radiation is emitted near the critical frequency (x=1)

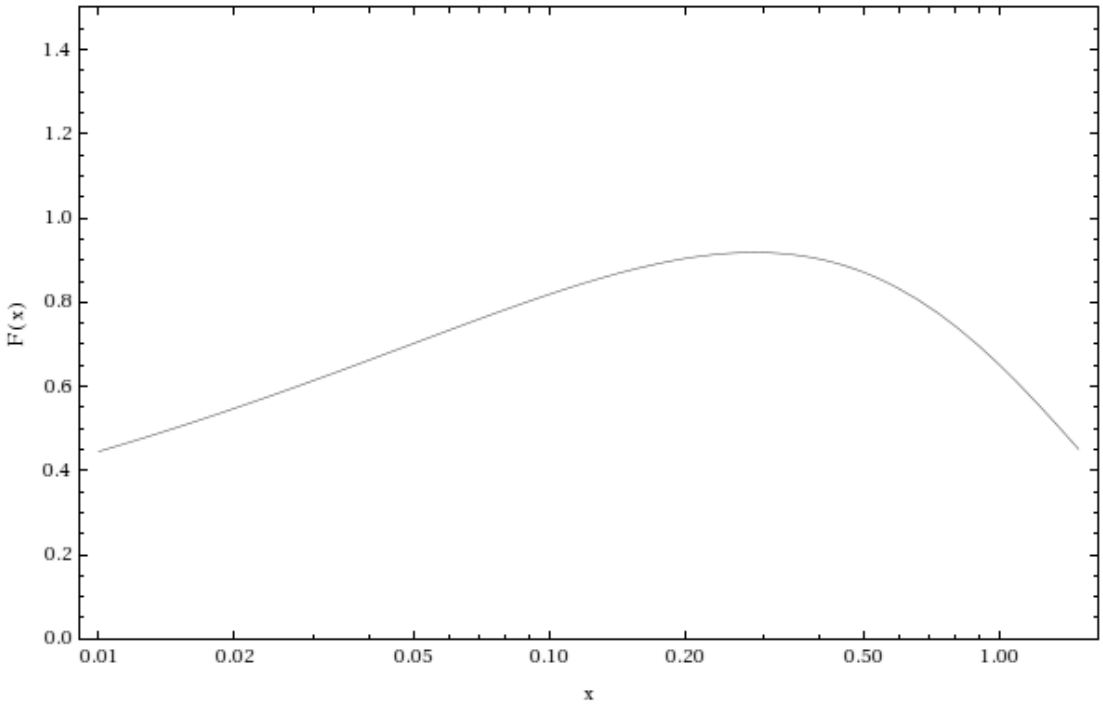

Figure 1.11: Plot of F(x) vs x where $x = \nu/\nu_c$ with a log scale on the x axis. The slope of this plot in its flat region is 1/3.

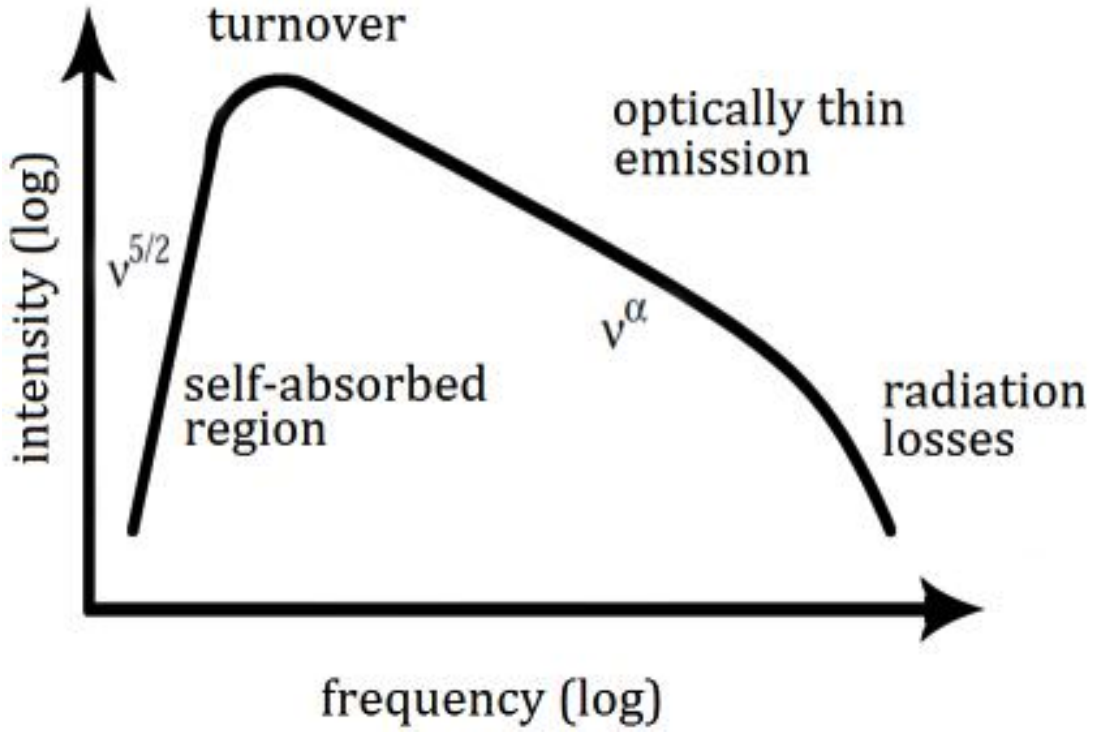

Figure 1.12: Synchrotron spectrum from a power-law distribution of relativistic electrons. Before the turnover frequency the emission region is optically thick (self absorbed) while after the turnover frequency it is optically thin. (Image from Special Astrophysical Observatory website http://www.sao.ru).

to the projection of the magnetic field on the plane of the sky. For the unrealistic case described in the previous paragraph there is no $P_{\parallel}$ which then results in a degree of polarization of 1.

Equations for both $P_{\perp}$ and $P_{\parallel}$ are given in Rybicki & Lightman (1979) Chapter 6. They are

$$P_{\perp} = \frac{\sqrt{3}e^3 B \sin\phi}{2mc^2}[F(x) + G(x)] \tag{1.39}$$

$$P_{\parallel} = \frac{\sqrt{3}e^3 B \sin\phi}{2mc^2}[F(x) - G(x)] \tag{1.40}$$

where, as before, $F(x) \equiv x\int_x^{\infty} K_{5/3}(\xi)d\xi$ and $G(x) \equiv x\int_x^{\infty} K_{2/3}(\xi)d\xi$. Thus, the degree of polarization, m, for particles with a power law distribution of energies (described by γ) is given by

$$m_{thin} = \frac{\int G(x)E^{-p}\,\mathrm{d}E}{\int F(x)E^{-p}\,\mathrm{d}E} = \frac{\int G(x)x^{\frac{p-3}{2}}\,\mathrm{d}x}{\int F(x)x^{\frac{p-3}{2}}\,\mathrm{d}x} \tag{1.41}$$

Table 1.1: Expected degrees of polarization (m), for both optical thin and thick regions, for different values of α. $\alpha = 0.7$ corresponds to the spectral index most commonly observed in AGN.

α	p	m_{thin}	m_{thick}
0.5	2.0	0.69	0.12
0.7	2.4	0.72	0.11
1.0	3.0	0.75	0.10

Integrating from $x = 0$ to $x = \infty$ and, again, using Abramowitz and Stegun (1965), this can be described by

$$m = \left(\frac{2^{\frac{p+1}{2}}}{p+1}\right)\left(2^{\frac{p-3}{2}}\left(\frac{p-3}{4}+\frac{4}{3}\right)\right)^{-1} = \frac{p+1}{p+\frac{7}{3}} = \frac{3-3\alpha}{5-3\alpha} \tag{1.42}$$

The observed polarization will be dominated by radiation polarized in the plane perpendicular to the magnetic field.

In the optically thick region of the synchrotron spectrum the polarized component perpendicular to the plane of the magnetic field is the component that has the highest probability of being reabsorbed by the self synchrotron process. Due to this, the parallel component of the polarization, while less likely to be emitted, dominates in the optically thick region.

In the optically thick region the absorption coefficient (split into its $\perp$ and $\parallel$ components) is given in Ginzburg & Syrovatskii (1969) as

$$k_\nu^\perp = k_\nu\left(1+\frac{p+2}{p+\frac{10}{3}}\right) \tag{1.43}$$

$$k_\nu^\parallel = k_\nu\left(1-\frac{p+2}{p+\frac{10}{3}}\right) \tag{1.44}$$

Therefore, the degree of polarization, m, in an optically thick region is given by

$$m = \left|\frac{P_\perp k_\nu^\perp - P_\parallel k_\nu^\parallel}{P_\perp k_\nu^\perp + P_\parallel k_\nu^\parallel}\right| = \frac{3}{6p+13} = \frac{3}{19+12\alpha} \tag{1.45}$$

In this case, the observed polarization will be dominated by radiation polarized in the plane parallel to the magnetic field.

Example degrees of polarization for typical spectral indices and a completely

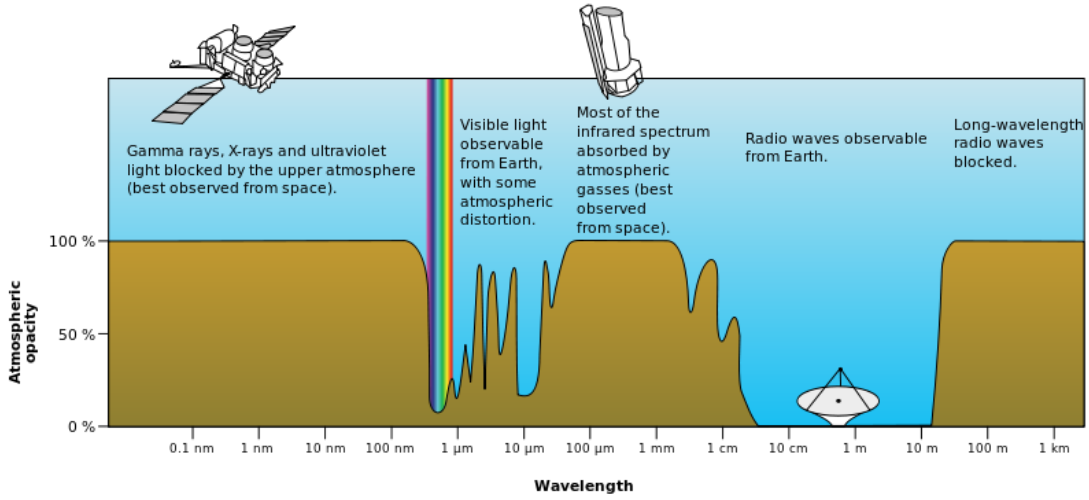

Figure 1.13: Electromagnetic opacity of the Earth's atmosphere. (Image from NASA's Astronomy Picture of the Day website http://apod.nasa.gov)

uniform magnetic field can be seen in Table 1.1.

1.5 Radio Astronomy

In order to study AGN or any other radio emitting astrophysical objects astronomers use radio telescopes. Observing astrophysical objects using radio telescopes offer many benefits over other types of telescope. Due to the long wavelengths of radio waves, radio radiation is less easily scattered than shorter wavelength radiation. Therefore, radio emission allows us to observe parts of the universe which would be obscured at other frequency ranges. The Earth's atmosphere has little effect on radio emission which allows the construction of ground based radio telescopes (Fig. 1.13). Observations at radio frequencies are also less affected by poor weather conditions as the wavelengths observed are long compared to the size of an average water droplet. Finally, while our Sun is a strong radio emitter, the radio emission from it is confined to a small part of the sky. Therefore, radio observations, for most sources, can be taken 24 hours a day.

However, while the relatively long wavelength of radio emission has many benefits for radio astronomy, it also adversely affects the maximum resolution achievable with a radio telescope. The angular resolution of any telescope is normally approximated as

Figure 1.14: Aerial View of the Arecibo radio telescope, Puerto Rico. (Image from NRAO website /http://www.nrao.edu)

$$\theta \approx \frac{\lambda}{D} \tag{1.46}$$

where θ is the angular resolution, λ is the observed wavelength and D is the diameter of the telescope.

Point-like sources separated by an angle smaller than the angular resolution cannot be resolved. In order to achieve an angular resolution of 0.1 arc-seconds at a wavelength of 520 nm (wavelength of yellow light) an optical telescope is required to be 1.2 m in diameter. To achieve the same resolution at radio wavelengths (for example, 2 cm) would require a radio telescope with a dish over 42 km in diameter. In contrast to this, the largest radio telescope in the world today is the Arecibo Observatory which has a diameter of only 305 m (Fig. 1.14).

The poor angular resolution of radio astronomy can be overcome by a technique known as radio interferometry in which two or more radio telescopes are used in conjunction.

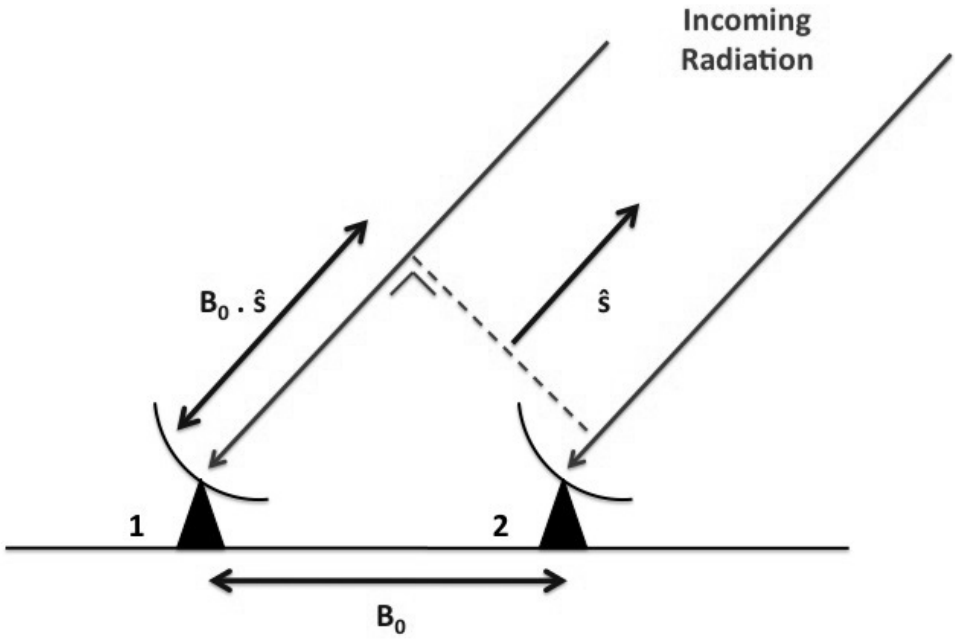

Figure 1.15: Radio Interferometry with 2 telescope array.

1.5.1 Radio Interferometry

In interferometry, a source is observed with two or more radio telescopes simultaneously. As the telescopes are separated spatially, radio emission from a source arrives at different antennae at different times. In much the same way that a Michelson interferometer produces fringes when non-synchronous light beams interfere constructively and destructively, radio fringes are formed by such an array of radio telescopes. These fringes are not detected directly since the beams arriving at 2 different antennae do not physically interfere with one another. Instead, the signals from pairs of antennas are combined electronically in a correlation process. This process was once done by specifically designed pieces of hardware called correlators. However, recent advances in computer technology has allowed for such correlation to be be done by significantly less expensive computers.

In order to understand how radio interferometry function we first consider the simplest case, a two element interferometer observing a point source (Fig. 1.15). The vector connecting the two antennae is known as the baseline, $\mathbf{B_0}$. The incoming light from the very distance point source can be assumed to be parallel and the direction to this source is given by the unit vector $\hat{\mathbf{s}}$. The path difference

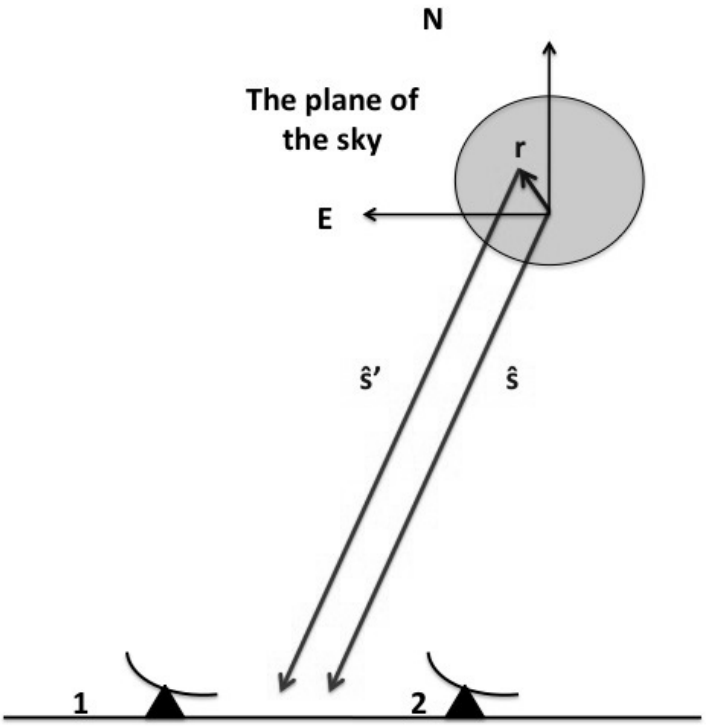

Figure 1.16: Response of an interferometer to an extended source.

between two incoming light waves is therefore given by $\mathbf{B_0} \cdot \hat{\mathbf{s}}$. The voltages induced at both antennae by the incoming radio waves can be written as

$$v_1 \propto E \cos \omega(t + \tau)$$
$$v_2 \propto E \cos \omega t$$

where $\tau = \frac{\mathbf{B_0} \cdot \hat{\mathbf{s}}}{c}$, ω is the angular frequency of the incident radiation and c is the speed of light.

The correlator then calculates the time average of the product of the first induced voltage with the complex conjugate of the second induced voltage. The response of this interferometer to this point source is given by

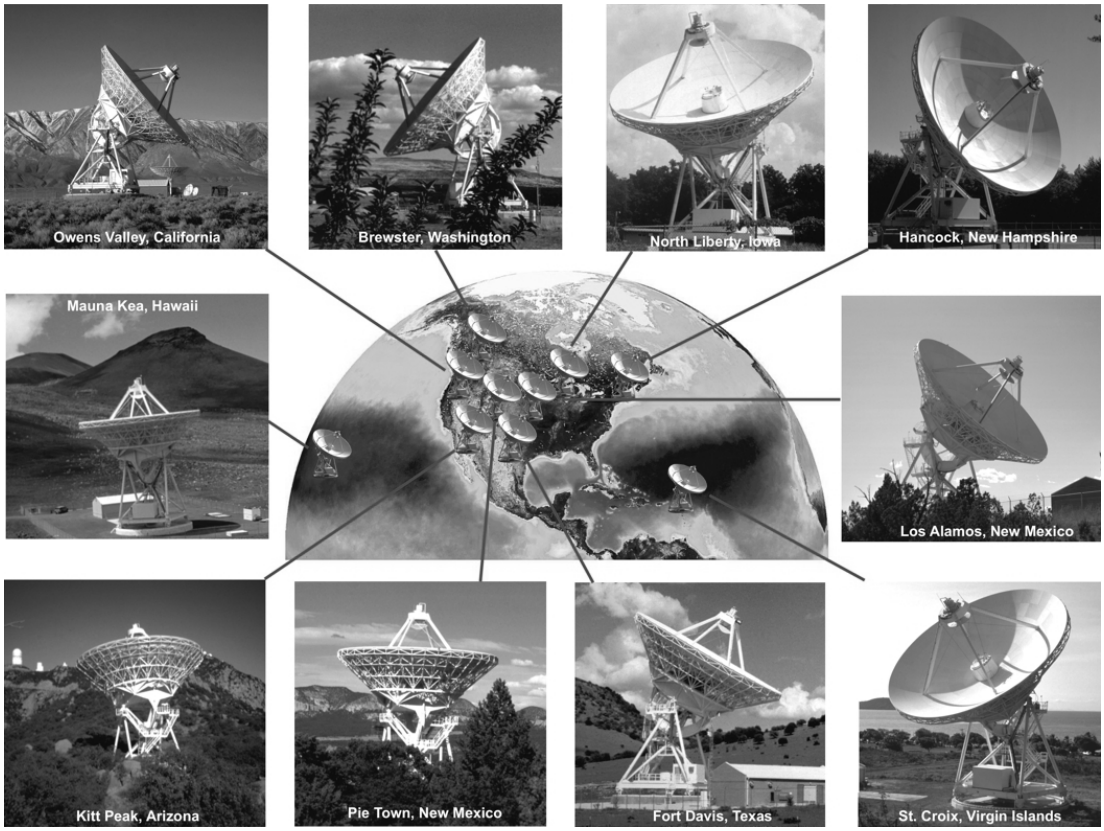

Figure 1.17: The ten radio telescopes of the Very Long Baseline Array (VLBA). (Image from NRAO website /http://www.nrao.edu)

$$\begin{aligned}
\langle v_1 v_2^* \rangle &\propto \langle E^2 \cos\omega t \cos\omega(t+\tau) \rangle \\
&\propto E^2(\cos\omega\tau\langle\cos^2\omega t\rangle - \sin\omega\tau\langle\cos\omega t\sin\omega t\rangle) \\
&\propto E^2\cos\omega\tau \\
&\propto I\cos\left(\tfrac{2\pi c}{\lambda}\tfrac{\mathbf{B_0}\cdot\hat{\mathbf{s}}}{c}\right) \\
&\propto I\cos\left(2\pi\mathbf{B}\cdot\hat{\mathbf{s}}\right)
\end{aligned}$$

where $I = E^2$ and $\mathbf{B} = \frac{\mathbf{B_0}}{\lambda}$, the baseline vector in units of the observing wavelength.

In the case of an extended source rather than a point source, the correlation between voltages induced by different parts of the source is taken to be zero since they are incoherent. The response of the correlator, in this case, is the sum of the contributions from each point of emission in the extended source. If $\mathbf{s'}$ is a vector pointing from Earth to a point of emission in an extended source then this can be expressed as the sum of a vector towards a reference point in that source ($\mathbf{s}$) and some other vector in the plane of the sky ($\mathbf{r}$). This gives, as seen in Fig.

1.16,

$$\mathbf{s}' = \mathbf{s} + \mathbf{r} \tag{1.47}$$

As the source can be assumed to be very far away $|\hat{\mathbf{s}}'| \simeq |\hat{\mathbf{s}}|$ this may be rewritten as

$$\hat{\mathbf{s}}' = \hat{\mathbf{s}} + \mathbf{a} \tag{1.48}$$

where $\mathbf{a} = \frac{\mathbf{r}}{|\mathbf{s}|}$ and the other two vectors are now unit vectors. For such an extended source, the response of the correlator to the emission at $\mathbf{s}'$ is proportional to

$$I(\mathbf{a}) \cos\left(2\pi \mathbf{B} \cdot (\hat{\mathbf{s}} + \mathbf{a})\right) \tag{1.49}$$

The total response is then given by the integral over the entire source. In complex notation this is written as

$$\langle v_1 v_2^* \rangle \propto \int I(\mathbf{a}) e^{(2i\pi \mathbf{B}\cdot(\hat{\mathbf{s}}+\mathbf{a}))} \, \mathrm{d}\mathbf{a} \tag{1.50}$$

$$\propto e^{2i\pi \mathbf{B}\cdot\hat{\mathbf{s}}} \int I(\mathbf{a}) e^{2i\pi \mathbf{B}\cdot\mathbf{a}} \, \mathrm{d}\mathbf{a} \tag{1.51}$$

$$\propto e^{2i\pi \mathbf{B}\cdot\hat{\mathbf{s}}} V(\mathbf{B}) \tag{1.52}$$

Here, $V(\mathbf{B})$ is known as the visibility function, the Fourier transform of the sky brightness distribution $I(\mathbf{a})$. As $\mathbf{a}$ is approximately perpendicular to $\hat{\mathbf{s}}$ it is possible to use coordinates in the plane of the sky. $\mathbf{B} \cdot \mathbf{a} \simeq \mathbf{b} \cdot \mathbf{a} \simeq$ where $\mathbf{b}$ is the projection of $\mathbf{B}$ in the plane of the sky. By taking two perpendicular axes in the plane of the sky (convention is to take North and East) $\mathbf{b}$ can be described by (u, v) while $\mathbf{a}$ can be described by (l, m) (Fig. 1.18). The brightness distribution and visibility function can now be written as a 2D Fourier pair.

$$V(u, v) = \int I(l, m) e^{2i\pi(ul+vm)} \, \mathrm{d}l \, \mathrm{d}m \tag{1.53}$$

$$I(l, m) = \int V(u, v) e^{-2i\pi(ul+vm)} \, \mathrm{d}u \, \mathrm{d}v \tag{1.54}$$

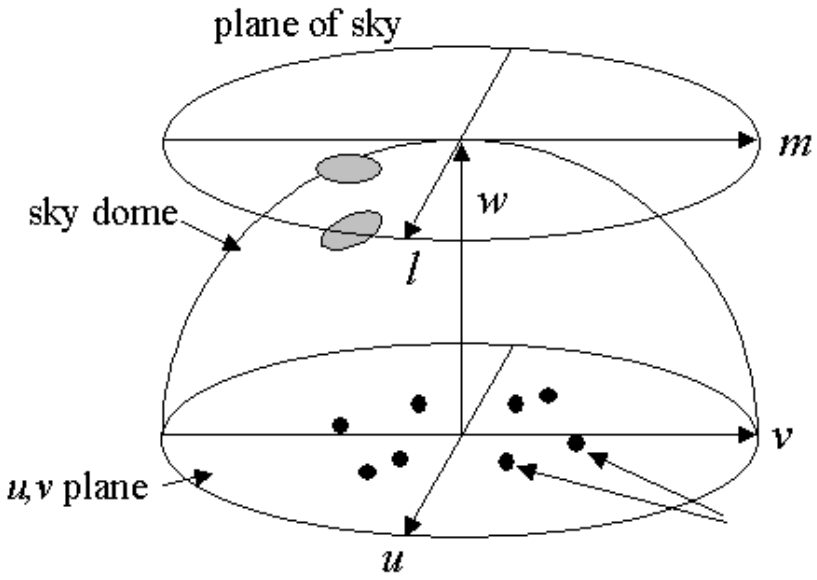

Figure 1.18: The (u, v) and (l, m) coordinate system (from the Radio Astronomy lecture notes of Prof. Dale Gary, New Jersey Institute of Technology)

As $V(u, v)$ and $I(l, m)$ are Fourier pairs, a baseline of length u will correspond to a sky scale of $l \simeq \frac{1}{u}$. Thus, an interferometer with antennae separated by a distance B_0 has an effective angular resolution of

$$\theta \approx \frac{\lambda}{B_0} \tag{1.55}$$

For an array of multiple antennae, B_0 is replaced by the maximum baseline of the array. The poor effective resolution of a radio telescope is, therefore, countered by using multiple such telescopes in an array.

A radio telescope array known as the Very Long Baseline Array (VLBA) was used to take the observations used throughout this thesis. The VLBA consists of 10 25m radio dishes stretching from Mauna Kea on the Big Island of Hawaii to St. Croix in the U.S. Virgin Islands. The VLBA has a maximum baseline of about 8,611 kilometres. (See Fig. 1.17)

1.5.2 The CLEAN Algorithm

In practice, astronomers do not know the complete visibility function $V(u, v)$. Instead parts of this visibility function are measured at discrete pairs of values

of u and v corresponding to the available baselines (Fig. 1.19). The sampled visibility function $S(u,v)V(u,v)$ is the actual data provided by the array, and by performing the inverse Fourier Transform we recover the "dirty image" $I_D(l,m)$, given by

$$I_D(l,m) = \int S(u,v)V(u,v)e^{-2i\pi(ul+vm)}dudv \tag{1.56}$$

The convolution theorem states that the Fourier Transform of a product of two functions is the convolution of the Fourier Transforms of the individual functions, and vice versa. Hence,

$$I_D(l,m) = \int V(u,v)e^{-2i\pi(ul+vm)}dudv \ * \int S(u,v)e^{-2i\pi(ul+vm)}dudv \tag{1.57}$$

$$= I(l,m) \ * \int S(u,v)e^{-2i\pi(ul+vm)}dudv \tag{1.58}$$

$$= I(l,m) \ * \ B(l,m) \tag{1.59}$$

where $I(l,m)$ is the brightness distribution of the source and $B(l,m)$ is known as the "dirty beam" and $*$ denotes convolution. $B(l,m)$ is also the image that would be obtained if a unit point source at the phase centre was observed. For this reason it is also known as the point source function (PSF).

The dirty map is therefore made up from the sum of dirty beam patterns at each point of emission in a source. Sidelobes appear in the dirty beam as the result of gaps in (u,v) coverage and effectively put a limit on the resolution on the observations. By maximising (u,v) coverage these sidelobes are minimised. An array of N radio telescopes consists of $\frac{N(N-1)}{2}$ baselines. If observations are taken over a relatively long time period the rotation of the Earth builds up additional values in the (u,v) plane as the orientation of the telescopes towards the source changes.

While sidelobes can be minimised by maximising (u,v) coverage they cannot be removed completely and, as such, it is very important to distinguish between the real source emission and the fake emission observed as a result of these sidelobes.

Högbom (1974) developed an algorithm known as the CLEAN algorithm to reconstruct the brightness distribution from the dirty map. The algorithm removes any fake emission associated with the sidelobes of the beam.

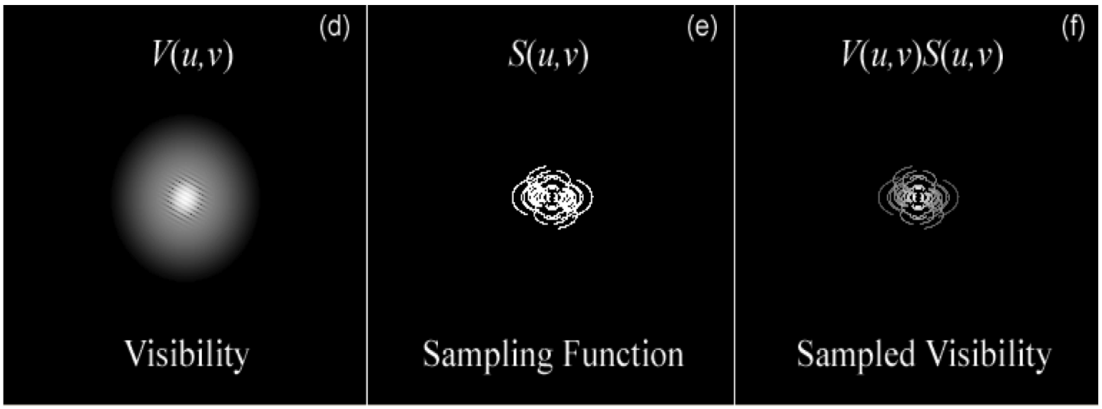

Figure 1.19: Figure describing what is meant by Sampled Visibility (from the Radio Astronomy lecture notes of Prof. Dale Gary, New Jersey Institute of Technology).

The CLEAN algorithm works as follows (see Fig. 1.20),

1. The UV data is gridded and a Fast Fourier Transform (FFT) of this data is constructed. This produces the dirty map.
2. The peak of the dirty map is located. The peak value and location of this emission is recorded in a table of "CLEAN Components". This step is normally restricted to smaller areas of the map if there is some reason to believe that the true emission is confined there.
3. Subtract from the dirty image at this location the dirty beam B multiplied by peak strength and gain factor $g < 1$.
4. Go to (2) and repeat unless the new remaining peak is below some user-specified level. The remaining map is known as the residual map.
5. Convolve the accumulated point source model (CLEAN components) with an idealised CLEAN beam usually an elliptical Gaussian of the same size and shape as the inner part of the dirty beam.
6. Add the residual map from step (4) to this CLEAN image.

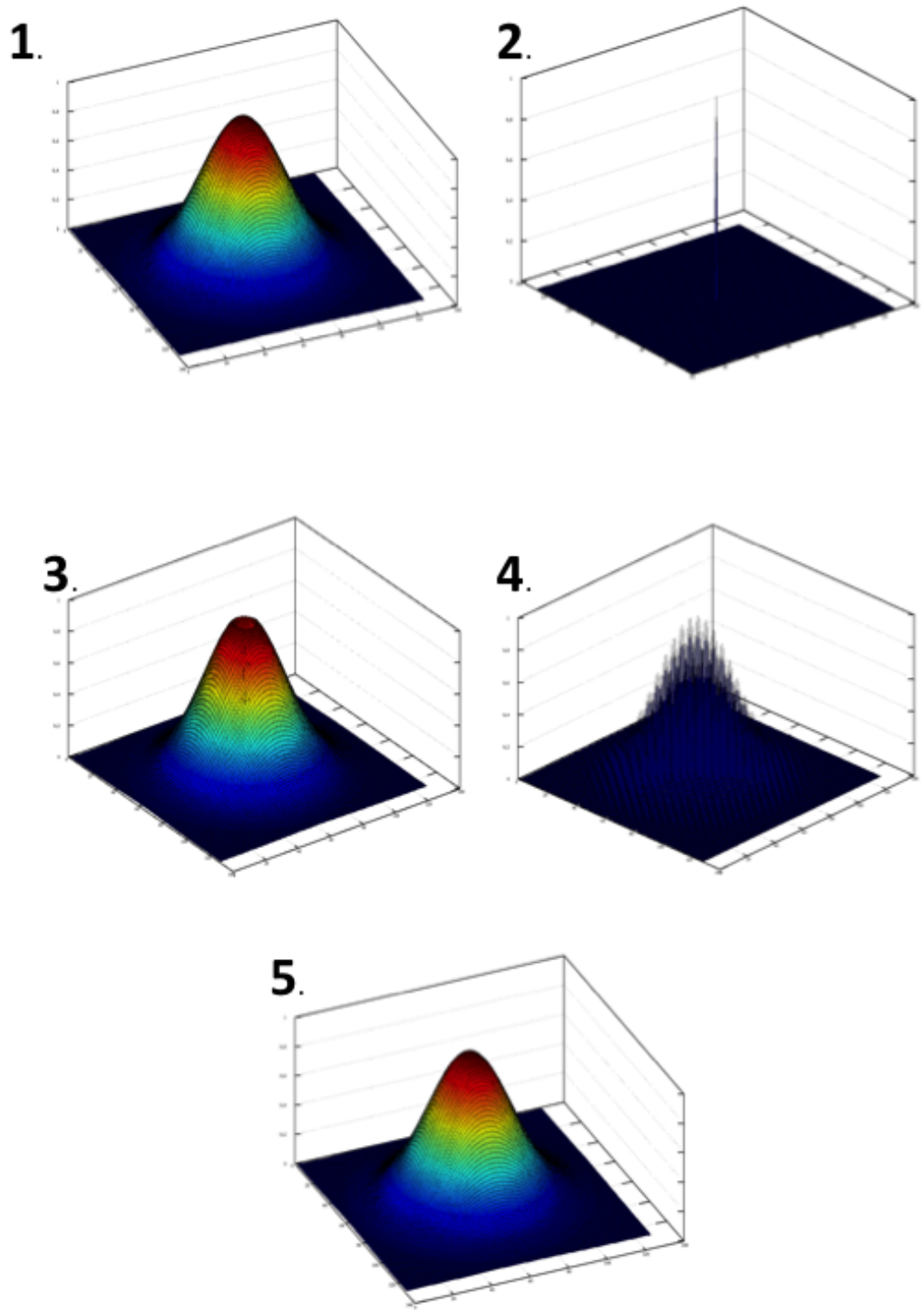

Figure 1.20: Highly idealised description of the CLEAN algorithm. The peak of the dirty map (1.) is found and added to a table of "CLEAN components" (2.). The dirty beam multiplied by the peak strength and the gain and subtracted from the dirty map (3.). This is repeated until a complete table of "CLEAN components" is found (4.). This table is convolved with the restoring beam to produce the final CLEANed image (5.)

1.5.3 Polarization Observations using Interferometry

Of special importance for the work carried out in this thesis is polarization observations taken using radio interferometry.

Each antenna in the radio telescope array has two feeds, one which responds to right circularly polarized (RCP) radiation and one which responds to left circularly (LCP) polarized radiation. Therefore, it is possible to construct the distribution of polarized radiation from a source in addition to the previous brightness distribution of that source. While, in theory, it is possible to construct both circularly polarized and linearly polarized maps of the source, the fraction of the incident radiation which is circularly polarized is almost negligible.

The Stokes parameters, introduced by Sir George Stokes in 1852, offer an alternative method of completely specifying the polarization of radiation. As these parameters are easier to use and more intuitive than directly dealing with RCP and LCP the radio astronomy community have adopted them.

The 4 Stokes parameters (I, Q, U & V) are given by.

$$I = \langle E_A^2 \rangle + \langle E_B^2 \rangle = \langle E_C^2 \rangle + \langle E_D^2 \rangle = \langle E_R^2 \rangle + \langle E_L^2 \rangle \tag{1.60}$$

$$Q = \langle E_A^2 \rangle - \langle E_B^2 \rangle \tag{1.61}$$

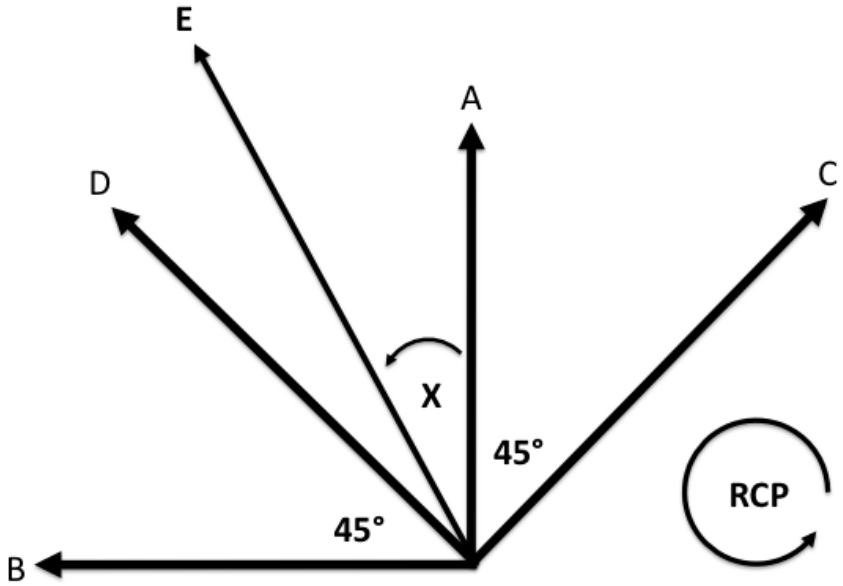

Figure 1.21: Definitions of orthogonal modes for Stokes parameters and definition for the direction of RCP radiation.

$$U = \langle E_C^2 \rangle - \langle E_D^2 \rangle \tag{1.62}$$

$$V = \langle E_R^2 \rangle - \langle E_L^2 \rangle \tag{1.63}$$

where the subscripts A, B, C and D refer to the electric field amplitudes in the directions defined in Fig. 1.21 and the subscripts R and L correspond to the RCP and LCP intensities described earlier. In all cases, the angular brackets ($\langle\ \rangle$) denote the time averaged value of the electric field. I corresponds to the total intensity, V corresponds to the circularly polarized intensity while Q & U together describe the degree of linear polarization and the polarization position angle of the radiation (sometimes referred to as the Electric Vector Position angle EVPA)

In order to determine the connection between Q, U and the source polarization, we consider a source that has a polarized electric field component E_p with EVPA χ (measured from north through east) and an unpolarized (completely random EVPA direction) component E_u. In this case

$$E_A = \frac{E_u}{\sqrt{2}} + E_p \cos\chi \tag{1.64}$$

$$E_B = \frac{E_u}{\sqrt{2}} + E_p \sin\chi \tag{1.65}$$

$$E_C = \frac{E_u}{\sqrt{2}} + E_p \sin(45 - \chi) \tag{1.66}$$

$$E_D = \frac{E_u}{\sqrt{2}} + E_p \cos(45 - \chi) \tag{1.67}$$

A feed orientated in any of these four directions will detect the same amount of power due to the unpolarised emission component. Using the above expressions, Equations 1.61 and 1.62 and, noting that $\langle E_u E_p \rangle = 0$ as they are uncorrelated, we find

$$Q = \left\langle \left(\frac{E_u}{\sqrt{2}} + E_p \cos\chi \right)^2 \right\rangle - \left\langle \left(\frac{E_u}{\sqrt{2}} + E_p \sin\chi \right)^2 \right\rangle \tag{1.68}$$

$$Q = E_p^2 \left(\cos\chi^2 - \sin\chi^2 \right) \tag{1.69}$$

$$Q = E_p^2 \cos 2\chi \tag{1.70}$$

$$U = \left\langle \left(\frac{E_u}{\sqrt{2}} + E_p \sin(45 - \chi) \right)^2 \right\rangle - \left\langle \left(\frac{E_u}{\sqrt{2}} + E_p \cos(45 - \chi) \right)^2 \right\rangle \tag{1.71}$$

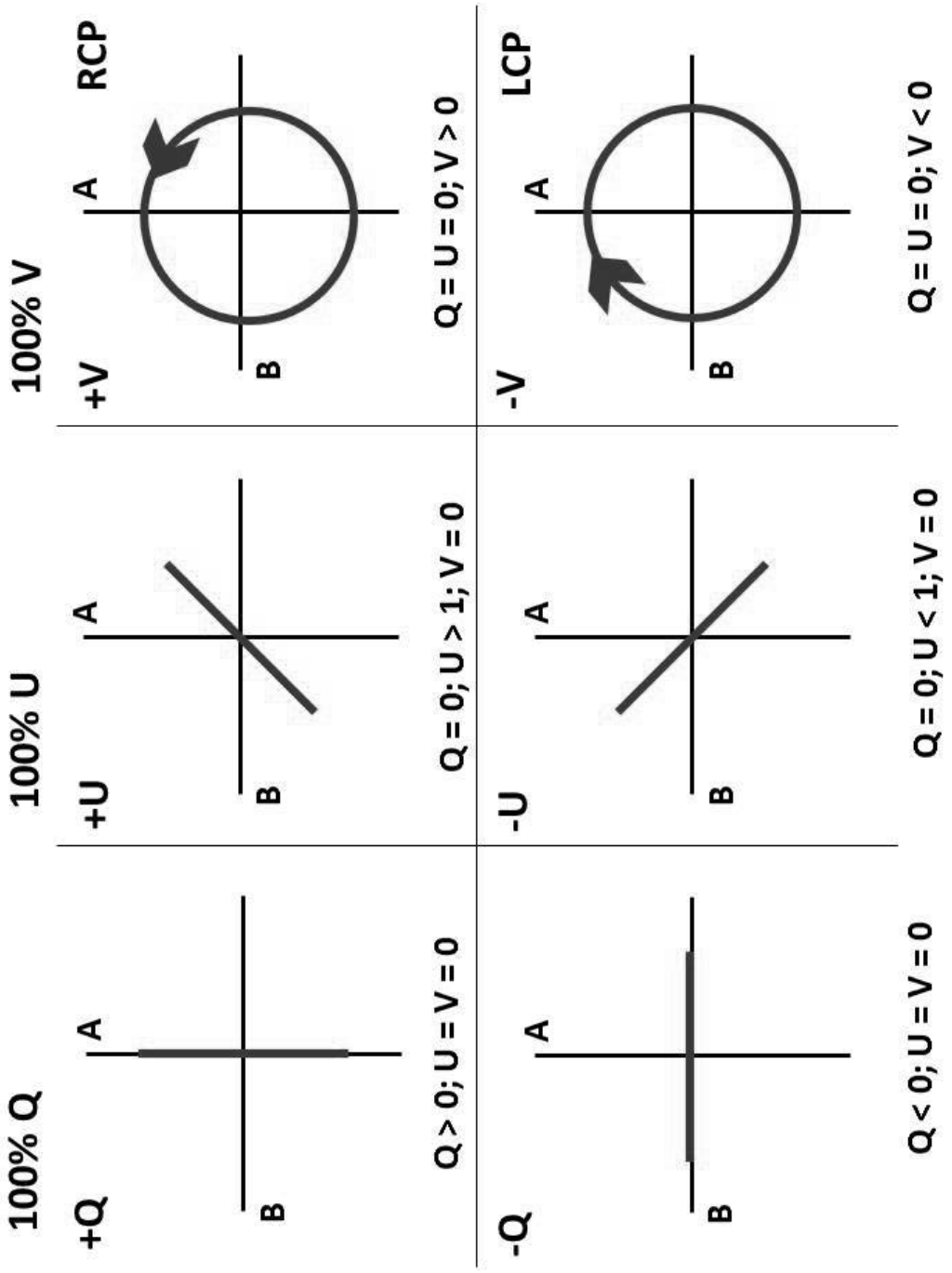

Figure 1.22: Stokes Parameter and convention of right and left circular polarized waves as used in radio astronomy. (Source: Wikimedia Commons)

$$U = E_p^2 \left(\sin\left(45 - \chi\right)^2 - \cos\left(45 - \chi\right)^2\right) \tag{1.72}$$

$$U = E_p^2 \sin 2\chi \tag{1.73}$$

Therefore

$$E_p = \sqrt{Q^2 + U^2} \tag{1.74}$$

$$\chi = \frac{1}{2} \arctan \frac{U}{Q} \tag{1.75}$$

Thus we can construct a complex quantity called the complex polarized flux (P) given by $Q + iU$ with amplitude mI (where m is the degree of polarization) and phase of 2χ.

$$P \equiv Q + iU = mIe^{2i\chi} \tag{1.76}$$

Connection with Correlator Output

As previously stated, radio telescopes feature antennas which have both a RCP and a LCP feed. Therefore, the following four correlations are possible between 2 antennas.

$$\langle LL^*(u,v)\rangle$$
$$\langle LR^*(u,v)\rangle$$
$$\langle RL^*(u,v)\rangle$$
$$\langle RR^*(u,v)\rangle$$

where R and L correspond to the RCP and LCP responses. Therefore, it is clear from the definitions of the Stokes parameters that

$$\langle LL^*(u,v)\rangle = I - V \tag{1.77}$$

$$\langle RR^*(u,v)\rangle = I + V \tag{1.78}$$

The $\langle LL^*(u,v)\rangle$ and $\langle RR^*(u,v)\rangle$ correlations contain information about both the total intensity and the circularly polarized intensity. To understand the formulation $\langle LR^*\rangle$ and $\langle RL^*\rangle$ in terms of the Stokes parameters, the electric field components along A and B are written in terms of their RCP and LCP components. These components are chosen such that the RCP and LCP components line up along A at $t = 0$.

$$E_A = E_L \cos\omega t + E_R \cos\omega t = (E_L + E_R)e^{i\omega t} \tag{1.79}$$
$$E_B = E_R \sin\omega t - E_L \sin\omega t = i(E_L - E_R)e^{i\omega t} \tag{1.80}$$
$$E_R = \tfrac{1}{2}(E_A + iE_B)e^{-i\omega t} \tag{1.81}$$
$$E_L = \tfrac{1}{2}(E_A - iE_B)e^{-i\omega t} \tag{1.82}$$

Similarly, we can write E_C and E_D as

$$E_C = \tfrac{1}{\sqrt{2}}(E_A - E_B) \tag{1.83}$$
$$E_D = \tfrac{1}{\sqrt{2}}(E_A + E_B) \tag{1.84}$$

giving

$$U = \langle E_C^2\rangle - \langle E_D^2\rangle \tag{1.85}$$
$$= \tfrac{1}{2}((\langle E_A\rangle + \langle E_B\rangle)^2 - (\langle E_A\rangle - \langle E_B\rangle)^2) \tag{1.86}$$
$$= 2\langle E_A E_B\rangle \tag{1.87}$$

The correlation between R and L can now be written as

$$\langle RL^*\rangle(u,v)\rangle = \tfrac{1}{4}\langle (E_A + iE_B)(E_A + iE_B)\rangle \tag{1.88}$$
$$= \tfrac{1}{4}(\langle E_A^2\rangle - \langle E_B^2\rangle) + \tfrac{i}{2}\langle E_A E_B\rangle \tag{1.89}$$
$$= Q + iU = P \tag{1.90}$$
$$\langle LR^*\rangle(u,v)\rangle = \tfrac{1}{4}\langle (E_A - iE_B)(E_A - iE_B)\rangle \tag{1.91}$$
$$= Q - iU = P^* \tag{1.92}$$

Due to the almost negligible amount of detectable circularly polarized radiation detected ($V \approx 0$) we can assume

$$\langle LL^* \rangle \approx \langle RR^* \rangle \approx I \tag{1.93}$$

All 4 of these Stokes parameters have Fourier transform counterparts in the image plane. These are given by

$$\begin{aligned}
\langle RL^*(u,v) \rangle &= P(u,v) && (1.94)\\
&= \int m\widetilde{I}(x,y) e^{2i\chi} e^{2i\pi(ux+vy)} dx\ dy && (1.95)\\
\langle LR^*(u,v) \rangle &= P^*(u,v) && (1.96)\\
&= \int m\widetilde{I}(x,y) e^{-2i\chi} e^{2i\pi(ux+vy)} dx\ dy && (1.97)\\
&= \int m\widetilde{I}(x,y) e^{2i\chi} e^{-2i\pi(ux+vy)} dx\ dy && (1.98)\\
&= \langle RL^*(-u,-v) \rangle && (1.99)
\end{aligned}$$

where $\widetilde{I}(x,y)$ is the Fourier transform of $I(u,v)$.

1.5.3.1 Polarization Calibration

The RCP and LCP antennae used in radio observations are not perfect, with each antenna detecting some contribution from the opposite mode of circular polarization. Therefore, the induced complex voltages are actually given by

$$\begin{aligned}
v_R &= G_R \left[E_R e^{-i\phi_p} + D_R E_L e^{i\phi_p} \right] && (1.100)\\
v_L &= G_L \left[E_L e^{i\phi_p} + D_L E_R e^{-i\phi_p} \right] && (1.101)
\end{aligned}$$

where G_R and G_L are complex gain factors (determined during amplitude calibration), E_R and E_L are the induced electric fields, D_R and D_L are known as the "D-Terms" and ϕ_p is the parallactic angle. This angle is defined as the angle between the arcs connecting the source and the zenith and the source and the north pole. Telescopes with an azimuthal mount (such as those in the VLBA) can track a source as it moves across the sky and, in doing so, observe the source

at multiple different parallactic angles. As the instrumental polarization terms change with parallactic angle while the source polarization terms do not, the "D-Terms" can be determined by carefully observing a source with simple polarization structure over a range of parallactic angles. As these "D-Terms" are approximately constant over the timescales of a typical VLBI observation, they can be used throughout the rest of the observation.

Chapter 2

Helical Magnetic Fields and AGN Jets

The chapter briefly describes the observational evidence for the existence of helical magnetic fields threading the jets of AGN. It also contains a derivation of the primary equation which describes Faraday Rotation and a description of a Poynting Robertson battery.

2.1 Observational Evidence for Helical Magnetic Fields

As described in Section 1.4.3 the polarization structure of jets provides information about the structure of their magnetic fields, which in turn influence their evolution and emission properties. Magnetic field structures in AGN jets are of great importance, for instance, they affect jet stability. A knowledge of magnetic field structure is required in order to translate radio images into jet structure and also provides constraints on jet formation models. Despite much observational effort, the magnetic field structures of AGN are not yet well understood.

Three types of observational results inform our present thinking about the magnetic field structures in parsec-scale jets.

1. There is a tendency for polarization angles to lie either parallel or perpendicular to the jet. A tendency for BL Lac objects and quasars to display magnetic polarization directions respectively perpendicular and parallel to the jets has long been known (e.g. Gabuzda et al. 1992; Cawthorne et al.

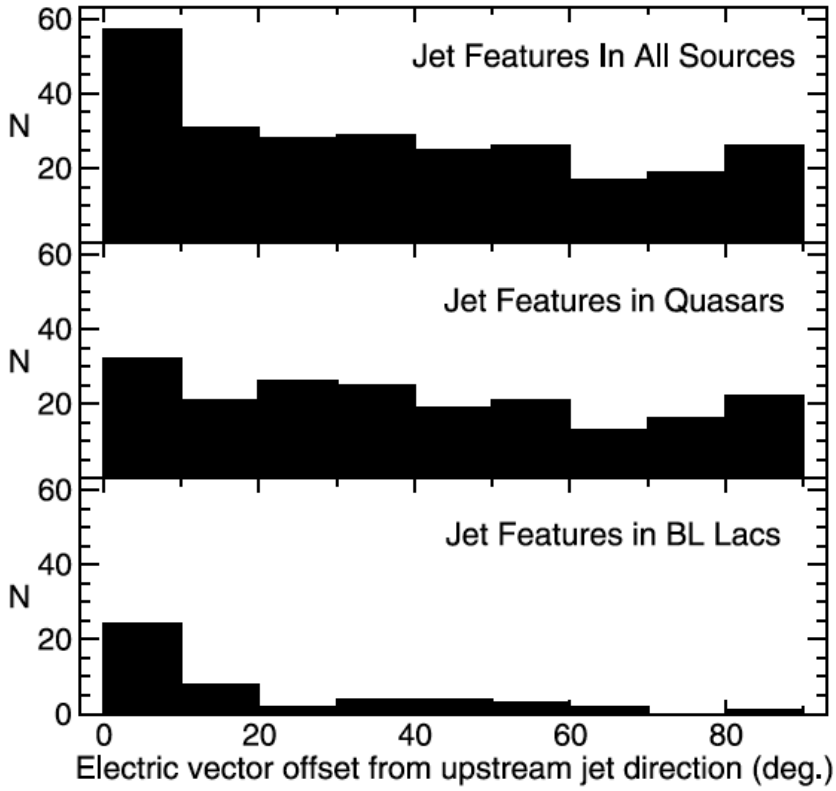

Figure 2.1: Distribution of the electric vector offsets with respect to the upstream jet direction at the locations of jet components in the full MOJAVE sample (top panel) and for optical subclasses (bottom panels) from Homan & Lister (2005). The upstream jet direction is defined as the position angle to the nearest component located closer to the core. The BL Lac and quasar distributions differ at greater than 99.99% confidence according to a Wilcoxon test.

1993), and modern surveys (Lister & Homan 2005) have confirmed these general trends. In quasars, there is a broad distribution of misalignments but such differences are often reduced when Faraday rotation is taken into account (e.g. Hutchison et al. 2001). This type of polarization structure requires an axisymmetric magnetic field; a helical magnetic field is one example, although the production of apparent jet magnetic fields that are either parallel or perpendicular to the jet direction is not a unique property of helical fields (See Fig. 2.1).

2. Transverse Faraday rotation gradients have been reported across a number of AGN jets (e.g. Asada et al. (2002, 2008a, 2008b, 2012) and Gabuzda et al. (2004, 2008, 2013)). Although the reliability of these results has been questioned by some (e.g. Zavala & Taylor 2010), they clearly suggest the existence of a toroidal magnetic field component (See Fig. 2.2).

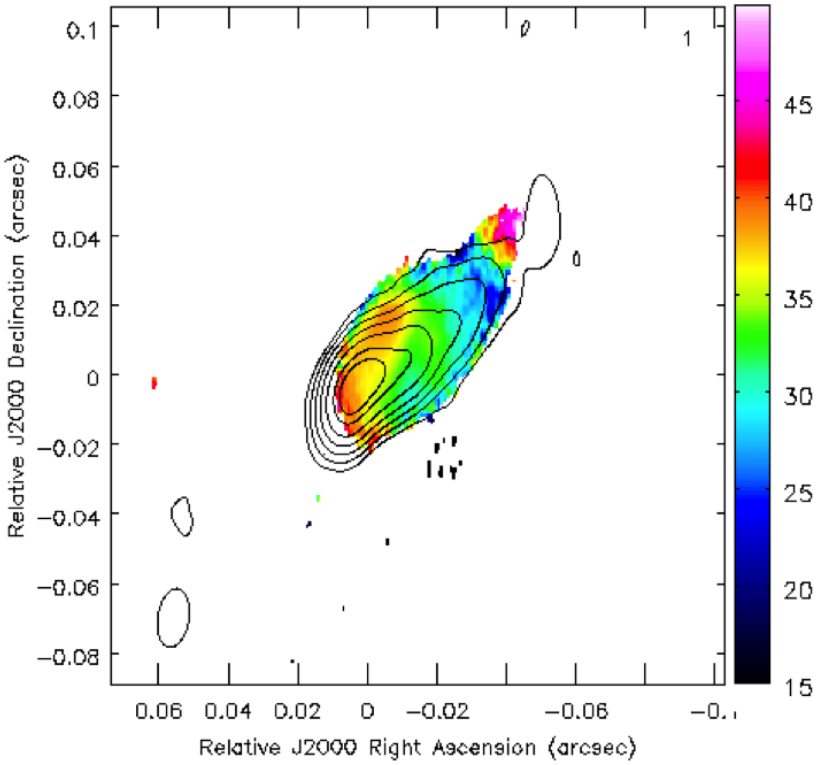

Figure 2.2: Total intensity contours with the distribution of the RM superposed, made using four-wavelength 18–22 cm data of 3C380 analyzed by Gabuzda, Cantwell & Cawthorne (2013). An RM gradient across the jet is clearly visible by eye, and proves to have a significance of about 4σ.

3. A significant number of AGN jets possess obvious asymmetries in total intensity and linear polarization or other transverse structures that are reminiscent of those revealed in the helical field simulations of Laing (1981) (2.3). Note that the presence of transverse Faraday rotation gradients does not provide any information about whether or not the poloidal field component is ordered. Generally, speaking, it is only the asymmetry of the transverse intensity and polarization profiles that can distinguish observationally between a helical field (with an ordered poloidal field component) and a toroidal field (with a disordered poloidal field component). This is described in much greater detail in Chapter 3.

These observational results lead to the main question addressed in this chapter: can a helical magnetic field explain the observed intensity and polarization profiles of parsec-scale AGN jets?

Of course, asymmetries in the transverse profiles could also be attributed to phys-

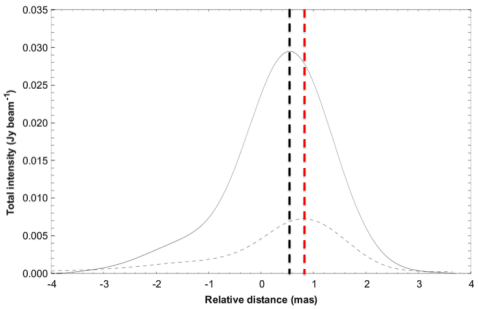

(a) 8GHz total and polarized intensity transverse profiles of the jet in 4C71.07, 6mas away from the core. The convolution beam is ~ 1.5mas.

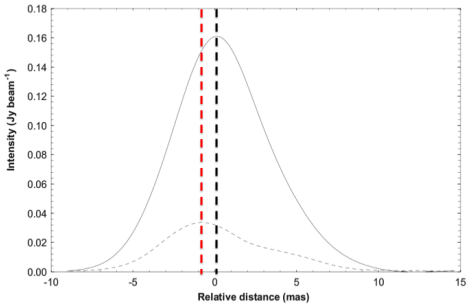

(b) 1.6GHz total and polarized intensity transverse profile of the jet in 3C380, 16mas away from the core. The convolution beam is ~ 4.0mas.

Figure 2.3: Figure highlighting asymmetries in total intensity and linear polarization structure based on original figure in Papageorgiou (2005). Solid line corresponds to total intensity, dashed line corresponds to polarized intensity. Thick black and red dashed lines correspond to peak total intensity and peak polarized intensity positions respectively.

ical asymmetries, such as pressure gradients or other forms of jet asymmetry. However, a helical magnetic field threading the jet of an AGN could potentially describe the observations without requiring special conditions in the jet environment. The main advantage of such models is that they can produce the observed transverse structures while avoiding physical asymmetries which might cause the jet to deflect or possibly destabilise.

Multiple numerical 3D general relativistic magnetohydrodynamic (GRMHD) jet formation simulations have successfully produced highly collimated jets which are collimated by helical magnetic fields. In these simulations the magnetic fields originate in the accretion disk of the central engine of the AGN and are wound up by the rapid rotation of the accretion disk. This rapid rotation results in the magnetic field eventually obtaining a helical structure. Sample rotation measure maps for such a simulation performed by Broderick & McKinney (2010) can be seen in Fig. 2.4 .

.

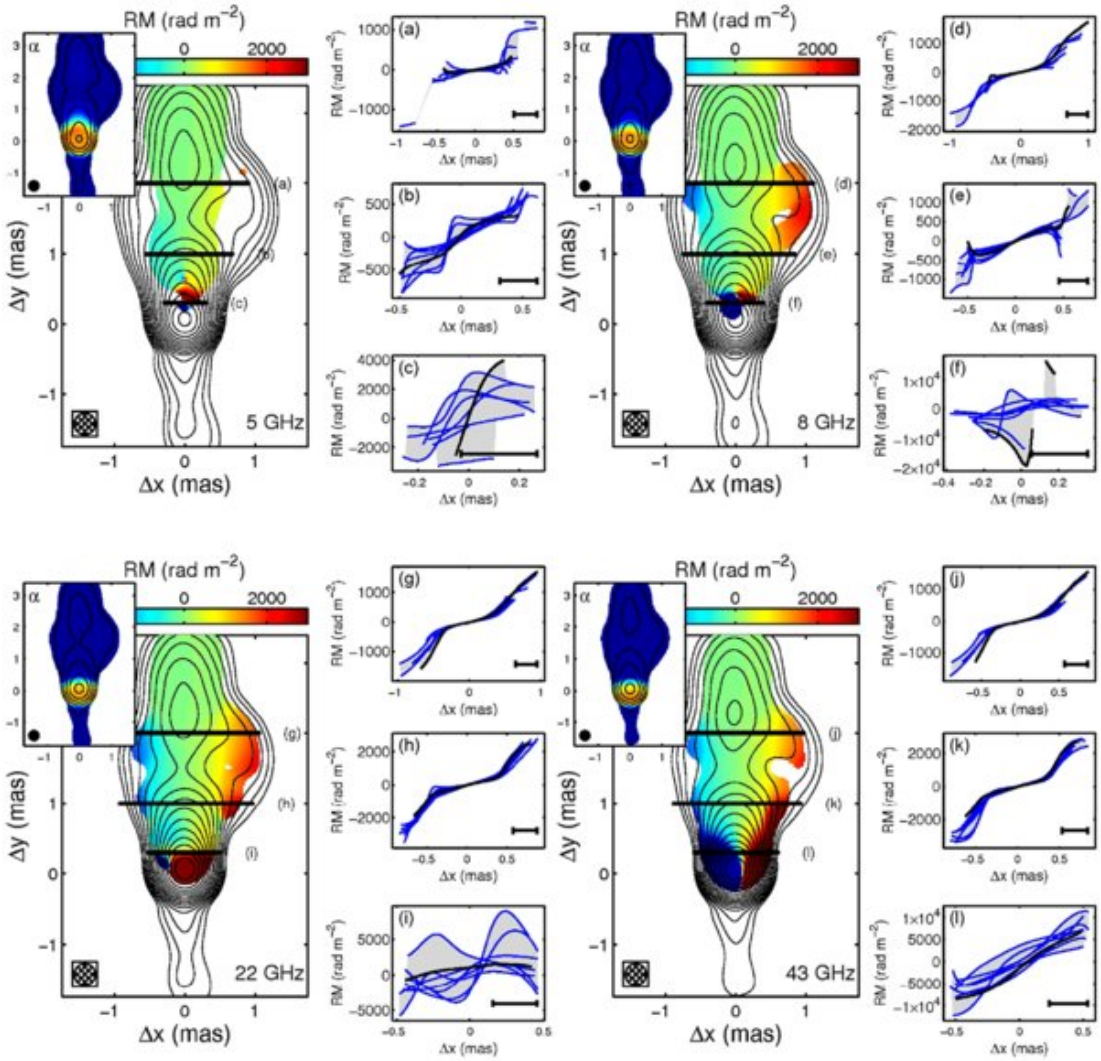

Figure 2.4: RM maps produced by the canonical GRMHD model of Broderick & McKinney (2010) as observed at ν = 5 GHz, 8 GHz, 22 GHz, and 43 GHz (observation frequencies are listed in the lower right of each RM map). In all cases, the beam size is fixed to 0.3 mas. The beam-convolved spectral index map is shown in the upper left inset of each RM map, in which the colours range from –0.5 (dark blue) to 0.5 (dark red), indicating the size of the photosphere at each frequency. For reference total flux contours are overlaid, in logarithmic factors of 2 (factors of 8 in the α map insets), with the minimum contour corresponding to 0.98 mJy mas–2. RM solutions are shown only where the polarized flux exceeds 1 mJy mas^{-2}. To the right of each RM map, illustrative transverse RM profiles corresponding to the labeled bars are shown (black) along with those from a variety of azimuthal viewing angles (blue). In all maps and transverse sections, the beam size is shown in the lower left and lower right, respectively.

2.2 Faraday Rotation

Faraday Rotation was first discovered experimentally by Michael Faraday in 1845. He discovered that the direction of polarization of light, passing though a dielectric in the presence of a magnetic field, would be rotated and that the amount of rotation depended on the strength of the magnetic field.

Faraday Rotation is not restricted to dielectrics and can also occur when an electromagnetic wave propagates through a charged plasma in the presence of a magnetic field. Therefore, the magnetic field threading the jets of AGN should result in the highly linearly polarized synchrotron emission undergoing Faraday Rotation.

2.2.1 Faraday Rotation in Plasma

The primary reference for material in this section was the 'Classical Electromagnetism' lecture notes of Dr. Richard Fitzpatrick at the University of Texas.

Consider a high frequency electromagnetic wave propagating, along the z axis, through a plasma with a longitudinal equilibrium magnetic field $\vec{B} = B_0\hat{z}$. An electron in such a field experiences a force given by

$$\vec{F}_e = -e\vec{E} - e\vec{v} \times \vec{B} \tag{2.1}$$

This can be rewritten as

$$m_e \frac{d\vec{v}}{dt} = -e(\vec{E} + B_0\vec{v} \times \hat{z}) \tag{2.2}$$

Here $\vec{v} = \frac{d\vec{r}}{dt}$ where $\vec{r}$ is the electron displacement from its equilibrium position, m_e is the electron mass and e is the charge of a single electron. Now suppose that all perturbed quantities vary with time like $e^{\iota\omega t}$ where ω is the wave frequency. Simple differentiation then yields

$$m_e\omega^2 x = e(E_x - \iota B_0\omega y) \tag{2.3}$$

$$m_e\omega^2 y = e(E_y + \iota B_0\omega x) \tag{2.4}$$

The following identities are utilized to help simplify these equations.

$$d_{\pm} \equiv x \pm \iota y \tag{2.5}$$

$$E_{\pm} \equiv E_x \pm \iota E_y \tag{2.6}$$

Adding Equations 2.3 and 2.4 and using these identities gives

$$m_e \omega^2 d_{\pm} = e(E_{\pm} \mp B_0 \omega d_{\pm}) \tag{2.7}$$

$$d_{\pm} = \frac{eE_{\pm}}{m_e \omega(\omega \pm \Omega)} \tag{2.8}$$

where Ω is the cyclotron frequency given by $\frac{eB_0}{m_e}$. In terms of $d_{\pm}$ the electron displacement can now be written as

$$\vec{r} = d_+ e^{\iota(k_+ z - \omega t)} e_+ + d_- e^{\iota(k_- z - \omega t)} e_- \tag{2.9}$$

where $e_{\pm} = \frac{1}{2}(\hat{x} \mp \iota \hat{y})$. The electric field can now be described by

$$\vec{E} = E_+ e^{\iota(k_+ z - \omega t)} e_+ + E_- e^{\iota(k_- z - \omega t)} e_- \tag{2.10}$$

Here, E_+ corresponds to a constant amplitude electric field which rotates anti-clockwise in the x-y plane (looking down the z axis) as the wave propagates in the z direction, whereas E_- corresponds to a constant amplitude electric field which rotates clockwise. The former type of wave is termed right-hand circularly polarised, whereas the latter is termed left-hand circularly polarised.

The induced dipole moment per unit volume of n electrons is given by

$$\vec{P} = -ned_{\pm} \tag{2.11}$$

Using Eqn. 2.8 and noting that $\vec{P} = \epsilon_0(\epsilon - 1)\vec{E}$ gives

$$\epsilon_{\pm} = 1 - \left(\frac{\omega_p^2}{\omega(\omega \pm \Omega)} \right) \tag{2.12}$$

where $\omega_p = \sqrt{\frac{ne^2}{\epsilon_0 m_e}}$ is the plasma frequency, $\omega^2 = \frac{k^2c^2}{\epsilon}$, e_0 is the permittivity of free space and c is the speed of light in a vacuum. Rewriting this in terms of k results in

$$k_\pm^2 c^2 = \omega^2 \left[1 - \frac{\omega_p^2}{\omega(\omega \pm \Omega)}\right] \tag{2.13}$$

In order to advance two assumptions must be made. The first is that $\omega \gg \omega_p$. This is a reasonable as we observe the synchrotron emission coming from the Faraday rotation region. If $\omega \simeq \omega_p$ there would be large amounts of reflection occurring in the plasma and we would not observe any synchrotron emission. The second assumption is that $\omega \gg \Omega$. This is also a reasonable assumption as $\Omega \approx 10$ MHz for the typical magnetic fields found in the jets of AGN. This value is significantly smaller than the typical ω used in the observations investigated in this thesis ($\omega \approx 1$ GHz). Taking these two assumptions into account and performing multiple Taylor expansions results in

$$k_\pm = k \pm \Delta k \tag{2.14}$$

$$k = \frac{\omega}{c}\left[1 - \frac{1}{2}\left(\frac{\omega_p}{\omega}\right)^2\right] \tag{2.15}$$

$$\Delta k = \frac{1}{2}\left(\frac{\omega_p}{\omega}\right)^2 \frac{\Omega}{c} \tag{2.16}$$

Therefore, in a magnetized plasma, right circularly polarized wave and left circularly polarized waves of the same frequency have slightly different wave-numbers. This will result in Faraday rotation.

The electric field of a linearly polarised wave is given by

$$\vec{E} = E_0 \left(e^{\iota(k_+ z - \omega t)} + e^{\iota(k_- z - \omega t)}\right) \tag{2.17}$$

Taking the real part of this equation and using basic trigonometrical identities results in

$$\vec{E} = E_0[\cos(kz - \omega t)\cos(\Delta k z),\ \cos(kz - \omega t)\sin(\Delta k z),\ 0] \tag{2.18}$$

The angle of polarization (χ) for such a wave is given by

$$\chi = \arctan\left(\frac{E_y}{E_x}\right) = \arctan\left(\frac{\sin(\Delta kz)}{\cos(\Delta kz)}\right) = \Delta kz \tag{2.19}$$

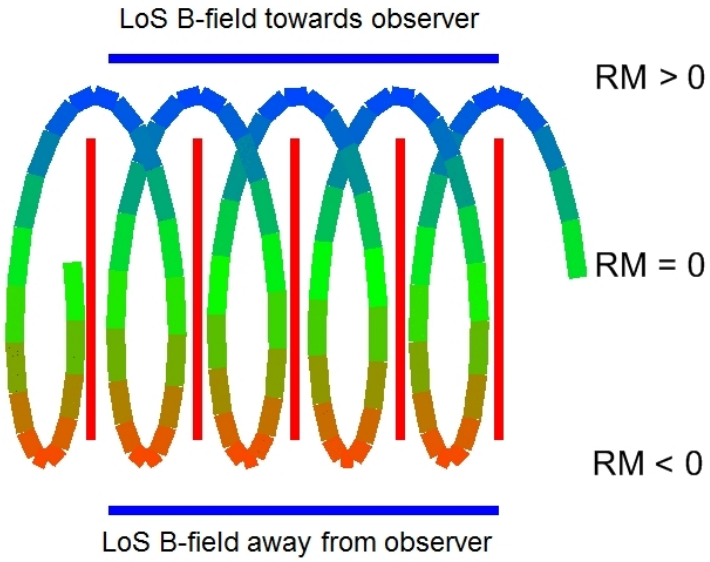

Figure 2.5: Schematic illustration how a helical magnetic field gives rise to to a gradient in the observed RM from Reichstein (2012). The viewing angle is near 90° to the jet axis in the jets' rest frame. Due to the different directions of the line-of-sight B field on either side of the jet, the rotation measure has opposite signs.

Therefore

$$\frac{d\chi}{dz} = \Delta k = \frac{1}{2}\left(\frac{\omega_p}{\omega}\right)^2 \frac{\Omega}{c} = \frac{e^3}{2\epsilon_0 m_e^2 c}\frac{n_e B_0}{\omega^2} \tag{2.20}$$

Hence, a linearly polarized electromagnetic wave which propagates through a plasma with a (slowly) varying electron number density, $n_e(z)$, and longitudinal magnetic field, $B_0(z)$, has its plane of polarization rotated through a total angle of

$$\Delta\chi = \chi - \chi_0 = \frac{e^3}{2\epsilon_0 m_e^2 c}\frac{1}{\omega^2}\int_0^d n_e(z) B_0(z)\ \mathrm{d}z \tag{2.21}$$

Rewriting the above equation in terms of wavelength instead of frequency and in terms of **B**, the magnetic field vector, and assuming a constant electron number density gives

$$\Delta\chi = \lambda^2 \frac{e^3}{8\pi^2\epsilon_0 m_e^2 c^3} \int n_e \mathbf{B} \cdot \mathrm{d}\mathbf{l} \tag{2.22}$$

This is often represented by $\Delta\chi = RM\lambda^2$ where RM is called the Rotation Measure which is given by

$$RM = \frac{e^3}{8\pi^2\epsilon_0 m_e^2 c^3} \int n_e \mathbf{B} \cdot \mathrm{d}\mathbf{l} \tag{2.23}$$

The RM is therefore dependant on both the electron number density and the line of sight magnetic field. As RM is inversely proportional to m^2 any contribution to the total Faraday Rotation from protons is negligible compared to that from electrons and can be ignored.

2.2.2 Faraday Rotation in a Helical Magnetic field.

If a helical magnetic fields threads the jet of an AGN a transverse gradient in observed RM is expected (Fig 2.5). From Eqn. 2.23 the RM will change as the line of sight magnetic field changes. Depending on the pitch angle of the helical magnetic field and the viewing angle, a positive to negative RM transition may be observed. In cases were this isn't the true, a RM gradient will still be present. While a transverse RM gradient can also be produced by changes in electron number density, n_e, across a given slice such a gradient will never change sign. Therefore, observed RM gradients in the jets of AGN offer an excellent analysis method to probe the magnetic field present in the jet.

2.3 Poynting Robertson Battery

In a Poynting Robertson Battery radiation from the active nucleus appears slightly anisotropic in the rest frame of the accretion disk resulting in a net drag force. This drag force experienced by a particle is directly proportional to its Thompson cross-sectional area, $\frac{8\pi}{3}\left(\frac{e^2}{mc^2}\right)^2$, and so acts predominantly on the lower mass electrons present in the jet; resulting in much lower electron velocities than proton velocities in the accretion disk. This disparity in velocities results in the generation of electric currents in the direction of disc rotation. These azimuthal currents give rise to a poloidal magnetic field whose direction is directly related to the direction of the disc rotation.

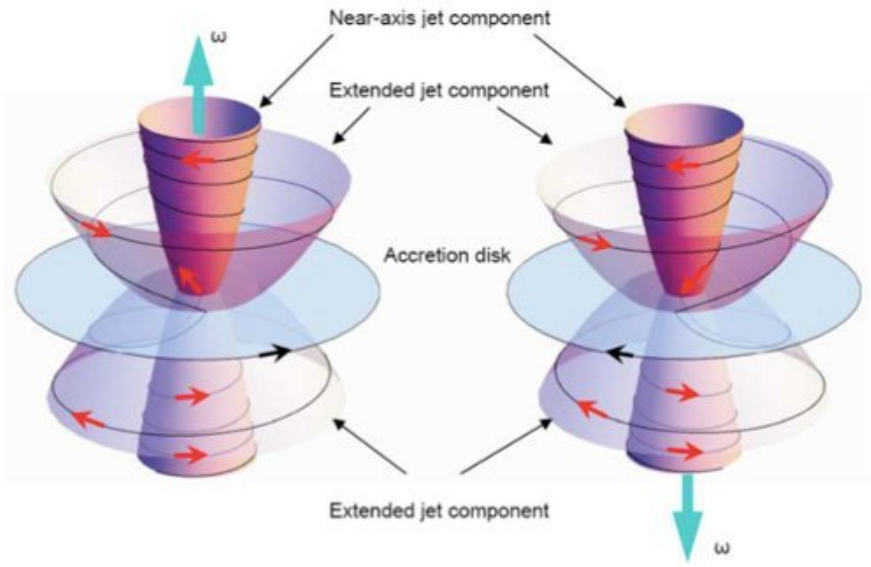

Figure 2.6: Illustration of the jet magnetic field generated by a Poynting Robertson battery near the axis and periphery of the jet. The magnetic field is shown by the black line and its direction by the red arrows.The direction of the disc rotation is shown by the black arrows in the disk and the corresponding angular velocity vector by the cyan arrows. The observer is located in the northern hemisphere of the disk on the left hand image and the southern hemisphere of the disk on the right hand image. Image from Contopoulus et al.(2009)

In this model the magnetic-field loops generated by the Poynting Robertson battery and anchored in the inner and outer accretion disc become twisted in the azimuthal direction by the differential rotation of the disk. These loops open up and separate into an "inner" component near the disc symmetry axis and an "outer" component (Fig. 2.6). The poloidal fields of the two components are in opposite directions, one parallel and the other antiparallel to the angular velocity vector. The direction of the poloidal magnetic field is therefore determined by the direction of the disk rotation. (Contopoulos & Kazanas 1998)

The helical field pitch angle, γ, of the inner and outer fields may be different, with the inner field being more tightly wound. The observed RM in such a case will include contributions from both fields, corresponding to the volumes of both the rotating regions that lie along the line of sight between the observer and the emission region. As is evident from Fig. 2.6, the direction of the RM gradients associated with each region will be opposite. Therefore, the direction of the observed gradient will be determined by which region contributes the larger contribution to the net RM.

In this model it is possible for the direction of the observed RM gradient to "flip" in certain jet regions. This could occur if, for example, the outer region of the helical field usually dominates the observed RM distribution but, due to an increase in electron number density or magnetic field strength, the inner region temporarily dominates the outer regions. Further, it is plausible that the inner region of helical field dominates on relatively small scales, while the outer region dominates on larger scales, leading to a single reversal in the direction of the net observed RM gradient.

Recent results by Mahmud et al. show a reversal of the direction of the observed RM gradient in time in 1803+784 (Mahmud et al. 2009) and a reversal with distance from the core of the transverse RM gradients observed in 0716+714 and 1749+701 (Mahmud et al. 2013). This last result is discussed in further detail in Section 5.3.

2.4 Thesis Summary

The aim of this thesis is threefold. Firstly, it explores methods of inferring the structure of magnetic fields threading the jets of AGN at both parsec and kiloparsec scales. Secondly, it explores the resolution requirements needed to observe RM gradients in the jets of AGN observed using Very Long Baseline Interferometry (VLBI). Thirdly, it considers the likelihood of occurrence of spurious monotonic RM gradients across AGN jets that could be mistakenly interpreted as evidence for helical or toroidal magnetic fields.

Chapter 3 describes the simple helical magnetic field model that was used in the analyses carried out in this thesis.

Chapter 4 presents results of fitting total intensity and polarization profiles in VLBI images of astrophysical jets to profiles calculated using the simple theoretical model described in Chapter 3. Specifically, the polarization structures of both Markarian 501 and M87 are fitted and key jet magnetic field parameters are derived in addition to other fundamental jet parameters. The results presented in this chapter have been published in Murphy, Cawthorne and Gabuzda (2013)

Chapter 5 investigates how finite resolution affects the ability of VLBI to reliably detect RM gradients. Real observed radio images have finite resolution, usually expressed via convolution with a Gaussian beam whose size corresponds to the central lobe of the point source response function. This will tend to blur

transverse structure in the jet profile, raising the question of how well resolved a jet must be in the transverse direction in order to reliably detect transverse structure. This chapter presents results of simulated intensity, polarization and Faraday rotation images designed to directly investigate the effect of finite resolution on observed transverse jet structures. The results of Section 5.3 have been published in Mahmud et al. (2013). The rest of this chapter's results will be published in a paper currently in preparation.

Chapter 6 considers the occurrence of spurious monotonic RM gradients across AGN jets due purely to noise and limited baseline coverage, and compares the results with those obtained in the analogous studies carried out earlier by Hovatta et al. (2012) and Algaba (2013). This chapter's results will be published in a paper currently in preparation.

Finally, Chapter 7 summarizes the conclusions that can be drawn from this thesis work.

Chapter 3

Simple Helical Magnetic field Model

Laing (1981) investigated three different helical magnetic field models, which can be used to predict the total intensity and polarization profiles across a jet using only two parameters, the helical pitch angle γ' and the jet's angle to the line of sight δ', both defined in the co-moving frame; it is assumed that the velocity of the jet remains constant across the jet width. In applying these models to the parsec-scale jets of several AGNs, Papageorgiou (2005) found the best agreement between observed and model profiles arose for the third of these models, in which a helical magnetic field of constant pitch angle threads an optically thin cylindrical jet. It is therefore this model that is the focus of the present work.

3.0.1 Simple Helical Field Model

The following section comprises the full derivation of the simple helical field model proposed by Laing in 1981. It fixes a typo in the original paper. Papageorgiou (2005) was the first to introduce a tangled field to this model. The core of my work in this area has not been in creating this model but in providing a new, more efficient method of comparing this model to observations.

The emissivity of synchrotron radiation is described by

$$\epsilon \propto B^{\alpha+1} |\sin\theta|^{\alpha+1} \tag{3.1}$$

where B is the magnetic field strength, α is the spectral index and θ is the angle

between the **B** field and the viewing angle (δ') This equation stems from Eqn. 1.31. Laing (1981) described a helical magnetic field of constant pitch angle threading an optically thin cylindrical jet in which the Total Intensity I, Stokes Q intensity and Stokes U intensity are given by

$$I(x) = \frac{1}{\sin\delta'}\int_{|x|}^{R}\frac{K(r)B(r)^{\alpha+1}|\sin\theta|^{\alpha+1}}{\sqrt{1-\frac{x^2}{r^2}}}\,\mathrm{d}r \tag{3.2}$$

$$Q(x) = \frac{p_0}{\sin\delta'}\int_{|x|}^{R}\frac{K(r)B(r)^{\alpha+1}|\sin\theta|^{\alpha+1}\cos 2\chi}{\sqrt{1-\frac{x^2}{r^2}}}\,\mathrm{d}r \tag{3.3}$$

$$U(x) = \frac{p_0}{\sin\delta'}\int_{|x|}^{R}\frac{K(r)B(r)^{\alpha+1}|\sin\theta|^{\alpha+1}\sin 2\chi}{\sqrt{1-\frac{x^2}{r^2}}}\,\mathrm{d}r \tag{3.4}$$

where χ is the Electric Vector Position Angle (EVPA), R is the radius of the jet, x is position along a slice transverse to the jet such that $-R \le x \le R$. The constants which comprise $K(r)$ can be seen in Eqn. 1.31 and it is, most importantly, directly proportional to the number density of radiating electrons. In the case of a simple helix

$$\sin\theta = \left[1-\left(\frac{x}{r}\sin\gamma'\sin\delta' - \cos\gamma'\cos\delta'\right)^2\right]^{\frac{1}{2}} \tag{3.5}$$

where γ' is the helical pitch angle and δ' is the viewing angle in the rest frame of the jet. The total intensity of this simple helical model, (I_{SHM}), along this slice can therefore be written as

$$I_{SHM}(x) = \frac{1}{\sin\delta'}\int_{|x|}^{R}\frac{C(r)\left[1-\left(\frac{x}{r}\sin\gamma'\sin\delta' - \cos\gamma'\cos\delta'\right)^2\right]^{\frac{\alpha+1}{2}}}{\sqrt{1-\frac{x^2}{r^2}}}\,\mathrm{d}r \tag{3.6}$$

where $C(r) \propto K(r)B(r)^{\alpha+1}$. By assuming $C(r)$ to be constant (ie, that the number density of radiating electrons and the magnetic field strength is constant) and a spectral index (α) of 1 this equation becomes analytically solvable. Careful integration yields

$$I_{SHM}(x) = \frac{C}{\sin\delta'}\left[a(1-\cos^2\gamma'\cos^2\delta') + b\sin 2\gamma'\sin 2\delta' - c\sin^2\gamma'\sin^2\delta'\right] \tag{3.7}$$

in which

$$a = \sqrt{1 - \frac{x^2}{R^2}} \tag{3.8}$$

$$b = \frac{x}{2R} \ln \left| \frac{R(1+a)}{x} \right| \tag{3.9}$$

$$c = \frac{|x|}{R} \arccos \frac{|x|}{R} \tag{3.10}$$

Because the quantity $\sin 2\chi$ is antisymmetric, where χ is the electric vector position angle (EVPA), the contributions to the integral of U along the line of sight made by the far and near sides of the helical field cancel, so that this integral is zero; therefore, the polarization distribution across the cylinder corresponds fully to Q

$$Q_{SHM}(x) = \frac{C\ p_0}{\sin \delta'} \left[a(\sin^2 \gamma' - \cos^2 \gamma' \sin^2 \delta') - b \sin 2\gamma' \sin 2\delta' - c \sin^2 \gamma (1 + \cos^2 \delta') \right] \tag{3.11}$$

in which a, b and c remain unchanged. The total polarized flux for this simple model is therefore

$$P(x) = |Q(x)|$$

with

$$\chi = \begin{cases} 90^\circ & \text{if } Q > 0 \\ 0^\circ & \text{if } Q < 0 \end{cases}$$

Alternatively, the integrated magnetic vector position angle (MVPA) is transverse for Q > 0 and longitudinal for Q < 0

The analysis of Papageorgiou (2005) showed that this helical-field model produced profiles that are considerably more strongly polarized than observed. The model was therefore modified by introducing a disordered (tangled) magnetic field component (see, e.g., Burn 1966). This requires a third model parameter, the degree of entanglement, f, defined as the fraction of the magnetic field energy density in tangled form:

$$\frac{\langle B_T^2 \rangle}{\langle B_H^2 \rangle} = \frac{f}{1-f} \tag{3.12}$$

where $\langle B_T^2 \rangle$ and $\langle B_H^2 \rangle$ are proportional to the magnetic energy densities of the tangled and helical magnetic field components. $f = 0$ corresponds to no tangled field, $f = 1$ corresponds to no ordered helical field and $f = 0.5$ corresponds to the magnetic energy density of both fields being equal.

The synchrotron emission coefficient from a helical magnetic field with a tangled component is

$$\epsilon_{Total} = \epsilon_{Helical} + \langle \epsilon_{Tangled} \rangle \tag{3.13}$$

where the brackets denote the average over all angles.

$$\langle \epsilon_{Tangled} \rangle = \int_0^{\pi} K(r) \left[\sqrt{f} B(r) \right]^{\alpha+1} |\sin\theta|^{\alpha+1} \frac{2\pi \sin\theta}{4\pi} \, \mathrm{d}\theta \tag{3.14}$$

Assuming $\alpha = 1$ this gives

$$\langle \epsilon_{Tangled} \rangle = \frac{2}{3} C f \tag{3.15}$$

Using the above equation and Eqn. 3.13 gives an equation for the total intensity observed due to synchrotron radiation resulting from a helical magnetic field with a tangled component.

$$I(x) = \frac{2}{3} C f \frac{\sqrt{R^2 - x^2}}{\sin\delta'} + (1-f) I_{SHM}(x) \tag{3.16}$$

The tangled component does not contribute to polarization. Therefore

$$Q(x) = (1-f)\, Q_{SHM} \tag{3.17}$$

Increasing the degree of entanglement in the field (i.e. increasing f) reduces the degree of asymmetry of the total intensity profiles predicted by the model in addition to decreasing the degree of polarization (Fig. 3.1)

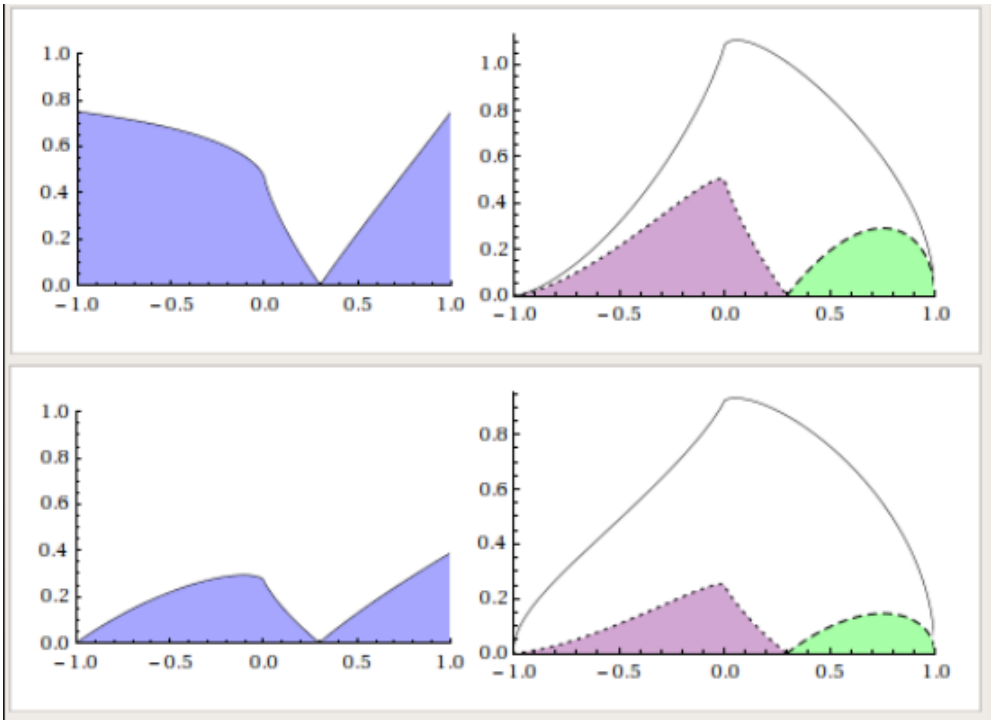

Figure 3.1: Effect of tangled magnetic field component on the observed transverse structures. This figure shows percentage polarization profiles (left) and observed total intensity and polarization profiles (right). On right hand side solid lines correspond to total intensity, purple regions to longitudinal polarization (EVPAs aligned with the jet) and green regions to transverse polarization (EVPAs orthogonal to the jet). Top and bottom image correspond to $f = 0$ and $f = 0.5$ respectively. Contribution of entangled magnetic field reduces observed percentage polarization and makes total intensity profile more symmetric. The domain of the x axis corresponds to distance along a transverse jet slice from one jet edge (-1) to the other jet edge (+1).

3.0.2 Model Predictions

For convenience, the most notable features predicted by this model (Laing 1981), visible in the sample grid of profiles of total and polarized intensity for a range of γ' and δ' values given in Fig. 3.2, are summarised here.

1. Except for purely toroidal magnetic fields ($\gamma' = 90°$) or viewing angles (in the rest frame of the jet) perpendicular to the cylinder axis ($\delta' = 90°$), the distributions of total and polarized intensity are usually asymmetric. These asymmetries arise because the change in the sky-projected magnetic-field direction occurs most rapidly along the helical field line on the side of the jet where the angle between the field and the line of sight is smallest. This results in a greater level of polarization cancellation along the line of sight on one side of the jet than the other. The profile asymmetries are clearly

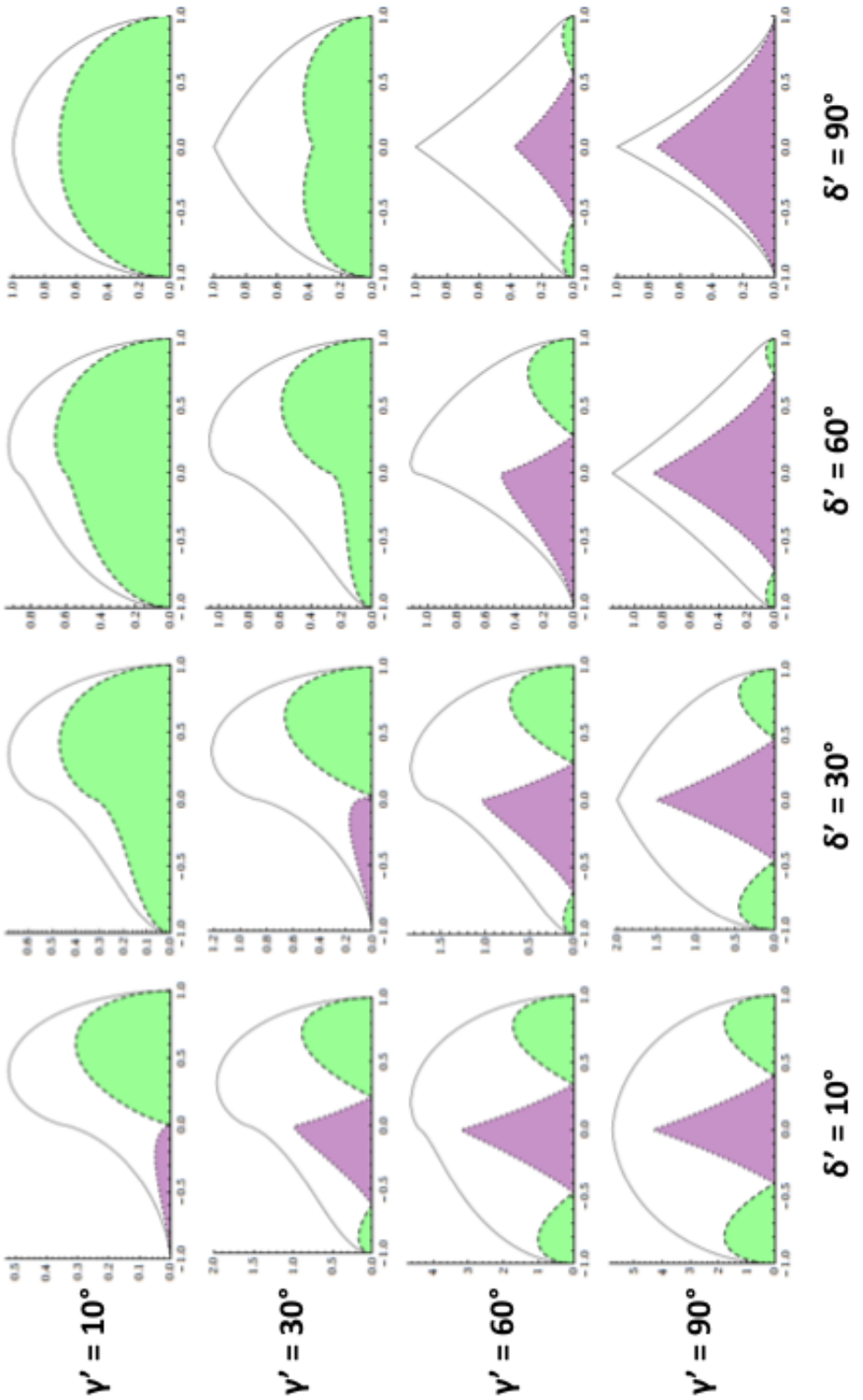

Figure 3.2: Transverse structure produced by the model considered, for various viewing angles, δ', and helix pitch angles, γ'. Solid lines correspond to total intensity, purple regions to longitudinal polarization (EVPAs aligned with the jet) and green regions to transverse polarization (EVPAs orthogonal to the jet). The domain of the x axis corresponds to distance along a transverse jet slice from one jet edge (-1) to the other jet edge (+1).

seen in cases where neither the helical pitch angle nor the viewing angle equals 90° in Fig. 3.2.

2. Displacements between the total intensity profile maxima and polarized intensity profile maxima are common.
3. The fractional polarization varies considerably across the profile.
4. The polarized intensity distribution can have one, two or three local maxima, and the orientation of the projected magnetic field can be either longitudinal, transverse or a combination of both within a given profile.

Further examination of the polarization profiles produced by this model shows that 4 different magnetic field distributions are possible, as can be seen in Fig. 3.2.

1. Longitudinal all across the jet; e.g., $\gamma' = 10°$ and $\delta' = 30°$
2. Longitudinal on one side and transverse on the other; e.g., $\gamma' = 30°$ and $\delta' = 30°$
3. Longitudinal at the edges and transverse at the centre; e.g., $\gamma' = 30°$ and $\delta' = 10°$
4. Transverse all across; e.g., $\gamma' = 90°$ and $\delta' = 90°$

Configuration 2 only occurs when $\gamma' = \delta'$ and configuration 4 only occurs when $\gamma' = \delta' = 90°$. These special cases would not often be expected in nature. However, the effects of finite resolution, in which the true jet profile is convolved with a Gaussian beam, increase the range of parameter values for which configurations 2 and 4 are observed. Fig. 3.3 demonstrates how convolution with a Gaussian beam changes which parameters correspond to different polarization configurations. As the Gaussian beam size increases with respect to the jet width, the range of parameters which correspond to configurations 1, 2 and 4 increase while the range of parameters which correspond to configuration 3, "spine-sheath structure", decrease.

This model was used as a basis to test the consistence of transverse total intensity and linear polarization (Stokes Q) profiles observed across AGN jets, displaying some of the characteristic structures described above, with the expectations of this simple helical magnetic field model. These studies and the results that they yielded are discussed in more detail in Chapter 4.

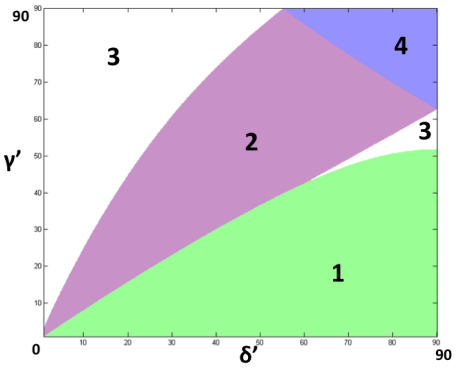

(a) Intrinsic jet width of 2 beam widths.

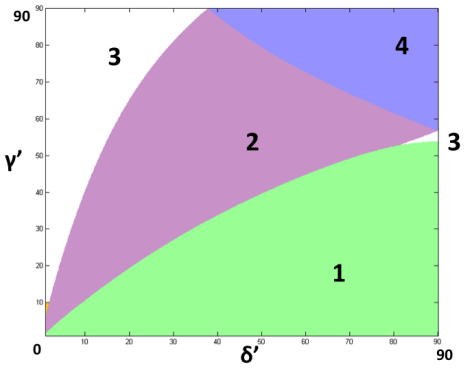

(b) Intrinsic jet width equal to 1 beam width.

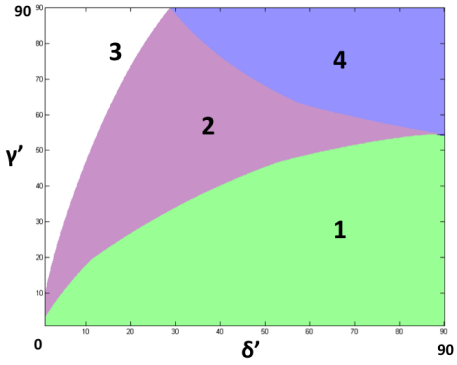

(c) Intrinsic jet width equal to 0.5 beam width.

Figure 3.3: Effect of finite resolution on the observed magnetic field configurations. Region numbers correspond to the configuration types listed in Section 3.0.2. As the intrinsic jet width decreases relative to the beam width the δ' and γ' values required for different polarization configurations change.

Chapter 4

Analysis of Transverse Polarized Structure

Previous work performed by Papageorgiou (2005) in analysing the transverse polarization structure of AGN jets did not involve any formal model fitting, and matched the observed and model profiles using a number of simple criteria. This approach was time consuming, and did not necessarily result in the best fit in a "least-squares" sense. This technique was improved upon by generating a database of theoretical profiles to enable a quantitative comparison of the observed and model profiles. The results presented in Sections 4.1 - 4.2 have been published by Murphy, Cawthorne and Gabuzda (2013).

4.1 Fitting Procedure

In order to generate such a database an estimate of the intrinsic jet width must first be made. This was done by generating a series of jet profiles of increasing width, which were then convolved with the observing beam. Both Gaussian and top-hat model profiles were considered. A chart of observed jet width vs. intrinsic jet width was produced for each observing beam considered and the intrinsic jet width which resulted in the observed jet width closest to that observed was considered to be a suitable estimate of the actual intrinsic jet width. Both Gaussian and top-hat model profiles produced similar results. Since the jet width determined in this way is only an estimate, several trial values were used, as is described in Section 4.2.1.

Model transverse profiles were generated for a jet with angular width determined as described above and convolved with a Gaussian beam corresponding to the observing beam, varying the values of δ', γ' and f in increments of 1°, 1° and 0.05 respectively. A single database contained 79210 transverse profiles which were each 512 pixels in length took approximately 20 minutes (on an Intel Core 2 Duo) to generate. Decreasing the increment sizes of these parameters would drastically increases the time required to generate the databases. For example, incrementing δ' and γ' in steps of 0.1° would result in the databases requiring ~ 33 hours to be produced.

The best-fit model was taken to be the model giving the smallest residual χ^2 between the observed and theoretical profiles:

$$\chi^2 = \frac{Q_{max}}{I_{max}} \sum_{n=1}^{N} \frac{(I_n - I_n^0)^2}{\sigma_I^2} + \sum_{n=1}^{N} \frac{(Q_n - Q_n^0)^2}{\sigma_Q^2} \tag{4.1}$$

where N is the total number of data points, I_n and Q_n are the nth observed total and polarized intensity data points respectively, I_n^0 and Q_n^0 are the nth model total and polarized intensity model values respectively, and I_{max} and Q_{max} are the maximum values of the observed total and polarized intensity respectively.

The I profiles are therefore down weighted compared to the Q profiles by the factor Q_{max}/I_{max}. This factor is close to 0.10 for most of the profiles, and effectively gives the Q and I profiles comparable weights in the fitting, while also ensuring that the polarization structure of the best fit matches the observed polarization structure. This is very important as the polarization structure places the most constraints on the derived jet parameters. In effect, we are ignoring the higher signal-to-noise ratios of the I data, which is justifiable because the real errors that dominate the I image are not due to noise, but instead to mapping errors associated with CLEAN, and there is no reason to believe these should be much smaller than those for Q. The results of the fitting do not depend critically on the specific value of this weighting factor.

The thermal-noise components for both I and Q maps were determined in regions far from the region of source emission and these values were scaled by 1.8 to produce σ_I and σ_Q. This method for determining both σ_I and σ_Q was motivated by the studies carried out by Hovatta et al. (2012) based on Monte Carlo Simulations. These simulations included contributions associated with thermal noise and with uncertainty introduced by the CLEAN process; the contribution

of residual D-term uncertainty to σ_Q is negligible for our case, far from the total intensity peak.

Equations 3.7 and 3.11, which describe the model I and model Q profiles, are proportional to the strength of the magnetic field threading the jet and the number density of relativistic electrons. As both these quantities are unknown the database profiles were simply scaled so that the maximum total intensities of the observed and model profiles are equal. Matching the total flux densities of the observed and calculated I profiles would be more accurate; however, doing this would drastically increase the computational time required to complete the comparisons, as each theoretical profile would have to be numerically integrated. In addition, convolution with a beam to mimic the effects of finite resolution removes most of the asymmetries in the theoretical I profiles. As a result, most of the observed I profiles are roughly Gaussian in shape. Thus, the scaling factors corresponding to matching the observed and theoretical profile maxima or the observed and theoretical total fluxes are very similar, justifying this approach.

It is not possible to reliably apply standard statistical approaches to estimating the uncertainties in the resulting parameters without having well determined uncertainties in the fitted quantities — σ_I and σ_Q. Unfortunately, estimation of the uncertainties associated with values in individual pixels of the I and Q images is not straightforward, since the imaging process is complex and the values in neighbouring pixels will be correlated, due to convolution with the CLEAN beam. Our σ_I and σ_Q estimates should typically correspond to uncertainties in individual pixels that are correct to within a factor of a few; nevertheless, these estimates may not be good enough to yield fully accurate χ^2 values. Therefore, although the calculated χ^2 values can certainly be used to compare the profiles produced by different sets of model parameters and identify a set of parameters yielding a best fit, the χ^2 values cannot be used to evaluate the overall goodness of the fits obtained as the reduced $\chi^2 \gg 1$ for most cases (with an average value of approximately 100). Therefore an alternative method was used to obtain estimates of the uncertainties in the fitted parameters.

Estimates of the parameter uncertainties were determined by carrying out Monte Carlo simulations. Model sources based on the simple, cylindrical model outlined in Section 3.0.1 were generated using the determined best-fit parameters. These model sources fell off in total intensity linearly along the jet axis and had an intrinsic jet width equal to that estimated for the observed jets. Stokes I and Q maps were generated using these "core-jet" like model sources.

The direct Fourier transforms of these model maps at UV point locations based on the original observation were calculated. Model visibility data was calculated and normally distributed random thermal noise was added to them. The levels of thermal noise added was chosen so that the observed RMS noise in the resultant maps was approximately equal to the noise observed in the original maps. 200 Monte Carlo realizations of noisy model maps corresponding to the determined jet parameters were generated and transverse profiles were taken across each of these realizations. Each of these transverse profiles were subject to the same fitting process as the real observed profiles and the resulting best-fit parameters were then compared to the parameters used to generate the model maps to estimate the uncertainty in the fitting process. This method of replacing observed visibilities from an existing observation with model visibilities to be used in error analysis was the foundation of the resolution studies performed in Chapters 5 and 6.

This fitting procedure was applied to profiles for slices along which the EVPA was either parallel or perpendicular to the jet direction. The Stokes parameters Q and U are defined such that Q is positive and $U = 0$ when the EVPA is parallel to the jet.

An ideal VLBI jet for an analysis based on the method described above would be one that is straight, well resolved and shows clearly visible transverse I and Q structure, with U small compared to Q. Well-resolved VLBI jets are rare, however, and most VLBI jets contain some bends (though many of these are most likely small bends amplified by projection). Thus, VLBI jets displaying clear transverse structure, especially in polarization, were sought, with the aim of determining whether profiles across such jets could plausibly be represented using the helical field model outlined in Section 3.0.1 . This requires measuring these profiles away from bends, along directions orthogonal to the local jet direction.

It is important to note that this method only fits transverse profiles to theoretical models of a cylindrical jet. It is unable to describe any variations in intensity longitudinal to the jet direction.

4.2 Markarian 501

Markarian 501 (also known as 1652+398 or Mrk501) is a blazar with a redshift of 0.034 (corresponding to a distance of ~ 140 Mpc). This redshift is relatively small, with quasars having an average redshift close to 2. The close proximity

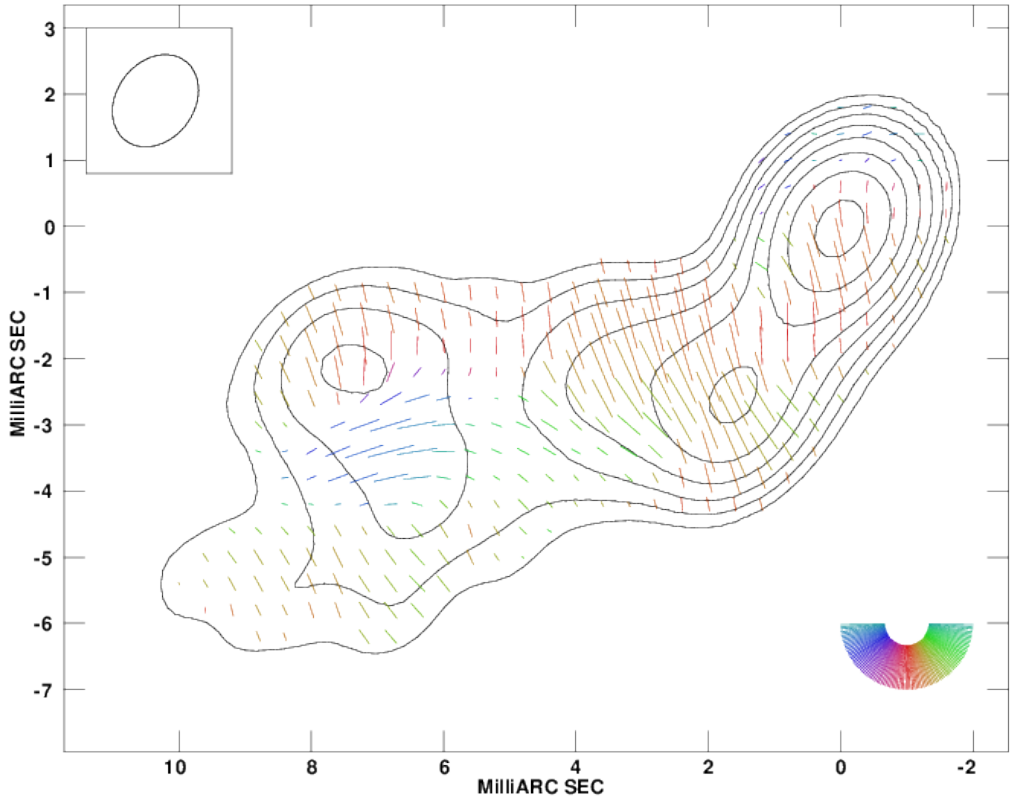

Figure 4.1: 4cm Polarization Map of Markarian 501 for February 1997 (Pushkarev et al. 2005). The polarization sticks are proportional to the polarized intensity. The peak intensity is 0.48 Jy/beam, and the contour levels are 0.60, 1.25, 2.5, 5.0, 10.0, 20.0, 40.0, and 80.0% of the peak.

of Markarian 501 to Earth means that more structural data for this source can be resolved than could be for its more remote counterparts. The elliptical galaxy hosting the blazar was first studied and catalogued by Benjamin Markarian in 1989 (Markarian et al. 1989).

The jet of Markarian 501 is almost certainly relativistic, as is shown by its one-sidedness; however, the shapes of the observed jet intensity and polarization profiles should be unaffected by this relativistic motion, if the jet has the same velocity across its width. Piner et al. (2010) have found apparent component speeds significantly less than the speed of light in the Markarian 501 jet. At first sight, this would suggest a non-relativistic jet, at variance with the one-sidedness of the jet (unless the VLBI jet was intrinsically one-sided). In the context of the standard model for VLBI jets, it seems far more likely that these low component speeds represent either relativistic motion at a very small angle to the line of sight or pattern speeds that do not directly reflect the speeds of the emitting plasma. In fact, a possible detection of superluminal motion with $v = (3.3 \pm 0.3)c$ based

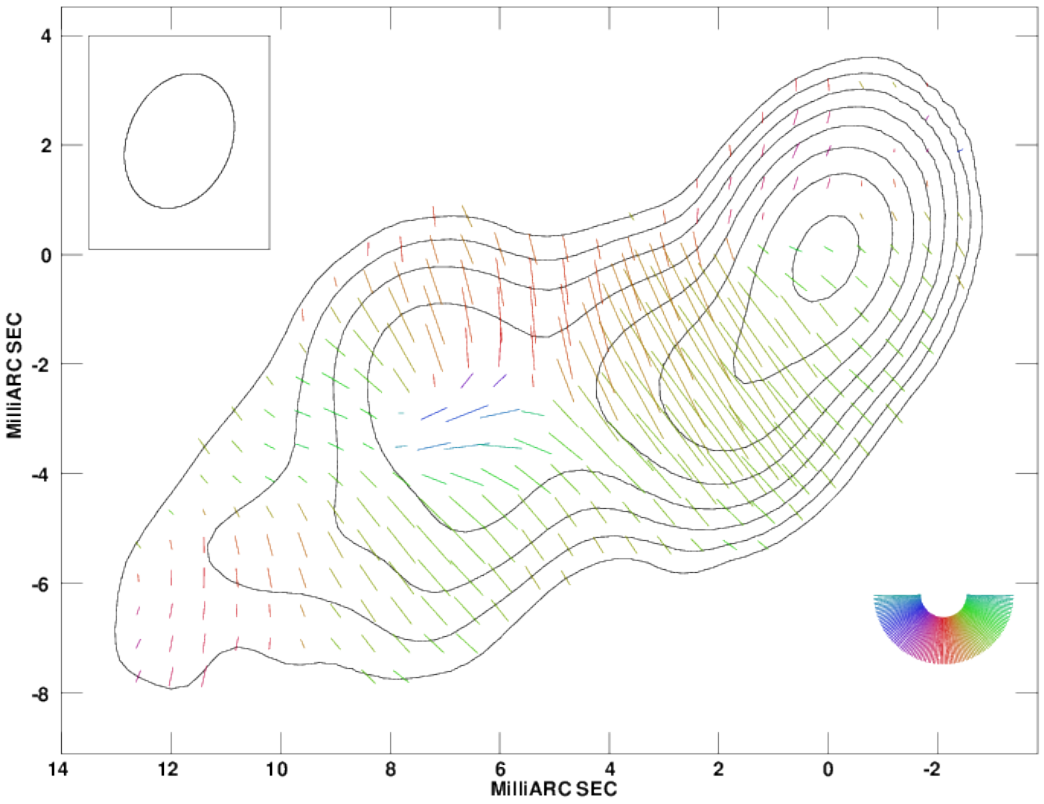

Figure 4.2: 6cm Polarization Map of Markarian 501 for February 1997 (Pushkarev et al. 2005). The polarization sticks are proportional to the polarized intensity. The peak intensity is 0.52 Jy/beam, and the contour levels are 0.60, 1.25, 2.5, 5.0, 10.0, 20.0, 40.0, and 80.0% of the peak.

on 43 and 86-GHz VLBI images has been reported for this source (Piner et al. 2009).

The most detailed multi-wavelength studies of Markarian 501 have been carried out by Giroletti et al. (2004, 2008). They derived constraints for two of Markarian 501's fundamental jet parameters; the intrinsic speed of the jet β and angle of the jet to the line of sight in the observer's frame δ on various scales, finding $\delta \leq 27°$ and $\beta \geq 0.88$, but with high values $\beta > 0.95$ allowed only for $10° < \delta < 27°$. They also found evidence for limb brightening in total intensity on somewhat larger scales than those studied here, which they attributed to transverse velocity structure of the jet. In particular, they proposed that the jet has a a fast spine and a slower sheath, as suggested by Laing (1996), with the two experiencing different degrees of Doppler boosting. The observed limb brightening could also have other origins, such as an enhancement in the synchrotron emission coefficient at the edges of the jet due to interaction of outer layers of the jet with the surrounding medium, or a helical magnetic field confined to a thin shell (e.g. Laing 1981).

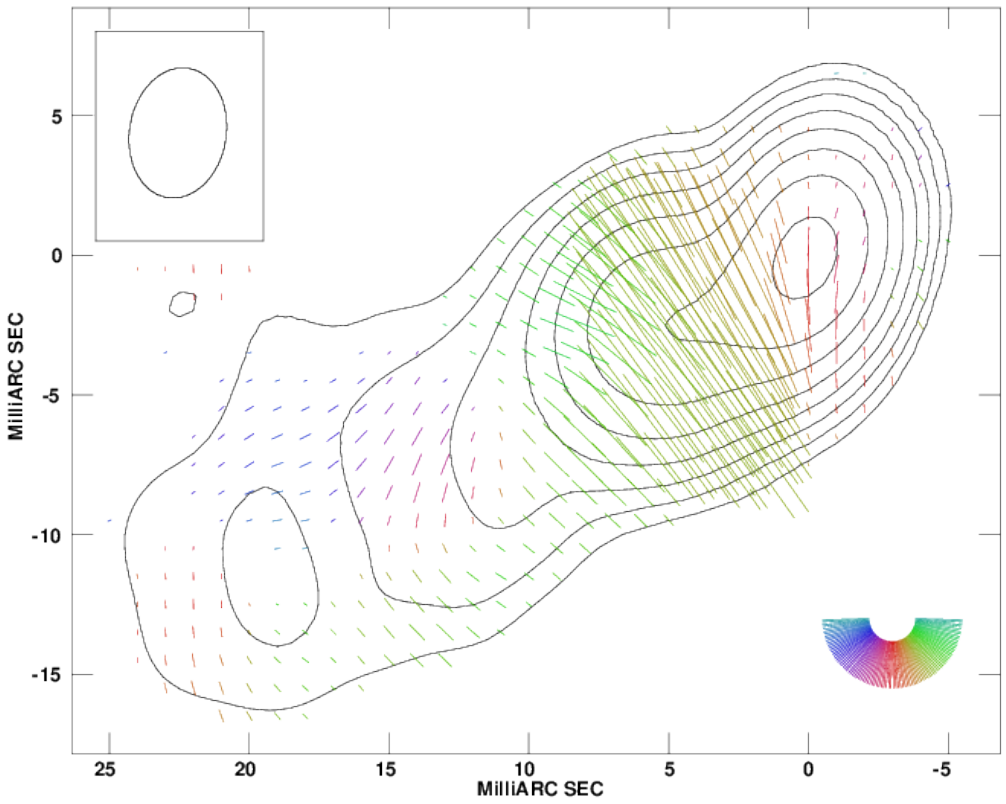

Figure 4.3: 13cm Polarization Map of Markarian 501 for May 1998 (Croke et al. 2010). The polarization sticks are proportional to the polarized intensity. The peak intensity is 0.64 Jy/beam, and the contour levels are 0.60, 1.25, 2.5, 5.0, 10.0, 20.0, 40.0, and 80.0% of the peak.

Markarian 501 shows a variety of transverse structures that could potentially be associated with a helical jet magnetic field, most notably a fairly clear 'spine–sheath' polarization structure, corresponding to configuration 3 of Fig. 3.2 (See Figs. 4.1 - 4.4 and Pushkarev et al. 2005).

4.2.1 Fitting Results

Fig. 4.2 shows a 6 cm total intensity map of this source with the polarization position-angle sticks superimposed, constructed from the same data as those of Pushkarev et al. (2005), from February 1997. Near the core, the EVPAs are predominantly perpendicular to the jet direction, maintaining this orientation as the jet direction begins to change about 6 mas from the core. Beyond this region, the EVPAs are perpendicular to the jet near the two edges and parallel in the centre, forming the spine–sheath polarization structure referred to above. The observational results of Giroletti et al. (2004, 2008) on comparable scales to those

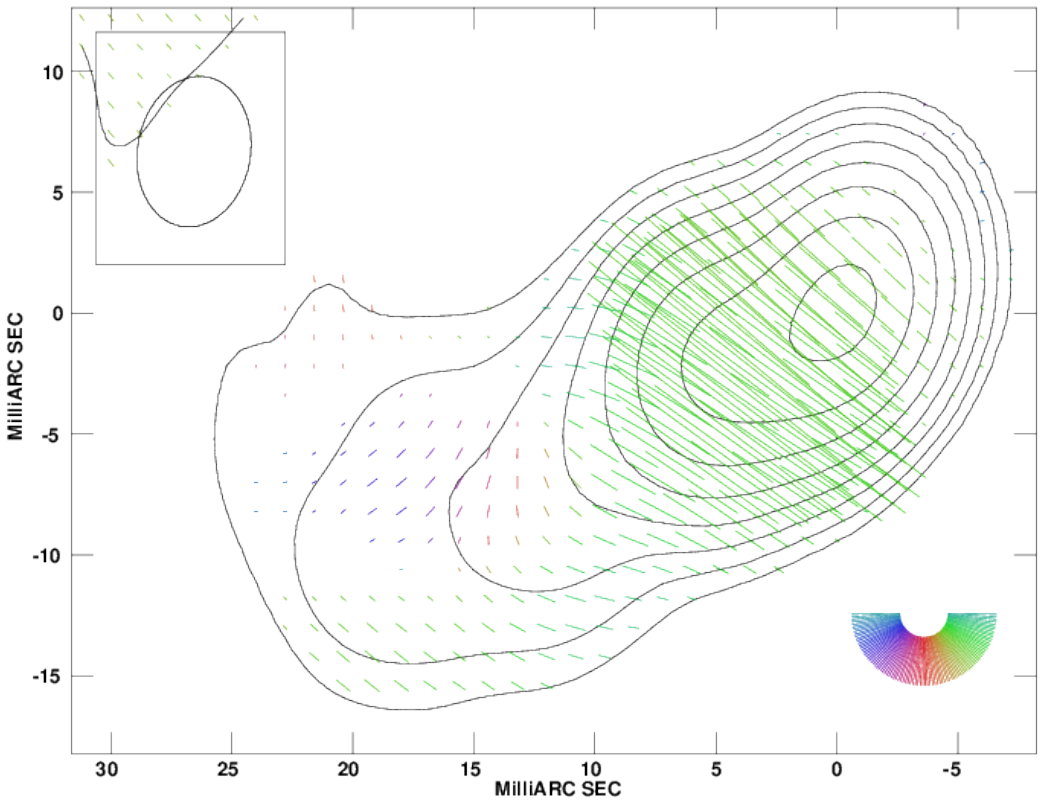

Figure 4.4: 18cm Polarization Map of Mrk501 for May 1998 (Croke et al. 2010). The polarization sticks are proportional to the polarized intensity. The peak intensity is 0.53 Jy/beam, and the contour levels are 0.60, 1.25, 2.5, 5.0, 10.0, 20.0, 40.0, and 80.0% of the peak.

studied here are broadly similar to those presented in Fig. 4.2, though at higher resolution, so that the transverse asymmetry is more apparent.

The choice of distances along the jet at which to analyse the transverse profiles is constrained by the need to find places where the EVPAs are either parallel or perpendicular to the jet (i.e., where U is close to close to zero all across the jet), and the Q profiles have sufficiently high signal-to-noise. The profiles to be analyzed were constructed at locations where these conditions are satisfied, far from positions where the jet bends. A further constraint on choice of position arises due to the fact that the jet is essentially unresolved in the immediate vicinity of the core.

The three 6 cm slices chosen for analysis are marked on Fig. 4.5. The profiles were sampled using the AIPS task 'SLICE', then compared to the database of model profiles (each convolved with the Gaussian observing beam) as described in Section 4, and the values of γ', δ' and f resulting in the best fit (minimum residual) identified (given in Table 4.1). The intervals between adjacent values of

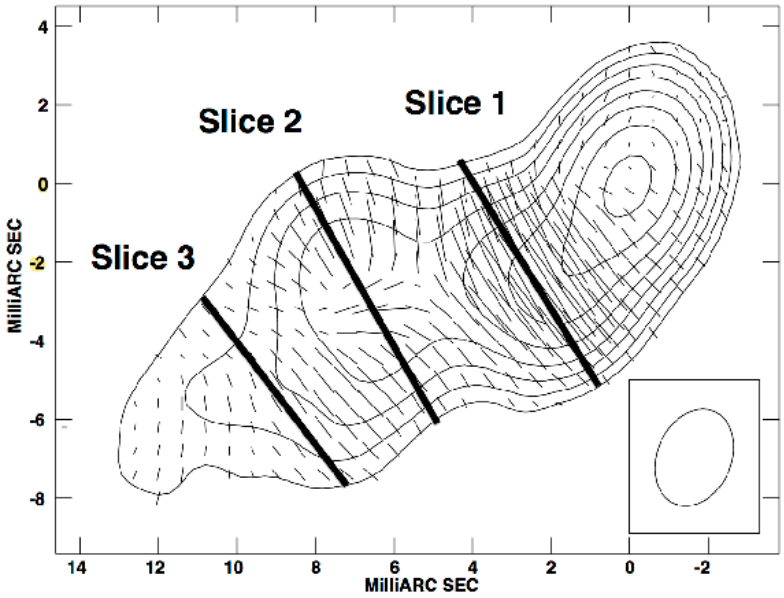

Figure 4.5: 6 cm Polarization Map of Markarian 501 for February 1997 (Pushkarev et al. 2005). The polarization sticks are proportional to the polarized intensity. The three lines across the jet show the transverse slices that were analysed. The peak intensity is 0.52 Jy/beam, and the contour levels are 0.60, 1.25, 2.5, 5.0, 10.0, 20.0, 40.0, and 80.0% of the peak. The three lines across the jet show the transverse slices that were analysed.

γ', δ' and f in the database were 1°, 1° and 0.05, respectively.

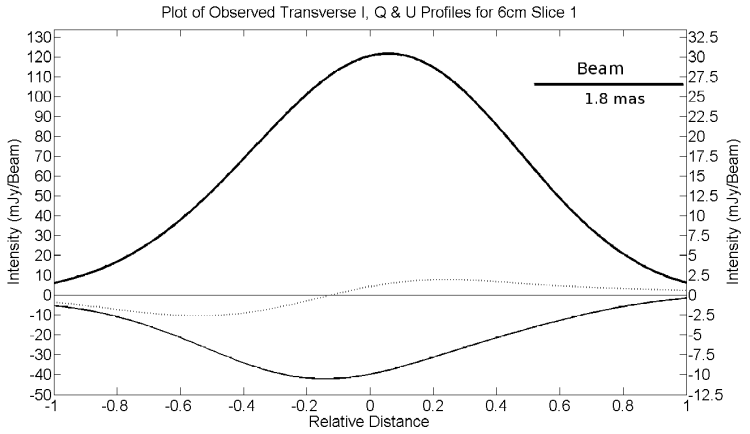

(a) Slice 1

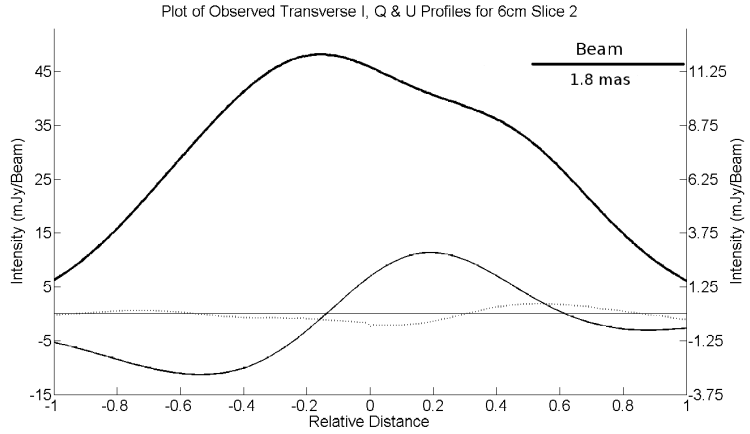

(b) Slice 2

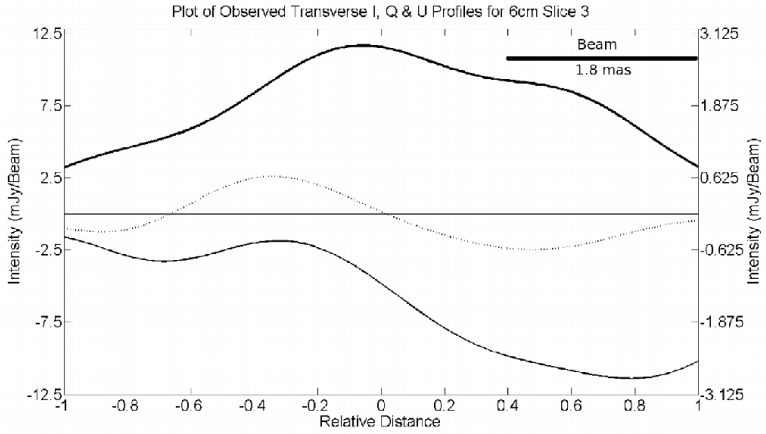

(c) Slice 3

Figure 4.6: Observed I (solid), Q (dashed) and U (dotted) profiles for Slices 1, 2 and 3 of the 6 cm Markarian 501 map (see Fig. 4.5). The scale for the I profile is given along the left-hand vertical axis and the scale for the Q and U profiles along the right-hand vertical axis. The beam is 1.8 mas along the slice and 2.4 mas transverse to the slice.

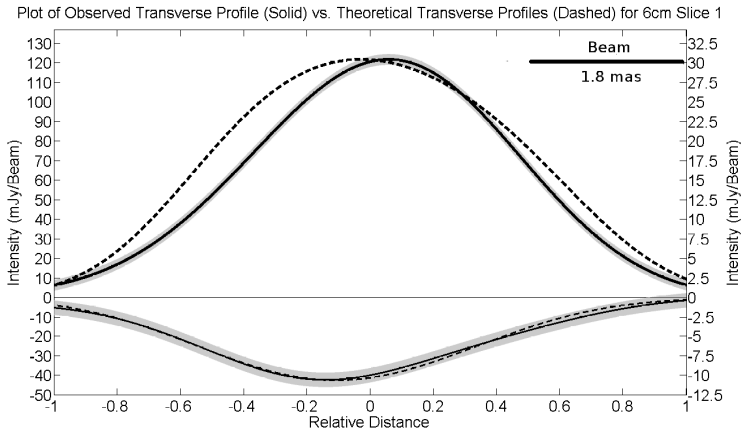

(a) Slice 1

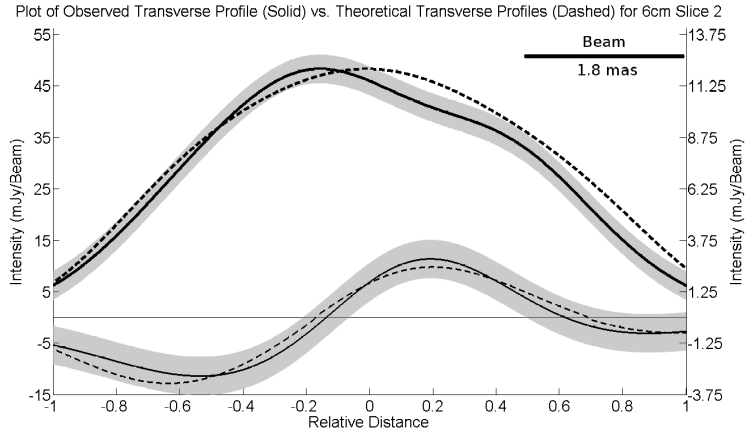

(b) Slice 2

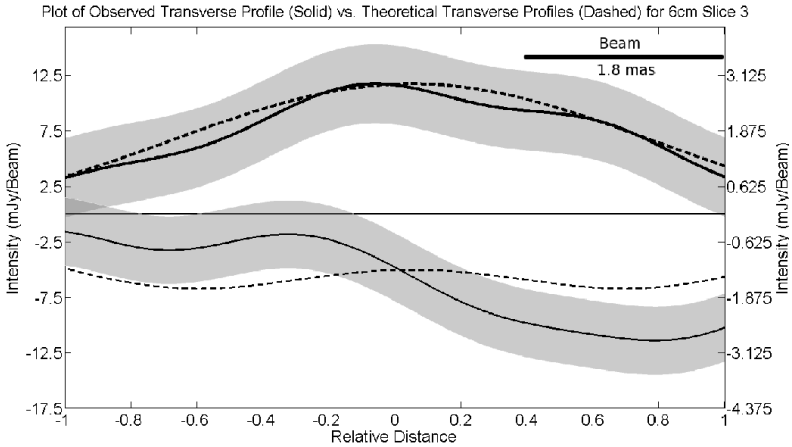

(c) Slice 3

Figure 4.7: Plots of observed and best-fit model I and Q profiles for Slices 1, 2 and 3 (top to bottom) of the 6 cm Markarian 501 map (see Fig. 4.5). The observed profiles are solid and the best-fit profiles dashed; the grey shaded areas surrounding the observed profiles correspond to the range of the 1σ uncertainties for Q and the 3σ uncertainties for I. The scale for the I profile is given along the left-hand vertical axis and the scale for the Q profile along the right-hand vertical axis. The beam is 1.8 mas along the slice and 2.4 mas transverse to the slice.

Table 4.1: Best fit Parameters for 6 cm Markarian 501 Slices (Epoch February 1997)

Slices	γ'	δ'	f	Intrinsic Jet Width
Slice 1	$41° \pm 3°$	$81° \pm 3°$	0.70 ± 0.05	3.1 mas
Slice 2	$53° \pm 1°$	$80° \pm 2°$	0.40 ± 0.05	5.7 mas
Slice 3	$47° \pm 1°$	$90° \pm 2°$	0.00 ± 0.10	4.8 mas

The observed I (solid), Q (dashed) and U (dotted) profiles for the three 6 cm slices are shown in Fig. 4.6. The left and right sides of the horizontal axis in this figure correspond to the North and South sides of the Markarian 501 jet. The Stokes parameters are defined such that Q is positive and U is zero for a polarization E field parallel to the jet. U must be small (much less than Q) for the model used to be valid; the plots show that this condition is satisfied for the three slices chosen.

The observed (solid) and best-fit model (dashed) profiles I and Q for the three slices are shown in Fig. 4.7. Here also, the left and right sides of the horizontal axis correspond to the North and South sides of the Markarian 501 jet. The I and Q curves in Fig. 4.7 are easily distinguishable, as the Q curves are much smaller in amplitude; the intensity scale for I is shown to the left and that for Q to the right. The shaded bands around the I and Q profiles in Fig.4.7 correspond to 3σ and 1σ uncertainties respectively, estimated in accordance with the approach of Hovatta et al. (2012).

Unconstrained fits for slice 3 yielded best-fit parameters corresponding to an opposite sense of the helicity of the magnetic field, compared to slices 1 and 2; this corresponds to the fact that Q changes from negative to positive across slice 2, but becomes more negative across slice 3 (Fig. 4.2). Since such a change in the helicity of the magnetic field threading the jet between slices 2 and 3 is physically implausible, fits to slice 3 were constrained so that the helicity of field was the same as that found for slices 1 and 2; this is the fit shown in Fig. 4.7 (and given in Table 4.1).

The best-fit model Q profiles for slices 1 and 2 lie within 1σ of the observed Q profile, while the best-fit Q profile for slice 3 lies within 2σ of the observed profile. The model and observed I profiles for slices 1 and 2 differ by more than 3σ over substantial fractions of these profiles, with the model profile being more symmetrical than the observed profile; the fitted and observed I profiles for slice 3 agree to within about 2σ.

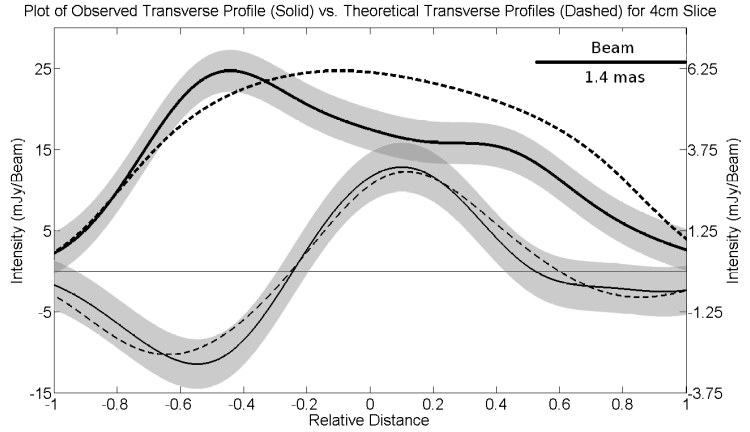

(a) 4 cm Slice

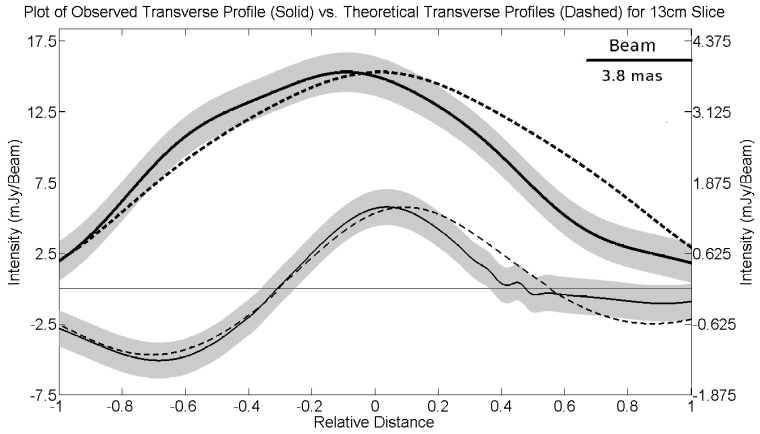

(b) 13 cm Slice

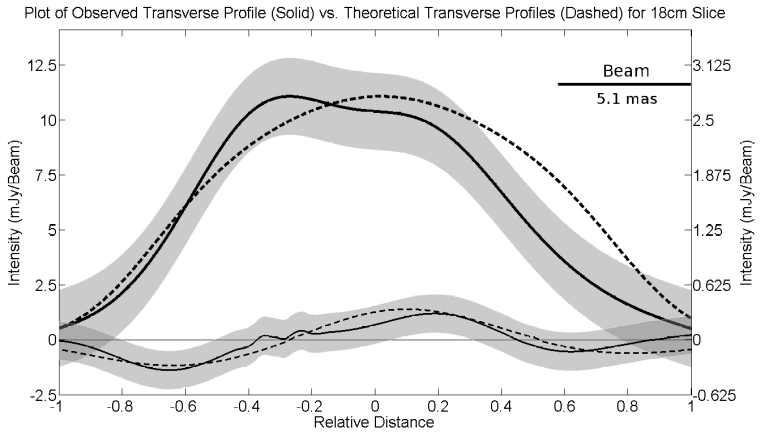

(c) 18 cm Slice

Figure 4.8: Plots of observed and best-fit model I and Q profiles for 4 cm, 13 cm and 18 cm slices taken in the same region as Slice 2 (see Fig. 4.5). The observed profiles are solid and the best-fit profiles dashed; the grey shaded areas surrounding the observed profiles correspond to the range of the 1σ uncertainties for Q and the 3σ uncertainties for I. The scale for the I profile is given along the left-hand vertical axis and the scale for the Q profile along the right-hand vertical axis.

Table 4.2: Best fit Parameters for Markarian 501 Slice 2 for 4 different wavelengths

Wavelength	γ'	δ'	f	Intrinsic Jet Width
4 cm	$53° \pm 1°$	$83° \pm 2°$	0.40 ± 0.20	5.5 mas
6 cm	$53° \pm 1°$	$80° \pm 2°$	0.40 ± 0.05	5.7 mas
13 cm	$54° \pm 1°$	$86° \pm 2°$	0.35 ± 0.05	21.6 mas
18 cm	$54° \pm 1°$	$81° \pm 2°$	0.60 ± 0.05	22.9 mas

Since the intrinsic (or unconvolved) angular jet width was estimated using the procedure outlined in Section 4.1, the fitting procedure was repeated for a series of intrinsic jet widths centred on the values used above and listed in Table 4.1. Changing the intrinsic jet width had only a very minor effect on the best fit γ' and δ' values while having a more pronounced effect on the degree of entanglement. However, in general, as the intrinsic jet width varied from its estimated value, the χ^2 value of the best fit profiles increased. While the intrinsic jet width that minimised the χ^2 value for a given slice is not exactly that found by fitting the I profile, the two never differed by more then 10%. Values differing by more than 15% yielded very large values of χ^2.

The line-of-sight angles, δ', for the first two slices in Table 4.1 agree to within a degree, and differ by less than 1σ, as expected if the intrinsic bends in this region of the jet are small. The value of δ' for slice 3 differs by about 10° ($\delta' = 90°$), which corresponds to about 3.5σ; however, as was previously pointed out, it was necessary to constrain the fit for slice 3 to have the same sense of helicity as slices 1 and 2. Therefore, the change in viewing angle implied by the nominal (constrained) best fit for slice 3 may not be significant.

The fitting results indicate a somewhat higher value of γ' for slice 2 than for slice 1, with this difference being about 4σ, suggesting that the variation in γ' between the slices may be real. In this case, this suggests that the appearance of a spine–sheath polarization structure at the position of slice 2 could be due to a (relatively small) change in the helical pitch angle. The value of γ' for slice 3 lies between the values for the other two slices; formally, γ' for slice 3 differs from the value for slice 2 by about 3.5σ, and from the value for slice 1 by slightly less than 2σ.

The values of f appear to decline with distance from the core, from 0.7 at slice 1 to 0.4 at slice 2. This trend may continue for slice 3 ($f = 0$), although this is unclear due to the uncertainty associated with slice 3 discussed above. The

difference between slices 1 and 2 appears to be significant: the two f values differ by approximately 4σ; physically, this represents a decrease in the disordered component of the magnetic field with distance from the core in the region of the jet sampled.

The fitting procedure was repeated for slice 2 using images at wavelengths of 4 cm for February 1997 (data of Pushkarev et al. 2005) and 13 cm and 18 cm for May 1998 (data of Croke et al. 2010). The results are given in Table 4.2 and shown in Fig. 4.8. It is clear that the observations at these other wavelengths yield consistent best-fit parameter values; the values of γ', δ' and f essentially all agree to within 1σ, with the largest differences not exceeding about 2σ.

4.2.2 Markarian 501 Spectral Index

As described in Section 3.0.1 a spectral index (α) of unity was assumed throughout the jet in order to make the equations that govern this model analytically solvable. However, observations of the spectral indices in the jets of AGN have shown that this value is typically $\simeq 0.5$. Fig. 4.9 shows a spectral index map for Markarian 501.

This gives rise to concerns about the trustworthiness of the fits obtained assuming $\alpha = 1.0$. To investigate this, model profiles were obtained numerically for two other spectral indices. Profiles for both I and Q were determined numerically by integrating equations using the Gauss-Kronrod quadrature. This method was required as the functions governing both I and Q have singularities at one of their limits.

Figure 4.10 shows the effect of variations in the spectral index on the I and Q profiles. The left and right hand plots show profiles for jets with $\alpha = 1$ and $\alpha = 0.5$ respectively, and the same values of γ', δ' and f. The differences between these profiles are very minor. The positions where the polarization angle changes by 90° are slightly different. In addition, the amount of longitudinal polarization has increased slightly, while the amount of transverse polarization has decreased. This second difference results in the configuration map for $\alpha = 0.5$ being slightly different to that for $\alpha = 1$ (see Fig. 4.11).

The effect of changing spectral index on the best fit model values of γ', δ' and f was examined using slices through the 13 cm images at the location of slice 2 in Fig. 4.5. Model databases were then generated numerically using values of

Table 4.3: Best fit Parameters for 13 cm Markarian 501 Slice for three values of α

α	γ'	δ'	f
1.000	$54° \pm 1°$	$86° \pm 2°$	0.35 ± 0.05
0.507	$53° \pm 3°$	$85° \pm 2°$	0.40 ± 0.05
0.248	$53° \pm 1°$	$84° \pm 2°$	0.40 ± 0.05

$\alpha = 0.507$ (the average value of α across the slice) and $\alpha = 0.248$ (the minimum value of α across the slice, representing the maximum deviation from unity) and the FWHM of the beam used in creating the 13 cm map. These databases were then used to obtain new best-fit parameters for the 13 cm slice. The results are shown in Table 4.3. The differences in the best fit parameters are extremely small with the γ', δ' and f values for the two numerically calculated best-fit profiles ($\alpha = .508$ and $\alpha = .248$) and the analytically calculated best-fit profile (for $\alpha = 1.0$) all coinciding within the 1σ errors.

4.2.3 Derivation of δ and $\beta = v/c$ in the Observer's Frame

The line of sight angle δ' in the rest frame of the jet is related to the corresponding angle in the observer's frame, δ, by

$$\sin\delta' = \frac{\sin\delta}{\Gamma[1 - \beta\cos\delta]} \tag{4.2}$$

where Γ is the Lorentz factor for the motion and $\beta = v/c$ (Rindler 1990).

In addition, the apparent speed of a component moving along the jet can be written

$$\beta_{app} = \frac{\beta\sin\delta}{1 - \beta\cos\delta} \tag{4.3}$$

$$= \Gamma\beta\sin\delta' \tag{4.4}$$

$$= \frac{\sin\delta'}{\sqrt{\beta^{-2} - 1}} \tag{4.5}$$

It follows that, if β_{app} is known from component motion and δ' is known, for example, from profile fitting such as that carried out in this chapter, Eqn. 4.5 can be rearranged to give

$$\beta = \left[1 + \frac{\sin^2\delta'}{\beta_{app}^2}\right]^{-1/2} \tag{4.6}$$

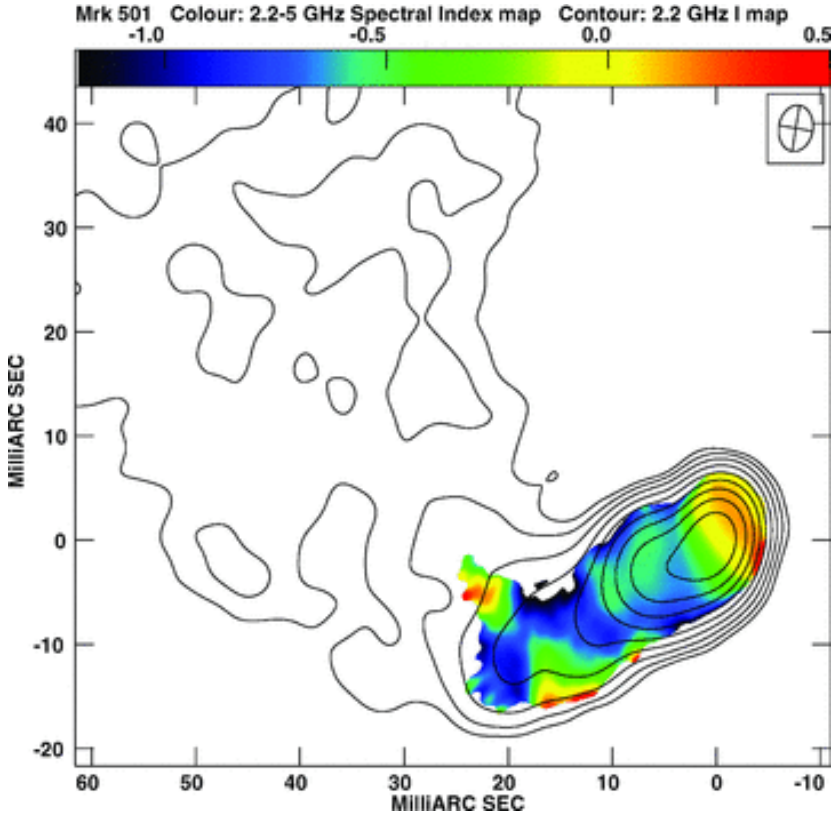

Figure 4.9: Spectral index distributions constructed from 6 cm and 13 cm data from Croke et al. (2010). The two I maps were both convolved with a beam with FWHM 4.5 × 3.5 mas and PA = −9° (corresponding to the 13 cm beam). The contours of total intensity at 13 cm are superimposed. The contour interval is a factor of 2, with the lowest contour level being 1.4 mJy beam^{-1} and a peak intensity of 683.6 mJy beam^{-1}. The colour scale ranges from $-1.2 < \alpha < 0.5$. Clip levels of I maps: 1.6 mJy (6 cm), 2.4 mJy.

The profile fitting has indicated $\delta' \simeq 83°$ for the Markarian 501 jet. Taking this together with the superluminal motion reported by Piner et al. (2009), $\beta_{app} = 3.3$, gives $\beta \simeq 0.96$ and $\delta \simeq 15°$. Using the range of δ' values given by the various profile fits, $80° - 86°$, does not change the resulting values of δ by more than $1°$. These results are consistent with the conclusion of Giroletti et al. (2004), based on completely different information, that $\delta \leq 27°$ and $\beta \geq 0.88$, with $\beta > 0.95$ allowed only for $10° < \delta < 27°$. Although these particular results are somewhat uncertain, since the relevant superluminal motion corresponds to a weak feature whose position is difficult to determine precisely, this illustrates the potential of this approach. Note as well that using the more typical subluminal speeds obtained for the jet of Markarian 501, e.g. $\beta_{app} \simeq 0.47$ (Piner et al. 2010), implies angles to the line of sight $\delta \simeq 60°$ and $\beta \simeq \beta_{app}$, which are not reasonable, since they cannot provide the observed one-sided VLBI structure. This implies that the very

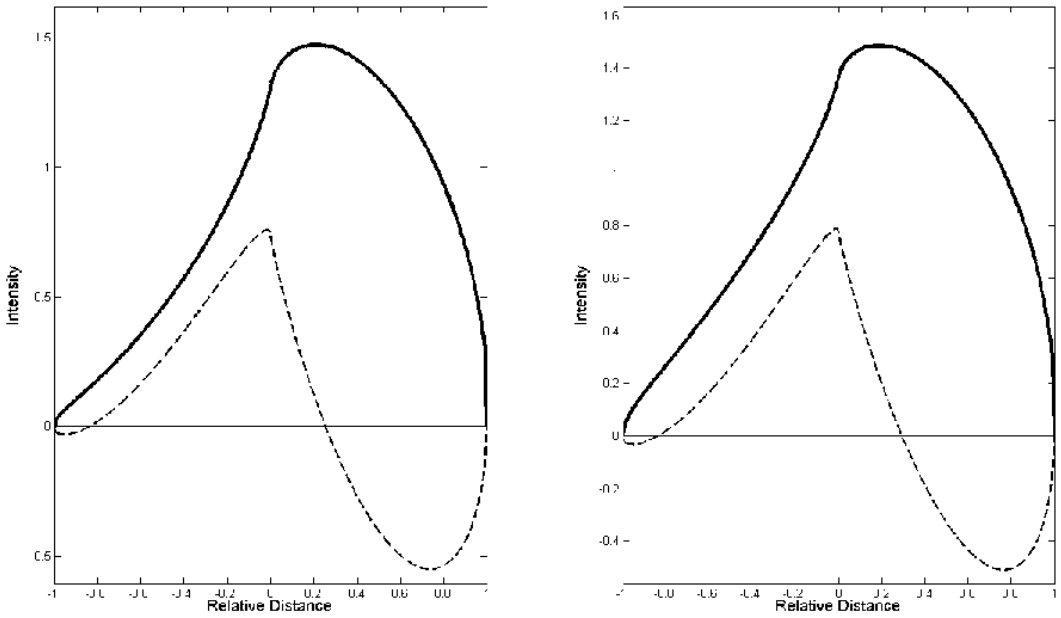

Figure 4.10: Theoretical profiles generated numerically for $\gamma' = 60$, $\delta' = 40$ and $f = 0$. The left and right profiles were determined for $\alpha = 1.0$ and $\alpha = 0.5$, respectively. The magnetic-field orientation is perpendicular to the polarization orientation.

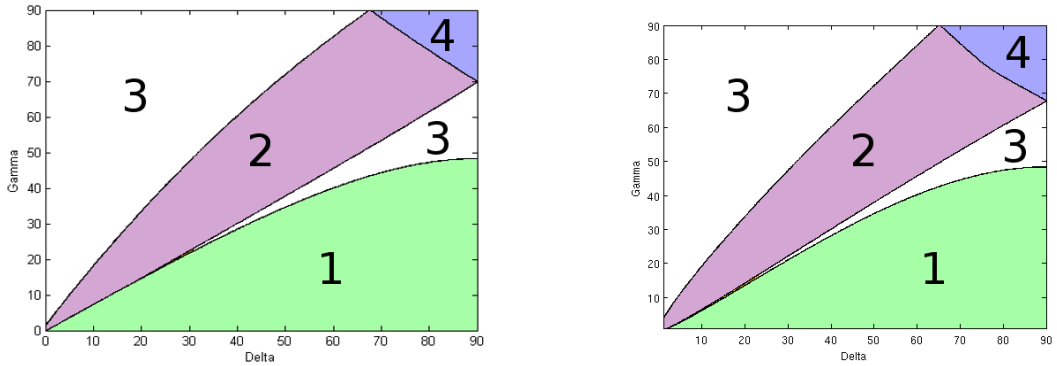

(a) Magnetic-field configuration maps for $\alpha = 1.0$

(b) Magnetic-field configuration maps for $\alpha = 0.5$

Figure 4.11: Magnetic-field configuration maps for different for spectral indices after convolution with a Gaussian beam with a FWHM one-quarter the size of the profile to mimic the effects of finite resolution. Region numbers correspond to the configuration types listed in Section 3.0.2.

low component speeds typically observed in Markarian 501 are incompatible with its observed polarization structure, and so must represent pattern speeds rather than physical speeds (in other words, they do not represent highly relativistic motion viewed at a very small angle).

The approach taken in this section is similar to that used by Canvin et al. (2005) on kiloparsec scales, in that both analyses fit a jet model to the observed profile in order to determine the angle between the jet axis and the line of sight in the rest frame of the flow. One advantage of applying this technique on parsec scales is that it is possible to obtain constraints on the underlying flow speed fairly directly using observations of superluminal components, whereas, in the kiloparsec case, more indirect estimate must be used, such as the jet–counterjet brightness ratio.

4.2.4 Agreement with Faraday Rotation Results

The fractional polarization from the helical field model is generally lower on the side of the jet where the field lines are closest to the line of sight as the observed polarization is determined by the component of the magnetic field in the plane of the sky. If the magnetic field threading the Faraday rotating medium is co-moving with the jet, the magnitude of the Faraday rotation measure will be highest on the side of the jet where the field lines are closest to the line of sight, i.e., on the side with the lower fractional polarization (Fig. 4.12).

Gabuzda et al. (2004) reported the detection of a transverse Faraday rotation measure (RM) gradient across the Markarian 501 jet, based on 2,4 & 6 cm VLBA polarization observations, and interpreted this as evidence for a helical magnetic field associated with this jet. Croke et al. (2010) subsequently reported a transverse RM gradient in the same sense based on 4, 6, 13 & 18 cm VLBA polarization observations.

In the regions of the jet considered here, comparing the two sides of the jet, the Northern side (corresponding to the left-hand sides of the plots in Figs. 4.7 & 4.8) generally displays higher fractional polarization, i.e., more negative values of Q/I. The Faraday rotation measures on the Northern side of the jet, RM_N, are therefore expected to be smaller in magnitude than those on the Southern side, RM_S. This is consistent with the observational results of Gabuzda et al. (2004), based on the same 2 – 6 cm VLBA data considered here: $\mathrm{RM}_N = -55 \pm 20$ rad/m^2, $\mathrm{RM}_S = 130 \pm 20$ rad/m^2. The effect of the measured Galactic rotation measure in the direction toward Markarian 501 [+42 rad/m^2, Rusk (1988)] was subtracted

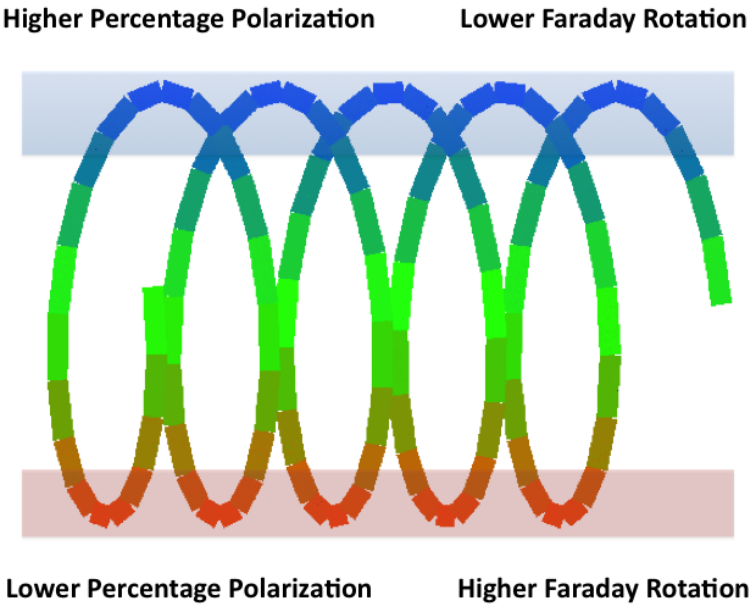

Figure 4.12: This figure highlights how the magnitude of the Faraday rotation measure will be highest on the side of the jet where the field lines are closest to the line of sight. The line of sight component of the magnetic field is greatest on this side as, as the magnitude for Faraday rotation is directly proportional to the line of sight magnetic field, the RM should be highest on this side. Conversely, as the observed polarization is directly proportional to the magnetic field component in the plane of the sky, the percentage polarization is expected to be lowest on this side.

from the observed polarization angles before the Faraday rotation map was constructed, so that the residual observed rotation measure should correspond to Faraday rotation occurring in the vicinity of the AGN. If the Galactic rotation measure is instead taken to be the value typical of the region within a few degrees of Markarian 501 in the catalog of Taylor, Stil and Sunstrum (2009), $\simeq +20$ rad/m^2, these two values become $\mathrm{RM}_N \simeq -35$ rad/m^2, $\mathrm{RM}_S \simeq 150$ rad/m^2.

The expected quantitative difference between the magnitudes of the Faraday rotation measures on either side of the jet can be estimated if the Faraday rotating material is concentrated in a relatively thin shell in outer layers of the jet.

From Eqn. 2.23

$$RM \propto \int n_e \mathbf{B} \cdot \mathrm{d}\mathbf{l} \tag{4.7}$$

$$RM \propto \int n_e B \mathrm{d}l \cos\theta \tag{4.8}$$

were $\cos\theta$ is the angle between the magnetic field and the line of sight. For a helical magnetic field this angle is given by

$$\cos\theta = \frac{x}{R}\sin\delta'\sin\gamma' + \cos\delta'\cos\gamma' \tag{4.9}$$

where R is the radius of the jet x is position along a slice transverse to the jet such that $-R \leq x \leq R$, γ' is the helical pitch angle and δ' is the viewing angle in the rest frame of the jet.

The percentage difference between the magnitudes of the RMs on either side of the jet ($x = \pm R$)can now be crudely estimated. Letting $A = \sin\delta'\sin\gamma'$ and $B = \cos\delta'\cos\gamma'$ this difference is given by

$$\frac{|A+B| - |B-A|}{|A+B|} \tag{4.10}$$

For $\gamma' = 40°$ and $\delta' = 80$, this indicates a difference of about 35%, somewhat smaller than the observed value of about $60 - 75\%$.

Considering this one case, and given the limited transverse resolution of the rotation-measure image of Gabuzda et al. (2004), it could be a coincidence that the model considered correctly predicts the side of the jet that should have the higher Faraday rotation. However, this analysis illustrates the sort of comparison that could, in principle, usefully be carried out once profile-fitting results for a greater number of AGNs are available. Of course, the sign of the Faraday rotation measures cannot be predicted by our model, as the polarization profiles do not depend on the polarity of the magnetic field.

4.3 M87

The work described in this section was carried out in collaboration with Juan Carlos Algaba. Juan Carlos supplied the calibrated I, Q U maps of M87 in addition to the final calibrated data used to produce these maps. I then analysed transverse slices taken across these maps.

Messier 87 (also known as M87, Virgo A or NGC 4486) is a supergiant elliptical galaxy. It is the second brightest galaxy within the northern Virgo Cluster and is located about 16.4 million parsecs from Earth (Bird et al. 2010). It was

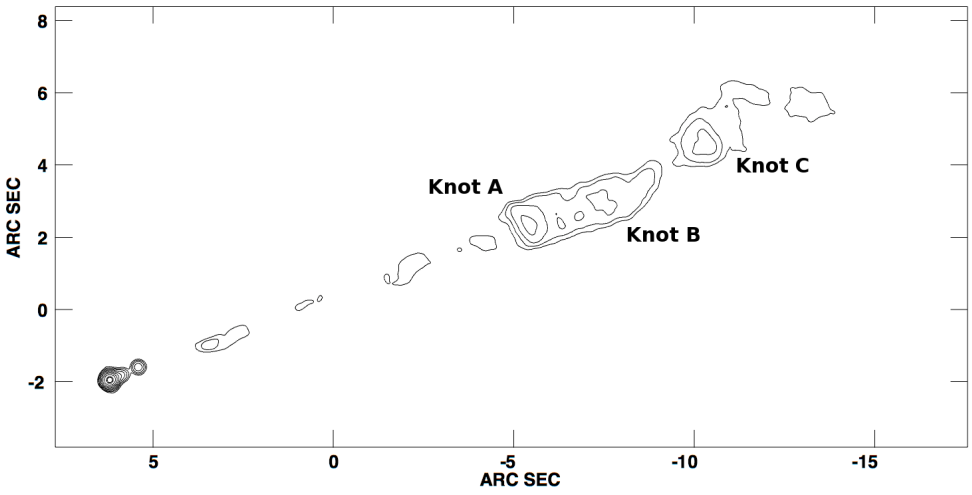

Figure 4.13: 3.75 cm Intensity Map of M87 (Algaba et al 2013). The peak intensity is 3.1 Jy/beam and the contour levels are .125, .25, .5, 1.0, 2.0, 4.0, 8.0, 16.0 and 32.0% of the peak. The locations of Knot A, B and C are shown.

discovered in 1781 by the French astronomer Charles Messier, who cataloged it as a nebulous feature. The radio jet of M87 is over 1.5 kiloparsec in length.

Similarly to Markarian 501, M87 is almost certainly relativistic. In addition to its one-sided jet structure (Fig. 4.16), numerous superluminal components with observed velocities of up to ~ 6c have been observed using the Faint Object Camera of the Hubble Space Telescope (Biretta et al. 1999). The exact classification of M87 is still a matter of some debate. Recently it has been proposed M87 may be a BL Lac object with a low-luminosity nucleus compared with the brightness of its host galaxy seen from an unfavourable angle. While M87 demonstrates most of the properties of of a BL Lac, its nucleus is very faint relative to the host galaxy and would not be detected if it were much further away. Tsvetanov et al. (1997) demonstrate that M87 is consistent with the idea that the faintness of the nucleus is primarily due to a relatively large angle between the jet axis and the line of sight.

The jet of M87 shows high polarization at kiloparsec scales (Owen et al. 1990,

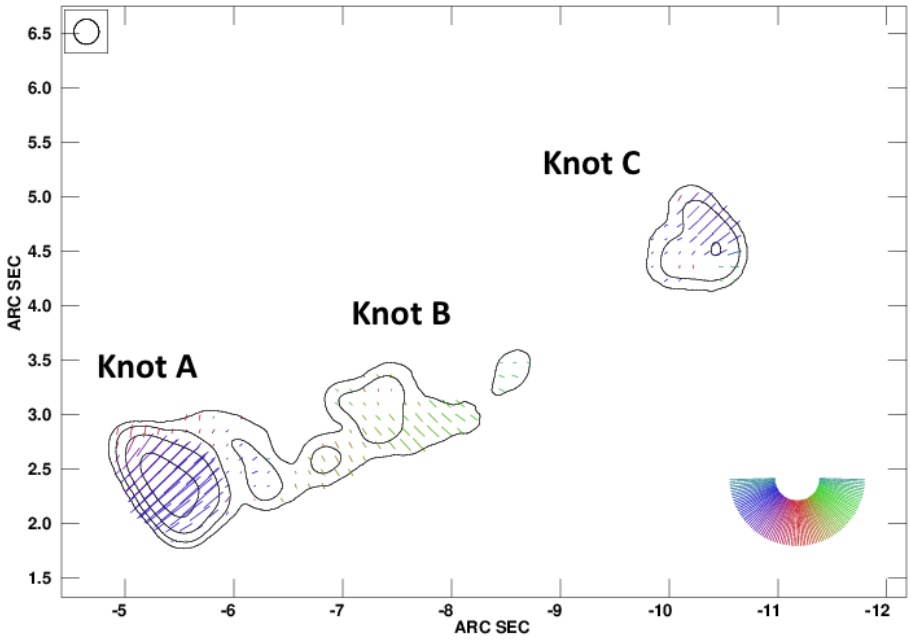

Figure 4.14: 1.36 cm Polarization Map of M87 (Algaba et al 2013). The map is of the Knot A - Knot C region of the source. The polarization sticks are proportional to the polarized intensity. The peak intensity is 2.4 Jy/beam and the contour levels are .125, .25, .5, 1.0, 2.0, 4.0, 8.0, 16.0, 32.0 and 64.0% of the peak.

Perlman et al. 1999) in addition to indications of higher degrees of fractional polarization at its jet edges (Owen et al. 1989). Very recent results from Algaba et al. (2013) presented evidence for a large-scale helical magnetic field structure in the kiloparsec jet of M87, based on the detection of multiple transverse RM gradients across the jet. Due to this evidence for helical magnetic field structure, the high levels of polarization and the highly resolved polarization structure, the jet M87 was chosen as another test-case for this analysis method.

4.3.1 Fitting Results

Figures 4.14 - 4.16 show polarization maps of the region of the M87 jet analysed. These images were produced using archival data of VLA data at 8, 15 and 22 GHz taken at multiple epochs between 2002 and 2005 and stacked atop one another (Algaba et al. 2013). At Knot A, the EVPAs are predominantly parallel to the jet direction. This EVPA orientation changes abruptly after Knot A with EVPAs predominantly longitudinal to the jet direction until Knot C. The region of the jet between Knot A and Knot B is commonly known as Knot A Diffuse or Knot

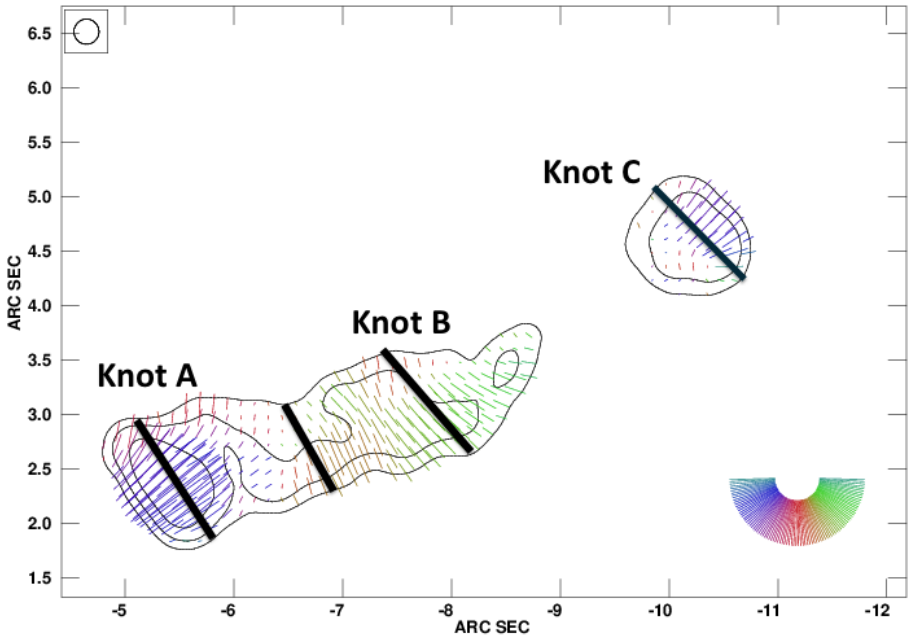

Figure 4.15: 2 cm Polarization Map of M87 (Algaba et al 2013). The map is of the Knot A - Knot C region of the source. The polarization sticks are proportional to the polarized intensity. The peak intensity is 2.8 Jy/beam and the contour levels are .25, .5, and 1.0% of the peak. Also marked on this figure are the approximate locations of the transverse slices that were taken during this analysis.

A Dif.

As before, the profiles were sampled using the AIPS task 'SLICE', then compared to the database of model profiles (each convolved with the Gaussian observing beam) as described in Section 4. The approximate locations of these slices can be seen in Fig. 4.15.

4.3.1.1 Knot A Diffuse & Knot B

Slices were first taken in the region of Knot A Diffuse and Knot B. These slices were taken perpendicular to the jet direction in regions where the Stokes Q polarization was significantly larger than the Stokes U. Values of γ', δ' and f resulting in the best-fit (minimum residual) identified for these slices are given in Table 4.4.

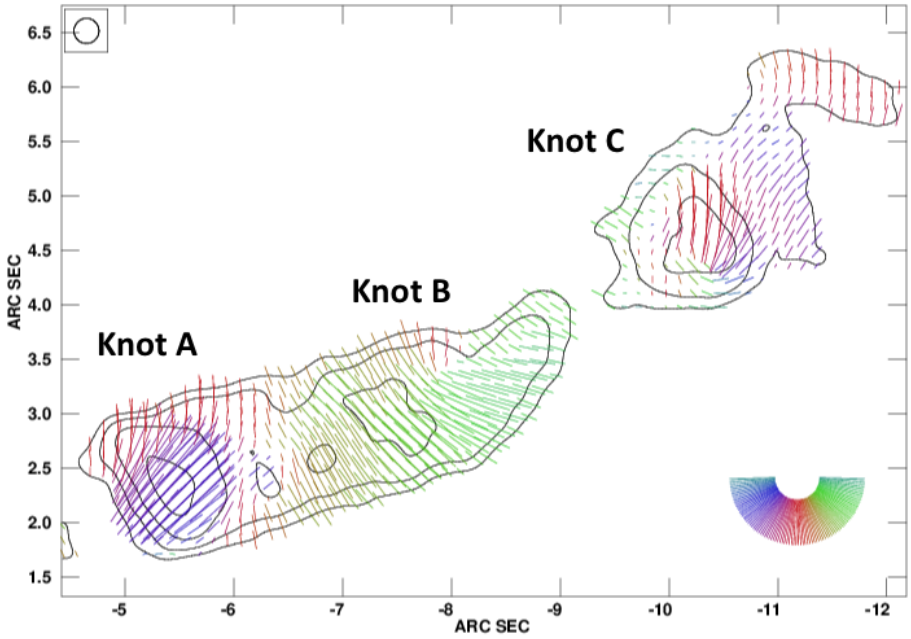

Figure 4.16: 3.75 cm Polarization Map of M87 (Algaba et al 2013). The map is of the Knot A - Knot C region of the source. The polarization sticks are proportional to the polarized intensity. The peak intensity is 3.1 Jy/beam and the contour levels are .25, .5, 1 and 2% of the peak.

Table 4.4: Best fit Parameters for M87 Knot A Diffuse & Knot B Slices

Knot	Wavelength	γ'	δ'	f
Knot A Dif	1.36 cm	$41° \pm 4°$	$74° \pm 3°$	0.40 ± 0.10
	2.00 cm	$43° \pm 3°$	$75° \pm 2°$	0.20 ± 0.15
	3.75 cm	$36° \pm 5°$	$68° \pm 4°$	0.40 ± 0.10
Knot B	1.36 cm	$37° \pm 3°$	$67° \pm 4°$	0.50 ± 0.10
	2.00 cm	$28° \pm 4°$	$73° \pm 3°$	0.50 ± 0.10
	3.75 cm	$34° \pm 3°$	$78° \pm 3°$	0.40 ± 0.10

The observed I, Q and U profiles for both Knots for all three wavelengths are shown in Fig. 4.17 while the observed and best-fit model profiles I and Q for the two slices are shown in Fig. 4.18. Unlike the Markarian 501 profiles, the left and right sides of the horizontal axis correspond to the South and North sides of the M87 jet respectively.

The fitted values of the viewing angles remain reasonably constant for a given knot. The errors on the fitting parameters were determined using the same method utilized when analysing Markarian 501. These errors are higher than

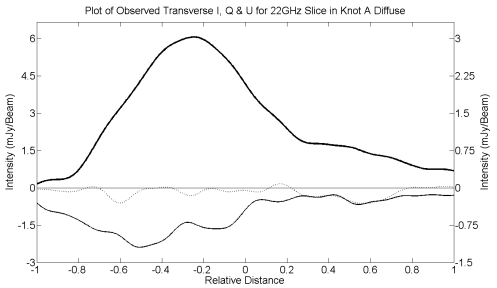

(a) 1.36 cm Knot A Diffuse

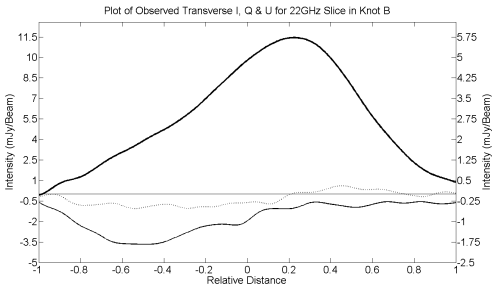

(b) 1.36 cm Knot B

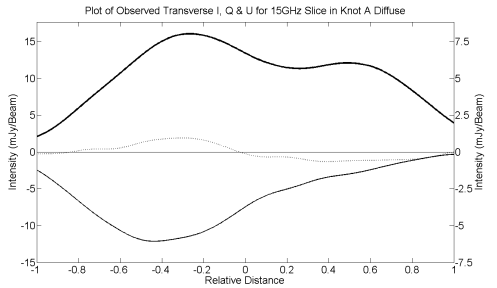

(c) 2.00 cm Knot A Diffuse

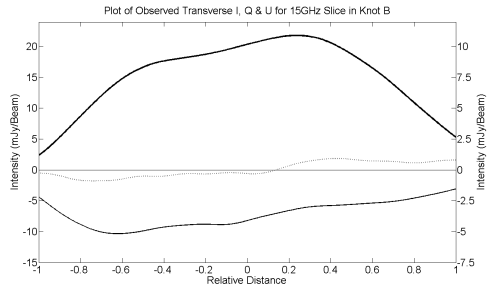

(d) 2.00 cm Knot B

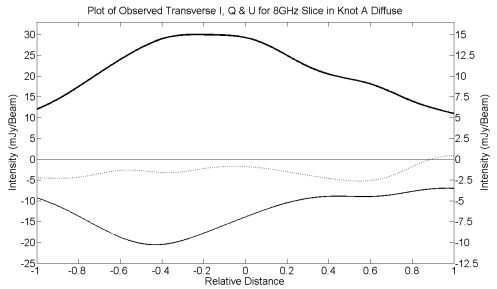

(e) 3.75 cm Knot A Diffuse

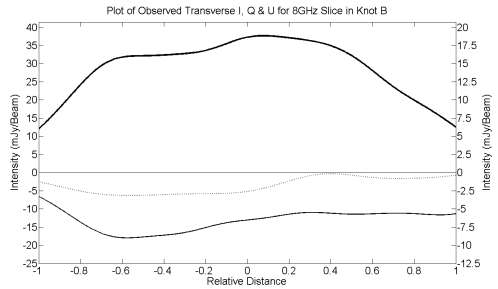

(f) 3.75 cm Knot B

Figure 4.17: Observed I, Q and U (dotted) profiles for the slices analysed from Knot A Diffuse and Knot B (see Fig. 4.5). The scale for the I profile is given along the left-hand vertical axis and the scale for the Q and U profiles along the right-hand vertical axis.

those determined for Markarian 501 due to the nature of the polarization being fitted. The shape of the polarization analysed in Markarian 501 can only be produced by a narrow range of parameters while the shape of the M87 can be produced by a slightly larger range of parameters, resulting in larger errors on the determined parameter values.

Biretta et al. (1999) investigated the proper motion of many of the knots visible in M87. Using this information Wang et al. (2008) investigated the intrinsic velocity field of M87 and successfully determined values for β_{app}, δ (the viewing angle to the line of sight of the jet flow in the observer's frame of reference) and

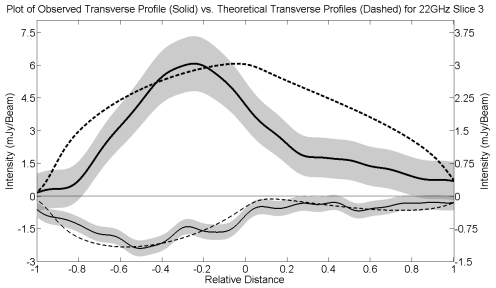

(a) 1.36 cm Knot A Diffuse

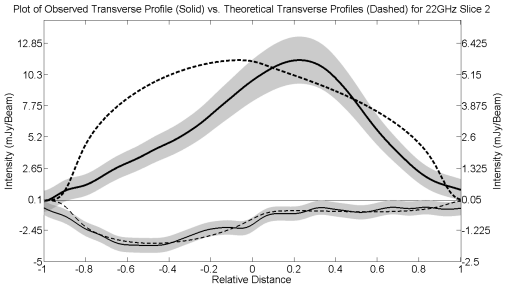

(b) 1.36 cm Knot B

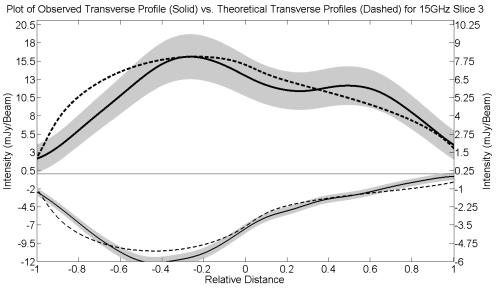

(c) 2.00 cm Knot A Diffuse

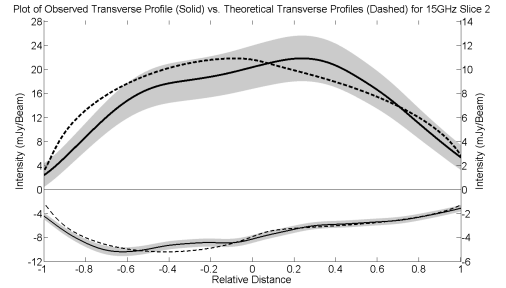

(d) 2.00 cm Knot B

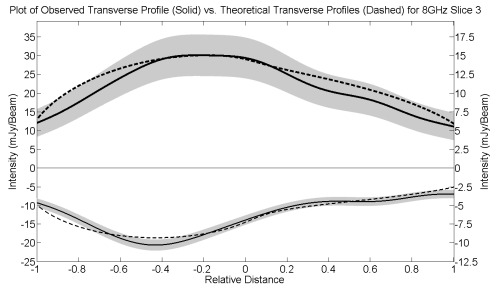

(e) 3.75 cm Knot A Diffuse

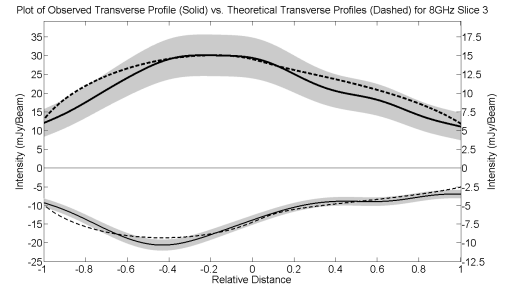

(f) 3.75 cm Knot B

Figure 4.18: Plots of observed and best-fit model I and Q profiles for Knot A Diffuse and Knot B of the 1.36, 2.00 and 3.75 cm (top to bottom) M87 maps The observed profiles are solid and the best-fit profiles dashed; the grey shaded areas surrounding the observed profiles correspond to the range of the 1σ uncertainties for Q and the 3σ uncertainties for I. The scale for the I profile is given along the left-hand vertical axis and the scale for the Q profile along the right-hand vertical axis.

Γ (the Bulk Lorentz factor) for most of M87's knots. Using the same method outlined in Section 4.2.3 and the values of β_{app} determined by Wang et al. (2008) it is possible to determine values for δ and Γ and the compare these values to those determined by Wang et al. (2008) using their method. This provides further evidence for the accuracy of the best fit magnetic field parameters

For the region of Knot A Dif and Knot B Wang et al. gives $\beta_{app} = 0.62$. Taking the average best-fit value of δ' of 72° this results in $\delta = 38° \pm 4°$ and $\Gamma = 1.21 \pm 0.04$. This value of Γ is very close to the value determined by Wang of $1.45 \pm .40$ which was calculated by investigating the proper motion of M87 in this jet region. The value of δ is larger than the value determined by Wang et al. (2008) of 14.9°±15.1°. However, the value determined by this method still lies within 1.5σ of Wang's value.

4.3.1.2 Knot A & Knot C

Similar fitting procedures were applied to both Knot A and Knot C. However, the simple helical model used was completely unable to reproduce the transverse polarization structure observed in these knots without very large values for the viewing angle δ'.

Table 4.5: Best fit Parameters for M87 Knot A Slices. No error analysis was carried out for these values due to the determined δ' values heavily disagreeing with the values calculated using proper motion observations for this knot.

Wavelength	γ'	δ'	f
1.36 cm	74°	90°	0.3
2.00 cm	71°	90°	0.3
3.75 cm	72°	89°	0.4

Fig. 4.19 shows the best-fit profile for a transverse slice across Knot A. It is clear from this image that the simple helical model used was less able to correctly reproduce the observed polarization structure, with a significant fraction of the model polarization and observed polarization differing by more than 1σ. Table 4.5 shows results of the best-fit analysis procedure for Knot A. These large values of δ' correspond to $\delta \sim 75°$, which greatly disagrees with the value, determined using proper motion observations for this knot, of 14.9°±15.1° (Wang et al. 2008). Due to the inability for the simple helical model to reproduce the polarization without large viewing angles and the overall poorness of the fits the polarization

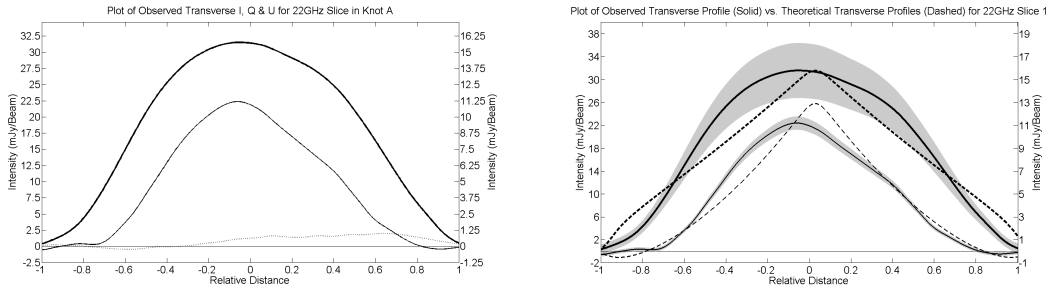

(a) (b)

Figure 4.19: (a) Observed I, Q and U (dotted) profile for slice transverse to Knot A at 2.00 cm . (b) Plot of observed and best-fit model I and Q profiles for Knot A 2.00 cm map. The observed profiles are solid and the best-fit profiles dashed; the grey shaded areas surrounding the observed profiles correspond to the range of the 1σ uncertainties for Q and the 3σ uncertainties for I. For both figures the scale for the I profile is given along the left-hand vertical axis and the scale for the Q and U profiles along the right-hand vertical axis.

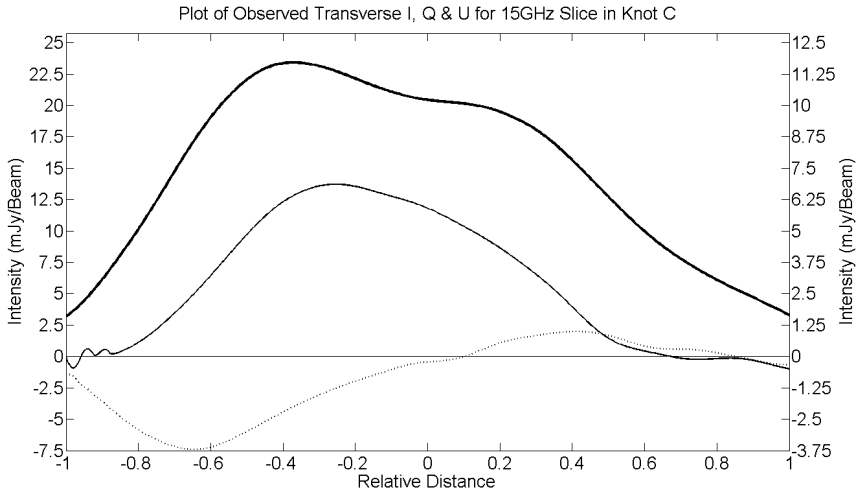

Figure 4.20: Observed I, Q and U (dotted) profile for a slice transverse to Knot C. The scale for the I profile is given along the left-hand vertical axis and the scale for the Q and U profiles along the right-hand vertical axis.

structure in this knot is likely due to the presence of very strong shocks rather than a helical magnetic field.

Several transverse slices were taken across Knot C in an attempt to carry out the fitting procedure. However, due to the fan like polarization present in the knot at each wavelength it was impossible to take a transverse slice which didn't feature non negligible amounts of U polarization. Fig. 4.20 is an example of the transverse slice which showed the minimum amount of U polarization. However, this best case slice still featured far too much U polarization to be correctly

described by the simple helical field model. For this reason, the fitting procedure was not applied to Knot C. The fan like structure of the polarization observed in Knot C is very similar to that predicted by Cawthorne et al (2013) using a conical shock model.

4.3.2 Agreement with Faraday Rotation Results

As described in Section 4.2.4 the magnitude of the Faraday rotation measure will be highest on the side of the jet where the the fractional polarization is lowest. Algaba et al. (2013) reported the detection of a transverse Faraday rotation measure (RM) gradient across multiple parts of the extended M87 jet. In the regions of the jet considered here, comparing the two sides of the jet, the Southern side (corresponding to the left-hand sides of the plots in Figs. 4.17) generally displays higher fractional polarization. The Faraday rotation measures on the Northern side of the jet, RM_N, are therefore expected to be larger in magnitude than those on the Southern side, RM_S. This is consistent with the observational results of Algaba et al. (2013), based on the same VLBA data considered here.

The expected quantitative difference between the magnitudes of the Faraday rotation measures on either side of the jet can also be crudely estimated using the previously determined best-fit parameters. For $\gamma' = 30°$ and $\delta' = 70°$ Eqn. 4.10 indicates a difference of about 56%. In the region of the jet considered here the average value of RM_N is ~ 400 rads m^{-2} while the average value of RM_S is ~ 200 rads m^{-2}, a difference of 50%. This value is highly consistent with the value determined using the best-fit parameters.

Chapter 5

Rotation Measure Resolution Requirements

The chapter describes a method of directly investigating the effects of finite resolution on RM observations. Firstly, Monte Carlo (MC) simulations of a source at +42° declination with a wavelength range of 18 - 22 cm are described. This was chosen as it is typical of those used in a standard VLBA observation with good UV coverage. This wavelength range is also highly sensitive to Faraday rotation due to its relatively long wavelength ($\chi = \chi_0 + RM\lambda^2$). Secondly, MC simulations of a source at +32° declination with a wavelength range of 1.9 - 3.8 cm are described. This was chosen as the wavelength range was identical to the range used by Hovatta et al (2012) and so allowed direct comparison between the results. Finally, MC simulations of a source at −7° declination with a wavelength range of 1.9 - 3.8 cm are described. This was chosen in order to investigate the effect that a relatively poor UV coverage (due to the low declination) would have on the visibility of RM gradients.

As discussed in Section 1.4.1 the emission properties and evolution of Active Galactic Nuclei (AGN) radio jets are dependent on the magnetic (B) fields that thread them. Faraday Rotation measurements are a very important way of investigating these B fields, and can provide information on the orientation and structure of the B field in the immediate vicinity of the jet; for example, a toroidal or helical B field component should give rise to a systematic gradient in the observed Faraday rotation across the jet, as well as characteristic intensity and polarization profiles. However, real observed radio images have finite resolution, usually expressed via convolution with a Gaussian beam whose size corresponds

to the central lobe of the point source response function. This will tend to blur the transverse structure of the jet, raising the question of how well resolved a jet must be in the transverse direction in order to reliably detect transverse structure.

In order to use transverse RM gradients as identifiers for potential helical magnetic structure in AGN, it is very important to understand the effects of finite resolution on observed RM profiles. Taylor and Zavala (2010) proposed that transverse RM distributions must have widths of at least 3 beam widths for an observed gradient to be reliable. This requirement was based on previous experience making RM maps rather than any quantitative analysis. Monte Carlo Simulations by Hovatta et al. (2012) demonstrated a lack of spurious gradients in RM distributions spanning 1.5 – 2 beams, if the RM differences were $> 3\sigma$.

5.1 Monte Carlo Analysis Procedure

In order to investigate the effects of finite resolution on observed RM profiles Monte Carlo simulations of model sources were analysed. Model sources based on a simple, cylindrical model which fell off in total intensity linearly along the jet axis with a total flux of 1.8 Jy were used (see Fig. 5.2). This resulted in a "core-jet" like model. These model sources were created with polarization longitudinal to the jet direction. A transverse RM gradient was then applied to the last three quarters of the model jets and the resultant Faraday rotated Stokes I, Q and U maps were generated using the wavelengths of an existing VLBA observation.

The direct Fourier transforms of these model maps at UV point locations based on VLBA "snapshot" coverage, where 8–10 individual observations lasting several minutes each and spread out over the time the source was visible to all or most of the VLBA antennas, were calculated. This resulted in model visibility (UV) data with realistic UV coverage. Model visibility data were calculated for each wavelength and random thermal noise and EVPA calibration uncertainties of up to 3° were added to them. The levels of thermal noise added was chosen so that the observed RMS noise in the resultant maps was $\approx 5 \times 10^{-4}$ mJy beam^{-1}.

The Stokes I, Q and U visibilities where then imaged in NRAO's CASA using an automatic mapping script written specifically for this task which used the CLEAN algorithm described in Section 1.5.2. The natural-weight beams of the highest wavelength UV coverage was used. The Q and U maps were then used to construct their corresponding polarization angle (PANG) images. A CASA RM

task was written which calculated a final RM image from these PANG images.

Monte Carlo RM Maps were constructed based on 100 independent realizations of the thermal noise and EVPA calibration uncertainties. An average RM map was derived by averaging together all 100 individual realizations of the RM distribution. Monte Carlo statistics were found by taking transverse RM slices across each Monte Carlo snapshot and determining the error on the RM difference found between the top and bottom of each slice. For each MC instance 20 transverse slices were taken every 0.5 mas from the beginning of the Faraday rotated region. Non-monotonic RM slices were ignored. As the edge of a jet can be hard to determine each slice edge was varied around a band of five pixels and edges which resulted in the highest σ result was used.

This entire procedure was repeated for model jets of different intrinsic jet width, polarized flux and RM range. This allowed for direct analysis of the effect of finite resolution on observed RM profiles in addition to the effects of fractional polarization and Faraday depolarization.

The CASA code and a description of how it was used throughout this analysis can be seen in Appendix A.

5.2 Monte Carlo Results

5.2.1 Monte Carlo Results for 18 – 22 cm Simulations source at declination +42°

The various model source parameters used for these simulations can be seen in Table 5.1. As described in Section 5.1, model sources were simulated for each of these parameters before being sampled at the UV points indicated in Fig. 5.1. This UV distribution corresponds to simultaneous, multi-wavelength VLBA observations at 18 cm, 20 cm, 21 cm and 22 cm (1.35, 1.43, 1.48 and 1.67 GHz).

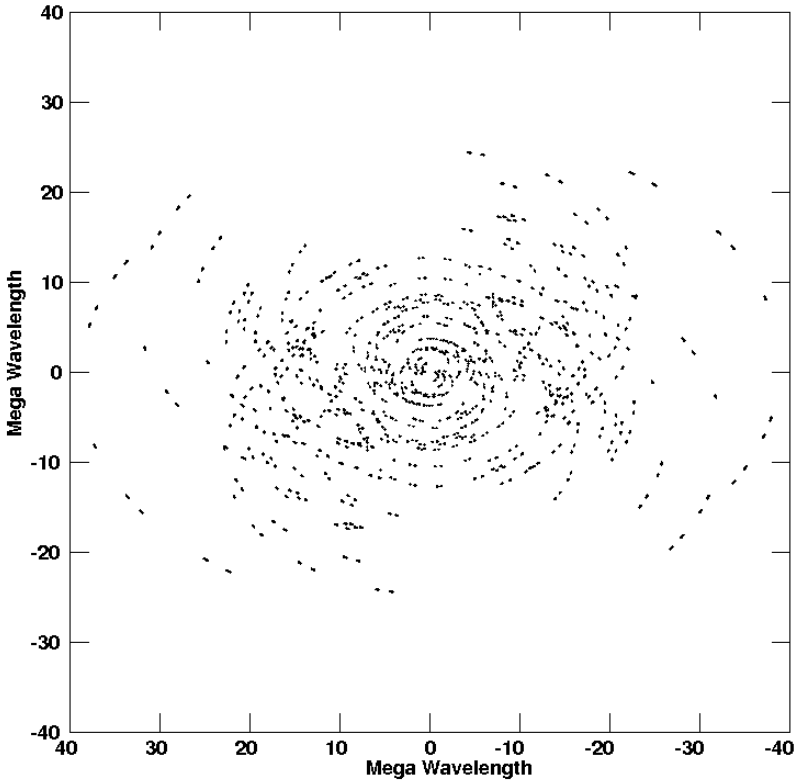

Figure 5.1: UV distribution for 22 cm visibility data for model source at +42° used in this analysis, based on existing VLBA snapshot observations.

Table 5.1: Parameters used for Monte Carlo Analysis for 18 – 22 cm wavelength, source at declination +42°. Each parameter combination was simulated resulting in 36 different model jets for the Monte Carlo simulations.

Intrinsic Jet Width	Percentage Polarization	Intrinsic RM Range
0.05 Beam Widths	25%	-30 to 30 rads m^{-2}
0.10 Beam Widths	15%	-15 to 15 rads m^{-2}
0.20 Beam Widths	05%	-8 to 8 rads m^{-2}
0.40 Beam Widths		

Figures 5.3 – 5.7 show the average Monte Carlo RM maps for this wavelength range and declination. MC Average maps were chosen as they clearly demonstrate any consistent trends observed in the individual MC instances. They were produced by averaging the 100 MC realizations of each parameter configuration. Pixels were blanked if at least one of the MC maps that produced it had an error value greater than 10 rads m^{-2} for that pixel. Errors were calculated using the method of Hovatta et al. (2012) for approximating the errors in both Stokes Q

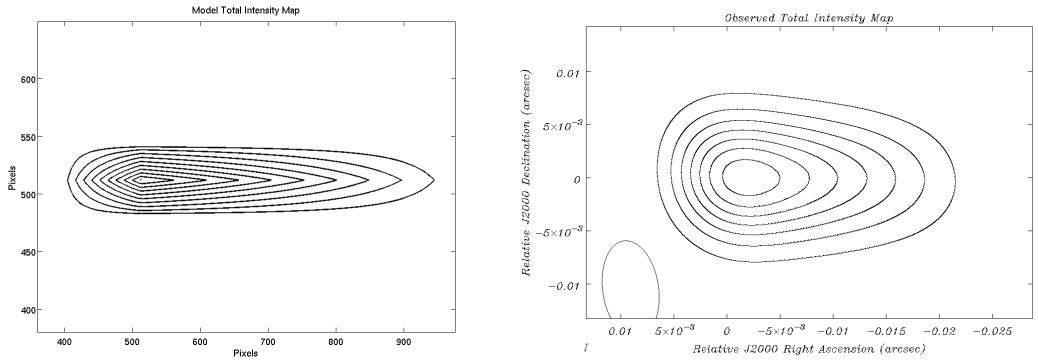

(a) (b)

Figure 5.2: (a) Model Intrinsic Total Intensity Map used in 18 cm–22 cm analysis (intrinsic jet width of 0.4 beam widths). 1 pixel corresponds to ~ 0.05 mas. (b) Observed Total Intensity Map created using the model intensity map (a) and the method outlined in Section 5.1.

and U, which corresponds to uncertainties of approximately 1.8 times their respective RMS values in regions where the contribution of residual instrumental polarization to the errors is negligible (which is true in our case). These figures demonstrate that, while the RM gradient is visible in most cases, the observed RM values are significantly suppressed by the effects of convolution. Therefore, while poor resolution rarely prevent gradients from being observed it does prevent observed RM values being used to estimate values for the magnetic field strength of the helical magnetic field or the electron number density of the jet.

Figures 5.8 - 5.16 show the fraction of Monte Carlo RM maps showing gradients spanning various multiples of the uncertainty σ ranging from 0 to at least 4. An intrinsic jet width of 0.4 beam widths corresponds to an observed width of $\approx$ 1.5 beam widths. This jet width is significantly smaller than the proposed criterion of Taylor and Zavala (2010) that an observed transverse RM gradient must span a width of at least 3 beam widths for it to be considered reliable. However, these Monte Carlo results clearly demonstrate that RM gradients can be reliably detected for jets much narrower than this. For many of the jet parameter configurations, with intrinsic jet widths of 0.20 and 0.40 beam widths, transverse RM gradients with significances of 3σ or higher are observed for the majority of their MC realizations. Jets with intrinsic jet widths as small as 0.05 beam widths also demonstrated 3σ gradients for multiple jet parameter configurations. For the cases for which this isn't true, the number of 2σ gradients is much higher than that expected for purely spurious gradients as demonstrated in Section 6.1.

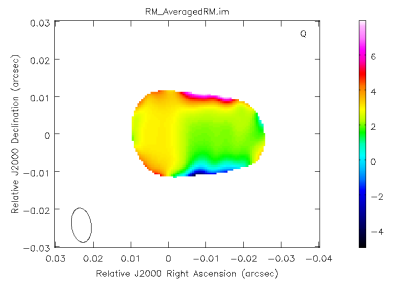

(a) 0.05 beam widths

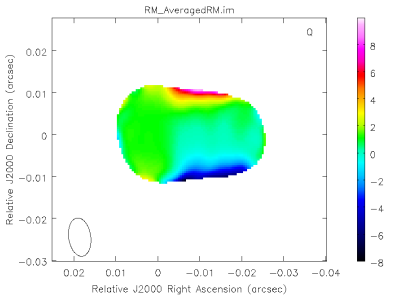

(b) 0.10 beam widths

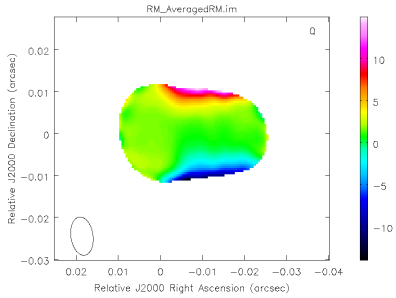

(c) 0.20 beam widths

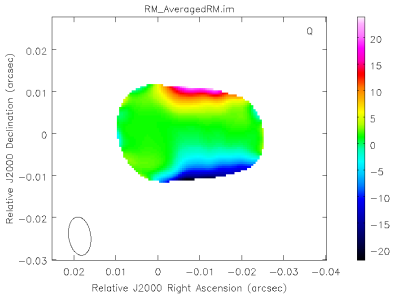

(d) 0.40 beam widths

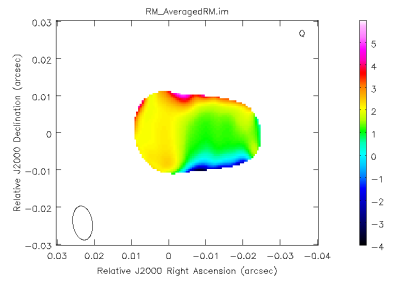

(e) 0.05 beam widths

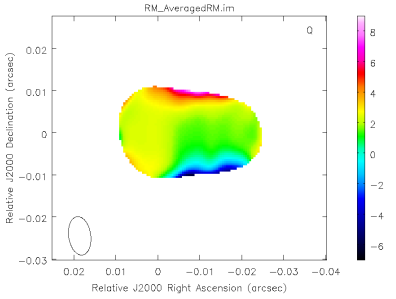

(f) 0.10 beam widths

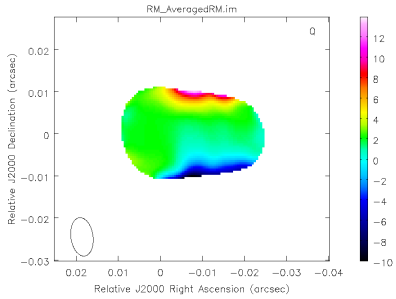

(g) 0.20 beam widths

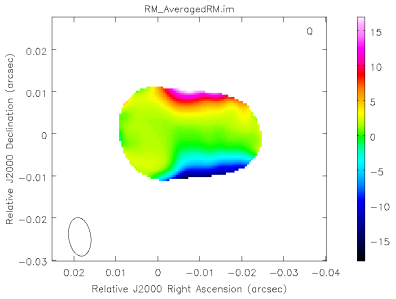

(h) 0.40 beam widths

Figure 5.3: First & Second sets of 18 – 22 cm Monte Carlo simulations. Shown are results for four different intrinsic jet widths. Figures (a) – (d) correspond to a RM range of -30 to +30 rads m^{-2} and a percentage polarized flux of 25%. Figures (e) – (h) correspond to a RM range of -30 to +30 rads m^{-2} and a percentage polarized flux of 15%. The error cutoff for these figures is 10 rads m^{-2}.

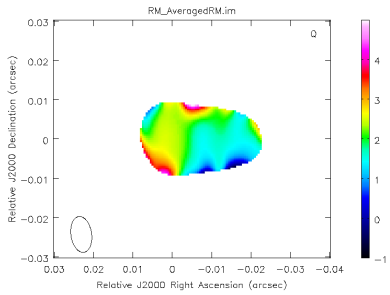

(a) 0.05 beam widths

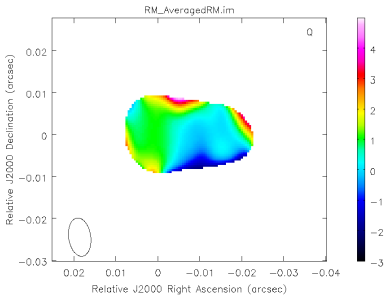

(b) 0.10 beam widths

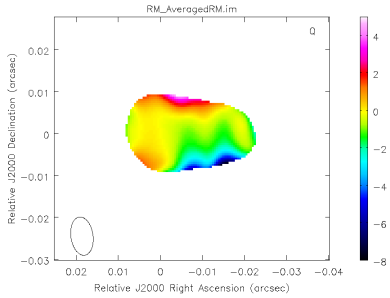

(c) 0.20 beam widths

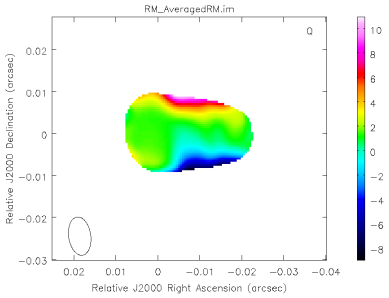

(d) 0.40 beam widths

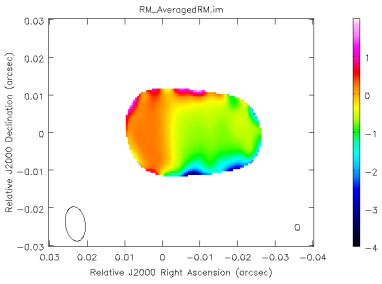

(e) 0.05 beam widths

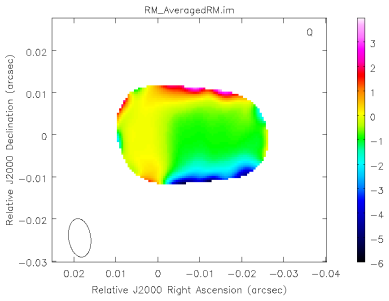

(f) 0.10 beam widths

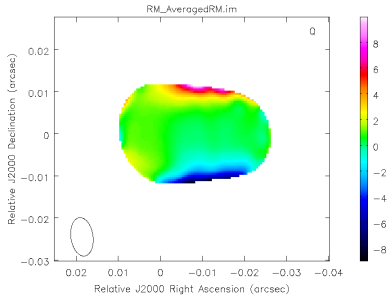

(g) 0.20 beam widths

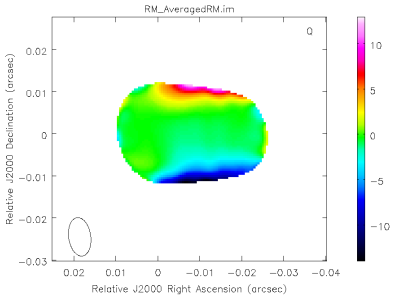

(h) 0.40 beam widths

Figure 5.4: Third & Fourth sets of 18 – 22 cm Monte Carlo simulations. Shown are results for four different intrinsic jet widths. Figures (a) – (d) correspond to a RM range of -30 to +30 rads m^{-2} and a percentage polarized flux of 5%. Figures (e) – (h) correspond to a RM range of -15 to +15 rads m^{-2} and a percentage polarized flux of 25%. The error cutoff for these figures is 10 rads m^{-2}.

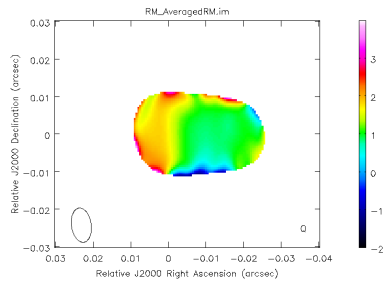

(a) 0.05 beam widths

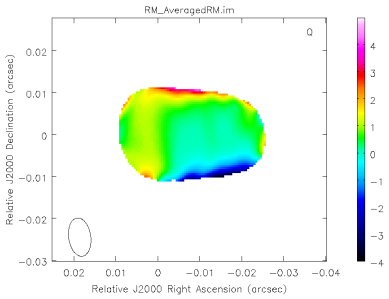

(b) 0.10 beam widths

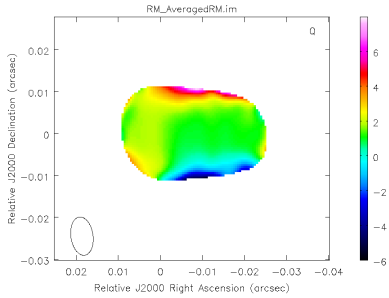

(c) 0.20 beam widths

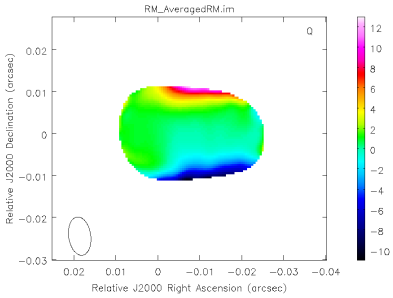

(d) 0.40 beam widths

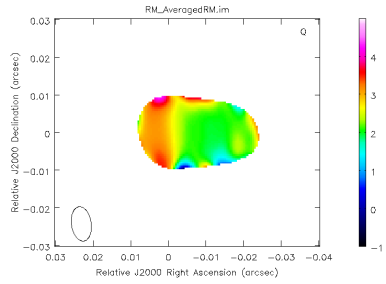

(e) 0.05 beam widths

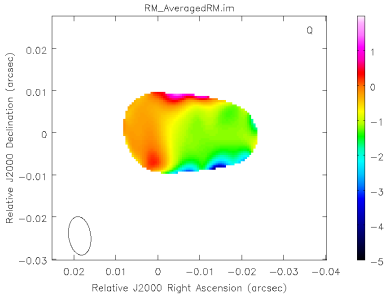

(f) 0.10 beam widths

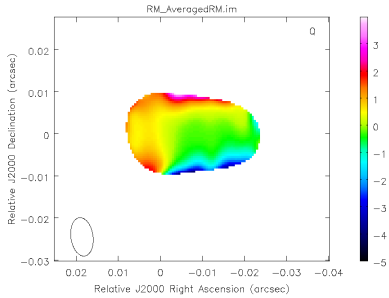

(g) 0.20 beam widths

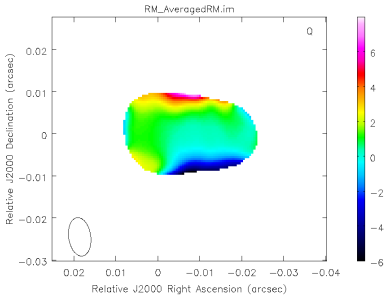

(h) 0.40 beam widths

Figure 5.5: Fifth & Sixth sets of 18 – 22 cm Monte Carlo simulations. Shown are results for four different intrinsic jet widths. Figures (a) – (d) correspond to a RM range of -15 to +15 rads m^{-2} and a percentage polarized flux of 15%. Figures (e) – (h) correspond to a RM range of -15 to +15 rads m^{-2} and a percentage polarized flux of 5%. The error cutoff for these figures is 10 rads m^{-2}.

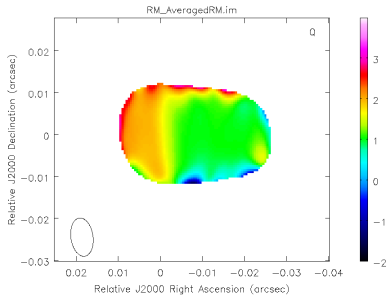

(a) 0.05 beam widths

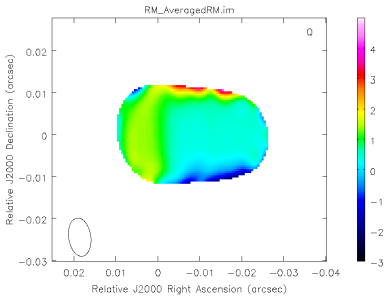

(b) 0.10 beam widths

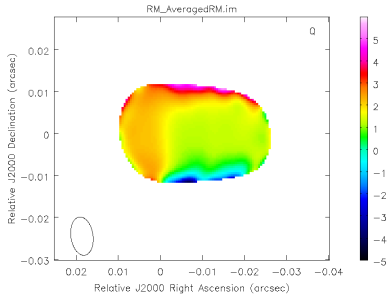

(c) 0.20 beam widths

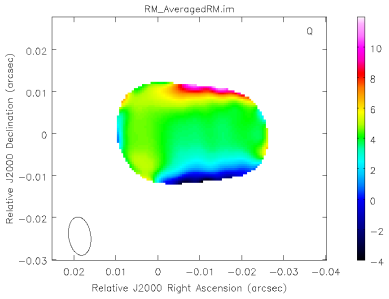

(d) 0.40 beam widths

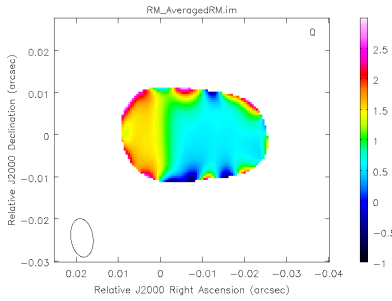

(e) 0.05 beam widths

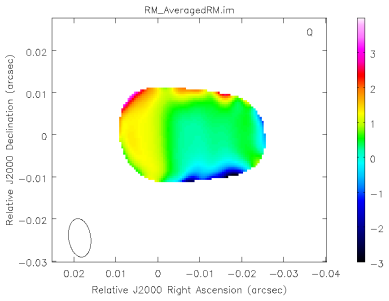

(f) 0.10 beam widths

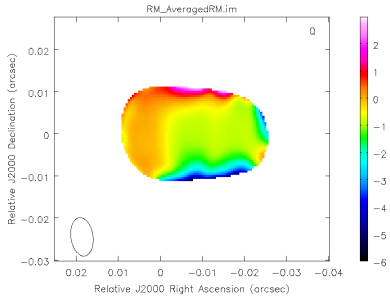

(g) 0.20 beam widths

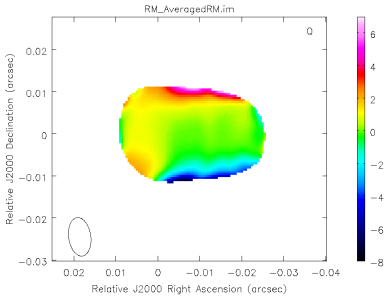

(h) 0.40 beam widths

Figure 5.6: Seventh & Eighth sets of 18 – 22 cm Monte Carlo simulations. Shown are results for four different intrinsic jet widths. Figures (a) – (d) correspond to a RM range of -8 to +8 rads m^{-2} and a percentage polarized flux of 25%. Figures (e) – (h) correspond to a RM range of -8 to +8 rads m^{-2} and a percentage polarized flux of 15%. The error cutoff for these figures is 10 rads m^{-2}.

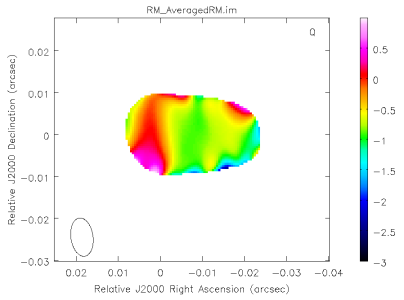

(a) 0.05 beam widths

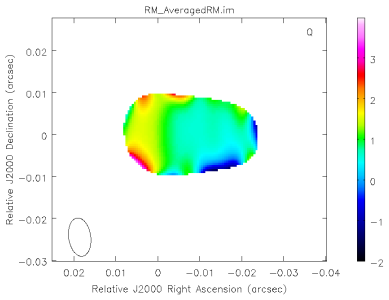

(b) 0.10 beam widths

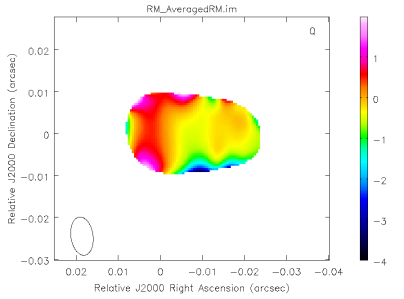

(c) 0.20 beam widths

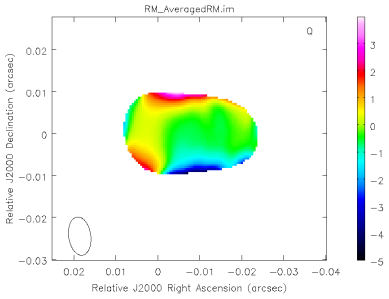

(d) 0.40 beam widths

Figure 5.7: Ninth set of 18 – 22 cm Monte Carlo simulations. Shown are results for four different intrinsic jet widths. Figures (a) – (d) correspond to a RM range of -8 to +8 rads m^{-2} and a percentage polarized flux of 5%. The error cutoff for these figures is 10 rads m^{-2}.

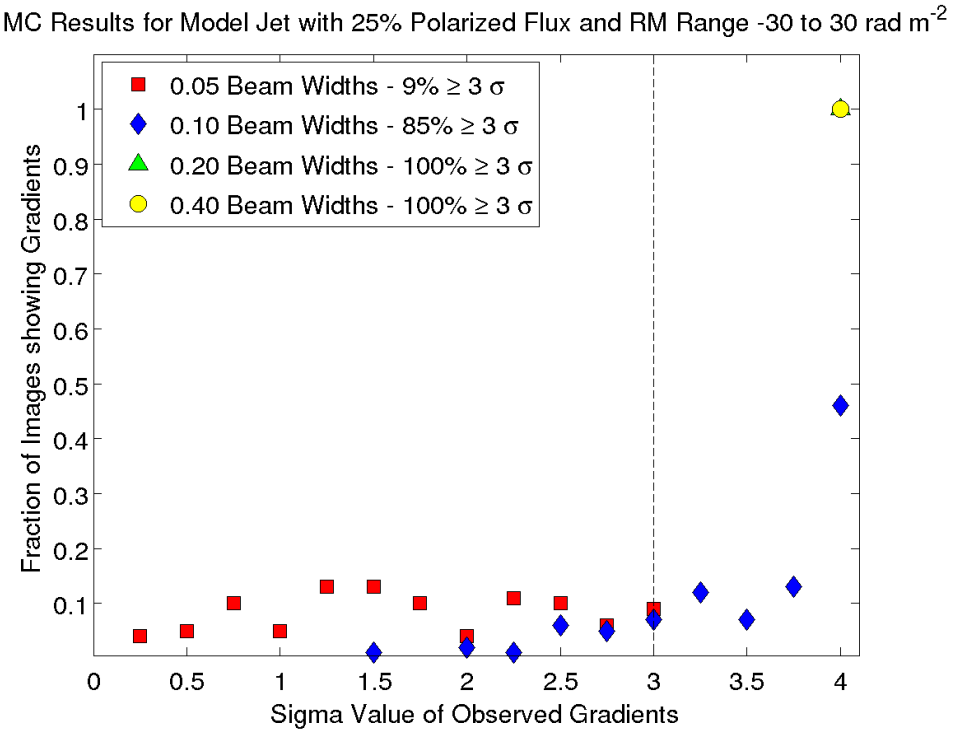

Figure 5.8: MC results for first set of 18 – 22 cm simulations.

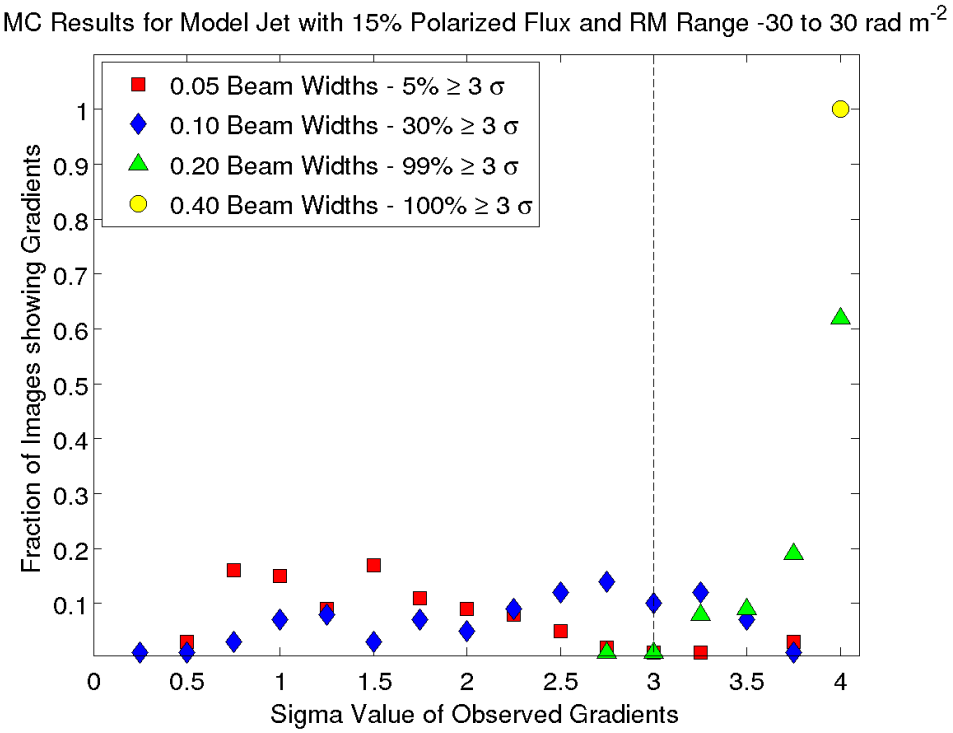

Figure 5.9: MC results for second set of 18 – 22 cm simulations.

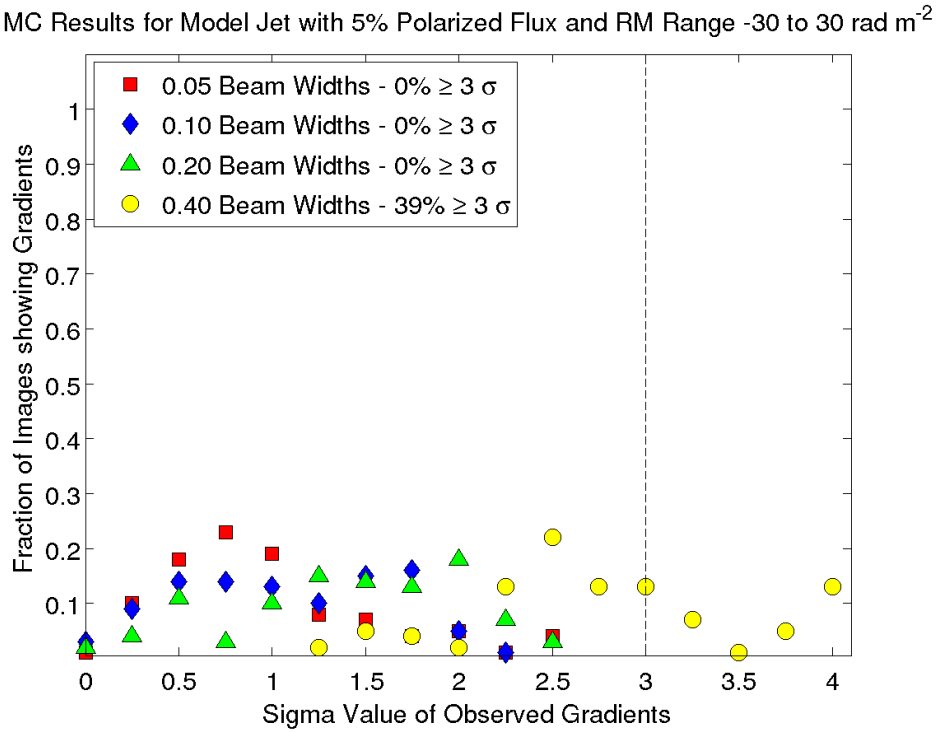

Figure 5.10: MC results for third set of 18 – 22 cm simulations.

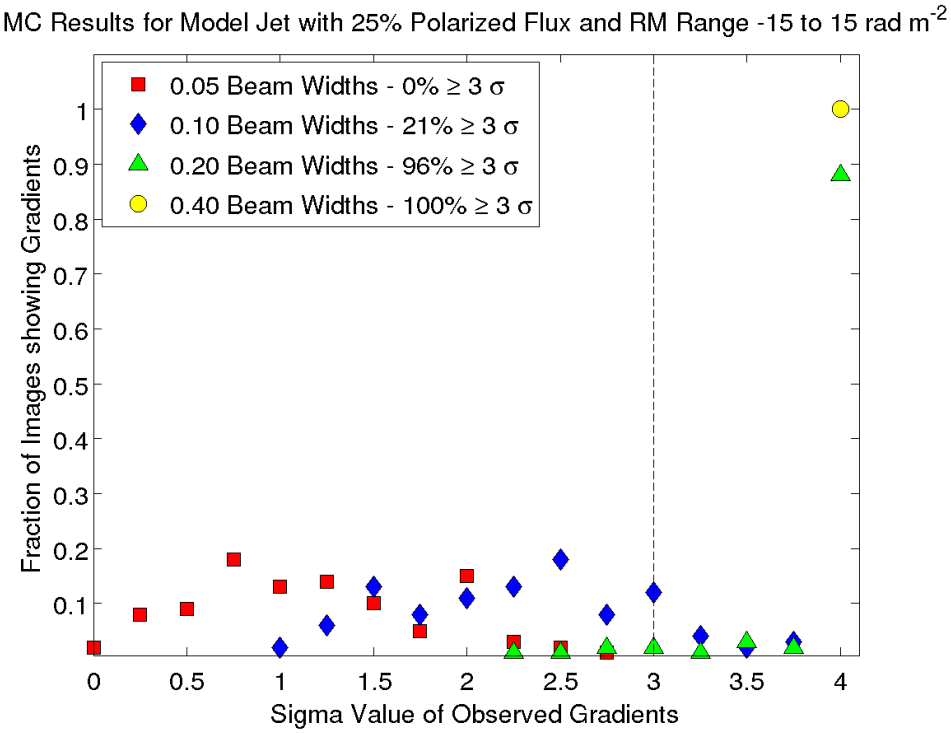

Figure 5.11: MC results for fourth set of 18 – 22 cm simulations.

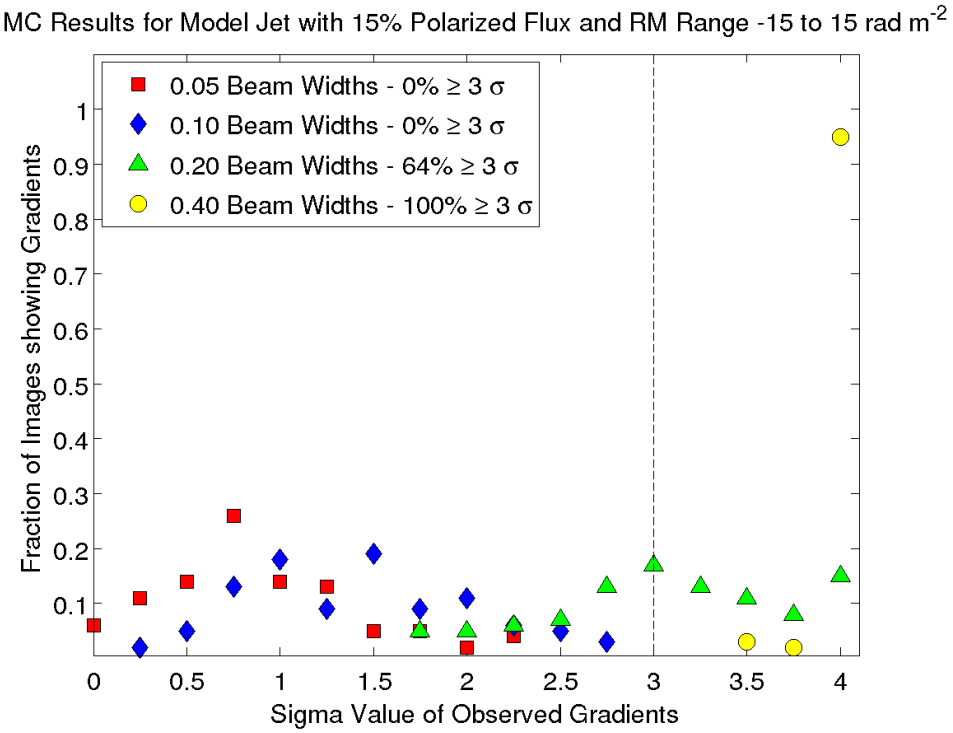

Figure 5.12: MC results for fifth set of 18 – 22 cm simulations.

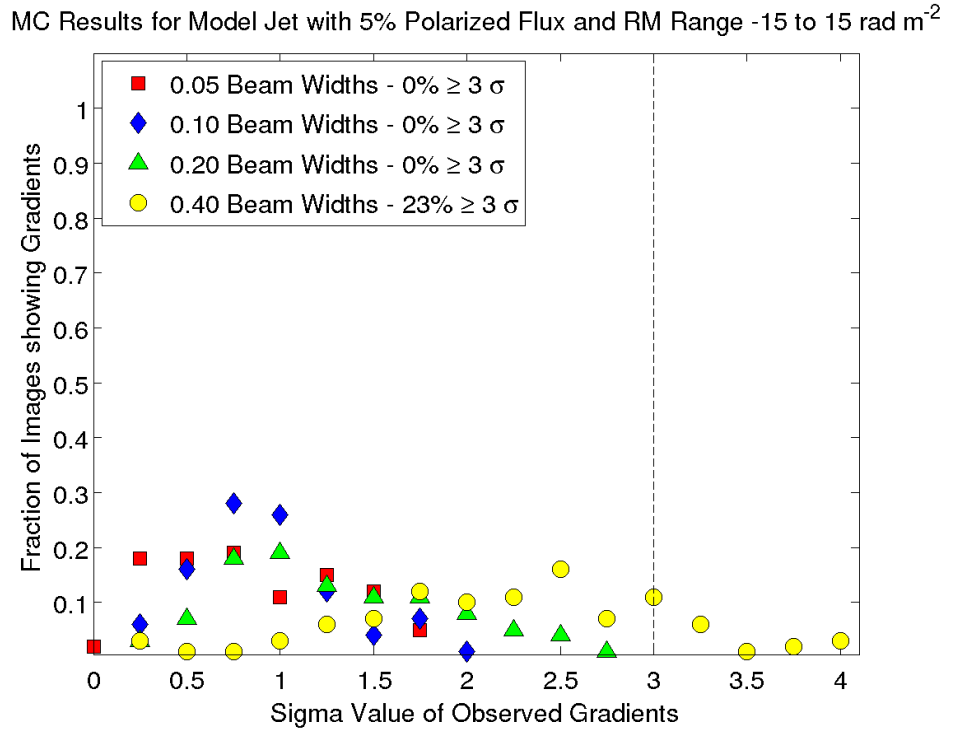

Figure 5.13: MC results for sixth set of 18 – 22 cm simulations.

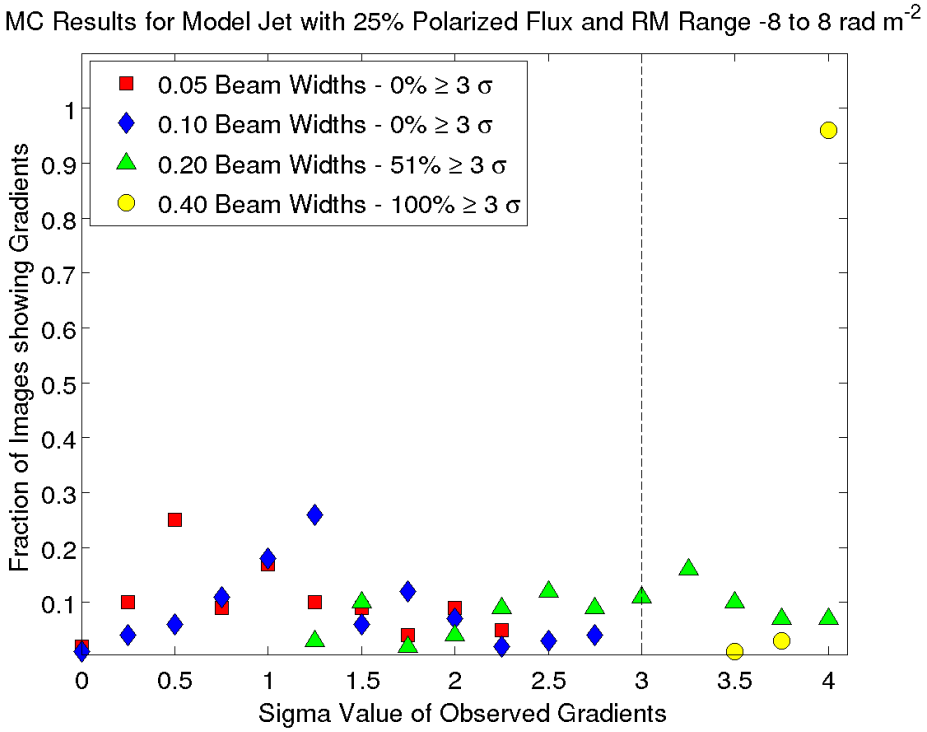

Figure 5.14: MC results for seventh set of 18 – 22 cm simulations.

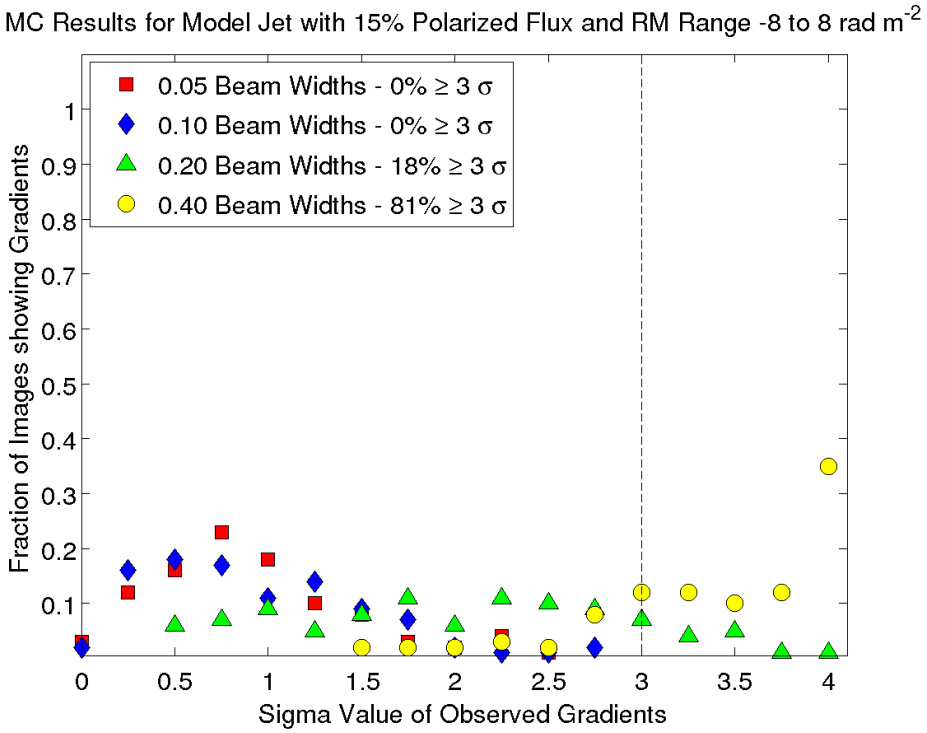

Figure 5.15: MC results for eighth set of 18 – 22 cm simulations.

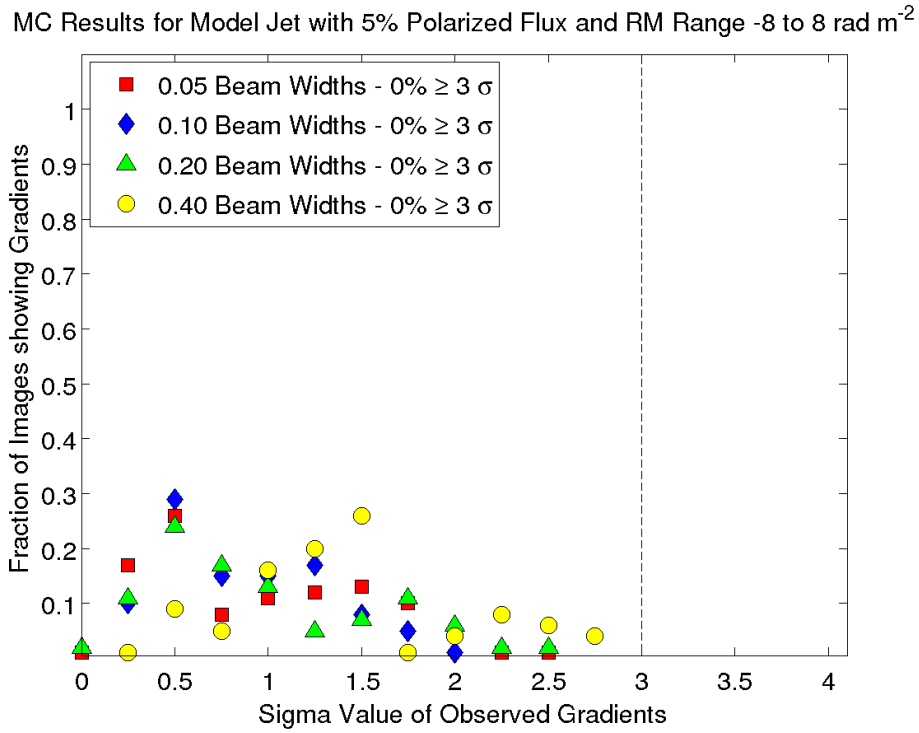

Figure 5.16: MC results for ninth set of 18 – 22 cm simulations.

5.2.2 Monte Carlo Results for 1.9 – 3.8 cm Simulations, Source at Declination +32°

The different model source parameters used for this source can be seen in Table 5.2. As described in Section 5.1, model sources were simulated for each of these parameters before being sampled at a set of UV points corresponding to those shown in Fig. 5.17. This UV distribution was based on simultaneous snapshot VLBA observations at 1.9 cm, 2.5 cm, 3.4 cm & 3.8 cm (the same wavelength range used in Hovatta et al. 2013). Due to the shorter wavelengths used in this observation the intrinsic RM Ranges used in these simulation were much higher than those used for the 18 – 22 cm simulations. The values chosen where picked so that the maximum rotation of the EVPA ($\Delta\chi = RM\lambda^2$) would be similar for both sets of simulations.

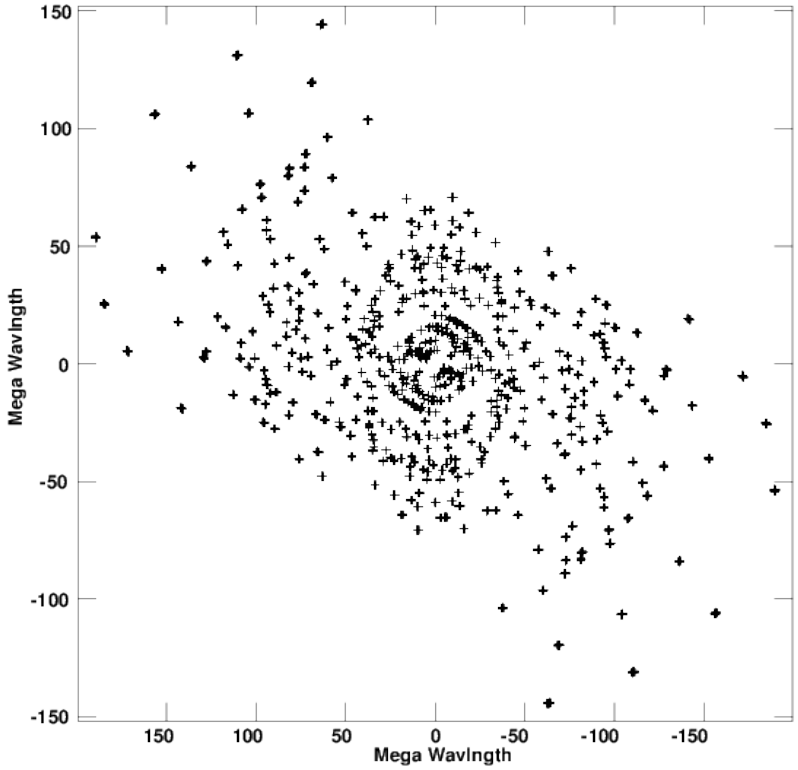

Figure 5.17: UV distribution for 3.8 cm visibility data for model source at +32° used in this analysis, based on existing VLBA snapshot observations.

Table 5.2: Parameters used for Monte Carlo Analysis for 1.9 – 3.8 cm wavelength source at declination +32°. Each parameter combination was simulated resulting in 36 different model jets for the Monte Carlo simulations.

Intrinsic Jet Width	Percentage Polarization	Intrinsic RM Range
0.05 Beam Widths	25%	-1000 to 1000 rads m^{-2}
0.10 Beam Widths	15%	-500 to 500 rads m^{-2}
0.20 Beam Widths	05%	-250 to 250 rads m^{-2}
0.40 Beam Widths		

Figures 5.18 - 5.22 show the average Monte Carlo RM maps for this wavelength range and declination. They were produced in the same way as in the 18 – 22 cm simulations. These figures demonstrate the same behaviour as those for the longer-wavelength simulations, with gradients becoming more pronounced as the intrinsic jet width increases. However, due to the poorer sensitivity to Faraday rotation at these wavelengths the gradients are not as clear as those seen for the 18 – 22 cm simulations and the observed RM values are very highly suppressed.

Figures 5.23 - 5.31 show the fraction of the MC RM maps showing gradients span-

ning various multiples of the uncertainty σ ranging from 0 to at least 4. Again, these figures demonstrate the same behaviour as seen for the 18 – 22 cm simulations, with 3σ gradients observed for many different parameter configurations and for observed jet widths much smaller than the three-beam-width criterion of Taylor & Zavala (2010).

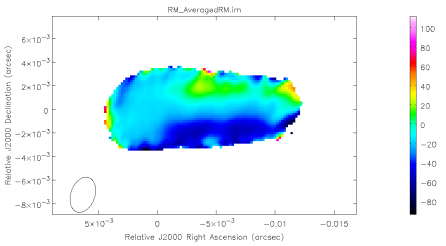

(a) 0.05 beam widths

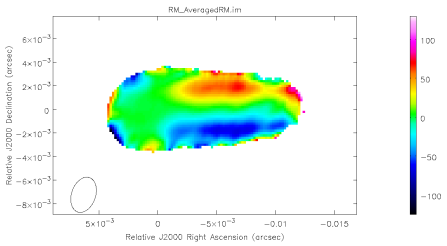

(b) 0.10 beam widths

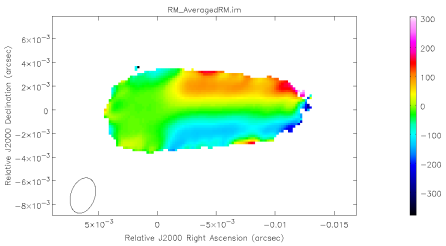

(c) 0.20 beam widths

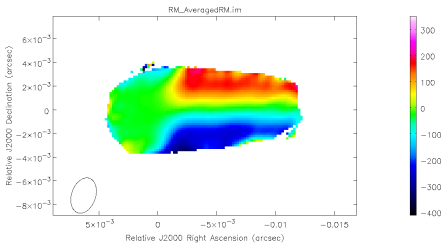

(d) 0.40 beam widths

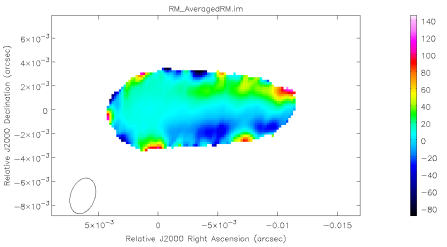

(e) 0.05 beam widths

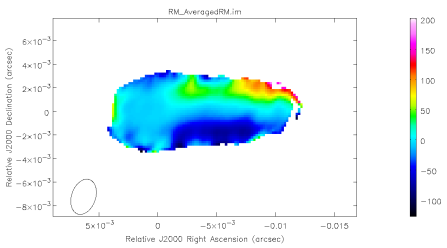

(f) 0.10 beam widths

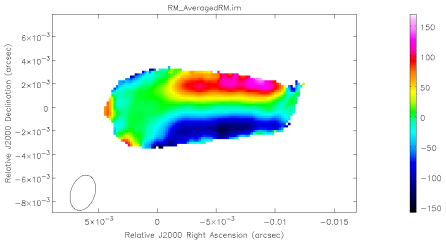

(g) 0.20 beam widths

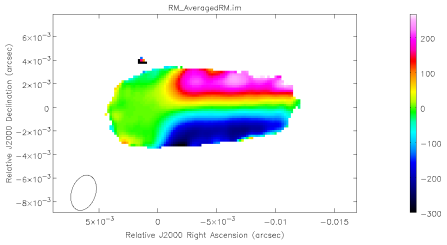

(h) 0.40 beam widths

Figure 5.18: First & Second sets of +32° declination 1.9 – 3.8 cm Monte Carlo simulations. Shown are results for four different intrinsic jet widths. Figures (a) – (d) correspond to a RM range of -1000 to +1000 rads m^{-2} and a percentage polarized flux of 25%. Figures (e) – (h) correspond to a RM range of -1000 to +1000 rads m^{-2} and a percentage polarized flux of 15%. The error cutoff for these figures is 50 rads m^{-2}.

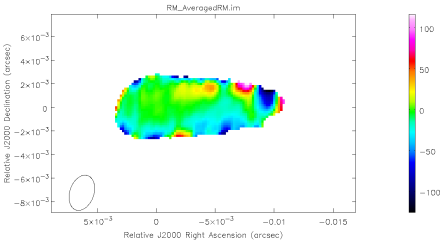

(a) 0.05 beam widths

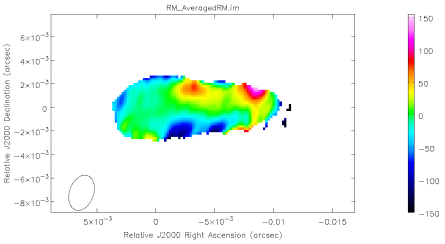

(b) 0.10 beam widths

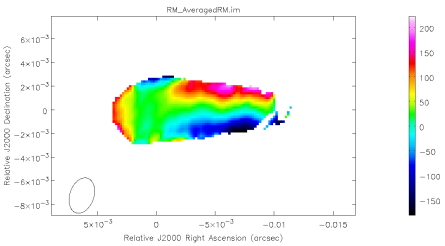

(c) 0.20 beam widths

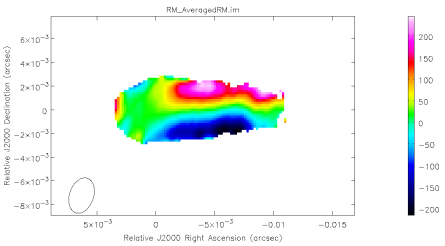

(d) 0.40 beam widths

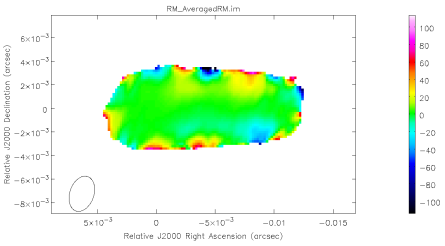

(e) 0.05 beam widths

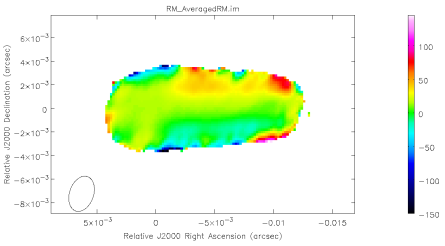

(f) 0.10 beam widths

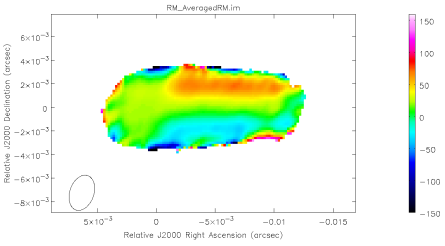

(g) 0.20 beam widths

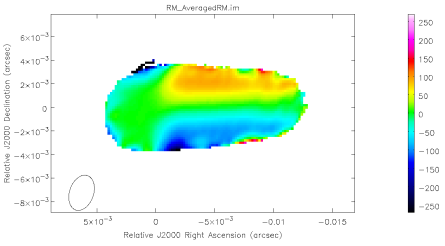

(h) 0.40 beam widths

Figure 5.19: Third & Fourth sets of +32° declination 1.9 – 3.8 cm Monte Carlo simulations. Shown are results for four different intrinsic jet widths. Figures (a) – (d) correspond to a RM range of -1000 to +1000 rads m^{-2} and a percentage polarized flux of 5%. Figures (e) – (h) correspond to a RM range of -500 to +500 rads m^{-2} and a percentage polarized flux of 25%. The error cutoff for these figures is 50 rads m^{-2}.

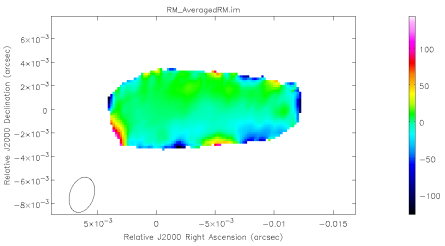

(a) 0.05 beam widths

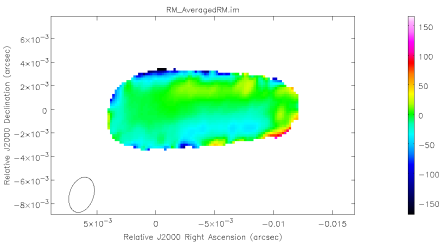

(b) 0.10 beam widths

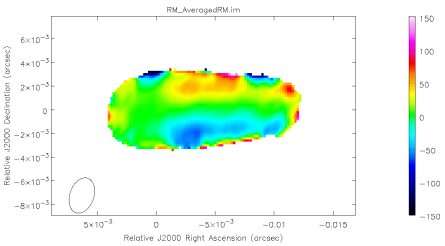

(c) 0.20 beam widths

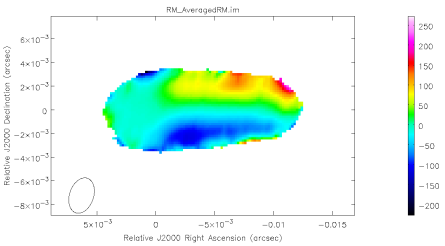

(d) 0.40 beam widths

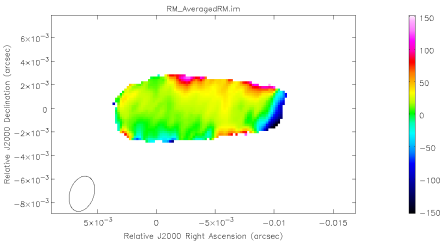

(e) 0.05 beam widths

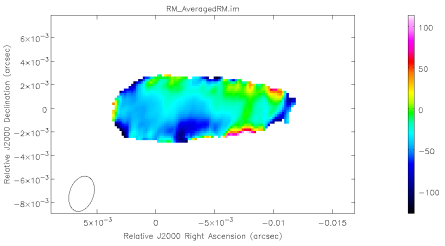

(f) 0.10 beam widths

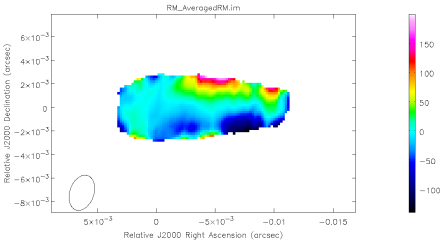

(g) 0.20 beam widths

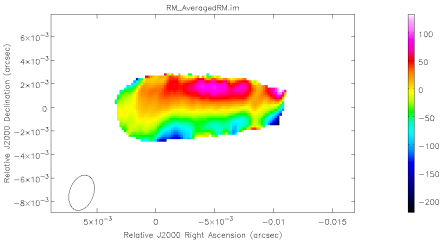

(h) 0.40 beam widths

Figure 5.20: Fifth & Sixth sets of +32° declination 1.9 – 3.8 cm Monte Carlo simulations. Shown are results for four different intrinsic jet widths. Figures (a) – (d) correspond to a RM range of -500 to +500 rads m^{-2} and a percentage polarized flux of 15%. Figures (e) – (h) correspond to a RM range of -500 to +500 rads m^{-2} and a percentage polarized flux of 5%. The error cutoff for these figures is 50 rads m^{-2}.

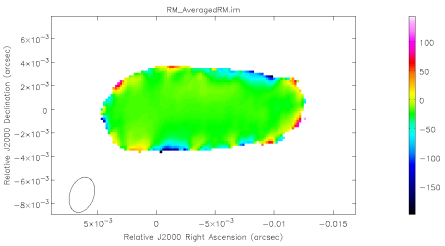

(a) 0.05 beam widths

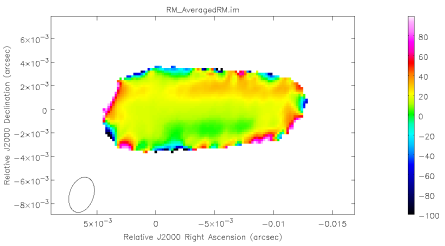

(b) 0.10 beam widths

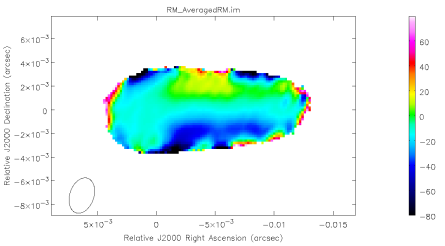

(c) 0.20 beam widths

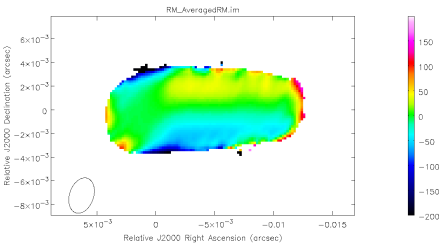

(d) 0.40 beam widths

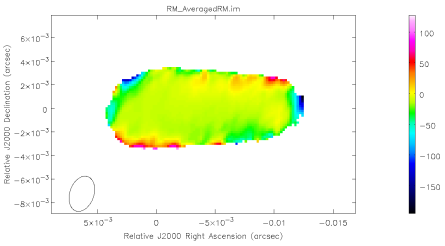

(e) 0.05 beam widths

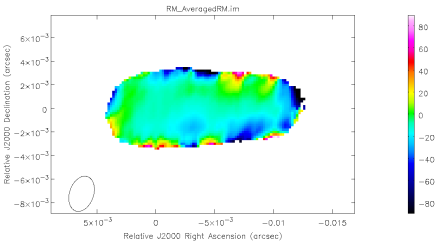

(f) 0.10 beam widths

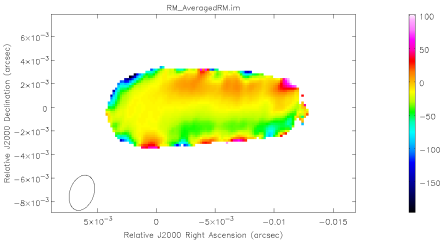

(g) 0.20 beam widths

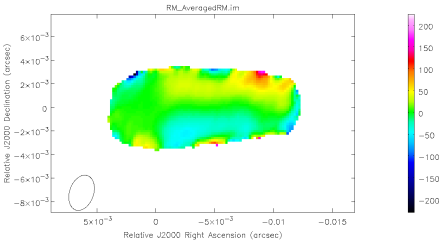

(h) 0.40 beam widths

Figure 5.21: Seventh & Eighth sets of +32° declination 1.9 – 3.8 cm Monte Carlo simulations. Shown are results for four different intrinsic jet widths. Figures (a) – (d) correspond to a RM range of -250 to +250 rads m^{-2} and a percentage polarized flux of 25%. Figures (e) – (h) correspond to a RM range of -250 to +250 rads m^{-2} and a percentage polarized flux of 15%. The error cutoff for these figures is 50 rads m^{-2}.

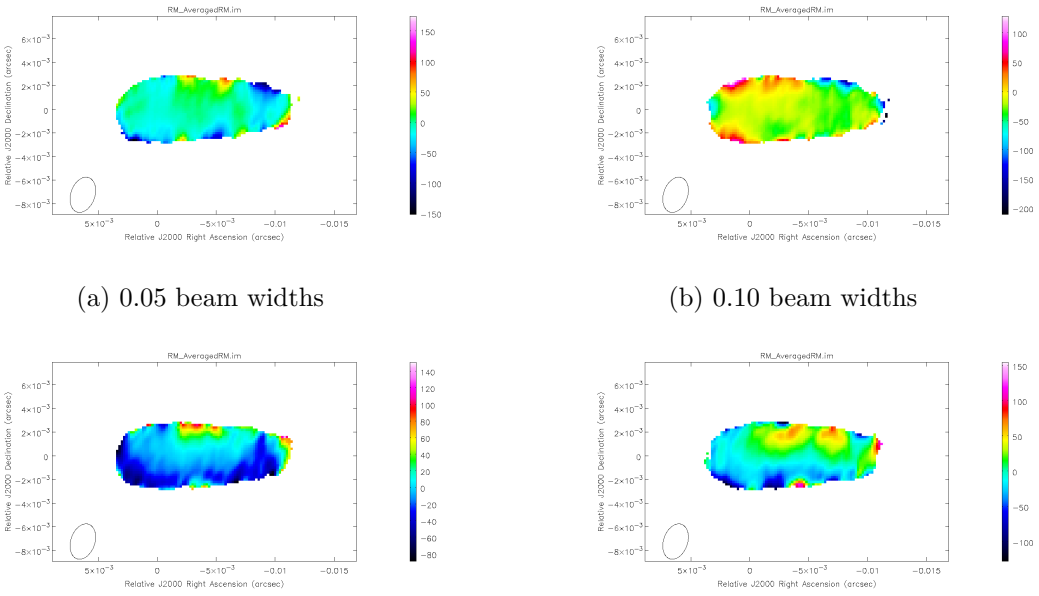

(a) 0.05 beam widths

(b) 0.10 beam widths

(c) 0.20 beam widths

(d) 0.40 beam widths

Figure 5.22: Ninth set of +32° declination 1.9 – 3.8 cm Monte Carlo simulations. Shown are results for four different intrinsic jet widths. Figures (a) – (d) correspond to a RM range of -250 to +250 rads m^{-2} and a percentage polarized flux of 5%. The error cutoff for these figures is 50 rads m^{-2}.

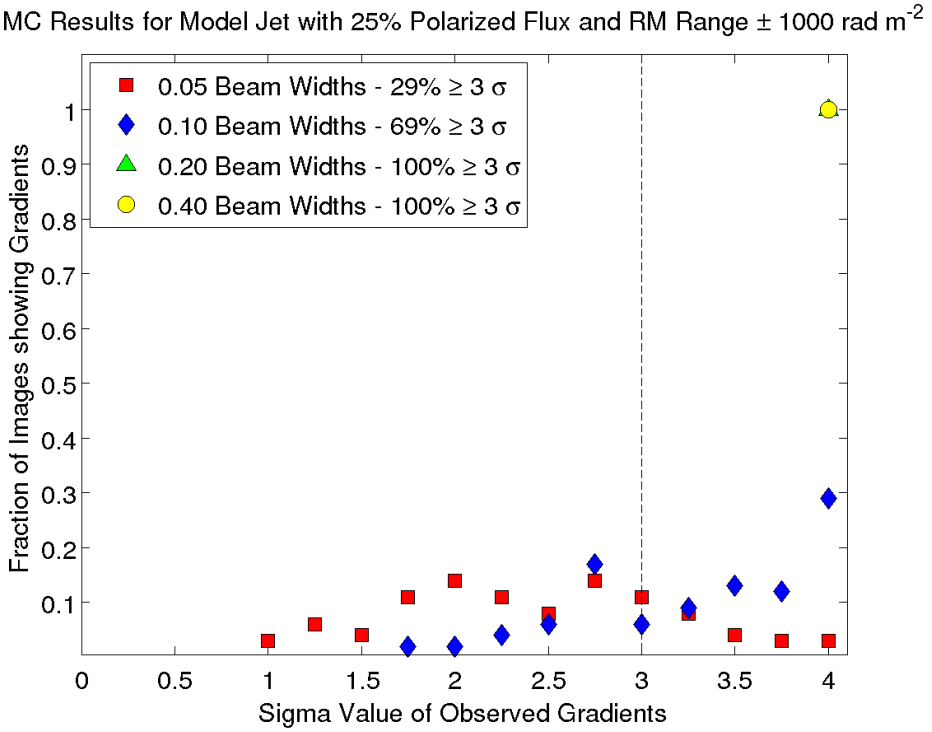

Figure 5.23: MC results for first set of 1.9 – 3.8 cm simulations at +32° declination.

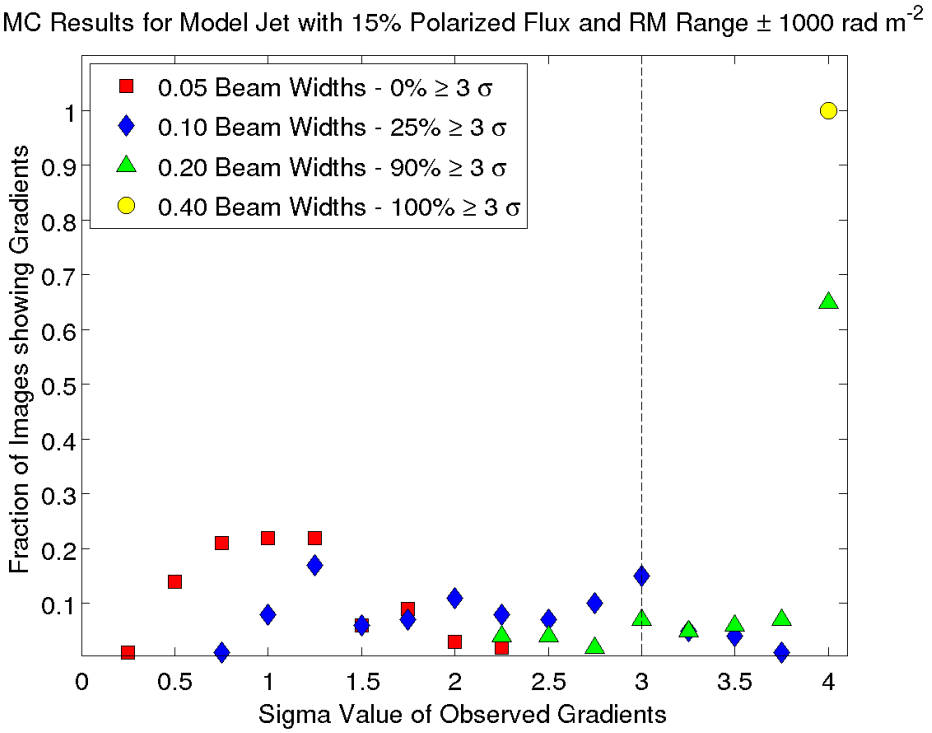

Figure 5.24: MC results for second set of 1.9 – 3.8 cm simulations at +32° declination.

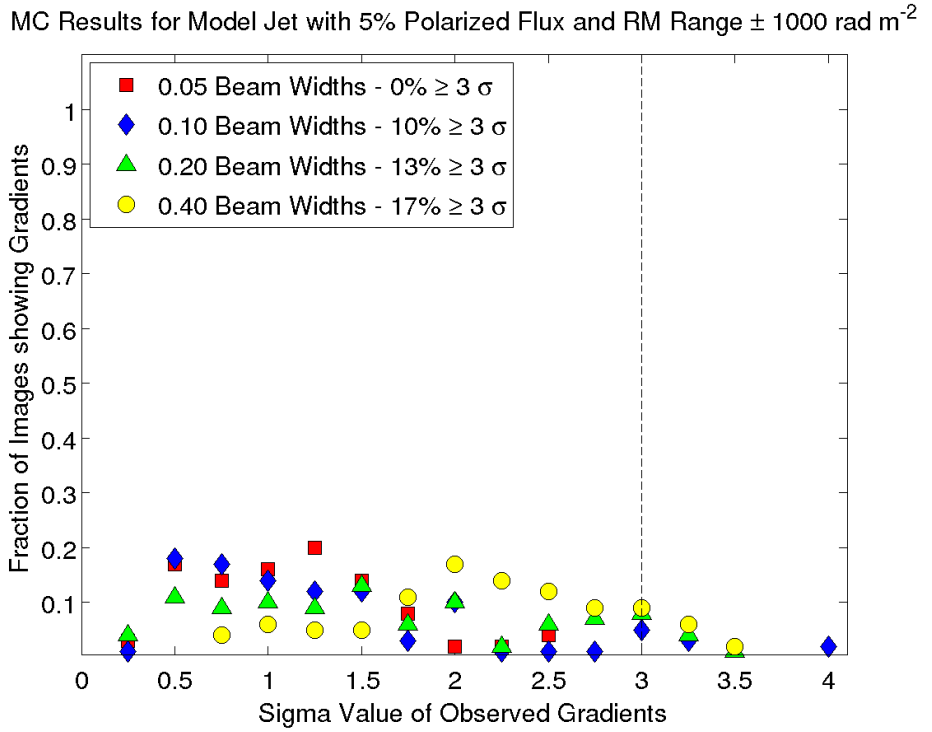

Figure 5.25: MC results for third set of 1.9 – 3.8 cm simulations at +32° declination.

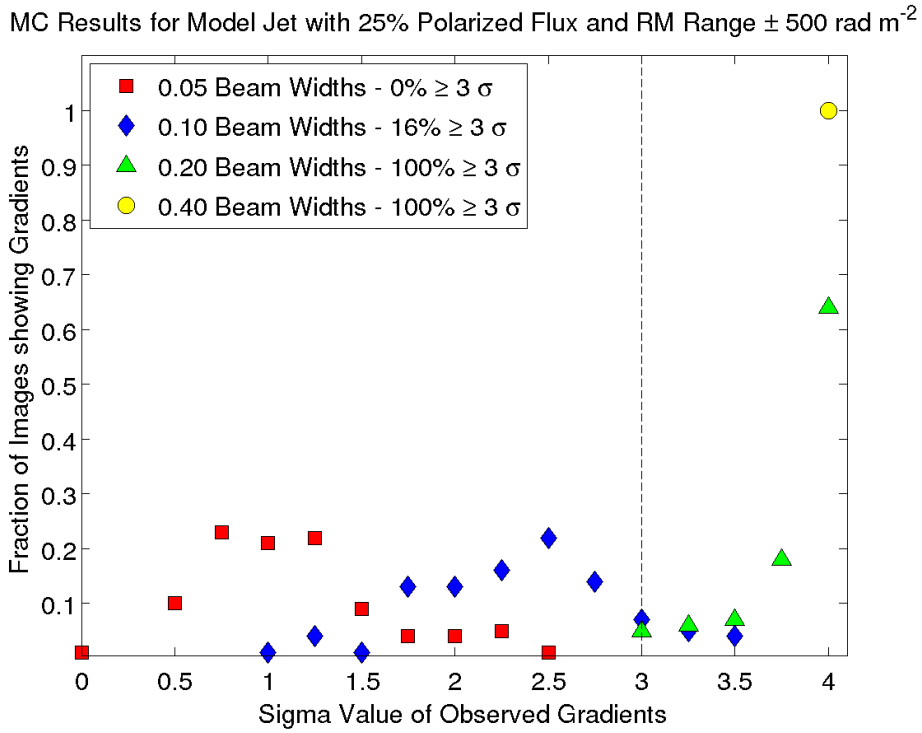

Figure 5.26: MC results for fourth set of 1.9 – 3.8 cm simulations at +32° declination.

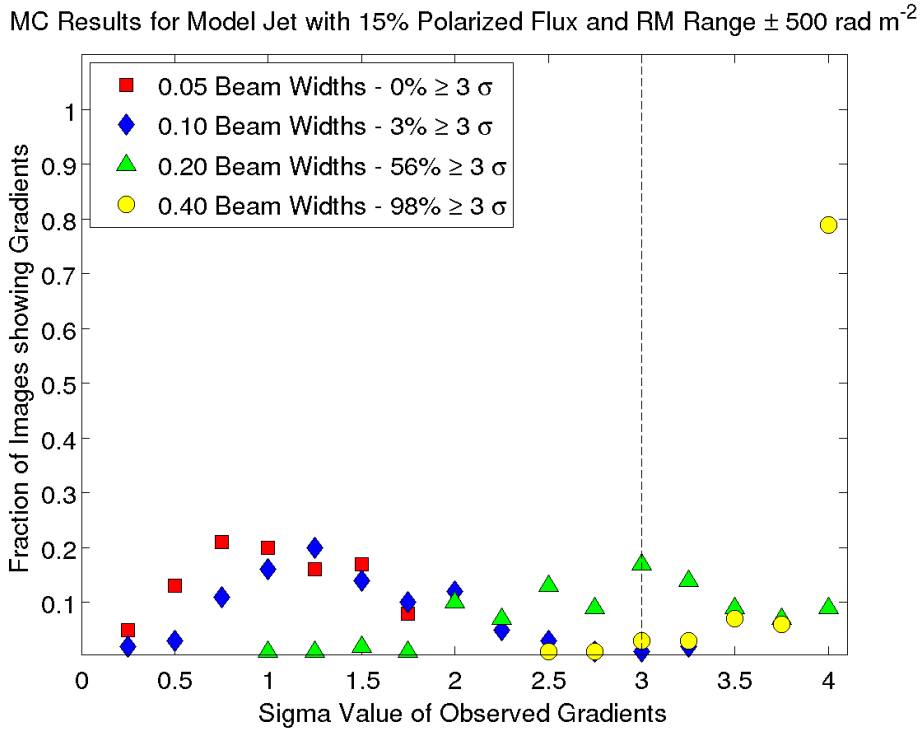

Figure 5.27: MC results for fifth set of 1.9 – 3.8 cm simulations at +32° declination.

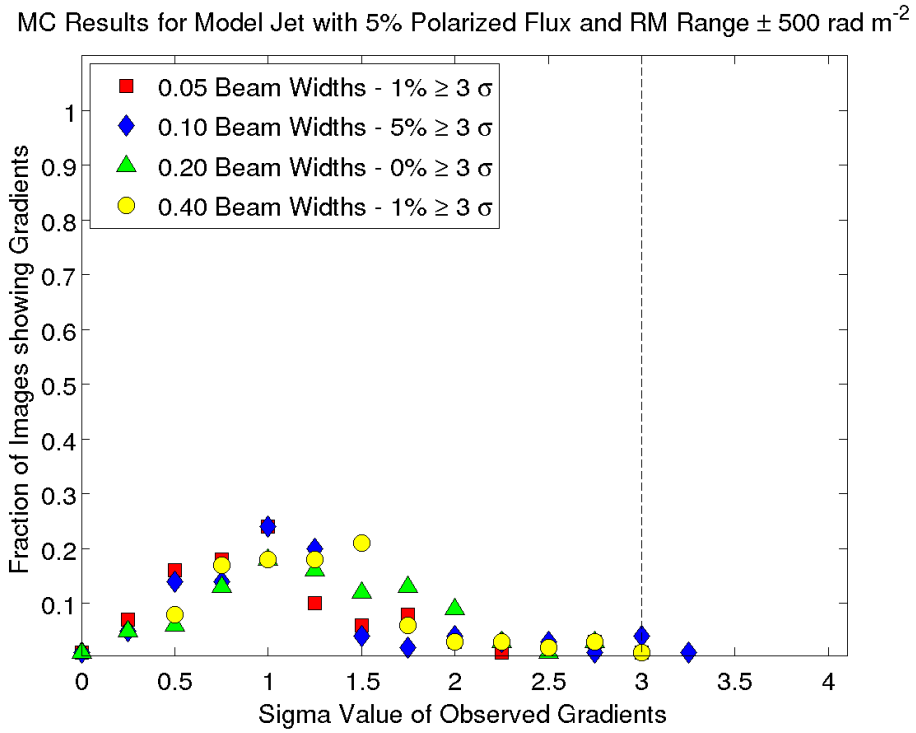

Figure 5.28: MC results for sixth set of 1.9 – 3.8 cm simulations at +32° declination.

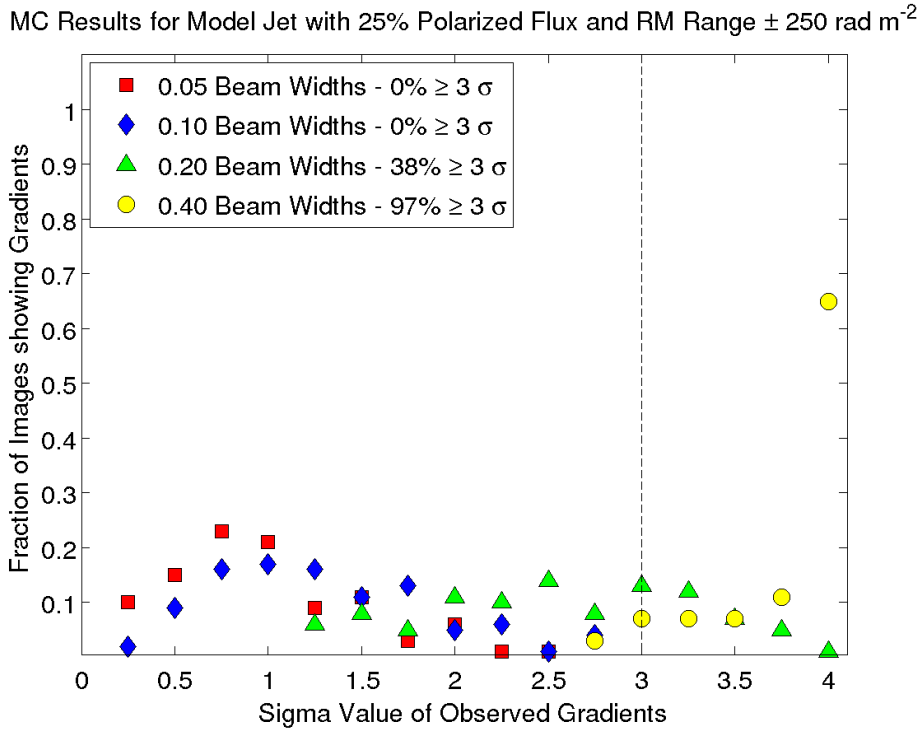

Figure 5.29: MC results for seventh set of 1.9 – 3.8 cm simulations at +32° declination.

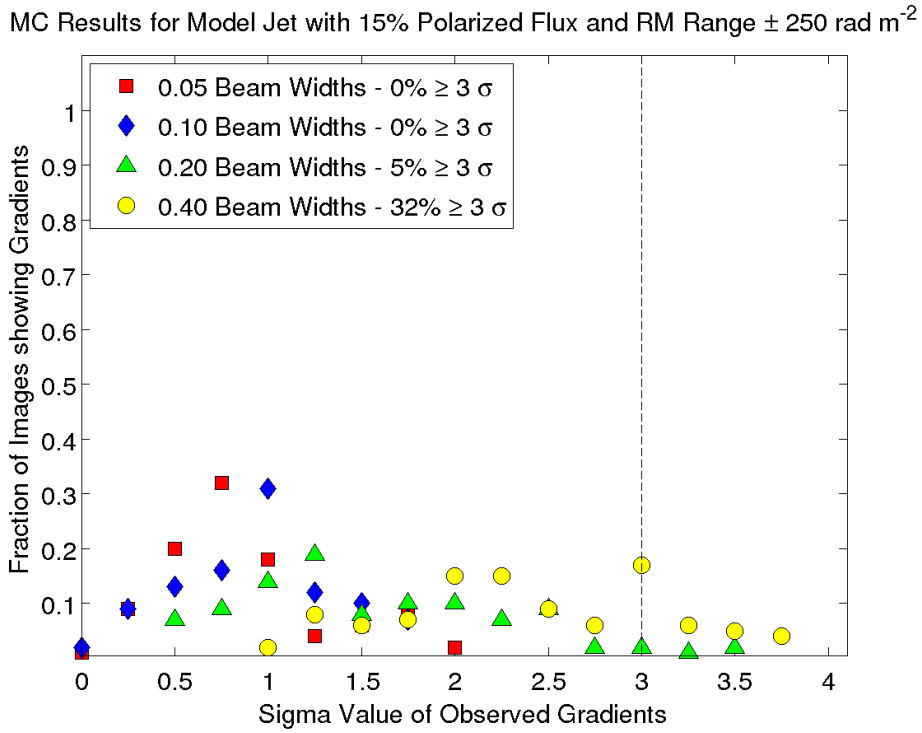

Figure 5.30: MC results for eighth set of 1.9 – 3.8 cm simulations at +32° declination.

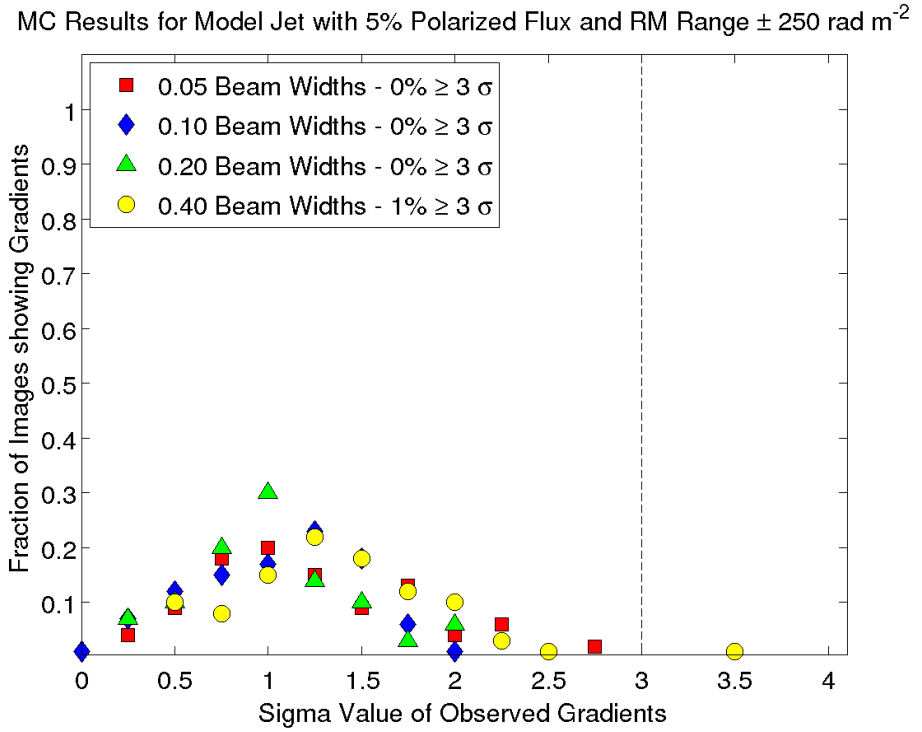

Figure 5.31: MC results for ninth set of 1.9 – 3.8 cm simulations at +32° declination.

5.2.3 Monte Carlo Results for 1.9 – 3.8 cm Simulations, Source at Declination −7°

The different model source parameters used for this source can be seen in Table 5.3. As described in Section 5.1, model sources were simulated for each of these parameters before being sampled at a set of UV points corresponding to those shown in Fig. 5.32. This UV distribution was based on simultaneous snapshot VLBA observations at 1.9 cm, 2.5 cm, 3.4 cm & 3.8 cm. As before the intrinsic RM Ranges used in these simulation were much higher than those used for the source at 18 – 22 cm. The values chosen where picked so that the maximum rotation of the EVPA ($\Delta\chi = RM\lambda^2$) would be similar for both sets simulations.

Table 5.3: Parameters used for Monte Carlo Analysis for 1.9 – 3.8 cm wavelength source at declination −7°. Each parameter combination was simulated resulting in 36 different model jets for the Monte Carlo simulations.

Intrinsic Jet Width	Percentage Polarization	Intrinsic RM Range
0.05 Beam Widths	25%	-1000 to 1000 rads m^{-2}
0.10 Beam Widths	15%	-500 to 500 rads m^{-2}
0.20 Beam Widths	05%	-250 to 250 rads m^{-2}
0.40 Beam Widths		

Figures 5.33 - 5.37 show the average Monte Carlo RM maps for this wavelength range and declination. Pixels were blanked if at least one of the MC instance maps that produced it had an error value greater than 50 rads m^{-2} for that pixel. These figures demonstrate the same behaviour as those for the previous sources. However, due mostly to the poorer UV coverage at this declination these RM average maps don't demonstrate gradients as clear as those seen in the +35° source despite both simulations using the same wavelength range.

Figures 5.38 - 5.46 show the fraction of the MC RM maps showing gradients spanning various multiples of the uncertainty σ ranging from 0 to at least 4. Unlike the previous two sources no 3σ gradients were observed for the narrowest intrinsic jet width for any value of polarized flux or intrinsic RM range. This difference is most likely due to the poorer UV coverage at this declination. This general trend is seen for each of the other intrinsic jet widths with lower percentages of 3σ gradients seen for almost all the model source parameters. Therefore, as expected, poor UV coverage can obscure RM gradients that would have been observed with better coverage. However, despite this, for the wider intrinsic jets widths, 3σ gra-

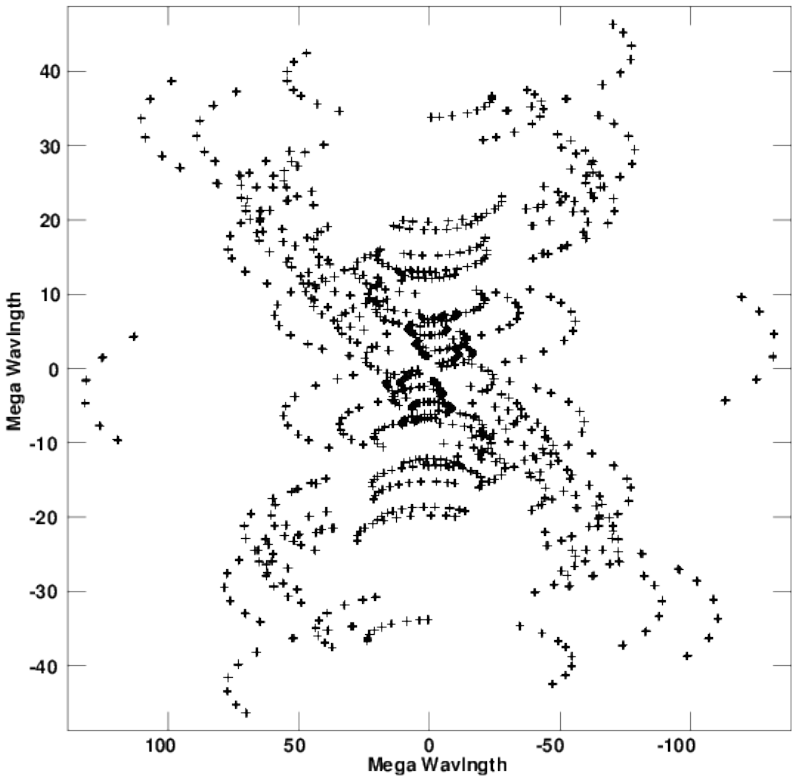

Figure 5.32: UV distribution for 3.8 cm visibility data for model source at −7° used in this analysis, based on existing VLBA snapshot observations.

dients were still observed in the majority of cases despite the observed jet width only being ∼ 1.5 beam widths.

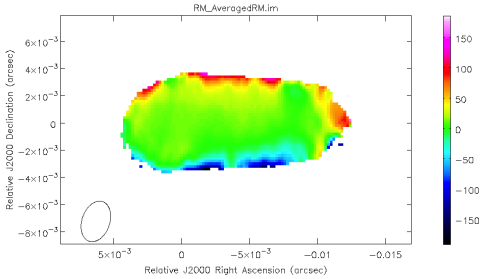

(a) 0.05 beam widths

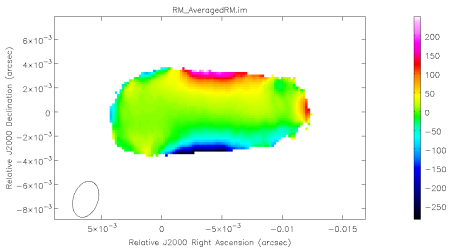

(b) 0.10 beam widths

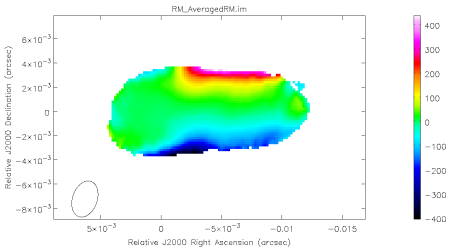

(c) 0.20 beam widths

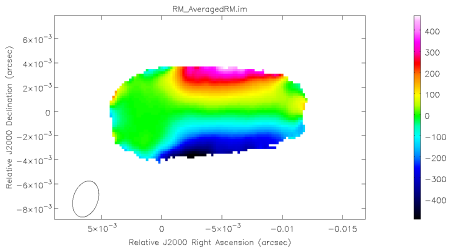

(d) 0.40 beam widths

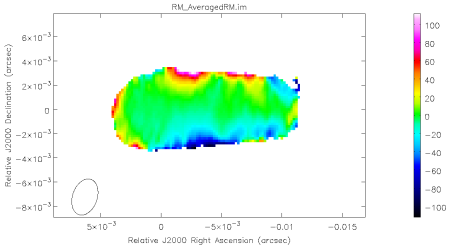

(e) 0.05 beam widths

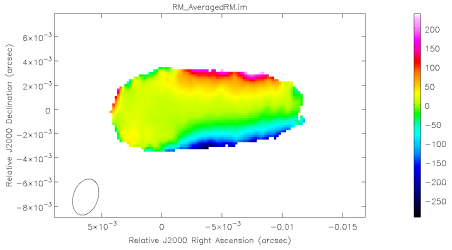

(f) 0.10 beam widths

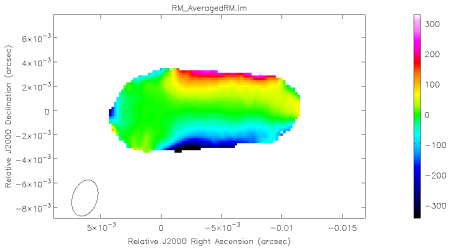

(g) 0.20 beam widths

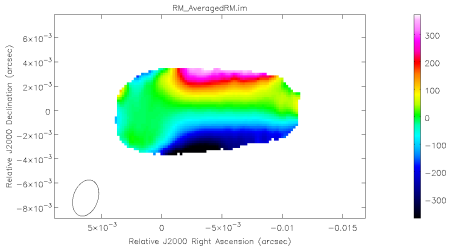

(h) 0.40 beam widths

Figure 5.33: First & Second sets of −7° declination 1.9 – 3.8 cm Monte Carlo simulations. Shown are results for four different intrinsic jet widths. Figures (a) – (d) correspond to a RM range of -1000 to +1000 rads m^{-2} and a percentage polarized flux of 25%. Figures (e) – (h) correspond to a RM range of -1000 to +1000 rads m^{-2} and a percentage polarized flux of 15%. The error cutoff for these figures is 50 rads m^{-2}.

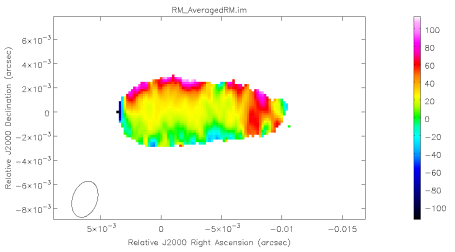

(a) 0.05 beam widths

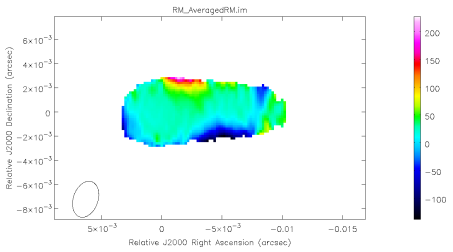

(b) 0.10 beam widths

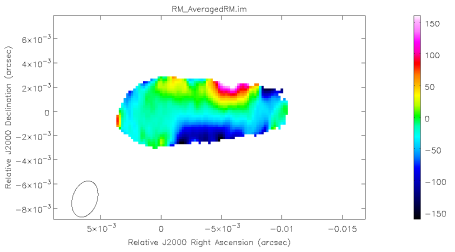

(c) 0.20 beam widths

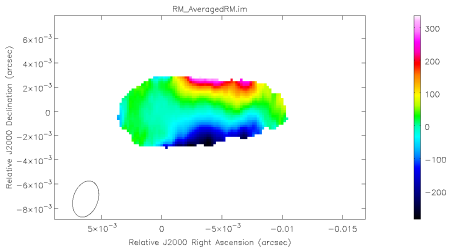

(d) 0.40 beam widths

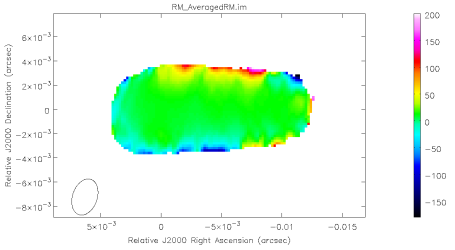

(e) 0.05 beam widths

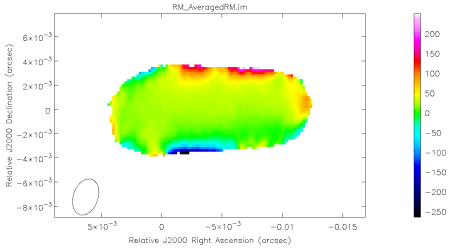

(f) 0.10 beam widths

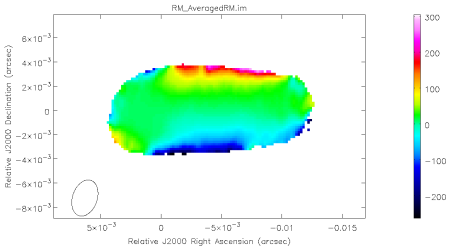

(g) 0.20 beam widths

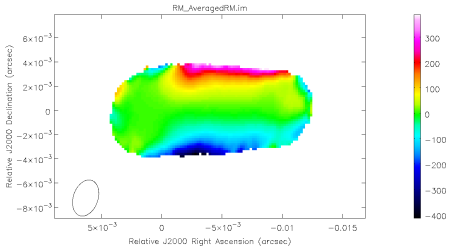

(h) 0.40 beam widths

Figure 5.34: Third & Fourth sets of −7° declination 1.9 – 3.8 cm Monte Carlo simulations. Shown are results for four different intrinsic jet widths. Figures (a) – (d) correspond to a RM range of -1000 to +1000 rads m^{-2} and a percentage polarized flux of 5%. Figures (e) – (h) correspond to a RM range of -500 to +500 rads m^{-2} and a percentage polarized flux of 25%. The error cutoff for these figures is 50 rads m^{-2}.

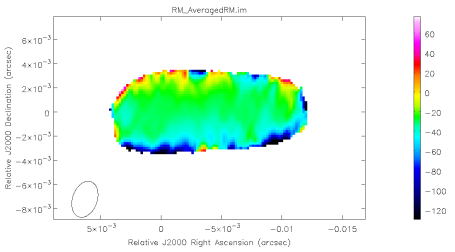

(a) 0.05 beam widths

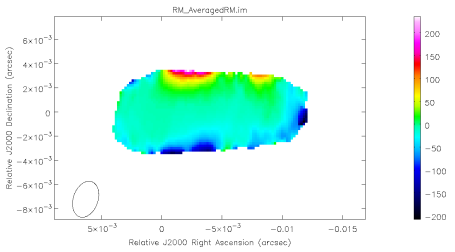

(b) 0.10 beam widths

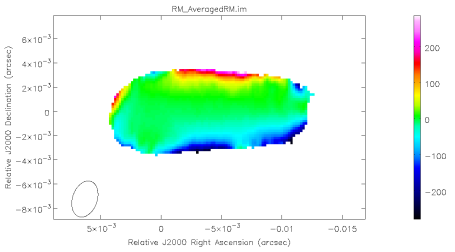

(c) 0.20 beam widths

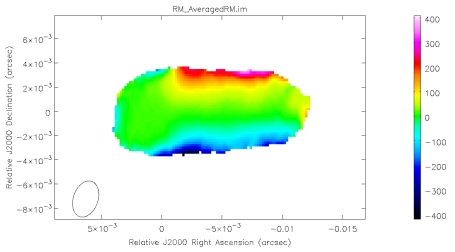

(d) 0.40 beam widths

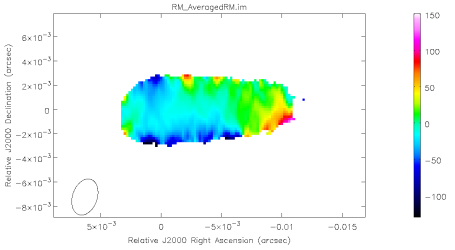

(e) 0.05 beam widths

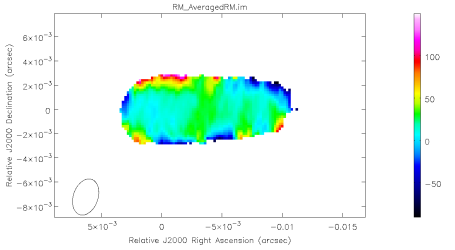

(f) 0.10 beam widths

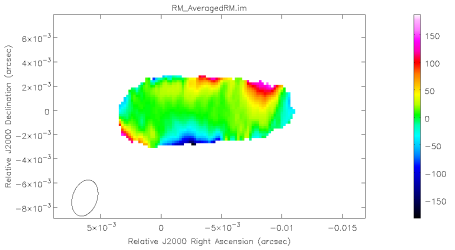

(g) 0.20 beam widths

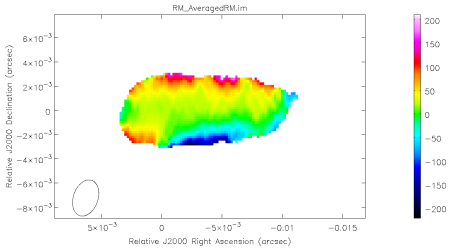

(h) 0.40 beam widths

Figure 5.35: Fifth & Sixth sets of −7° declination 1.9 – 3.8 cm Monte Carlo simulations. Shown are results for four different intrinsic jet widths. Figures (a) – (d) correspond to a RM range of -500 to +500 rads m^{-2} and a percentage polarized flux of 15%. Figures (e) – (h) correspond to a RM range of -500 to +500 rads m^{-2} and a percentage polarized flux of 5%. The error cutoff for these figures is 50 rads m^{-2}.

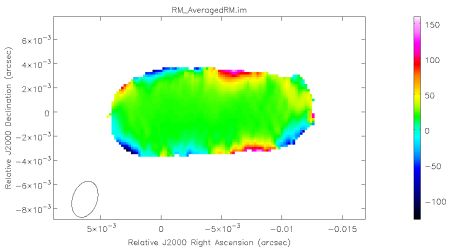

(a) 0.05 beam widths

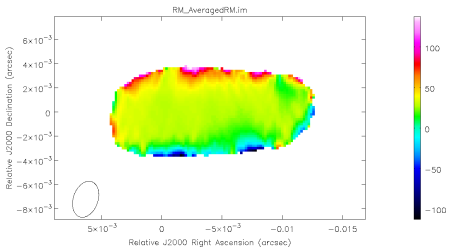

(b) 0.10 beam widths

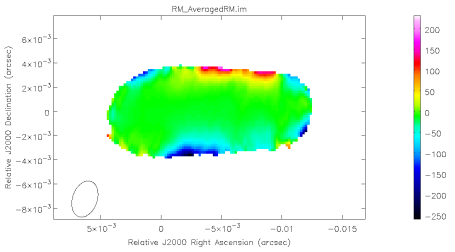

(c) 0.20 beam widths

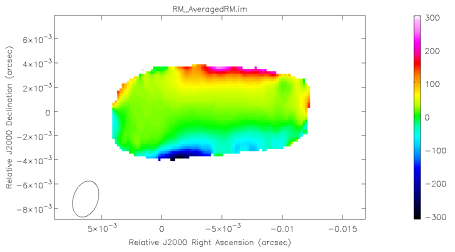

(d) 0.40 beam widths

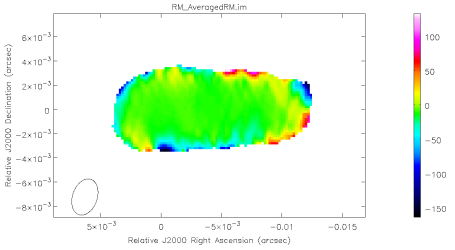

(e) 0.05 beam widths

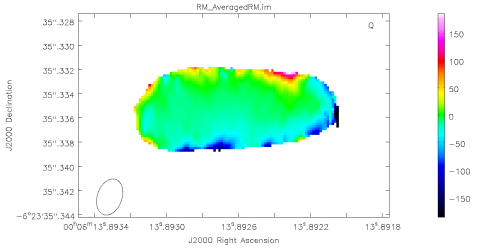

(f) 0.10 beam widths

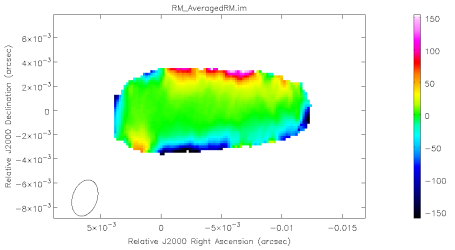

(g) 0.20 beam widths

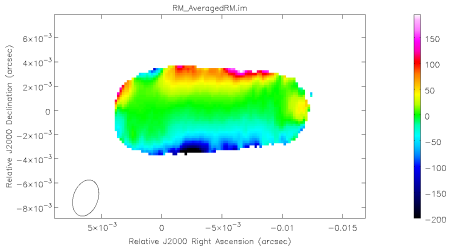

(h) 0.40 beam widths

Figure 5.36: Seventh & Eighth sets of −7° declination 1.9 – 3.8 cm Monte Carlo simulations. Shown are results for four different intrinsic jet widths. Figures (a) – (d) correspond to a RM range of -250 to +250 rads m^{-2} and a percentage polarized flux of 25%. Figures (e) – (h) correspond to a RM range of -250 to +250 rads m^{-2} and a percentage polarized flux of 15%. The error cutoff for these figures is 50 rads m^{-2}.

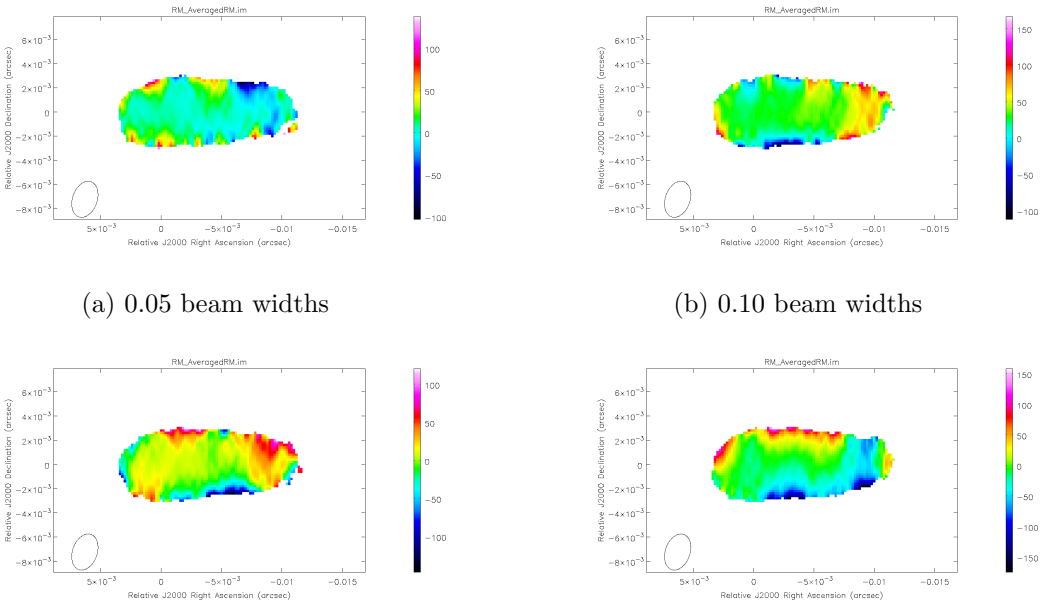

(a) 0.05 beam widths

(b) 0.10 beam widths

(c) 0.20 beam widths

(d) 0.40 beam widths

Figure 5.37: Ninth set of −7° declination 1.9 – 3.8 cm Monte Carlo simulations. Shown are results for four different intrinsic jet widths. Figures (a) – (d) correspond to a RM range of -250 to +250 rads m^{-2} and a percentage polarized flux of 5%. The error cutoff for these figures is 50 rads m^{-2}.

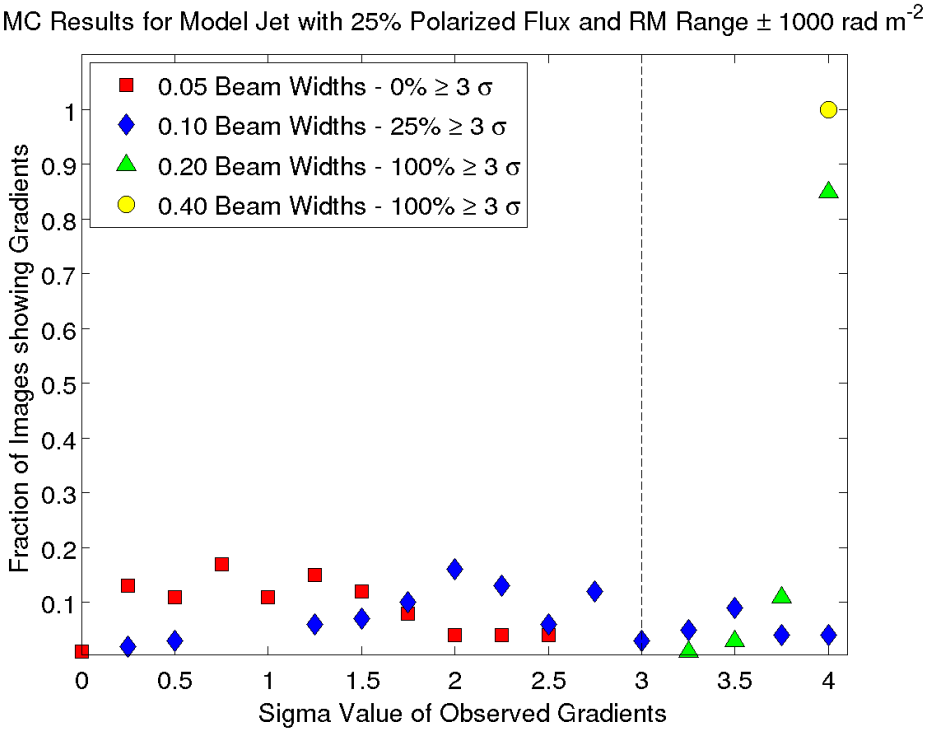

Figure 5.38: MC results for first set of 1.9 – 3.8 cm simulations at −7° declination.

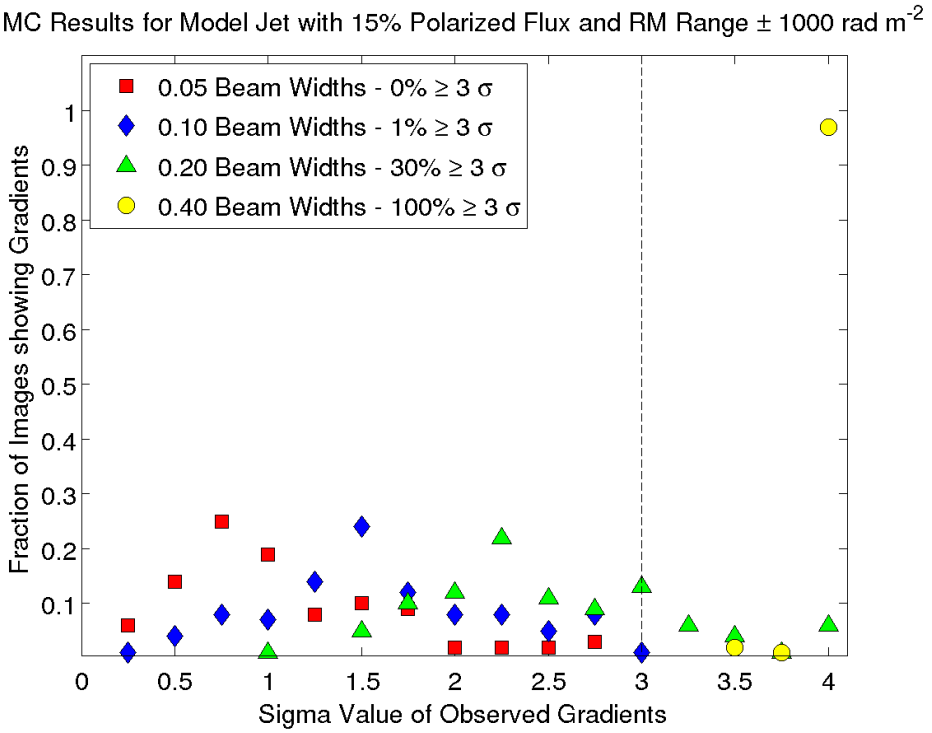

Figure 5.39: MC results for second set of 1.9 – 3.8 cm simulations at −7° declination.

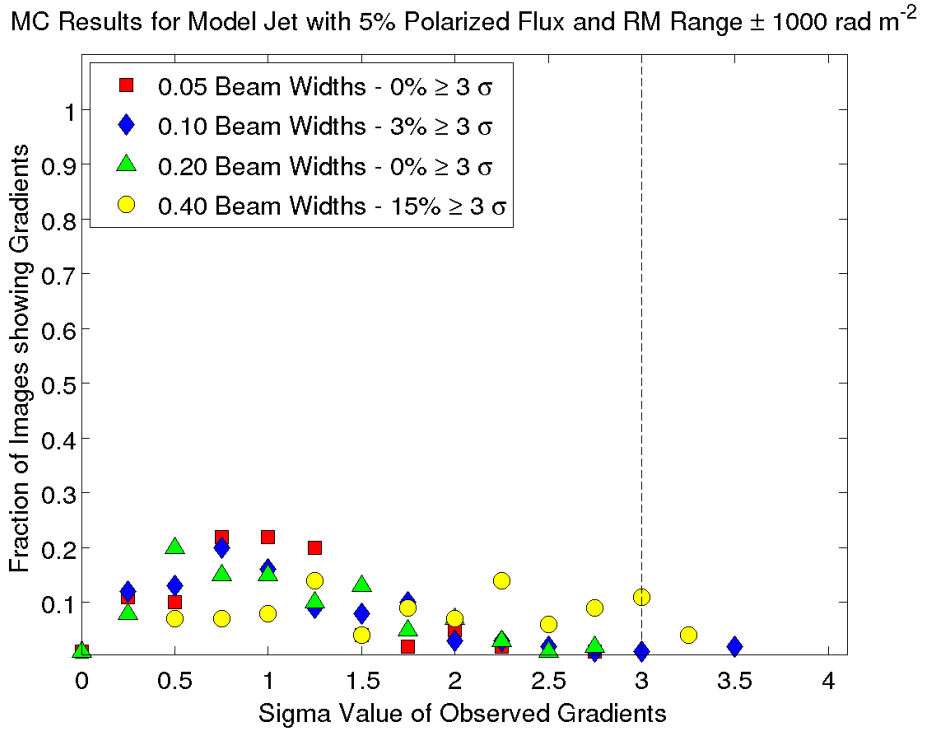

Figure 5.40: MC results for third set of 1.9 – 3.8 cm simulations at −7° declination.

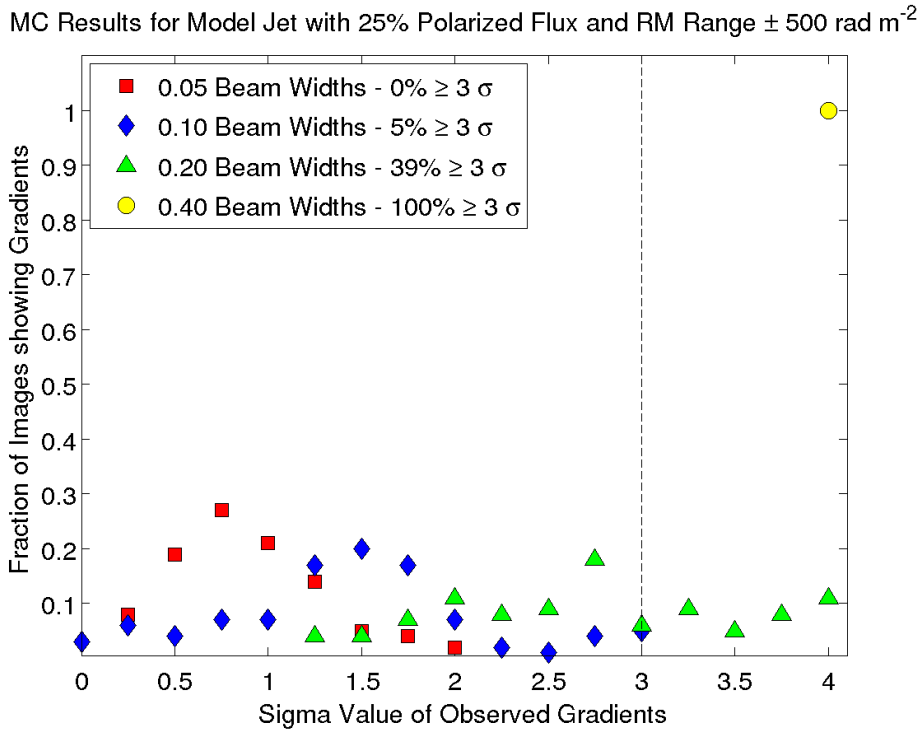

Figure 5.41: MC results for fourth set of 1.9 – 3.8 cm simulations at −7° declination.

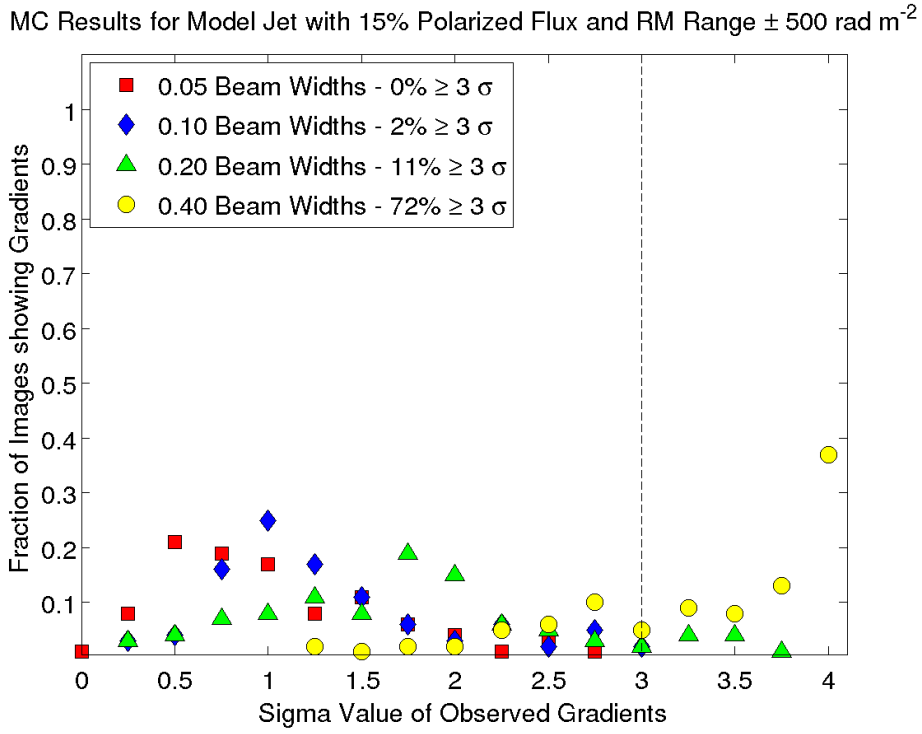

Figure 5.42: MC results for fifth set of 1.9 – 3.8 cm simulations at −7° declination.

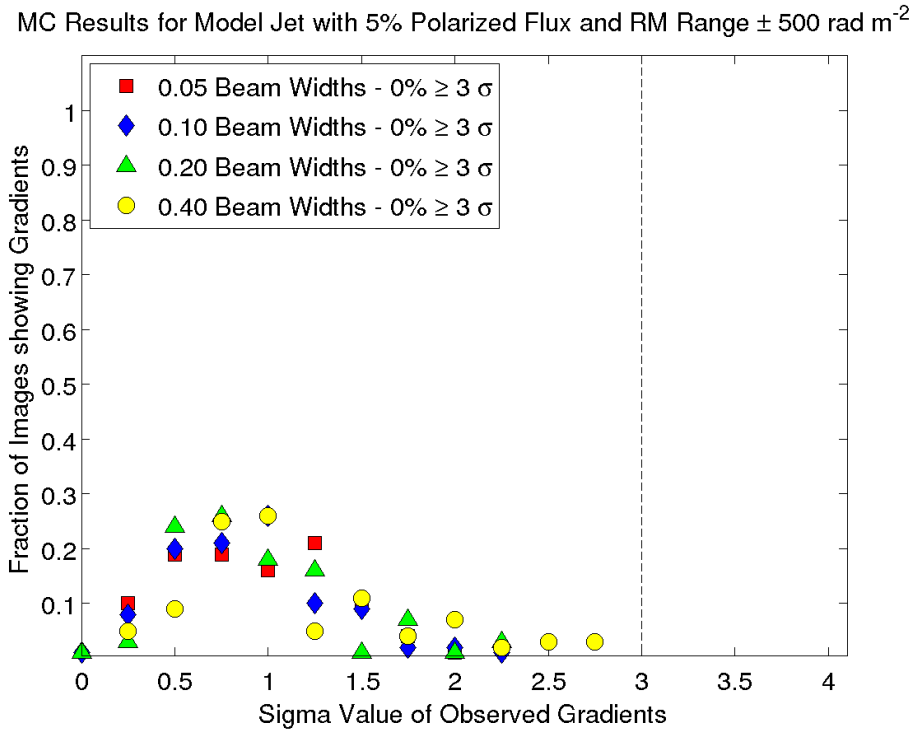

Figure 5.43: MC results for sixth set of 1.9 – 3.8 cm simulations at −7° declination.

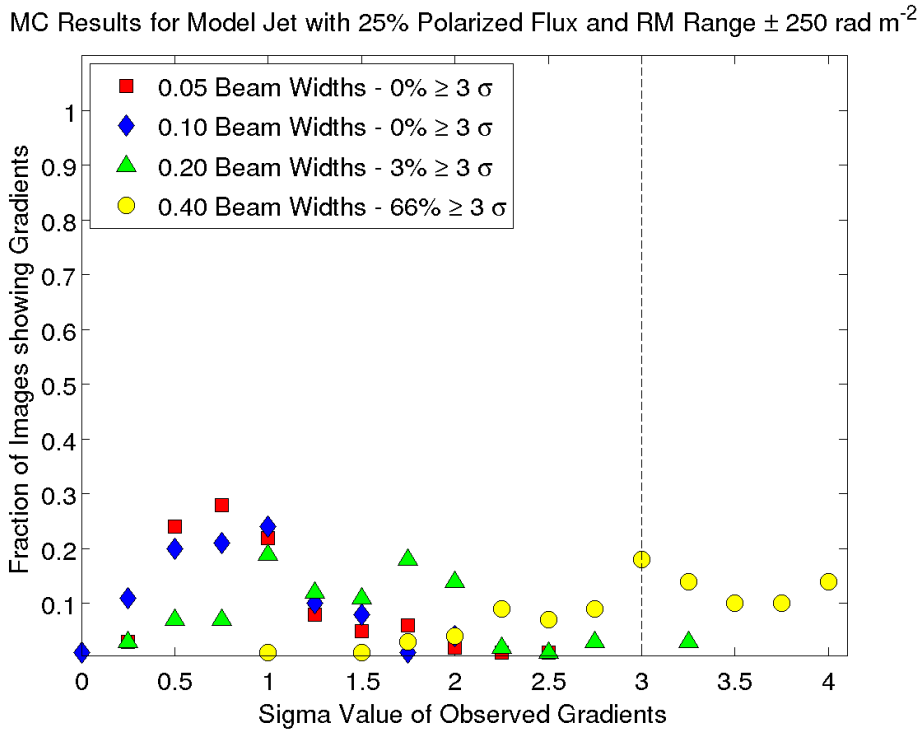

Figure 5.44: MC results for seventh set of 1.9 – 3.8 cm simulations at −7° declination.

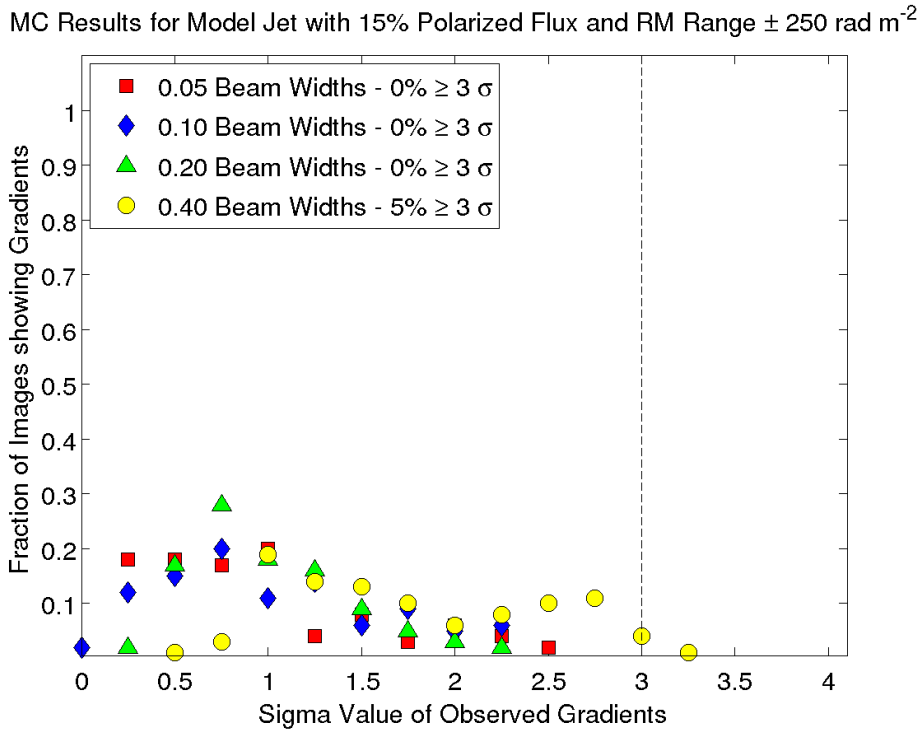

Figure 5.45: MC results for eighth set of 1.9 – 3.8 cm simulations at −7° declination.

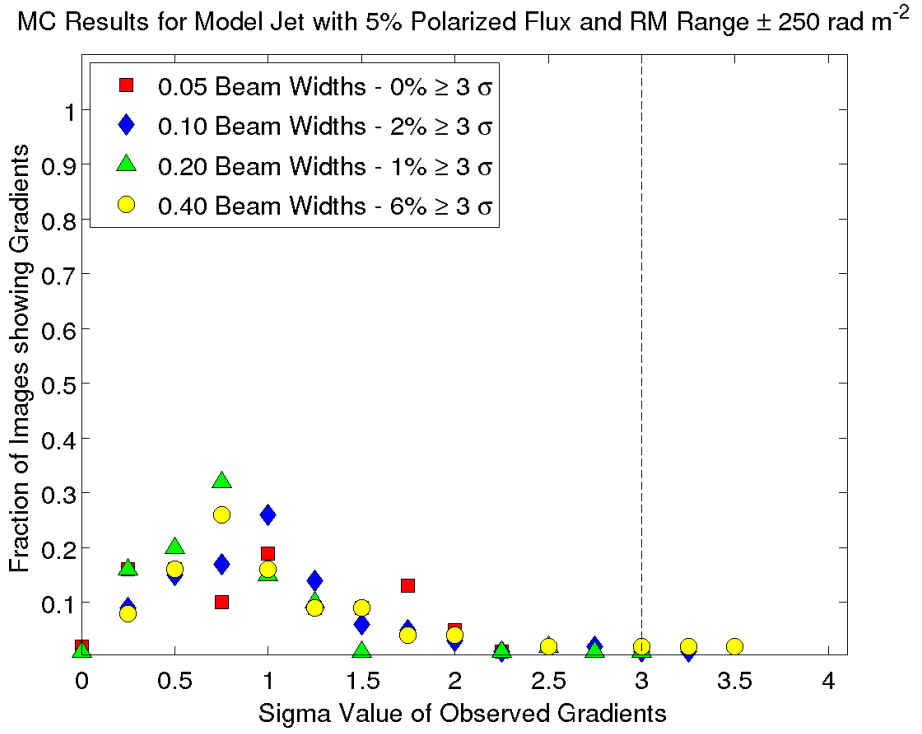

Figure 5.46: MC results for ninth set of 1.9 – 3.8 cm simulations at −7° declination.

5.2.4 Faraday Depolarization

Faraday depolarization can occur if a large RM gradient is present in the jet. As the polarization angle χ is rotated different amounts across a given slice, the Q and U Stokes polarization along this slice can quickly transition from positive to negative. This results in bands of positive and negative Stokes Q and U transverse to the intrinsic jet. After convolution with a beam these negative and positive regions blur into one another and cancel out resulting in a much lower observed percentage polarization.

Faraday depolarization proves a useful check to ensure that the analysis method used in this chapter is functioning correctly. Figure 5.47 shows percentage polarized maps for a model jet affected by Faraday depolarization. The regions of these model jets which had a large Faraday RM gradient applied have significantly lower percentage polarization. As Sections 5.2.1 and 5.2.2 demonstrate, percentage polarization is very important in observing RM gradients. Therefore, a knowledge of the effects of Faraday depolarization is needed when attempting to detect RM gradients. Larger RM gradients may be more reliably detected with lower wavelength observations despite their relatively poorer sensitivity to Faraday rotation.

5.3 RM Gradient Reversal

The results presented here have been published in Mahmud et al. (2013). The work described in this section was carried out in collaboration with Colm Coughlan. I created the model jets used in the comparison and the method of replacing existing visibilities with new model visibilities while Colm carried out the imaging and comparisons.

Recent work by Mahmud et al. (2013) showed evidence of a RM gradient reversal in the jet of 0716+714 (Fig. 5.48). Very high resolution observations of this source by Kardashev et al. (2013) observed using a combination of the European VLBI Network (EVN) and the *RadioAstron* space radio telescope have measured the size of a feature in the 6.2 cm core region to be about 0.07 mas. This is significantly narrower that the beam used for the images of Mahmud et al. (2013)

In order to demonstrate that such a gradient reversal could be observed at such resolutions, a model source with a transverse RM gradient across its jet was

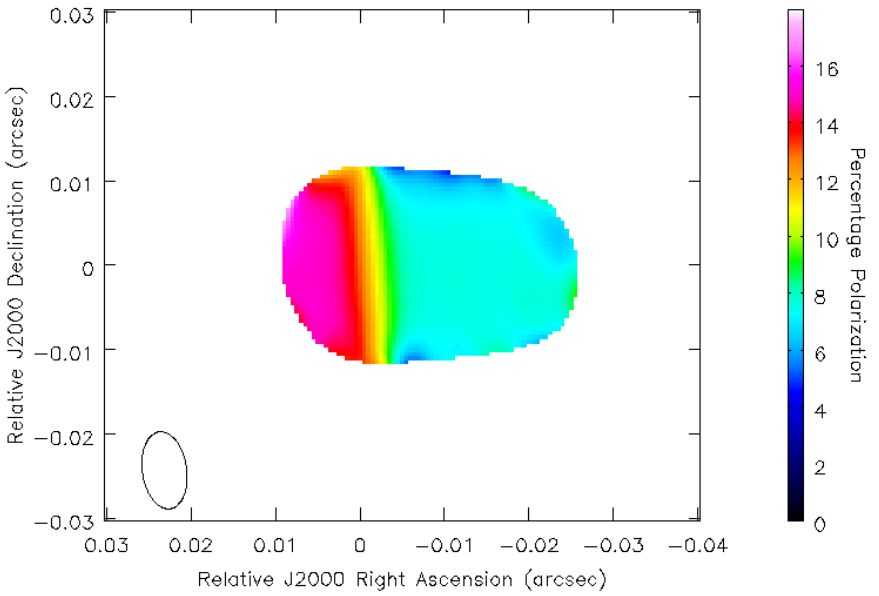

(a) 18 cm percentage polarization map for model jet.

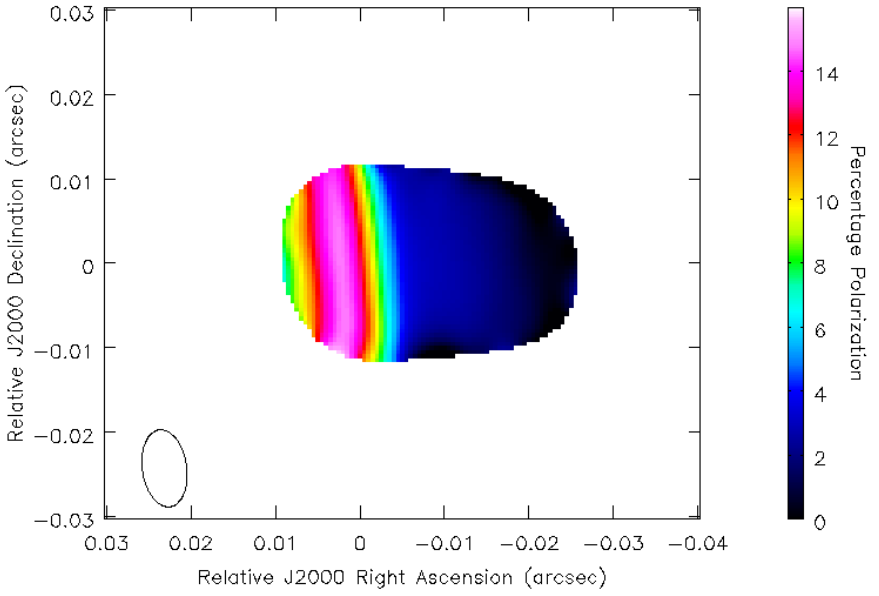

(b) 22 cm percentage polarization map for model jet.

Figure 5.47: Percentage polarization maps for 18 cm and 22 cm model jet with RM gradient from -100 rads m^{-2} to +100 rads m^{-2} applied to three quarters of jet. The intrinsic percentage polarization for both maps is 15 %. The minimum observed percentage polarization for the 18 cm map and 22 cm map are approximately 6% and 2%. This reduction in observed polarized flux is due to Faraday depolarization. The difference between the maps is due to the 22 cm map experiencing a larger rotation in polarization angle χ as per Eqn. 2.23.

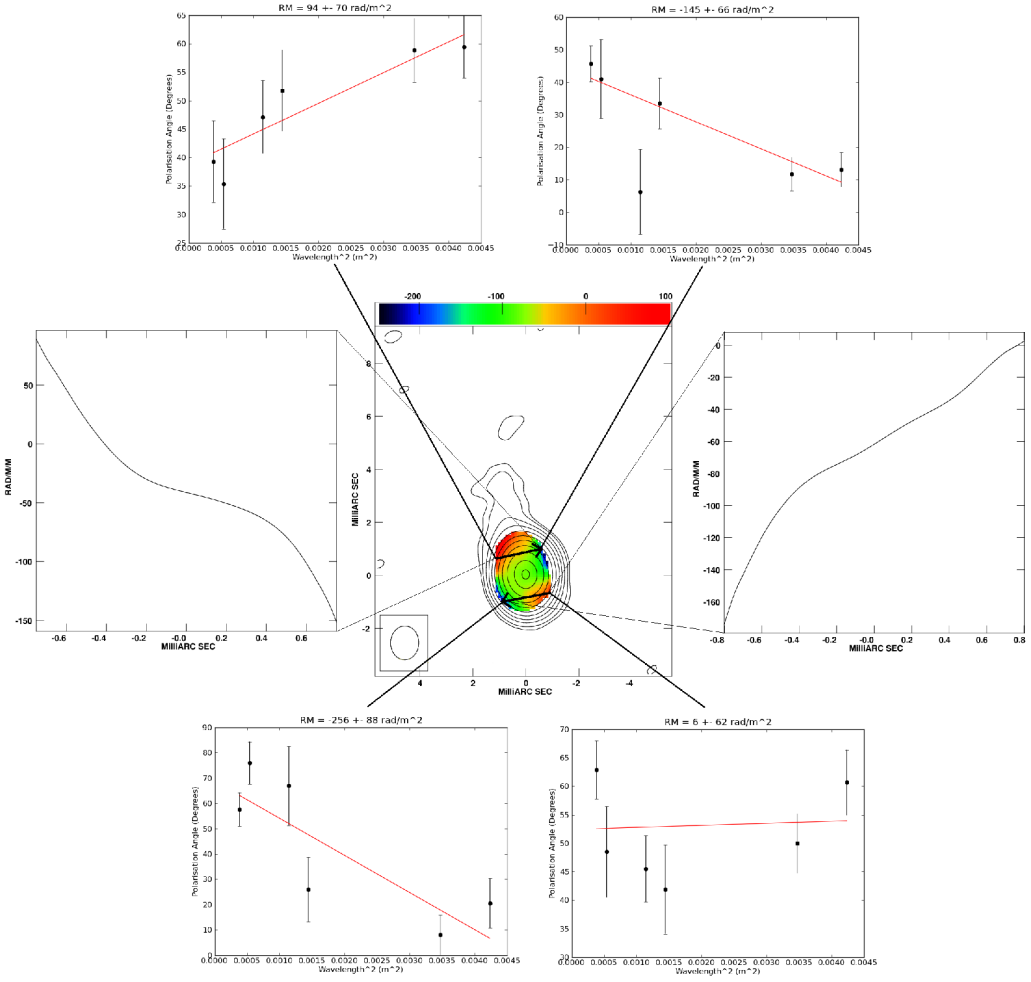

Figure 5.48: RM map of 0716 + 714 at 4.6–15.4 GHz (Mahmud et al. 2013). The accompanying panels show slices of the RM distributions across the jet and core, and polarization angle (χ) vs. wavelength-squared (λ^2) plots for pixels on either side of the core and jet. The errors shown in the plots are 1σ, and include the estimated random errors and the EVPA uncertainties added in quadrature. The peak of the I map is 1.3 Jy/beam and the bottom contour is 1.0 mJy/beam. The beam used to construct the I and RM maps was 1.28 × 1.06 mas in position angle −0.8°.

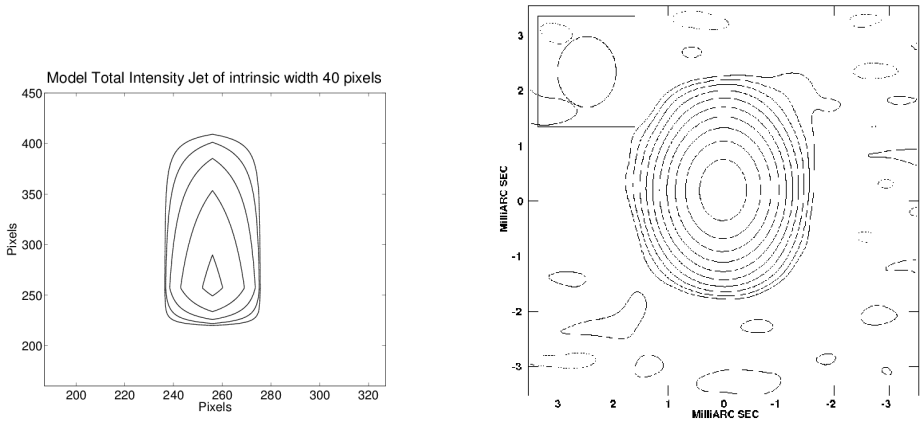

(a) (b)

Figure 5.49: (Left) Intrinsic total intensity image of the model core–jet-like source with an intrinsic length of 1.0 mas (200 pixels) and an intrinsic width of 0.20 mas (40 pixels), used for the Monte Carlo simulations. (Right) One realisation of a "noisy" intensity map produced during the simulations. The convolving beam is 1.28 mas×1.06 mas in PA = −0.84° (shown in the upper left-hand corner of the convolved image). The peak of the unconvolved image is 5.62×10^{-4} Jy, and the contours are 5, 10, 20, 40, and 80% of the peak. The peak of the convolved image is 1.11 Jy beam^{-1}, and the contours are −0.125, 0.125, 0.25, 0.5, 1, 2, 4, 8, 16, 32, and 64% of the peak.

constructed, and Monte Carlo simulations based on this model source were carried out. The model source used can be seen in Fig. 5.49. The resulting appearance of the model emission region is broadly speaking "core–jet-like".

Model visibility data were generated for the six frequencies used in the original observations (4.612, 5.092, 7.916, 8.883, 12.939 and 15.383 GHz). The amount of thermal noise added was chosen to yield RMS values in the simulated images that were comparable to those in the observations of Mahmud et al. (2013). The polarization of the model was chosen to yield a degree of polarization in the lower half of the convolved model image (the "core" region) of about 5% and a degree of polarization in the upper half of the convolved model image of about 10% – similar to the observed values for 0716+714.

This procedure was carried out for a number of model sources, all with a length of 1 mas and with transverse widths of 0.35, 0.20. 0.10 and 0.05 mas. This narrowest jet width was chosen to be slightly smaller than that observed by Kardashev et al. (2012). Two different types of monotonic transverse RM gradients were applied to these model sources.

- Orientated in one direction along the entire source structure

- Oriented in one direction in the "core" region and in the opposite direction in the "jet" region (i.e., showing a reversal)

5.3.1 Monte Carlo Results

The results of these RM Monte Carlo Simulation can be seen in Figures 5.50 - 5.53. The colour scales for the three maps in a corresponding set have been individually chosen to highlight the RM patterns present, and may differ somewhat in some cases.

In all cases, the RM gradients that were introduced into the simulated data are visible in the "noisy" RM maps that were obtained, even when the intrinsic width of the jet was approximately $\frac{1}{20}$ of the beam width. As before, the magnitudes of the RM gradients are reduced by the convolution more and more as the size of the beam relative to the intrinsic size of the jet width increases, but the RM gradients that were initially introduced into the simulated data remain visible. In the case of jet widths much less than the beam width, the appearance of individual realizations can sometimes be fairly strongly distorted by noise; however, in all cases, averaging together all the individual realizations confirms the presence of the RM gradients in the simulated images.

These results indicate that it is possible to reliably detect RM gradient reversals in such a source even though the intrinsic jet width is only $\sim \frac{1}{20}$ beam widths across. Therefore, the observed RM gradient reversal seen in 0716 + 714 by Mahmud et al. (2013) should not be dismissed as spurious or unreliable due to the resolution of the VLBA observations.

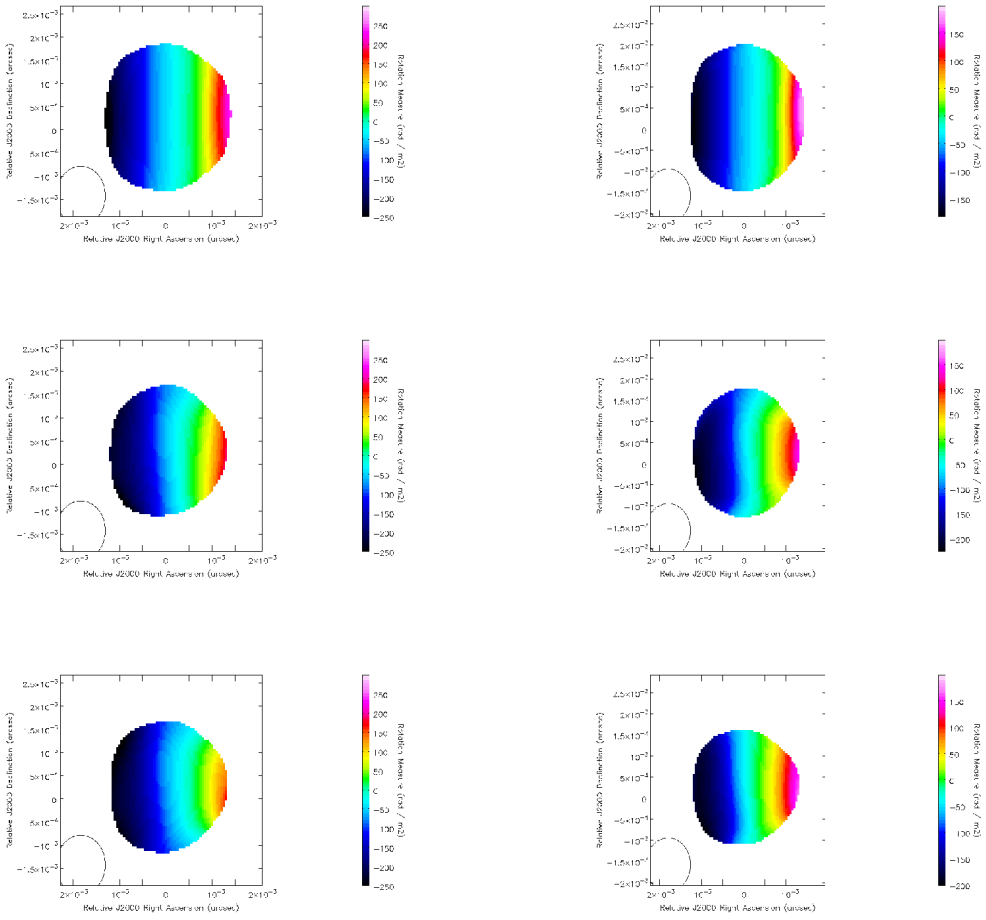

Figure 5.50: Monte Carlo results using model core–jet sources with uniformly directed monotonic transverse RM gradients. The convolving beam (1.28 mas×1.06 mas in PA = −0.84°) is shown in the lower left-hand corner of each panel. The top panels shows the RM image obtained by processing the model data as usual, but without adding random noise or EVPA calibration uncertainty; pixels with RM uncertainties exceeding 10 rad/m^2 were blanked. The remaining panels show two examples of the 200 individual RM images obtained during the simulations; pixels with RM uncertainties exceeding 80 rad/m^2 were blanked. The left hand panels are for a model source in which the intrinsic width of the jet (RM gradient) is 0.35 mas. The right hand panels are for a model source in which the intrinsic width of the jet (RM gradient) is 0.20 mas.

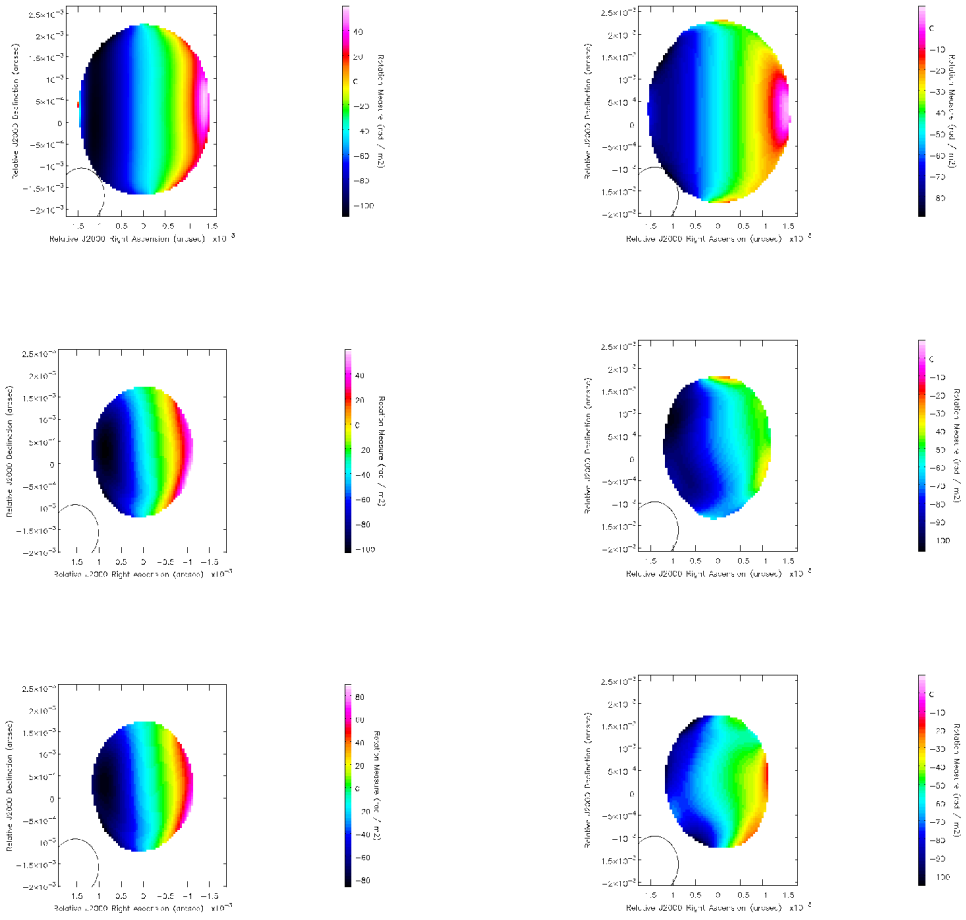

Figure 5.51: Monte Carlo results using model core–jet sources with uniformly directed monotonic transverse RM gradients. The convolving beam (1.28 mas×1.06 mas in PA = −0.84°) is shown in the lower left-hand corner of each panel. The top panels shows the RM image obtained by processing the model data as usual, but without adding random noise or EVPA calibration uncertainty; pixels with RM uncertainties exceeding 10 rad/m^2 were blanked. The remaining panels show two examples of the 200 individual RM images obtained during the simulations; pixels with RM uncertainties exceeding 80 rad/m^2 were blanked. The left hand panels are for a model source in which the intrinsic width of the jet (RM gradient) is 0.10 mas. The right hand panels are for a model source in which the intrinsic width of the jet (RM gradient) is 0.05 mas.

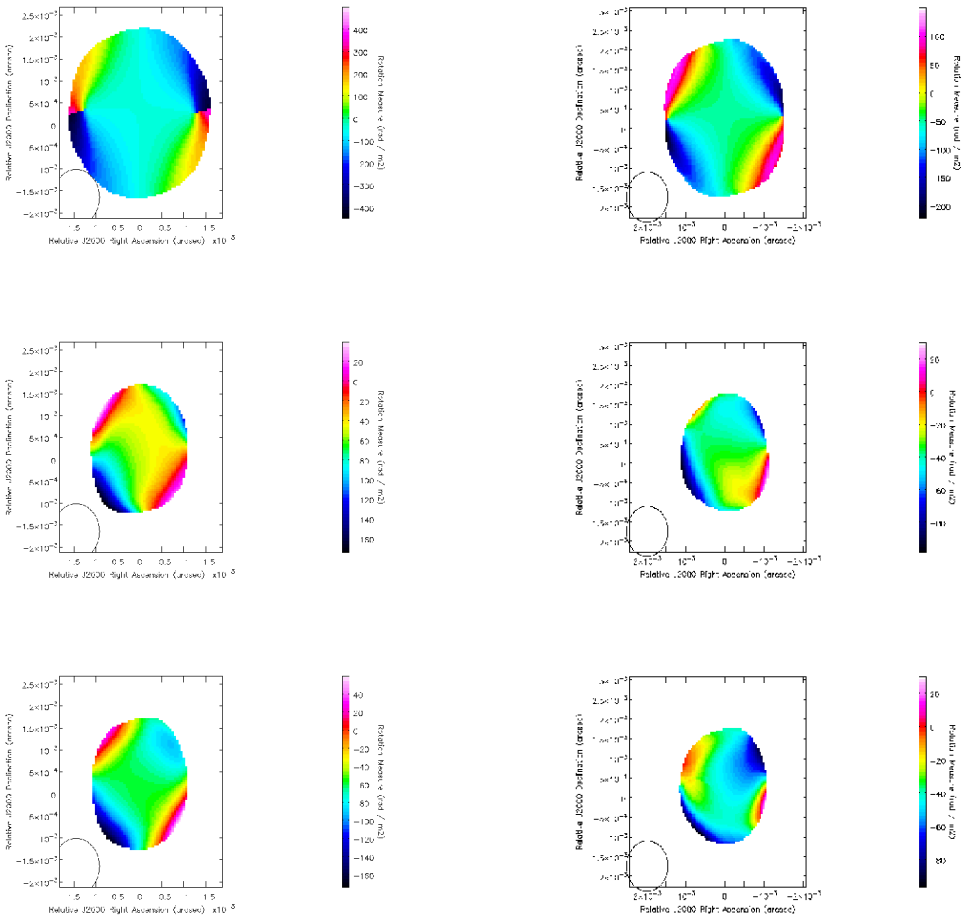

Figure 5.52: Monte Carlo results using model core–jet sources with oppositely directed transverse RM gradients in the core region and inner jet. The convolving beam (1.28 mas×1.06 mas in PA = −0.84°) is shown in the lower left-hand corner of each panel. The top panels shows the RM image obtained by processing the model data as usual, but without adding random noise or EVPA calibration uncertainty; pixels with RM uncertainties exceeding 10 rad/m^2 were blanked. The remaining panels show two examples of the 200 individual RM images obtained during the simulations; pixels with RM uncertainties exceeding 80 rad/m^2 were blanked. The left hand panels are for a model source in which the intrinsic width of the jet (RM gradient) is 0.35 mas. The right hand panels are for a model source in which the intrinsic width of the jet (RM gradient) is 0.20 mas.

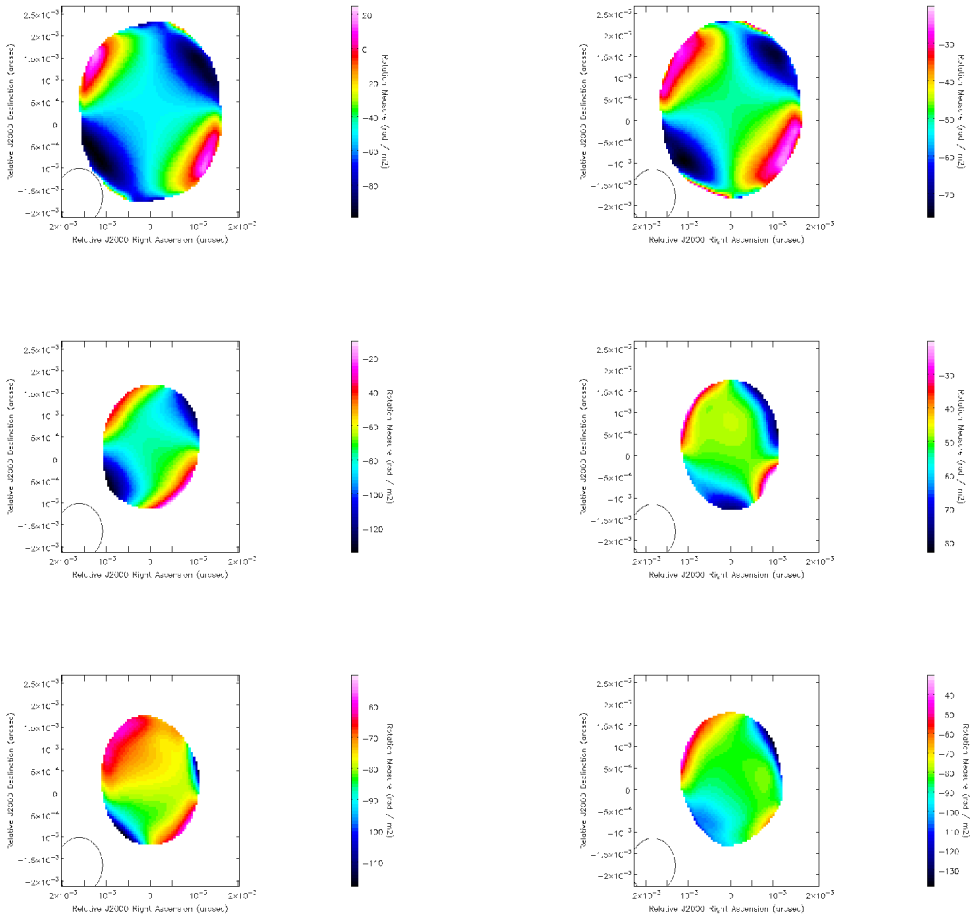

Figure 5.53: Results of Monte Carlo simulations using model core–jet sources with oppositely directed transverse RM gradients in the core region and inner jet. The convolving beam (1.28 mas×1.06 mas in PA = −0.84°) is shown in the lower left-hand corner of each panel. The top panels shows the RM image obtained by processing the model data as usual, but without adding random noise or EVPA calibration uncertainty; pixels with RM uncertainties exceeding 10 rad/m^2 were blanked. The remaining panels show two examples of the 200 individual RM images obtained during the simulations; pixels with RM uncertainties exceeding 80 rad/m^2 were blanked. The left hand panels are for a model source in which the intrinsic width of the jet (RM gradient) is 0.10 mas. The right hand panels are for a model source in which the intrinsic width of the jet (RM gradient) is 0.05 mas.

Chapter 6

Occurrence of Spurious Gradients

Utilizing the same procedure as outlined in Section 5.1 but adding no RM Gradient to the simulated Q and U maps allowed the probability of observing spurious gradients to be directly investigated. Simulated I, Q and U maps (with the same total intensity distributions as the sources used in Chapter 5) with a percentage polarized flux of 10% and constant polarization angle, χ of 22.5° were produced for jets of different intrinsic widths. This angle was chosen so that there would be equal amounts of Q and U polarized flux in the model jet. Rotation Measure Maps were constructed for 1000 independent realizations of the thermal noise and EVPA calibration uncertainty, and transverse slices were taken across each of these realizations.

As the jet edges can be hard to determine exactly, a band of possible jet edges was used for each transverse slice. This band was normally chosen to be 5 pixels wide centred around a jet edge pixel chosen by eye when investigating intensity maps of the model sources. Each possible jet slice was checked to see if the observed RM gradient along the slice was strictly monotonic. If so, the difference between the RM values at the two ends of the slice was determined and its associated error calculated. The jet edges which produced the most appreciable spurious gradient was used for the Monte Carlo analysis.

Since no RM gradient had been applied to the data, any monotonic RM gradients identified in this way were spurious. Therefore, we were able to determine the probability of finding spurious gradients with various significances for different intrinsic jet widths.

6.1 Monte Carlo Statistics for Spurious Gradients

Figures 6.1 - 6.3 show the results of this analysis for the three different wavelength and declination combinations used in Chapter 5. These figures show the fraction of false transverse RM gradients observed in the simulations as a function of the observed width of the RM gradient after convolution. As expected, the number of observed spurious gradients decreases as observed jet width increases. The number of observed spurious gradients is lowest for the 18 – 22 cm simulations. This is due to the higher sensitivity of this wavelength range (18, 20, 21 & 22 cm) to Faraday rotation, compared to the other wavelength range considered (1.9, 2.5, 3.4 and 3.8 cm) The number of observed spurious gradients is highest for the 1.9 – 3.8 cm simulations for the source at −7° as a result of both its relatively low sensitivity to Faraday rotation and its relatively poorer UV coverage.

In all cases, spurious 4σ transverse RM gradients were very rarely observed. For the narrowest jet width 4σ gradients were observed at most in $\sim 2\%$ of cases. A spurious 4σ gradient was never observed for observed jet widths of 2 beam widths. Spurious 3σ gradients were also quite rare, and were observed in at most $\sim 3\%$ of cases for the worst case: an intrinsic jet width of 0.05 beam widths, wavelength range 1.9 – 3.8 cm and declination of −7°. In other words, the probability that observed RM gradients spanning values corresponding to $\geq 3\sigma$ in sources that are not at very low declinations are spurious is no more than $\sim 1\%$, for both the wavelength ranges considered here.

Spurious 2σ gradients were observed in at most ~15% of cases. Inspection of Figs. 6.1 - 6.3 which show results for simulated RM gradients indicates that the fraction of images showing gradients at the 2σ level can appreciably exceed the fraction of spurious 2σ gradients. Therefore, the possible reality of an observed 2σ RM gradient should not be completely ruled out, and such gradients should be taken to be tentative results, that must be confirmed by further data, as was also pointed out by Hovatta et al. (2012).

While not shown on these figures, 1σ gradients were the most often observed spurious gradients in most cases, observed more than no gradient at all . The minimum percentage of observed 1σ spurious gradients was 46% for the model source at +42° (observed at 18, 20, 21 & 22 cm). Accordingly, as expected, an observed 1σ gradient should never be considered evidence for real RM gradients.

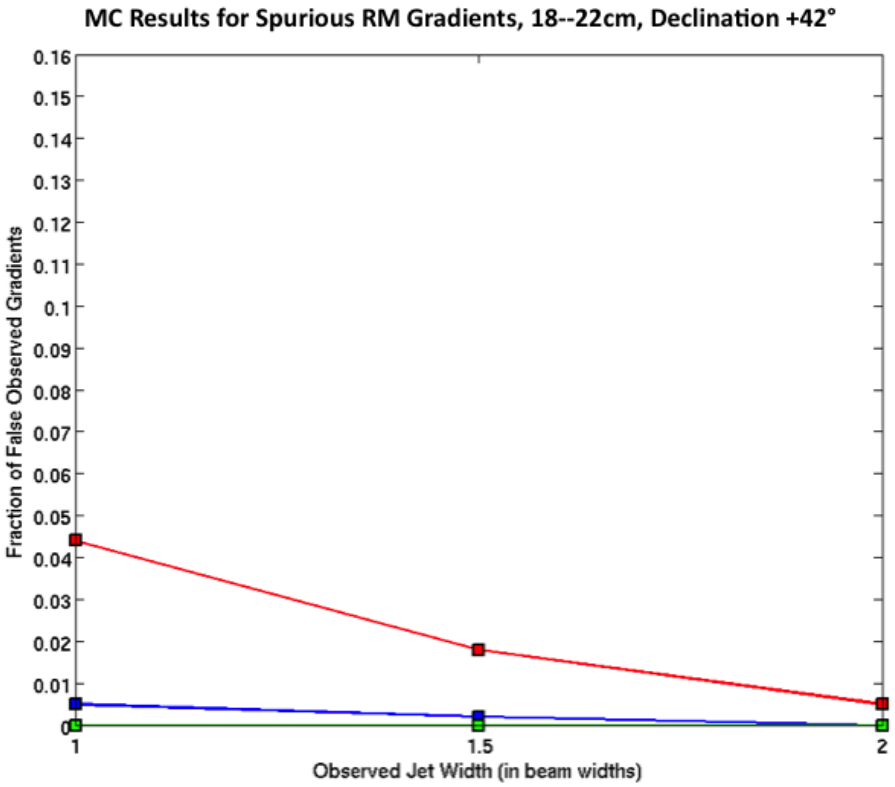

Figure 6.1: Fraction of spuriously detected RM gradients vs. observed jet width after convolution for 18 – 22 cm simulations (source at +42° declination). Red, blue and green lines correspond to fraction of 2σ, 3σ and 4σ detections respectively.

6.2 Additional Frequencies

As demonstrated in Section 6.1 the percentage of observed spurious gradients is highest for the wavelength range of 1.9 cm, 2.5 cm, 3.4 cm and 3.8 cm due to the lower sensitivity to Faraday rotation at these wavelengths. However, the observations on which these simulations were based were actually carried out at six wavelengths: the four indicated, plus two near 6 cm. Therefore, it is possible to include 2 additional wavelengths into this Monte Carlo analysis in order to investigate how additional wavelengths can enhance the sensitivity of the observations to Faraday rotation and reduce the number of spurious RM gradients observed.

Figure 6.4 shows the results of including these two additional wavelengths (5.9 cm and 6.5 cm) in the Monte Carlo analysis of spurious gradients. This figure clearly demonstrates that, in all cases, the addition of these additional 2 wavelengths (and the resulting increase in the wavelength range) reduces the number of ob-

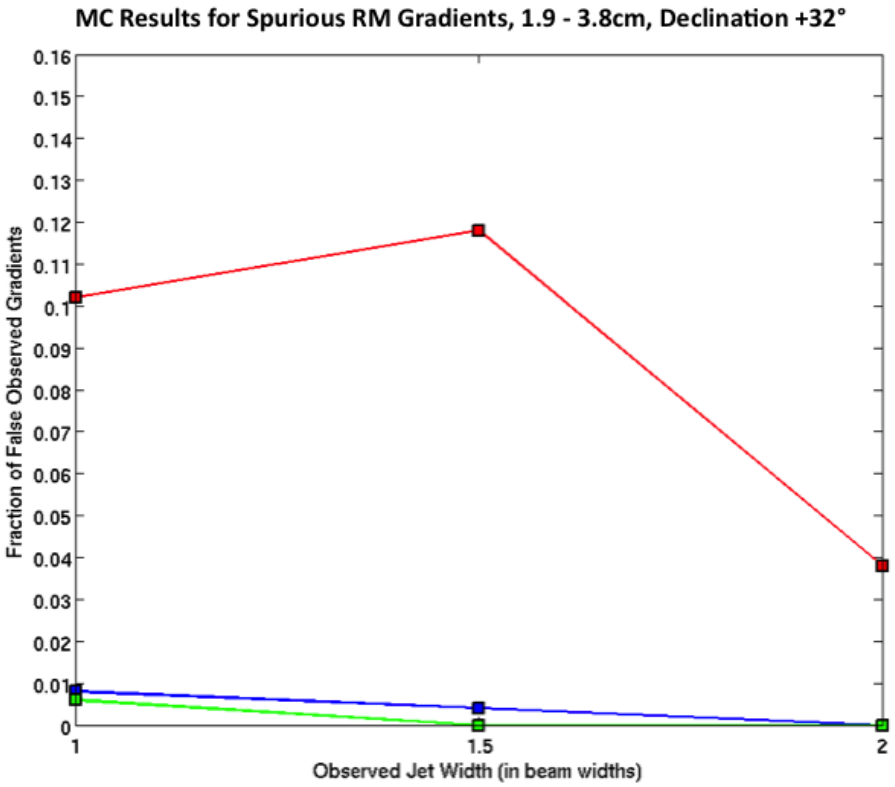

Figure 6.2: Fraction of spuriously detected RM gradients vs. observed jet width after convolution for 1.9 – 3.8 cm simulations (source at +32° declination). Red, blue and green lines correspond to fraction of 2σ, 3σ and 4σ detections respectively.

served spurious gradients. It is clear from these results that despite the lower sensitivity of these wavelengths to Faraday rotation, compared to the 18 – 22 cm observations, the additional wavelengths successfully mitigate the lower sensitivity. This is a very important result as Section 5.2.4 demonstrates that longer wavelength observations, while highly sensitive to Faraday rotation, are also far more susceptible to the effects of Faraday depolarization. Therefore, relatively short wavelength observations of AGN are a very important tool in investigating RM gradients despite their lower sensitivity to Faraday rotation, which can be offset by increasing the number of wavelengths and the wavelength range used in observations.

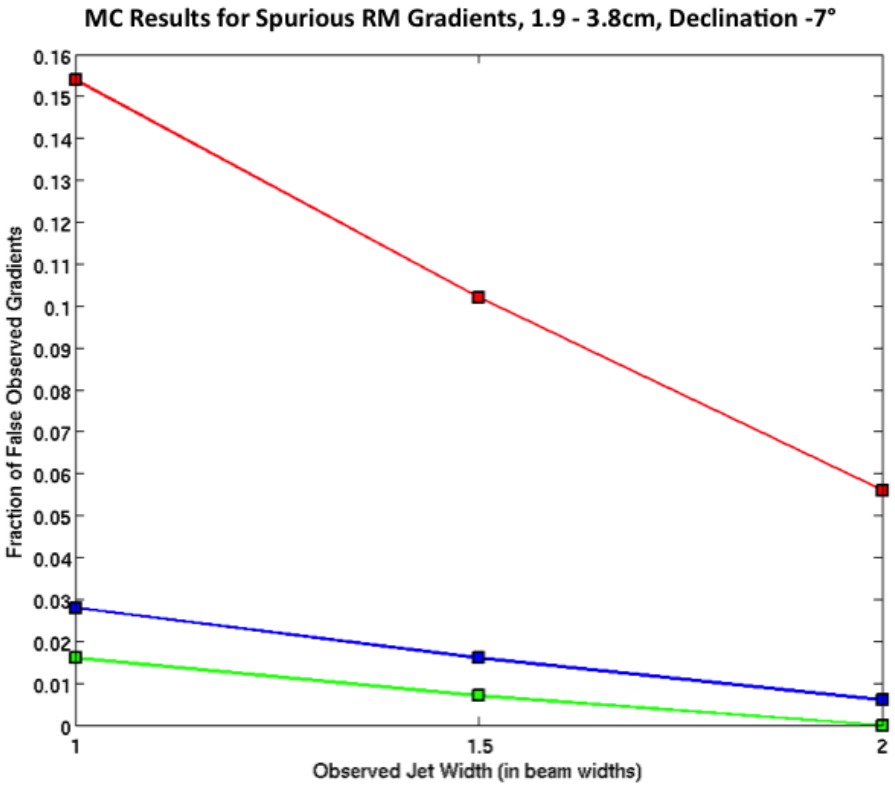

Figure 6.3: Fraction of spuriously detected RM gradients vs. observed jet width after convolution for 1.9 – 3.8 cm simulations (source at −7° declination). Red, blue and green lines correspond to fraction of 2σ, 3σ and 4σ detections respectively.

6.3 Comparison to Hovatta et al. & Algaba

Hovatta et al. (2012) also used Monte Carlo simulations to investigate the effects of finite resolution on the visibility of spurious RM gradients. However, rather than using an artificial model source as was used in the simulations described in previous sections, they used existing AGN jets in their simulations as follows

1. A total intensity map of a real source was created using calibrated UV data, in the Difmap software.
2. Stokes Q and U model maps were created by setting Q and U as fractions of Stokes I resulting in a uniform fractional polarization and EVPA across the source.
3. The original calibrated data file was loaded into NRAO's AIPS and the task UVMOD was used to replace the real data with the values produced in step 2. Normally distributed normal noise was also added at this step.

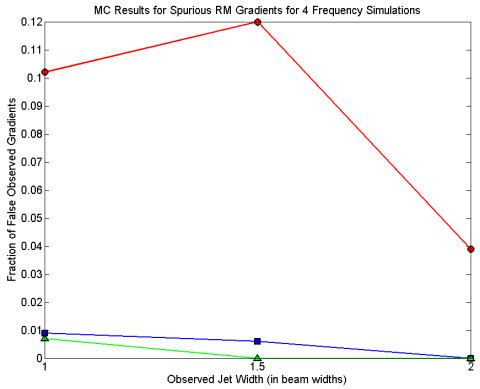

(a) 4 wavelengths at +35° declination

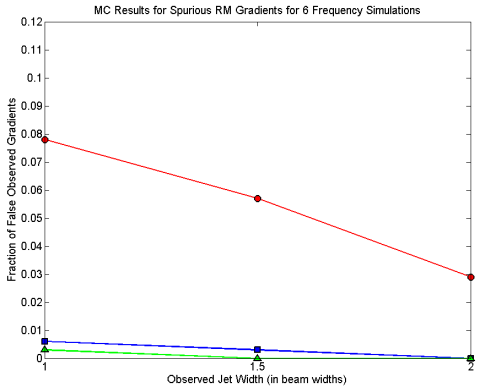

(b) 6 wavelengths at +35° declination

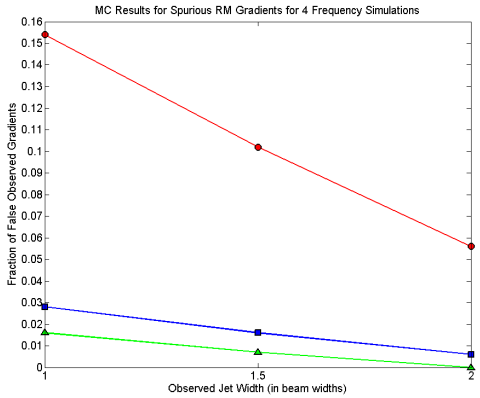

(c) 4 wavelengths at −7° declination

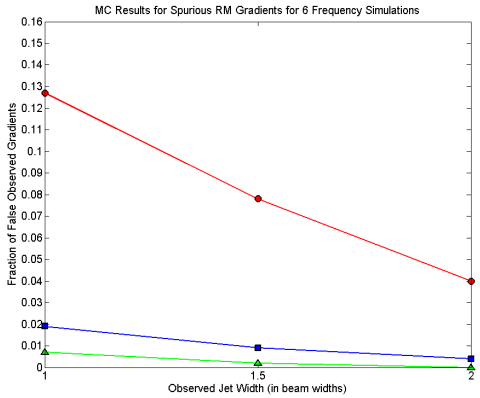

(d) 6 wavelengths at −7° declination

Figure 6.4: Results for Monte Carlo simulations to evaluate the reduction in observed spurious RM gradients when wavelength range is increased. Observed wavelengths are 1.9 cm, 2.5 cm, 3.4 cm and 3.8 cm on the left and 1.9 cm, 2.5 cm, 3.4 cm, 3.8 cm, 5.9 cm and 6.5 cm on the right. In all cases increasing the total number of wavelengths and wavelength range reduced the number of observed spurious RM gradients.

4. Step 3 was repeated to produce 100 simulated UV datasets. These datasets were then exported from AIPS and imaged in Difmap to be used in the analysis.

The main difference between this method and the method used in this thesis is that Hovatta et al. (2012) were restricted to only examining existing jets. Therefore, they had very little control over the jet widths of the sources they used in their analysis and they had no knowledge of the intrinsic jet width of their sources. The individual transverse gradients examined also featured multiple different UV distributions making it difficult to know whether the spurious gradients observed at a certain jet width were due to the jet width or due to poor

UV coverage. In addition, rather than examining the difference in RM between edge pixels Hovatta et al. (2012) fitted a simple line to the transverse profiles and then looked at the distributions of the slopes in order to determine the maximum spurious gradient in rad m^{-2} mas^{-1}. While both methods can successfully detect spurious gradients, spurious gradients detected using one method may, rarely, not be observed using the other method. This difference could, therefore, explain any minor disparities between the results.

Figure 6.5 shows the results of Hovatta et al (2012). Despite the different approach to running their Monte Carlo simulations their results are very similar to those found in this thesis. Spurious 4σ gradients were not observed while 3σ spurious gradients were observed in only $\sim 2\%$ of cases for the narrowest jet width (1.5 beam widths) 2σ spurious gradients were observed in $\sim 7\%$ of cases for the narrowest jet width. Accordingly, these results agree with the results in Section 6.1 in that 3σ spurious gradients are so rarely observed that they can be used as positive identifiers of Faraday RM gradients for observed jet widths appreciably narrower than 3 beam widths. In addition, the possibility of an observed 2σ RM gradient being real is appreciable for jet widths larger than ~ 2 beam widths. Spurious 1σ gradients were observed less often in these results. This disparity is possibly due to the difference in detecting RM gradients.

Algaba (2013) used the same method used by Hovatta et. al to investigate the detection of spurious RM gradients due to poor resolution. However, unlike Hovatta et al. (2012) and the simulations presented in this thesis, Algaba (2013) did not require transverse RM profiles to be monotonic when performing the Monte Carlo simulations. Figure 6.6 shows the results of these simulations, which are similar to those found in this thesis and by Hovatta et al. (2012). In general, the results show a higher fraction of observed spurious gradients at the narrowest jet widths. This difference is, most likely, due to not requiring spurious gradients to be monotonic as, in doing so, transverse RM gradients which would not normally be considered as real are included in the results. Nevertheless, for jets of more than 1.5 beam widths the results are in agreement with those found in this thesis. At 1.5 beam widths, spurious 3σ gradients are observed in only $\sim 1\%$ of cases while spurious 2σ gradients are observed in only $\sim 5\%$ of cases. These results also demonstrate that 3σ RM gradients can be used as identifiers of real structured magnetic fields even for observed jet widths appreciably narrower than 3 beam widths. In addition, and in agreement with Hovatta et al. (2012) and the work carried out in this thesis, these results show that 2σ gradients should not be immediately dismissed for jet widths larger than 1.5 beam widths and should

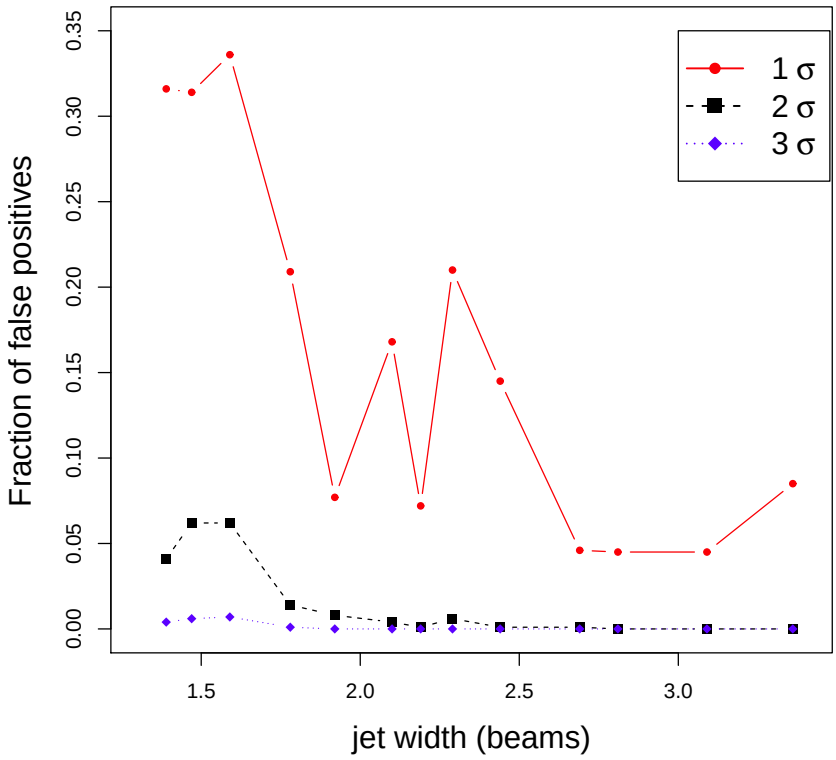

Figure 6.5: Fraction of total gradients vs. slice width from the Monte Carlo simulations of Hovatta et al. (2012) exceeding 1σ (red), 2σ (black) or 3σ (blue).

be taken as tentative evidence for real RM gradients which should be confirmed with further analysis.

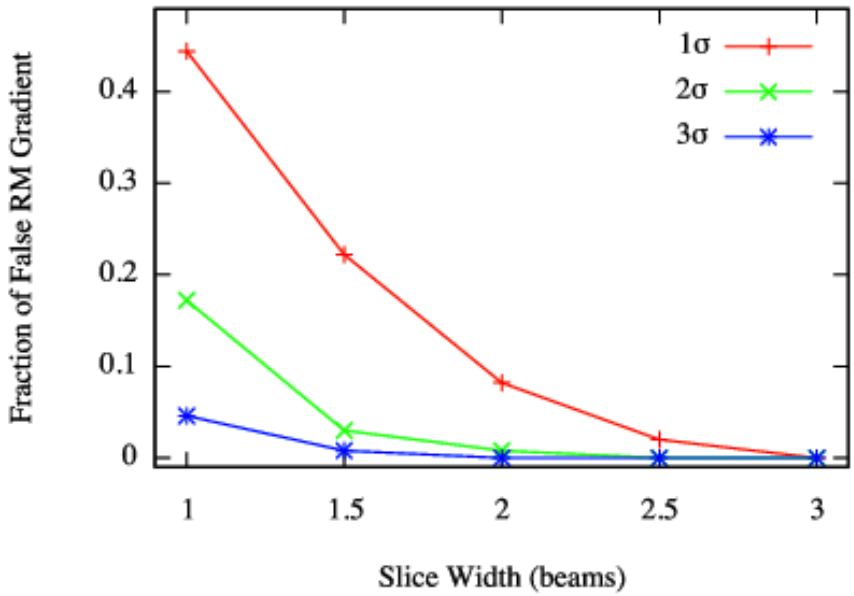

Figure 6.6: Fraction of total gradients vs. slice width from the Monte Carlo simulations of Algaba (2013) exceeding 1σ (red), 2σ (green) or 3σ (blue).

Chapter 7

Conclusions

This thesis investigates various methods of analysing the transverse structure of AGN jets.

The first is a method for comparing model and data transverse profiles for total intensity and polarization in astrophysical jets. Although broadly similar to the analyses carried out by Papageorgiou (2005), the approach used here represents a substantial improvement, in particular through the compilation of databases of model profiles to use in fitting the observed profiles. The method has been used to compare observed profiles of the parsec-scale jet of Markarian 501 and the kiloparsec scale jet of M87 with the predictions of a model in which a cylindrical jet is permeated by a magnetic field with a uniform helical component and a disordered component.

The jet of Markarian 501 shows several characteristics that are consistent with a helical jet magnetic field, most strikingly a region of spine–sheath transverse polarization structure. The best model fits obtained correspond to pitch angles in the jet rest frame $\gamma' \simeq 40 - 50°$ and viewing angles in the jet rest frame $\delta' \simeq 83°$. These fits describe the polarization structure well, though the total intensity fits are generally poorer. However, given the extremely simple nature of the helical-field model, for example its rigid cylindrical symmetry and uniformity of emission, its success in reproducing the general features of the Q profiles is noteworthy.

The best fit values of the line-of-sight angle are very similar for all the analysed 4 cm, 6 cm, 13 cm and 18 cm slices across the Markarian 501 jet, within the estimated 1σ uncertainties (apart from the fitted viewing angle for the somewhat more uncertain third slice, which differs from the other values by $2 - 3\sigma$). This indicates that, as expected, the large apparent changes in jet direction are in fact

very small bends that are greatly amplified by projection. The fitted pitch angle increases from the first to the second 6 cm slice, bringing about the observed transition in polarization structure. The fraction of energy in the disordered magnetic-field component seems to decrease with distance along the jet.

A new method for deriving the velocity and viewing angle of the jet in the observer's frame has been developed. Together with the tentative superluminal speed reported by Piner et al. (2009), $\beta_{app} \simeq 3.3$, the estimate for the viewing angle in the jet rest frame obtained through the profile fitting, $\delta' \simeq 83°$, enables determination of the viewing angle and jet velocity in the observer's frame, $\delta \approx 15°$ and $\beta \approx 0.96$. Although these values are somewhat uncertain in the case of Markarian 501, since this superluminal velocity was determined for a weak feature whose position is only poorly defined, the joint analysis of transverse polarization profiles and apparent superluminal speeds provides a new tool for disentangling δ and β. The jet of Markarian 501 must be fairly close to the line of sight, yet carrying out this analysis for the typically subluminal speeds observed in the Markarian 501 VLBI jet yields viewing angles of about 60°; this essentially demonstrates that these subluminal motions must represent pattern speeds in a much more highly relativistic flow, rather than highly relativistic motion viewed at a very small angle.

The kiloparsec jet of M87 also shows several characteristics which are consistent with a helical magnetic field. The Faraday RM map of Algaba et al. (2013) demonstrates consistent RM gradients through the extended jet of M87. The best model fits obtained correspond to pitch angles in the jet rest frame $\gamma' \simeq 33 - 40°$ and viewing angles in the jet rest frame $\delta' \simeq 72°$. As for Markarian 501, these fits describe the polarization structure well while poorly representing the total intensity profiles. The best fit values of the line-of-sight angle are very similar for all the analysed 1.36 cm, 2 cm and 2.75 cm slices across the Markarian 501 jet, mostly well within the estimated 1σ uncertainties.

Superluminal speed and viewing angles in the rest frame of the jet reported by Wang et al. (2008) allowed for comparison between these estimates of the jet Lorentz factor Γ and viewing angle δ obtained from our estimate of the viewing angle in the jet rest frame and values determined using other methods. Despite the simple nature of the helical-field model used the value for Γ (1.21 ± 0.04) is in agreement with that determined by Wang et al. (2008) $(1.45 \pm .40)$. The determined value of δ $(38° \pm 4°)$ is larger than the value calculated by Wang et' al. (2008) $(14.9° \pm 15.1°)$ but still lies within 1.5σ of Wang's value. The derived

values of γ' and δ' results in the Faraday rotation measures on the northern side of the jet to be larger in magnitude than those on the southern side by 56%. This strongly agrees with the RM map of Algaba et al. (2013) in which the RM values of the northern side of the jet are $\sim 50\%$ larger than the RM values of the southern side in the region investigated here.

Calculation of I and Q profiles for the helical-field model is greatly simplified if the spectral index α is assumed to be unity. Whilst this is almost certainly incorrect (observed values are usually $\simeq 0.5$) the assumption that $\alpha = 1$ has been shown to have very little impact on the profiles, and hence on the values of the best-fit model parameters.

The results demonstrate that this method provides a new approach to studying the magnetic fields in parsec-scale jets.

The second method outlined in this thesis utilises Monte Carlo simulations to investigate the effects of resolution on observed transverse RM gradients. Monte Carlo simulations of cylindrical jet-like structures were carried out to investigate the effects of 3 key jet parameters on the detection of observing RM gradients: intrinsic jet width, polarized flux and intrinsic RM range, for simulated multi-wavelength observations at 18 – 22 cm (declination +42°) and 1.9 – 3.8 cm (declinations +32° and −7°). These simulations show that 3σ RM gradients remain clearly visible for model jets with reasonable levels of polarized flux and intrinsic jet widths substantially smaller than the beam width, though the actual RM values are suppressed by convolution.

Further Monte Carlo simulations were performed to directly investigate the statistics of observing spurious RM gradients. 4σ RM gradients were observed extremely rarely for these simulations and only for jet widths which were one beam width across. We propose that any observed 4 σ RM gradient should be carefully considered regardless of resolution, as the chance of such a gradient being spurious is at most 1.8% for an intrinsic jet width of only 1% the beam width (for the 1.9 – 3.8 cm observation at −7° declination). Spurious RM gradients at the 3σ level occurred in less than 1% of our simulations using model data without RM gradients in our 18 cm – 22 cm observations, even in the case of very narrow jets (intrinsic jet widths of 0.01 beam width). While the 1.9 – 3.8 cm was less sensitive to Faraday rotation, 3σ spurious gradients were observed in at most 3% of cases (for the −7° declination). Including an additional 2 wavelengths (extending the wavelength range to 1.9 – 6.5 cm) to these simulations reduced the probability of observing 3σ spurious gradients to $\sim 2\%$ and 4σ spurious gradients to $\sim 0.8\%$ for

this declination. Thus, we propose that in the absence of other grounds for doubt (e.g. poor RM fits), monotonic transverse RM gradients spanning RM differences of 3σ or more can be considered reliable, even if the transverse distance spanned is comparable to the beam width. These results are broadly consistent with the results of Hovatta et al. (2012) and Algaba (2013), but substantially extend those results.

The three beam width criterion of Taylor and Zavala (2010) was intended to ensure that observed transverse RM gradients were sufficiently well resolved. However, our demonstration that transverse RM gradients can be detected even when the transverse structure is poorly resolved (intrinsic jet width much less than a beam width) shows that such a criteria is not justified or meaningful. The proposed three beam width criterion is, therefore, too severe. Observed RM gradients should not be dismissed based on their observed width. Instead, their reliability should be estimated based on the RM difference across the jet ($\geq 3\sigma$ for narrow jets and potentially $\geq 2\sigma$ for observed jet widths larger then 2 beam widths), the extent of the RM gradient along the jet, the percentage polarization, the quality of the RM fits and the possibility of distortion by optical depth effects.

Depending on the observed wavelength, Faraday depolarization can significantly reduce the observed percentage polarization which has a large effect on the visibility of RM gradients. Future observations being scheduled in order to observe Faraday Rotation should try to include relatively short radio wavelengths in addition to longer wavelengths. While the observed rotation of the polarization angle χ will be much smaller for these shorter wavelengths, the higher levels of polarized flux may make RM gradients easier to reliably detect.

Mahmud et al. (2013) reported that the 2 – 6 cm Faraday rotation image of the AGN 0716+714 displayed two oppositely directed transverse RM gradients in the core region and inner jet. Monte Carlo simulations of model jets with reversing transverse RM gradients show that the RM reversals introduced into the simulated data are visible in the "noisy" model RM maps that were produced, even when the intrinsic width of the jet is only about 1/20 of the beam width. This demonstrates that relative complex RM structures such as a reversing transverse gradient can also plausibly be reliably detected in real RM maps.

The methods used in these Monte Carlo simulations are not restricted to the study of transverse RM gradients. Using the method outlined and the code given in Appendix A any type of model source can be imaged using the UV distribution of any existing VLBI observation (not restricted to just the VLBA). This allows

for any theoretical model to be imaged in such a way as to determine if the model predictions could be reliably detected using VLBI observations. It also allows for imaged sources to be compared to their infinite resolution model sources in order to investigate any systematic errors introduced by the imaging process.

Bibliography

Achterberg, A., Ackermann, M., Adams, J., Ahrens, J., Atlee, D., Bahcall, J., Bai, X., Baret, B., Bartelt, M., Barwick, S., Bay, R., Beattie, K., Becka, T., Becker, J., Becker, K.-H., Berghaus, P., Berley, D., Bernardini, E., Bertrand, D., Besson, D., Blaufuss, E., Boersma, D., Bohm, C., Böser, S., Botner, O., Bouchta, A., Braun, J., Burgess, C., Burgess, T., Castermans, T., Chirkin, D., Clem, J., Collin, B., Conrad, J., Cooley, J., Cowen, D., D'Agostino, M., Davour, A., Day, C., De Clercq, C., Desiati, P., DeYoung, T., Dreyer, J., Duvoort, M., Edwards, W., Ehrlich, R., Ellsworth, R., Evenson, P., Fazely, A., Feser, T., Filimonov, K., Gaisser, T., Gallagher, J., Ganugapati, R., Geenen, H., Gerhardt, L., Goldschmidt, A., Goodman, J., Greene, M., Grullon, S., Groß, A., Gunasingha, R., Hallgren, A., Halzen, F., Han, K., Hanson, K., Hardtke, D., Hardtke, R., Harenberg, T., Hart, J., Hauschildt, T., Hays, D., Heise, J., Helbing, K., Hellwig, M., Herquet, P., Hill, G., Hodges, J., Hoffman, K., Hoshina, K., Hubert, D., Hughey, B., Hulth, P., Hultqvist, K., Hundertmark, S., Ishihara, A., Jacobsen, J., Japaridze, G., Jones, A., Joseph, J., Kampert, K.-H., Karle, A., Kawai, H., Kelley, J., Kestel, M., Kitamura, N., Klein, S., Klepser, S., Kohnen, G., Kolanoski, H., Köpke, L., Krasberg, M., Kuehn, K., Landsman, H., Lang, R., Leich, H., Leuthold, M., Liubarsky, I., Lundberg, J., Madsen, J., Mase, K., Matis, H., McCauley, T., McParland, C., Meli, A., Messarius, T., Mészáros, P., Minor, R., Miočinović, P., Miyamoto, H., Mokhtarani, A., Montaruli, T., Morey, A., Morse, R., Movit, S., Münich, K., Nahnhauer, R., Nam, J., Nieß en, P., Nygren, D., Ögelman, H., Olbrechts, P., Olivas, A., Patton, S., Peña Garay, C., Pérez de los Heros, C., Pieloth, D., Pohl, A., Porrata, R., Pretz, J., Price, P., Przybylski, G., Rawlins, K., Razzaque, S., Refflinghaus, F., Resconi, E., Rhode, W., Ribordy, M., Richter, S., Rizzo, A., Robbins, S., Rott, C., Rutledge, D., Sander, H.-G., Schlenstedt, S., Schneider, D., Seckel, D., Seo, S., Seunarine, S., Silvestri, A., Smith, A., Solarz, M., Song, C., Sopher, J., Spiczak, G., Spiering, C., Stamatikos, M.,

Stanev, T., Steffen, P., Steele, D., Stezelberger, T., Stokstad, R., Stoufer, M., Stoyanov, S., Sulanke, K.-H., Sullivan, G., Sumner, T., Taboada, I., Tarasova, O., Tepe, A., Thollander, L., Tilav, S., Toale, P., Turčan, D., van Eijndhoven, N., Vandenbroucke, J., Voigt, B., Wagner, W., Walck, C., Waldmann, H., Walter, M., Wang, Y.-R., Wendt, C., Wiebusch, C., Wikström, G., Williams, D., Wischnewski, R., Wissing, H., Woschnagg, K., Xu, X., Yodh, G., Yoshida, S., Zornoza, J., & Biermann, P. 2006, Astroparticle Physics, 26, 282

Algaba, J., Asada, K., & Nakamura, M. 2013a, eprint arXiv:1308.5429

Algaba, J. C. 2013, Monthly Notices of the Royal Astronomical Society, 429, 3551

Algaba, J. C., Asada, K., & Nakamura, M. 2013b

Antonucci, R. 1993, Annual Review of Astronomy and Astrophysics, 31, 473

Asada, K., Inoue, M., Kameno, S., & Nagai, H. 2008a, The Astrophysical Journal, 675, 79

Asada, K., Inoue, M., Nakamura, M., Kameno, S., & Nagai, H. 2008b, The Astrophysical Journal, 682, 798

Asada, K., Nakamura, M., Inoue, M., Kameno, S., & Nagai, H. 2010, The Astrophysical Journal, 720, 41

Asada, Keiichi, Inoue, Makoto, Uchida, Yutaka, Kameno, Seiji, Fujisawa, Kenta, Iguchi, Satoru, & Mutoh, Mutsumi. 2002, Publications of the Astronomical Society of Japan

Balbus, S. & Hawley, J. 1998, Reviews of Modern Physics, 70, 1

Baum, S. A., Zirbel, E. L., & O'Dea, C. P. 1995, The Astrophysical Journal, 451, 88

Begelman, M., Blandford, R., & Rees, M. 1984, Reviews of Modern Physics, 56, 255

Binggeli, B., Tammann, G. A., & Sandage, A. 1987, The Astronomical Journal, 94, 251

Bird, S., Harris, W. E., Blakeslee, J. P., & Flynn, C. 2010

Biretta, J. A., Sparks, W. B., & Macchetto, F. 1999, The Astrophysical Journal, 520, 621

Blandford, R. D., McKee, C. F., & Rees, M. J. 1977a, Nature, 267, 211

—. 1977b, Nature, 267, 211

Blandford, R. D. & Znajek, R. L. 1977, Monthly Notices of the Royal Astronomical Society, 179, 433

Bridle, A. H. 1984, The Astronomical Journal, 89, 979

Broderick, A. E. & McKinney, J. C. 2010, The Astrophysical Journal, 725, 750

Canvin, J. R., Laing, R. A., Bridle, A. H., & Cotton, W. D. 2005, Monthly Notices of the Royal Astronomical Society, 363, 1223

Cawthorne, T. V. & Cobb, W. K. 1990, The Astrophysical Journal, 350, 536

Cawthorne, T. V., Jorstad, S. G., & Marscher, A. P. 2013, The Astrophysical Journal, 772, 14

Cawthorne, T. V., Wardle, J. F. C., Roberts, D. H., Gabuzda, D. C., & Brown, L. F. 1993, The Astrophysical Journal, 416, 496

Clausen-Brown, E., Lyutikov, M., & Kharb, P. 2011, Monthly Notices of the Royal Astronomical Society, 415, 2081

Contopoulos, I., Christodoulou, D. M., Kazanas, D., & Gabuzda, D. C. 2009, The Astrophysical Journal, 702, L148

Contopoulos, I. & Kazanas, D. 1998, The Astrophysical Journal, 508, 859

Coughlan, C., Murphy, R., McEnery, K., Patrick, H., Hallahan, R., & Gabuzda, D. 2010, "Proceedings of the 10th European VLBI Network Symposium and EVN Users Meeting: VLBI and the new generation of radio arrays. September 20-24

Croke, S. M., O'Sullivan, S. P., & Gabuzda, D. C. 2010, Monthly Notices of the Royal Astronomical Society, 402, 259

Falcke, H., Wilson, A. S., & Simpson, C. 1998, The Astrophysical Journal, 502, 199

Fanaroff, B. L. & Riley, J. M. 1974, Monthly Notices of the Royal Astronomical Society, 167

Fender, R. P., Belloni, T. M., & Gallo, E. 2004, Monthly Notices of the Royal Astronomical Society, 355, 1105

Gabuzda, D. C., Cantwell, T., & Cawthorne, T. V. 2013, MNRAS, in press

Gabuzda, D. C. & Cawthorne, T. V. 1996, Monthly Notices of the Royal Astronomical Society, 283, 759

Gabuzda, D. C., Cawthorne, T. V., Roberts, D. H., & Wardle, J. F. C. 1992, The Astrophysical Journal, 388, 40

Gabuzda, D. C., Murray, E., & Cronin, P. 2004, Monthly Notices of the Royal Astronomical Society, 351, L89

Gabuzda, D. C., Vitrishchak, V. M., Mahmud, M., & O'Sullivan, S. P. 2008, Monthly Notices of the Royal Astronomical Society, 384, 1003

Ginzburg, V. L. & Syrovatskii, S. I. 1968, Astrophysics and Space Science, 1, 442

Giroletti, M., Giovannini, G., Cotton, W. D., Taylor, G. B., Pérez-Torres, M. A., Chiaberge, M., & Edwards, P. G. 2008, Astronomy and Astrophysics, 488, 905

Giroletti, M., Giovannini, G., Feretti, L., Cotton, W. D., Edwards, P. G., Lara, L., Marscher, A. P., Mattox, J. R., Piner, B. G., & Venturi, T. 2004, The Astrophysical Journal, 600, 127

Hardcastle, M. J., Birkinshaw, M., Cameron, R. A., Harris, D. E., Looney, L. W., & Worrall, D. M. 2002

Högbom, J. A. 1974, Astronomy and Astrophysics Supplement, 15

Hovatta, T., Lister, M. L., Aller, M. F., Aller, H. D., Homan, D. C., Kovalev, Y. Y., Pushkarev, A. B., & Savolainen, T. 2012, The Astronomical Journal, 144, 105

Hutchison, J. M., Cawthorne, T. V., & Gabuzda, D. C. 2001, Monthly Notices of the Royal Astronomical Society, 321, 525

Kardashev, N. S., Khartov, V. V., Abramov, V. V., Avdeev, V. Y., Alakoz, A. V., Aleksandrov, Y. A., Ananthakrishnan, S., Andreyanov, V. V., Andrianov, A. S., Antonov, N. M., Artyukhov, M. I., Arkhipov, M. Y., Baan, W., Babakin, N. G., Babyshkin, V. E., Bartel', N., Belousov, K. G., Belyaev, A. A., Berulis, J. J., Burke, B. F., Biryukov, A. V., Bubnov, A. E., Burgin, M. S., Busca, G., Bykadorov, A. A., Bychkova, V. S., Vasil'kov, V. I., Wellington, K. J., Vinogradov, I. S., Wietfeldt, R., Voitsik, P. A., Gvamichava, A. S., Girin, I. A., Gurvits, L. I., Dagkesamanskii, R. D., D'Addario, L., Giovannini, G., Jauncey, D. L., Dewdney, P. E., D'yakov, A. A., Zharov, V. E., Zhuravlev, V. I., Zaslavskii, G. S., Zakhvatkin, M. V., Zinov'ev, A. N., Ilinen, Y., Ipatov, A. V., Kanevskii, B. Z., Knorin, I. A., Casse, J. L., Kellermann, K. I., Kovalev,

Y. A., Kovalev, Y. Y., Kovalenko, A. V., Kogan, B. L., Komaev, R. V., Konovalenko, A. A., Kopelyanskii, G. D., Korneev, Y. A., Kostenko, V. I., Kotik, A. N., Kreisman, B. B., Kukushkin, A. Y., Kulishenko, V. F., Cooper, D. N., Kut'kin, A. M., Cannon, W. H., Larionov, M. G., Lisakov, M. M., Litvinenko, L. N., Likhachev, S. F., Likhacheva, L. N., Lobanov, A. P., Logvinenko, S. V., Langston, G., McCracken, K., Medvedev, S. Y., Melekhin, M. V., Menderov, A. V., Murphy, D. W., Mizyakina, T. A., Mozgovoi, Y. V., Nikolaev, N. Y., Novikov, B. S., Novikov, I. D., Oreshko, V. V., Pavlenko, Y. K., Pashchenko, I. N., Ponomarev, Y. N., Popov, M. V., Pravin-Kumar, A., Preston, R. A., Pyshnov, V. N., Rakhimov, I. A., Rozhkov, V. M., Romney, J. D., Rocha, P., Rudakov, V. A., Räisänen, A., Sazankov, S. V., Sakharov, B. A., Semenov, S. K., Serebrennikov, V. A., Schilizzi, R. T., Skulachev, D. P., Slysh, V. I., Smirnov, A. I., Smith, J. G., Soglasnov, V. A., Sokolovskii, K. V., Sondaar, L. H., Stepan'yants, V. A., Turygin, M. S., Turygin, S. Y., Tuchin, A. G., Urpo, S., Fedorchuk, S. D., Finkel'shtein, A. M., Fomalont, E. B., Fejes, I., Fomina, A. N., Khapin, Y. B., Tsarevskii, G. S., Zensus, J. A., Chuprikov, A. A., Shatskaya, M. V., Shapirovskaya, N. Y., Sheikhet, A. I., Shirshakov, A. E., Schmidt, A., Shnyreva, L. A., Shpilevskii, V. V., Ekers, R. D., & Yakimov, V. E. 2013, Astronomy Reports, 57, 153

Laing, R. A. 1981, The Astrophysical Journal, 248, 87

Laing, R. A., Bridle, A. H., Parma, P., Feretti, L., Giovannini, G., Murgia, M., & Perley, R. A. 2008, Monthly Notices of the Royal Astronomical Society, 386, 657

Laing, R. A., Canvin, J. R., & Bridle, A. H. 2006a, Astronomische Nachrichten, 327, 523

—. 2006b, Astronomische Nachrichten, 327, 523

Laing, R. A., Canvin, J. R., Bridle, A. H., & Hardcastle, M. J. 2006c, Monthly Notices of the Royal Astronomical Society, 372, 510

Laing, R. A. 1996, Energy transport in radio galaxies and quasars Astronomical Society of the Pacific Conference Series, 100

Lister, M. L. & Homan, D. C. 2005, The Astronomical Journal, 130, 1389

Lobanov, A. P. 1998, Astronomy and Astrophysics Supplement Series, 132, 261

Lynden-Bell, D. 1996, Monthly Notices of the Royal Astronomical Society, 279, 389

Mahmud, M., Coughlan, C. P., Murphy, E., Gabuzda, D. C., & Hallahan, D. R. 2013, Monthly Notices of the Royal Astronomical Society, 431, 695

Mahmud, M., Gabuzda, D. C., & Bezrukovs, V. 2009, Monthly Notices of the Royal Astronomical Society, 400, 2

Markarian, B., Lipovetsky, V., Stepanian, J., Erastova, L., & Shapovalova, A. 1989, Soobshcheniya Spetsial'noj Astrofizicheskoj Observatorii

Marscher, A. P. 2006, in AIP Conference Proceedings, Vol. 856 (AIP), 1–22

Marscher, A. P., Jorstad, S. G., Gomez, J. L., McHardy, I. M., Krichbaum, T. P., & Agudo, I. 2007, The Astrophysical Journal, 665, 232

Murphy, E., Cawthorne, T. V., & Gabuzda, D. C. 2013, Monthly Notices of the Royal Astronomical Society, 430, 1504

Nakamura, M., Li, H., & Li, S. 2006, The Astrophysical Journal, 652, 1059

Owen, F. N., Eilek, J. A., & Keel, W. C. 1990, The Astrophysical Journal, 362, 449

Owen, F. N., Hardee, P. E., & Cornwell, T. J. 1989, The Astrophysical Journal, 340, 698

Papageorgiou, A. 2005, PhD thesis, University of Central Lancashire

Perlman, E. S., Biretta, J. A., Zhou, F., Sparks, W. B., & Macchetto, F. D. 1999, The Astronomical Journal, 117, 2185

Peterson, B. M. 1997a, An Introduction to Active Galactic Nuclei (Cambridge University Press), 256

—. 1997b, An Introduction to Active Galactic Nuclei (Cambridge University Press), 238

Piner, B. G., Pant, N., & Edwards, P. G. 2010a, The Astrophysical Journal, 723, 1150

—. 2010b, The Astrophysical Journal, 723, 1150

Piner, B. G., Pant, N., Edwards, P. G., & Wiik, K. 2009, The Astrophysical Journal, 690, L31

Pushkarev, A. B., Gabuzda, D. C., Vetukhnovskaya, Y. N., & Yakimov, V. E. 2005, Monthly Notices of the Royal Astronomical Society, 356, 859

Reichstein, A. 2012, PhD thesis, University College Cork

Rusk, R. 1988, PhD thesis, University of Toronto

Ruszkowski, M. & Begelman, M. C. 2002, The Astrophysical Journal, 573, 485

Rybicki, G. B. & Lightman, A. P. 2008, Radiative Processes in Astrophysics (Google eBook) (John Wiley & Sons), 400

Schmidt, M. 1963, Nature, 197, 1040

Taylor, A. R., Stil, J. M., & Sunstrum, C. 2009, The Astrophysical Journal, 702, 1230

Taylor, G. B. & Zavala, R. 2010, The Astrophysical Journal, 722, L183

Thompson, A. R., Moran, J. M., & Jr., G. W. S. 2001, Interferometry and Synthesis in Radio Astronomy (Wiley-VCH), 715

Tsvetanov, Z. I., Hartig, G. F., Ford, H. C., Dopita, M. A., Kriss, G. A., Pei, Y. C., Dressel, L. L., & Harms, R. J. 1998, The Astrophysical Journal, 493, L83

Urry, C. 2003, American Astronomical Society Meeting 202, 35

Urry, C. M. & Padovani, P. 1995, Publications of the Astronomical Society of the Pacific, 107, 803

Véron-Cetty, M.-P. & Véron, P. 2010, Astronomy and Astrophysics, 518, A10

Vitrishchak, V. M., Gabuzda, D. C., Algaba, J. C., Rastorgueva, E. A., O'Sullivan, S. P., & O'Dowd, A. 2008, Monthly Notices of the Royal Astronomical Society, 391, 124

Wang, C.-C. & Zhou, H.-Y. 2009, Monthly Notices of the Royal Astronomical Society, 395, 301

Wardle, J., Homan, D., Ojha, R., & Roberts, D. 1998, Nature, 395, 457

Appendix A

CASA Code

This appendix includes the python scripts used with CASA in order to complete the Monte Carlo Simulations. All the programs described in this appendix will eventually be made available for download at `http://physics.ucc.ie/radiogroup/index.html`.

The Monte Carlo Simulations were completed as follows.

1. Model Source CSV files for Stokes I, Q & U were generated using a MATLAB script.
2. These model CSV files were used to replace the visibilites in an existing observation using Visibility Replacer (see A.1)
3. 200 Stokes Q and U maps were imaged for each frequency using Mapper (see A.2)
4. Each instance of Stokes Q and U maps where used to make RM maps using RM (see A.3)
5. The Sigma of multiple slices across each RM map was determined using Sigma Checker (see A.4)

A.0.1 Code Verification

In order to ensure that the python script used to replace the visibilites in an existing observation with model visibilities was functioning correctly the code was verified using the following procedure.

1. Multiple model sources of various shapes were produced.

2. These model sources were used to replace the visibilites in an existing observation using Visibility Replacer.
3. Stokes I maps were produced for each source and the beam parameters used by the CLEAN algorithm were noted down.
4. The original model sources were convolved with a beam described by the CLEAN beam parameters.
5. The post convolution model sources were subtracted from each of the cleaned maps resulting in difference maps.

   If the python code was working correctly any observed differences should have been very minor. This method of verification also allowed for a direct analysis of any systematic errors which may have arose due to the CLEAN algorithm.

   The RM code was verified by using it to produce RM maps of sources from data which had previously been used to produce RM maps using older RM code and ensuring that these maps were similar.

A.1 Visibility Replacer

This python script for CASA replaces the visibilities from an existing observation with those from a model source. This script can be run in CASA by executing the following

```
import Vis_Replacer
Vis_Replacer.Go(Wave,Factor,Total_Flux,Cellsize,NMap)
```

where

- Wave is the wavelength of the original observation.
- Factor is the percentage polarization required. 0.15 would correspond to 15% polarized flux.
- Total_Flux is the Total Flux in Jy of the model source.
- Cellsize is the cellsize you require. Changing this will change the model source size.

- NMap is the number of pixels you require (256, 512 etc). Changing this will also change the model source size.

The script this then executes can be seen below.

```
#  This program is called Vis_Replacer. It replaces the visibilities in
   ↪ a UV file with those from a model source in CASA.
#  Copyright (C) 2013 Eoin Murphy

#   This program is free software: you can redistribute it and/or modify
#   it under the terms of the GNU General Public License as published by
#   the Free Software Foundation, either version 3 of the License, or
#   (at your option) any later version.
#
#   This program is distributed in the hope that it will be useful,
#   but WITHOUT ANY WARRANTY; without even the implied warranty of
#   MERCHANTABILITY or FITNESS FOR A PARTICULAR PURPOSE. See the
#   GNU General Public License for more details.

#   You should have received a copy of the GNU General Public License
#   along with this program. If not, see <http://www.gnu.org/licenses/>.

import os
import time
import commands
import numpy
import sys
import scipy
from scipy import constants
from scipy import stats
from numpy.fft import *
import math
import csv
import warnings
from casa import table as tb

def ANT_to_Pixels(ANT_val="",Freq=""):
#Converts the UV locations given in the .MS Antenna Table to pixels

    ANT_val=ANT_val*(Freq*1E6)/constants.c
```

```
    return(ANT_val)

def Import_Maps(stem="",N="",Factor="",Total_Flux=""):
# Imports model source Stokes I, Q and U CSV files

    infilename=stem+"I.csv"

    if ( not os.path.exists( infilename ) ):
           raise Exception( "Error: file " + infilename + " does not
               ↪ exist " );

    try:
        infile = open(infilename, 'r')
    except IOError:
        print " Error: could not open file "+infilename
        sys.exit("Exiting program")

    lines = infile.readlines()

    IMap = scipy.zeros((N,N), dtype = float)

    for i in range(N):
        temp_str = lines[i].split(",")
        for j in range(N):
            IMap[i][j] = temp_str[j]

    infile.close()

    infilename=stem+"Q.csv"

    if ( not os.path.exists( infilename ) ):
           raise Exception( "Error: file " + infilename + " does not
               ↪ exist " );

    try:
        infile = open(infilename, 'r')
    except IOError:
        print " Error: could not open file "+infilename
        sys.exit("Exiting program")
```

```
lines = infile.readlines()

QMap = scipy.zeros((N,N), dtype = float)

for i in range(N):
    temp_str = lines[i].split(",")
    for j in range(N):
        QMap[i][j] = temp_str[j]

infile.close()

infilename=stem+"U.csv"

if ( not os.path.exists( infilename ) ):
        raise Exception( "Error: file " + infilename + " does not
            ↪ exist " );

try:
    infile = open(infilename, 'r')
except IOError:
    print " Error: could not open file "+infilename
    sys.exit("Exiting program")

lines = infile.readlines()

UMap = scipy.zeros((N,N), dtype = float)

for i in range(N):
    temp_str = lines[i].split(",")
    for j in range(N):
        UMap[i][j] = temp_str[j]

infile.close()

IMap=numpy.transpose(IMap)
QMap=numpy.transpose(QMap)
UMap=numpy.transpose(UMap)

div=numpy.sum(numpy.sum(IMap))
```

```
    IMap=Total_Flux*IMap/div
    QMap=Factor*Total_Flux*QMap/div
    UMap=Factor*Total_Flux*UMap/div

    return(IMap,QMap,UMap)

def DFT_Vis(ANT_Pix="",IMap="",QMap="",UMap="", NMap="", Nvis="",
    ↪ Cellsize=""):
#Performs a Direct Fourier Transform on the RR, LL, RL and LR maps at
    ↪ locations based on the existing observation. As this is a
    ↪ computationally intensive process some nummerical tricks are used
    ↪  to decrease computational time.

    UV=numpy.zeros([Nvis,6])
    Mat=numpy.zeros([NMap,NMap],complex)
    ANT=ANT_Pix

    RL=QMap+1J*UMap;
    LR=QMap-1J*UMap;

    Range=numpy.arange(-(NMap-1)/2,((NMap-1)/2+1))*Cellsize;

    for i in xrange(Nvis):

        if (i+1)%1000==0:
            print str(i+1)+" of "+str(Nvis)+" complete."

        X=ANT[i,0]
        Y=ANT[i,1]

        Exp1=numpy.exp(numpy.multiply(-2J*math.pi*X,Range))
        Exp2=numpy.exp(numpy.multiply(-2J*math.pi*Y,Range))


        for k in xrange(NMap):

            Mat[k,:]=numpy.multiply(Exp1[k],Exp2[:])

        DFTI=numpy.sum(numpy.sum(numpy.multiply(IMap,Mat)))
        DFTRL=numpy.sum(numpy.sum(numpy.multiply(RL,Mat)))
```

```
        DFTLR=numpy.sum(numpy.sum(numpy.multiply(LR,Mat)))


        UV[i,0]=DFTI.real
        UV[i,1]=DFTI.imag
        UV[i,2]=DFTRL.real
        UV[i,3]=DFTRL.imag
        UV[i,4]=DFTLR.real
        UV[i,5]=DFTLR.imag

    return(UV)

def Replace_Vis( uvw_list="", vis_list="", nvis="", out_ms=""):
#Replaces original visibilities with new visibilities from model source
    ↪ .


    if ( not os.path.exists( out_ms ) ):
        raise Exception( "Error: file " + out_ms + " does not exist" )
    tb.open(out_ms, nomodify = False)
    data=tb.getcol("DATA")

    for i in xrange(nvis):

        data[0][0].real[i] = vis_list[i][0]
        data[0][0].imag[i] = vis_list[i][1]
        data[1][0].real[i] = vis_list[i][2]
        data[1][0].imag[i] = vis_list[i][3]
        data[2][0].real[i] = vis_list[i][4]
        data[2][0].imag[i] = vis_list[i][5]
        data[3][0].real[i] = vis_list[i][0]
        data[3][0].imag[i] = vis_list[i][1]

    tb.putcol("DATA", data)

    data=tb.getcol("WEIGHT")
    for i in range(nvis):
        data[0][i] = 1
        data[1][i] = 1
        data[2][i] = 1
```

```
        data[3][i] = 1
    tb.putcol("WEIGHT", data)

    data=tb.getcol("SIGMA")
    for i in range(nvis):
        data[0][i] = 1
        data[1][i] = 1
        data[2][i] = 1
        data[3][i] = 1
    tb.putcol("SIGMA", data)

    data=tb.getcol("FLAG")
    j=[1,1,1]
    for i in range(nvis):
        data[0][0][i] = 0
        data[1][0][i] = 0
        data[2][0][i] = 0
        data[3][0][i] = 0



    tb.putcol("FLAG", data)

    tb.done()

    return(0)


def get_ANT(out_ms=""):
#Reads antenna information for the MS file of the original observation.

    if ( not os.path.exists( out_ms ) ):
        raise Exception( "Error: file " + out_ms + " does not exist " )
    tb.open(out_ms, nomodify = True)
    ANT=tb.getcol("UVW")

    ANT=numpy.transpose(ANT)

    Nvis=len(ANT)

    return(ANT,Nvis)
```

```
# Scripts Starts Here!

def Go(Wave="",Factor="", Total_Flux="",Cellsize="",NMap=""):

    vis_file_stem = ""
    #The visibility file stem. Code reads the Visibility CSV files in
        ↪ format of vis_file_stem+I/Q/U.csv This is defined here rather
        ↪ than calling it in the task as it could be a very long string
        ↪ if the visibility file is in a differernt folder to the one
        ↪ the code is being executed in.

    ms_file = ""
    #The ms file stem of the original observation. Code reads the MS
        ↪ file in format of ms_file.ms. This is defined here rather than
        ↪  calling it in the task as it could be a very long string if
        ↪ the ms file is in a differernt folder to the one the code is
        ↪ being executed in.


    #Script starts here

    Freq=(constants.c/(float(Wave)/100))/1E6

    Cellsize = Cellsize * (math.pi/(3600*180))

    print("Reading CSV Files..")
    New_ANT,Nvis=get_ANT(ms_file)

    ANT_pix=ANT_to_Pixels(New_ANT,Freq)
    IMap,QMap,UMap = Import_Maps(vis_file_stem,NMap,Factor,Total_Flux)

    print("Performing Fourier Transforms...")
    New_Vis=DFT_Vis(ANT_pix,IMap,QMap,UMap,NMap,Nvis,Cellsize)

    Replace_Vis(New_ANT,New_Vis,Nvis,ms_file)

    text_file = open("Output.txt", "w")
    text_file.write(ms_file)
    text_file.close()
```

```
    print("Operation was a success")
```

A.2 Mapper

This python script for CASA automatically cleans multiple Stokes Q & U maps using the standard CASA CLEAN task. This script can be run in CASA by executing the following

```
import Mapper
Mapper.Go(Noise,Mask,Beam,Tolerance,Cellsize,No_Pix,Nfiles)
```

where

- Noise is the scale of the normalised noise disrtribution to be added to the noiseless model visibilities.
- Mask is the CLEAN box to be used given as [blcx,blxy,trcx,trcy]
- Beam is the beam parameters to be used given as [bmaj,bmin,bpa].
- Tolerance is the value of the minimum clean component. CLEAN will continue to clean until an CLEAN component less than this Tolerance is found.
- No_Pix is the number of pixels you require. (256, 512 etc)
- Nfiles is the number of Q & U map pairs required.

The script this then executes can be seen below.

```
#  This program is called Mapper. It automatically CLEANS multiple
   ↪ images for use in Monte Carlo Simulations in CASA.
#  Copyright (C) 2013 Eoin Murphy

#   This program is free software: you can redistribute it and/or modify
#   it under the terms of the GNU General Public License as published by
#   the Free Software Foundation, either version 3 of the License, or
#   (at your option) any later version.
#
#   This program is distributed in the hope that it will be useful,
#   but WITHOUT ANY WARRANTY; without even the implied warranty of
```

```
#   MERCHANTABILITY or FITNESS FOR A PARTICULAR PURPOSE. See the
#   GNU General Public License for more details.

#   You should have received a copy of the GNU General Public License
#   along with this program. If not, see <http://www.gnu.org/licenses/>.

import time
import os
import commands
import numpy
import sys
import scipy
from scipy import constants
from scipy import stats
import math
import warnings
from casa import table as tb
from casa import clean
from casa import rmtables
import shutil
import subprocess

def Replace_Vis( uvw_list="", vis_list="", nvis="", out_ms=""):
#Replaces existing visibilities with new noisy ones.

    if ( not os.path.exists( out_ms ) ):
        raise Exception( "Error: file " + out_ms + " does not exist" )
    tb.open(out_ms, nomodify = False)
    data=tb.getcol("DATA")

    for i in xrange(nvis):

        data[0][0].real[i] = vis_list[i][0]
        data[0][0].imag[i] = vis_list[i][1]
        data[1][0].real[i] = vis_list[i][2]
        data[1][0].imag[i] = vis_list[i][3]
        data[2][0].real[i] = vis_list[i][4]
        data[2][0].imag[i] = vis_list[i][5]
        data[3][0].real[i] = vis_list[i][0]
        data[3][0].imag[i] = vis_list[i][1]
```

```
    tb.putcol("DATA", data)

    data=tb.getcol("WEIGHT")
    for i in range(nvis):
        data[0][i] = 1
        data[1][i] = 1
        data[2][i] = 1
        data[3][i] = 1
    tb.putcol("WEIGHT", data)

    data=tb.getcol("SIGMA")
    for i in range(nvis):
        data[0][i] = 1
        data[1][i] = 1
        data[2][i] = 1
        data[3][i] = 1
    tb.putcol("SIGMA", data)

    data=tb.getcol("FLAG")
    j=[1,1,1]
    for i in range(nvis):
        data[0][0][i] = 0
        data[1][0][i] = 0
        data[2][0][i] = 0
        data[3][0][i] = 0


    tb.putcol("FLAG", data)

    tb.done()

    return(0)

def get_ANT(out_ms=""):
#Reads antenna information.

    if ( not os.path.exists( out_ms ) ):
        raise Exception( "Error: file " + out_ms + " does not exist " )
    tb.open(out_ms, nomodify = True)
```

```
    ANT=tb.getcol("UVW")

    ANT=numpy.transpose(ANT)

    Nvis=len(ANT)

    return(ANT,Nvis)


def Add_Noise(Vis="",Noise="", Nvis=""):
#Adds noise to visibilities based on a normal distribution with scale
    ↪ equal to the Noise variable.

    Vis=numpy.add(Vis,stats.norm.rvs(loc=0.0, scale=Noise, size=(Nvis,6)
        ↪ ))

    return (Vis)


def get_VIS(Nvis="", out_ms=""):
#Reads visibility information for MS file.

    UV=numpy.zeros([Nvis,6])

    if ( not os.path.exists( out_ms ) ):
        raise Exception( "Error: file " + out_ms + " does not exist " )
    tb.open(out_ms, nomodify = False)
    data=tb.getcol("DATA")


    for i in xrange(Nvis):

         UV[i][0] = data[0][0].real[i]
         UV[i][1] = data[0][0].imag[i]
         UV[i][2] = data[1][0].real[i]
         UV[i][3] = data[1][0].imag[i]
         UV[i][4] = data[2][0].real[i]
         UV[i][5] = data[2][0].imag[i]

    return(UV)
```

```
def Go(Noise="",Mask="",Beam="", Tolerance="",Cellsize="",No_Pix="",
    ↪ Nfiles=""):



    ms_file = ""
    #The ms file stem of the observation being used. Code reads the MS
        ↪ file in format of ms_file.ms. This is defined here rather than
        ↪  calling it in the task as it could be a very long string if
        ↪ the ms file is in a differernt folder to the one the code is
        ↪ being executed in.
    map_file_stem=""
    #The map_file_stem of the maps to be produced. The code will make
        ↪ maps with names map_file_stem+Number.CLEAN.image



    #Script starts here

    owd = os.getcwd()
    shutil.copytree(ms_file,name)
    #In case of a crash ruining the original visibility file a copy is
        ↪ made and the rest of the code executes on this copy.

    Noise=Noise/math.sqrt(2)
    New_ANT,Nvis=get_ANT(ms_file)

    New_Vis=get_VIS(Nvis, name)

    for i in range(Nfiles):

        if os.path.exists(map_file_stem+str(i+1)+'U'+str(No)+'.CLEAN.
            ↪ image')==False:
        #CASA's CLEAN task currently has a small memory leak. This is
            ↪ only noticably when making 1000s of maps. If memory is
            ↪ filling up you can quit this task with CTRL+C and exit
            ↪ CASA. When you rerun this task it will find where it had
            ↪ stopped maping and start again.
```

```
        print "Making Width "+str(Width)+" "+map_file_stem+str(i+1)+
            ↪ 'Q'+str(No)+'.CLEAN.image'
        if (i+1)%20==0:
            os.chdir(root)
            rmtables(tablenames=["*psf","*residual","*model","*mask"
                ↪ ])
            os.chdir(owd)

        Noisy_Vis=Add_Noise(New_Vis,Noise, Nvis)
        Replace_Vis(New_ANT,Noisy_Vis,Nvis,name)



        clean(vis=name,imagename=map_file_stem+str(i+1)+'Q'+str(No)+
            ↪ '.CLEAN',stokes='Q',mask=Mask,uvtaper=False,
            ↪ restoringbeam=Beam,interactive=False,cell=Cellsize,
            ↪ threshold=Tolerance,imsize=No_Pix)

        clean(vis=name,imagename=map_file_stem+str(i+1)+'U'+str(No)+
            ↪ '.CLEAN',stokes='U',mask=Mask,uvtaper=False,
            ↪ restoringbeam=Beam,interactive=False,cell=Cellsize,
            ↪ threshold=Tolerance,imsize=No_Pix)

        time.sleep(3)

os.chdir(root)
#In order to save memory during the MC simulations all additonal
    ↪ maps are deleted at this step.
rmtables(tablenames=["*psf","*residual","*model","*mask","*flux"])
os.chdir(owd)
```

A.3 RM

This python script for CASA which produces RM and RM error maps from stokes Q & U maps. This script can be run in CASA by executing the following

```
import RM
RM.Go(In_Name,Out_Name,Max_Error,Freq,Shift,RM_Box,Noise_Box,Int_RM,
```

```
   ↪ NPix,EVPA)
```

where

- In_Name is the stem of the Q & U maps. The code will look for maps with the names "In_Name+Q1.CLEAN.image" and "In_Name+U1.CLEAN.image"
- Out_Name is the stem of the RM and RM Error maps the code will output. The code will output files with names "Out_Name+RM.im" and "Out_Name+eRM.im"
- Max_Error is the maximum error in the RM values before the value will be masked. This code currently masks values to 666666 rads m^{-2}
- Freq is the array of frequencies corresponding to the Stokes maps given as [Freq1,Freq2....FreqN] where FreqN corresponds to "In_Name+Qn.CLEAN.image" etc. This script can handle up to 7 frequencies.
- Shift is an array when specifies the maximum number of $n\pi$ shifts to be applied to each frequency. If this array was [1,2,3] it would shift the first frequency a maximum of 1π in each direction, the second frequency a maximum of 2π is each direction etc.
- RM_Box is an array specifying the region of the maps to find RM values given as [blcx,blcy,trcx,trcy]
- Noise_Box is an array specifying the region of the maps to calculate the RMS for each map. This value is then multiplied by 1.8 as per Hovatta et al (2012).
- Int_RM Any internal galactic Faraday Rotation to be applied to each map
- NPix is the number of pixels in each map (256, 512 etc).
- EVPA is an array of any EVPA corrections required for each frequency.

The script this then executes can be seen below.

```
#  This program is called RM. It makes Weighted Faraday Rotation Measure
   ↪  Maps in CASA.
#  Copyright (C) 2013 Eoin Murphy

#   This program is free software: you can redistribute it and/or modify
#   it under the terms of the GNU General Public License as published by
```

```
#   the Free Software Foundation, either version 3 of the License, or
#   (at your option) any later version.
#
#   This program is distributed in the hope that it will be useful,
#   but WITHOUT ANY WARRANTY; without even the implied warranty of
#   MERCHANTABILITY or FITNESS FOR A PARTICULAR PURPOSE. See the
#   GNU General Public License for more details.

#   You should have received a copy of the GNU General Public License
#   along with this program. If not, see <http://www.gnu.org/licenses/>.

import os
import commands
import numpy
import sys
import scipy
import csv
from scipy import constants
from scipy import special
import math
import shutil
from scipy import stats
from casa import table as tb

def Find_RMS(Map="",Box=""):
#Finds the RMS of the map from a box specified by Box. This is
    ↪ multiplied by 1.8 as per Hovatta et al. (2012)

    RMS=1.8*numpy.std(Map[(Box[0]-1):(Box[2]-1),(Box[1]-1):(Box[3]-1)])

    return(RMS)

def Error_PANG_Maps(Q="",U="",SigmaQ="",SigmaU="",N=""):
#Calculates the PANG map errors and their corresponding weights.

    Part1=1/(4*numpy.add(numpy.multiply(Q,Q),numpy.multiply(U,U)))
    Part2=numpy.sqrt(numpy.add(numpy.multiply(numpy.multiply(Q,Q),SigmaU
        ↪ *SigmaU),numpy.multiply(numpy.multiply(U,U),SigmaQ*SigmaQ)))

    Error=numpy.multiply(Part1,Part2)*180/math.pi
```

```
    Weight=1/(numpy.multiply(Error,Error))

    return(Error,Weight)

def Read_Maps(Image_Name="",N=""):
#Reads information from cleaned image map.

    tb.open(Image_Name,nomodify=False)
    data=tb.getcol("map")
    MAP=numpy.zeros([N,N])

    MAP[:,:]=data[:,:,0,0,0]

    tb.close()

    return(MAP)

def Make_Weighted_RM(PANG_Maps="",Weight="",Sigma="",Wave="",No="",
    ↪ Shift="",MaxRM="",MinRM="",RM_Box=""):
#Makes the Weighted RM map

    Temp=PANG_Maps[0]
    N=len(Temp)
    RM=666666*numpy.ones([N,N])
    eRM=666666*numpy.ones([N,N])
    Y=numpy.zeros(No)
    W=numpy.zeros(No)
    S=numpy.zeros(No)
    X=numpy.multiply(Wave,Wave)


    print "Calculating RM values..."

    for i in xrange(RM_Box[0],RM_Box[2]):

        per=math.ceil(100*(float(i-RM_Box[0])/float(RM_Box[2]-RM_Box[0])
            ↪ ))
        sys.stdout.write("\r"+str(per)+"% Complete...")
        sys.stdout.flush()
```

```
        for j in xrange(RM_Box[1],RM_Box[3]):

            for k in xrange(No):

                Y[k]=PANG_Maps[k][i,j]
                W[k]=Weight[k][i,j]
                S[k]=Sigma[k][i,j]


            RM[i,j],eRM[i,j]=RM_Shift(X, Y, W, S, No, Shift, MaxRM,
                ↪ MinRM)


    RM=RM*math.pi/180
    eRM=eRM*math.pi/180

    return(RM,eRM)

def RM_Shift(X="",Y="",W="",S="",No="",Shift="",MaxRM="",MinRM=""):
#Shifts the PANG values due to n*pi ambiguities till a best fit is
    ↪ found. The code shifts based on the array Shift. If this array
    ↪ was [1,2,3] it would shift the first wavelength a maximum of 1 pi
    ↪ , the second a maximum of 2 pi and the third a maximum of 3 pi. A
    ↪  value of n results in 2n+1 checks (for example 2 requires -2,
    ↪ -1, 0, 1 ,2) for each number. Therefore high values can slow down
    ↪  the code a great deal.

    nY=numpy.zeros(No)
    nChi2=10000000000000

    nRM=666666
    neRM=0
    nSigmaRM=0

    if No==2:
        for a in xrange(-Shift[0],Shift[0]+1):

            nY[0]=Y[0]+a*180
```

```
        for b in xrange(-Shift[1],Shift[1]+1):

            nY[1]=Y[1]+b*180

            RM,eRM,Chi2=RM_Calc(X,nY,W,S,No)

            if RM<=MaxRM and RM>=MinRM:
                if Chi2<nChi2:
                    nRM=RM
                    neRM=eRM
                    nChi2=Chi2


elif No==3:
    for a in xrange(-Shift[0],Shift[0]+1):

        nY[0]=Y[0]+a*180

        for b in xrange(-Shift[1],Shift[1]+1):

            nY[1]=Y[1]+b*180

            for c in xrange(-Shift[2],Shift[2]+1):

                nY[2]=Y[2]+c*180

                RM,eRM,Chi2=RM_Calc(X,nY,W,S,No)

                if RM<=MaxRM and RM>=MinRM:
                    if Chi2<nChi2:
                        nRM=RM
                        neRM=eRM
                        nChi2=Chi2

elif No==4:
    for a in xrange(-Shift[0],Shift[0]+1):

        nY[0]=Y[0]+a*180

        for b in xrange(-Shift[1],Shift[1]+1):
```

```
            nY[1]=Y[1]+b*180

            for c in xrange(-Shift[2],Shift[2]+1):

                nY[2]=Y[2]+c*180

                for d in xrange(-Shift[3],Shift[3]+1):

                    nY[3]=Y[3]+d*180

                    RM,eRM,Chi2=RM_Calc(X,nY,W,S,No)

                    if RM<=MaxRM and RM>=MinRM:
                        if Chi2<nChi2:
                            nRM=RM
                            neRM=eRM
                            nChi2=Chi2

elif No==5:
    for a in xrange(-Shift[0],Shift[0]+1):

        nY[0]=Y[0]+a*180

        for b in xrange(-Shift[1],Shift[1]+1):

            nY[1]=Y[1]+b*180

            for c in xrange(-Shift[2],Shift[2]+1):

                nY[2]=Y[2]+c*180

                for d in xrange(-Shift[3],Shift[3]+1):

                    nY[3]=Y[3]+d*180

                    for e in xrange(-Shift[4],Shift[4]+1):

                        nY[4]=Y[4]+e*180
```

```
                        RM,eRM,Chi2=RM_Calc(X,nY,W,S,No)

                        if RM<=MaxRM and RM>=MinRM:
                            if Chi2<nChi2:
                                nRM=RM
                                neRM=eRM
                                nChi2=Chi2
    elif No==6:
           for a in xrange(-Shift[0],Shift[0]+1):

               nY[0]=Y[0]+a*180

               for b in xrange(-Shift[1],Shift[1]+1):

                   nY[1]=Y[1]+b*180

                   for c in xrange(-Shift[2],Shift[2]+1):

                       nY[2]=Y[2]+c*180

                       for d in xrange(-Shift[3],Shift[3]+1):

                           nY[3]=Y[3]+d*180

                           for e in xrange(-Shift[4],Shift[4]+1):

                               nY[4]=Y[4]+e*180

                               for f in xrange(-Shift[5],Shift[5]+1):

                                   nY[5]=Y[5]+f*180

                                   RM,eRM,Chi2=RM_Calc(X,nY,W,S,No)

                                   if RM<=MaxRM and RM>=MinRM:
                                       if Chi2<nChi2:
                                           nRM=RM
                                           neRM=eRM
                                           nChi2=Chi2
```

```
elif No==7:
       for a in xrange(-Shift[0],Shift[0]+1):

           nY[0]=Y[0]+a*180

           for b in xrange(-Shift[1],Shift[1]+1):

               nY[1]=Y[1]+b*180

               for c in xrange(-Shift[2],Shift[2]+1):

                   nY[2]=Y[2]+c*180

                   for d in xrange(-Shift[3],Shift[3]+1):

                       nY[3]=Y[3]+d*180

                       for e in xrange(-Shift[4],Shift[4]+1):

                           nY[4]=Y[4]+e*180

                           for f in xrange(-Shift[5],Shift[5]+1):

                               nY[5]=Y[5]+f*180

                               for g in xrange(-Shift[6],Shift[6]+1):

                                   nY[6]=Y[6]+g*180;

                                   RM,eRM,Chi2=RM_Calc(X,nY,W,S,No)

                                   if RM<=MaxRM and RM>=MinRM:
                                       if Chi2<nChi2:
                                           nRM=RM
                                           neRM=eRM
                                           nChi2=Chi2

return(nRM,neRM)
```

```
def RM_Calc(X="",Y="",W="",S="",No=""):
#Calcules the slope of the best fit line (the RM value) using the
    ↪ standard weighted least squares method.

    aW=numpy.sum(W)
    aWxy=numpy.sum(numpy.multiply(numpy.multiply(X,Y),W))
    aWx=numpy.sum(numpy.multiply(X,W))
    aWy=numpy.sum(numpy.multiply(Y,W))
    aWxx=numpy.sum(numpy.multiply(numpy.multiply(X,X),W))

    eRM=0
    SigmaRM=0
    Chi2=0

    D=aW*aWxx-aWx*aWx

    RM=(aW*aWxy-aWx*aWy)/D

    Int=(aWy*aWxx-aWxy*aWx)/D

    for i in xrange(No):
        Chi2=Chi2+(Y[i]-(RM*X[i]+Int))*(Y[i]-(RM*X[i]+Int))

    for i in xrange(No):
        eRM=eRM+numpy.sqrt(S[i]*S[i]*((aW*W[i]*X[i]-W[i]*aWx)/D)*((aW*W[
            ↪ i]*X[i]-W[i]*aWx)/D))


    return(RM,eRM,Chi2)

def Mask_Map(RM="",eRM="",Max="",N=""):
#Sets every RM value with error great than Max equal to 666666.


    for i in xrange(N):

        for j in xrange(N):
```

```
            if abs(eRM[i,j])>Max:
                RM[i,j]=666666
                eRM[i,j]=666666

    return (RM,eRM)

def Output_Maps(RM="",eRM="",outname="",inname=""):
#Outputs RM map and its associated error map.

        inname=inname+"Q1.CLEAN.image"

        shutil.copytree(inname,outname+"_RM.im")
        tb.open(outname+"_RM.im",nomodify=False)
        data=tb.getcol("map")
        data[:,:,0,0,0]=RM
        tb.putcol("map",data)
        tb.putkeyword("units","rads/m/m")
        tb.close()


        shutil.copytree(inname,outname+"_eRM.im")
        tb.open(outname+"_eRM.im",nomodify=False)
        data=tb.getcol("map")
        data[:,:,0,0,0]=eRM
        tb.putcol("map",data)
        tb.putkeyword("units","rads/m/m")
        tb.close()


def Make_Arrays(Total="",N=""):
#Sets up all arrays together at start rather than when required to
    ↪ decrease code execution time.

    if Total==2:

        Q=numpy.array([numpy.zeros([N,N]),numpy.zeros([N,N])])
        U=numpy.array([numpy.zeros([N,N]),numpy.zeros([N,N])])
        Weight=numpy.array([numpy.zeros([N,N]),numpy.zeros([N,N])])
        Sigma=numpy.array([numpy.zeros([N,N]),numpy.zeros([N,N])])
        PANG=numpy.array([numpy.zeros([N,N]),numpy.zeros([N,N])])
```

```
    PPOL=numpy.array([numpy.zeros([N,N]),numpy.zeros([N,N])])

elif Total==3:

    Q=numpy.array([numpy.zeros([N,N]),numpy.zeros([N,N]),numpy.zeros
        ↪ ([N,N])])
    U=numpy.array([numpy.zeros([N,N]),numpy.zeros([N,N]),numpy.zeros
        ↪ ([N,N])])
    Weight=numpy.array([numpy.zeros([N,N]),numpy.zeros([N,N]),numpy.
        ↪ zeros([N,N])])
    Sigma=numpy.array([numpy.zeros([N,N]),numpy.zeros([N,N]),numpy.
        ↪ zeros([N,N])])
    PANG=numpy.array([numpy.zeros([N,N]),numpy.zeros([N,N]),numpy.
        ↪ zeros([N,N])])
    PPOL=numpy.array([numpy.zeros([N,N]),numpy.zeros([N,N]),numpy.
        ↪ zeros([N,N])])

elif Total==4:

    Q=numpy.array([numpy.zeros([N,N]),numpy.zeros([N,N]),numpy.zeros
        ↪ ([N,N]),numpy.zeros([N,N])])
    U=numpy.array([numpy.zeros([N,N]),numpy.zeros([N,N]),numpy.zeros
        ↪ ([N,N]),numpy.zeros([N,N])])
    Weight=numpy.array([numpy.zeros([N,N]),numpy.zeros([N,N]),numpy.
        ↪ zeros([N,N]),numpy.zeros([N,N])])
    Sigma=numpy.array([numpy.zeros([N,N]),numpy.zeros([N,N]),numpy.
        ↪ zeros([N,N]),numpy.zeros([N,N])])
    PANG=numpy.array([numpy.zeros([N,N]),numpy.zeros([N,N]),numpy.
        ↪ zeros([N,N]),numpy.zeros([N,N])])
    PPOL=numpy.array([numpy.zeros([N,N]),numpy.zeros([N,N]),numpy.
        ↪ zeros([N,N]),numpy.zeros([N,N])])


elif Total==5:

    Q=numpy.array([numpy.zeros([N,N]),numpy.zeros([N,N]),numpy.zeros
        ↪ ([N,N]),numpy.zeros([N,N]),numpy.zeros([N,N])])
    U=numpy.array([numpy.zeros([N,N]),numpy.zeros([N,N]),numpy.zeros
        ↪ ([N,N]),numpy.zeros([N,N]),numpy.zeros([N,N])])
```

```
    Weight=numpy.array([numpy.zeros([N,N]),numpy.zeros([N,N]),numpy.
        ↪ zeros([N,N]),numpy.zeros([N,N]),numpy.zeros([N,N])])
    Sigma=numpy.array([numpy.zeros([N,N]),numpy.zeros([N,N]),numpy.
        ↪ zeros([N,N]),numpy.zeros([N,N]),numpy.zeros([N,N])])
    PANG=numpy.array([numpy.zeros([N,N]),numpy.zeros([N,N]),numpy.
        ↪ zeros([N,N]),numpy.zeros([N,N]),numpy.zeros([N,N])])
    PPOL=numpy.array([numpy.zeros([N,N]),numpy.zeros([N,N]),numpy.
        ↪ zeros([N,N]),numpy.zeros([N,N]),numpy.zeros([N,N])])

elif Total==6:

    Q=numpy.array([numpy.zeros([N,N]),numpy.zeros([N,N]),numpy.zeros
        ↪ ([N,N]),numpy.zeros([N,N]),numpy.zeros([N,N]),numpy.zeros
        ↪ ([N,N])])
    U=numpy.array([numpy.zeros([N,N]),numpy.zeros([N,N]),numpy.zeros
        ↪ ([N,N]),numpy.zeros([N,N]),numpy.zeros([N,N]),numpy.zeros
        ↪ ([N,N])])
    Weight=numpy.array([numpy.zeros([N,N]),numpy.zeros([N,N]),numpy.
        ↪ zeros([N,N]),numpy.zeros([N,N]),numpy.zeros([N,N]),numpy.
        ↪ zeros([N,N])])
    Sigma=numpy.array([numpy.zeros([N,N]),numpy.zeros([N,N]),numpy.
        ↪ zeros([N,N]),numpy.zeros([N,N]),numpy.zeros([N,N]),numpy.
        ↪ zeros([N,N])])
    PANG=numpy.array([numpy.zeros([N,N]),numpy.zeros([N,N]),numpy.
        ↪ zeros([N,N]),numpy.zeros([N,N]),numpy.zeros([N,N]),numpy.
        ↪ zeros([N,N])])
    PPOL=numpy.array([numpy.zeros([N,N]),numpy.zeros([N,N]),numpy.
        ↪ zeros([N,N]),numpy.zeros([N,N]),numpy.zeros([N,N]),numpy.
        ↪ zeros([N,N])])

elif Total==7:

    Q=numpy.array([numpy.zeros([N,N]),numpy.zeros([N,N]),numpy.zeros
        ↪ ([N,N]),numpy.zeros([N,N]),numpy.zeros([N,N]),numpy.zeros
        ↪ ([N,N]),numpy.zeros([N,N])])
    U=numpy.array([numpy.zeros([N,N]),numpy.zeros([N,N]),numpy.zeros
        ↪ ([N,N]),numpy.zeros([N,N]),numpy.zeros([N,N]),numpy.zeros
        ↪ ([N,N]),numpy.zeros([N,N])])
    Weight=numpy.array([numpy.zeros([N,N]),numpy.zeros([N,N]),numpy.
        ↪ zeros([N,N]),numpy.zeros([N,N]),numpy.zeros([N,N]),numpy.
```

```
            ↪ zeros([N,N]),numpy.zeros([N,N])])
        Sigma=numpy.array([numpy.zeros([N,N]),numpy.zeros([N,N]),numpy.
            ↪ zeros([N,N]),numpy.zeros([N,N]),numpy.zeros([N,N]),numpy.
            ↪ zeros([N,N]),numpy.zeros([N,N])])
        PANG=numpy.array([numpy.zeros([N,N]),numpy.zeros([N,N]),numpy.
            ↪ zeros([N,N]),numpy.zeros([N,N]),numpy.zeros([N,N]),numpy.
            ↪ zeros([N,N]),numpy.zeros([N,N])])
        PPOL=numpy.array([numpy.zeros([N,N]),numpy.zeros([N,N]),numpy.
            ↪ zeros([N,N]),numpy.zeros([N,N]),numpy.zeros([N,N]),numpy.
            ↪ zeros([N,N]),numpy.zeros([N,N])])


    return(Q,U,Weight,Sigma,PANG,PPOL)

def Error_Check(Wave="",Shift="",In_Name="",Out_Name="", Total="",
    ↪ MaxRM="", MinRM=""):
#Checks for any common errors and stops code execution if any are found
    ↪ . Also informs user of those errors.

    Error=0

    if Total <2:
        print "Too few frequencies. 2 is the minimum number of allowed
            ↪ frequencies."
        Error=1

    if Total >7:
        print "Too many frequencies. 7 is the maximum number of allowed
            ↪ frequencies."
        Error=1

    if MaxRM <= MinRM:
        print "Maximum allowed RM is less than or equal to minimum
            ↪ allowed RM"
        Error=1

    if len(Wave)!=len(Shift):
        print "Wavelength & Shift arrays are of different lengths"
        Error=1
```

```
    for i in xrange(Total):
        if os.path.exists(In_Name+'Q'+str(i+1)+'.CLEAN.image')==0:
            print In_Name+'Q'+str(i+1)+'.CLEAN.image does not exist'
            Error=1
        if os.path.exists(In_Name+'U'+str(i+1)+'.CLEAN.image')==0:
            print In_Name+'U'+str(i+1)+'.CLEAN.image does not exist'
            Error=1

    if os.path.exists(Out_Name+'_RM.im')!=0:
        print Out_Name+'_RM.im already exists.'
        Error=1

    if os.path.exists(Out_Name+'_eRM.im')!=0:
        print Out_Name+'_eRM.im already exists.'
        Error=1


    return(Error)

def Make_RM(Image_Stem='',Out_Name="", Total='' , Wave='' , N='' ,
    ↪ Shift='' , Box = '' , Int_RM = '' , Max='' , MaxRM = '' , MinRM =
    ↪  '' , Do_CC = '',RM_Box='',EVPA=''):
#This is where the majority of code is executed.

    Int_RM=Int_RM*180/math.pi

    MaxRM=MaxRM*180/math.pi
    MinRM=MinRM*180/math.pi

    Error=Error_Check(Wave,Shift,Image_Stem,Out_Name,Total,MaxRM,MinRM)

    RM=0

    if Error==1:
        print "Operation Failed"

    else:

        print "Reading maps..."
```

```
        Q,U,Weight,Sigma,PANG,PPOL=Make_Arrays(Total,N)

        for i in xrange(Total):
            Q[i]=Read_Maps(Image_Stem+'Q'+str(i+1)+'.CLEAN.image',N)
            U[i]=Read_Maps(Image_Stem+'U'+str(i+1)+'.CLEAN.image',N)


        for i in xrange(Total):
            PANG[i]=numpy.multiply(0.5*numpy.arctan2(U[i],Q[i]),180/math
                ↪ .pi)

        for i in xrange(Total):
            SigmaQ=Find_RMS(Q[i],Box)
            SigmaU=Find_RMS(U[i],Box)
            [Sigma[i],Weight[i]]=Error_PANG_Maps(Q[i],U[i],SigmaQ,SigmaU
                ↪ ,N)

        for i in xrange(Total):
            PANG[i]=PANG[i]+EVPA[i]-Int_RM*Wave[i]*Wave[i]


        RM,eRM=Make_Weighted_RM(PANG,Weight,Sigma,Wave,Total,Shift,MaxRM
            ↪ ,MinRM,RM_Box)

        RM,eRM=Mask_Map(RM,eRM,Max,N)

        Output_Maps( RM, eRM , Out_Name , Image_Stem)

        print "\nOperation Complete!"

    return()


def Go(In_Name="",Out_Name="",Max_Error="",Freq="",Shift="",RM_Box="",
    ↪ Noise_Box="",Int_RM="",Npix="",EVPA=''):



    Total=len(Freq)
    Wave = numpy.divide(constants.c,Freq)
```

```
MaxRM=100000          #Maximum allowed RM (rad/m/m). If no RM in
    ↪ acceptable range is found, RM will equal 0
MinRM=-100000         #Minimum allowed RM (rad/m/m). If no RM in
    ↪ acceptable range is found, RM will equal 0



Make_RM( In_Name,Out_Name, Total , Wave , Npix , Shift , Noise_Box ,
    ↪  Int_RM , Max_Error , MaxRM , MinRM, Do_CC , RM_Box,EVPA)
```

A.4 Sigma Checker

This python script for CASA determines the σ fits This script can be run in CASA by executing the following

```
import Sigma_Checker as SC
SC.Sigma_Check(In_Name,Band, Slice, Shift, Box, Freq, Int_RM, Npix,
    ↪ Nmap, Name)
```

where

- In_Name is the stem of the Q & U maps. The code will look for maps with the names "In_Name+Q1.CLEAN.image" and "In_Name+U1.CLEAN.image"
- Band is the number of pixels required for the band around which the best RM difference is found at the slice edges. A value of N will result in the a Band ranging from Slice-N to Slice+N.
- Slice is an array given as [blcx,blcy,trcx,trcy]. This is the transverse slice to be analysed. If blcx and trcx are not equal the code will calculate the sigma value for N many slices where N is trcx - blcx+1
- Shift is an array when specifies the maximum number of $n\pi$ shifts to be applied to each frequency. If this array was [1,2,3] it would shift the first frequency a maximum of 1π in each direction, the second frequency a maximum of 2π is each direction etc.
- Box is an array specifying the region of the maps to calculate the RMS for each map. This value is then multiplied by 1.8 as per Hovatta et al (2012).

- Freq is the array of frequencies corresponding to the Stokes maps given as [Freq1,Freq2....FreqN]. This script can handle up to 7 frequencies.
- Int_RM Any internal galactic Faraday Rotation to be applied to each map
- NPix is the number of pixels in each map (256, 512 etc).
- Nmap is the number of maps to analyse.
- Name is the name desired for the outputted CSV file which will contain the σ fits.

The script this then executes can be seen below.

```
#  This program is called Sigma_Check. It determines the Sigma of
   ↪ Faraday RM transverse gradients in CASA.
#  Copyright (C) 2013 Eoin Murphy

#   This program is free software: you can redistribute it and/or modify
#   it under the terms of the GNU General Public License as published by
#   the Free Software Foundation, either version 3 of the License, or
#   (at your option) any later version.
#
#   This program is distributed in the hope that it will be useful,
#   but WITHOUT ANY WARRANTY; without even the implied warranty of
#   MERCHANTABILITY or FITNESS FOR A PARTICULAR PURPOSE. See the
#   GNU General Public License for more details.

#   You should have received a copy of the GNU General Public License
#   along with this program. If not, see <http://www.gnu.org/licenses/>.

import os
import commands
import numpy
import sys
import scipy
import csv
from scipy import constants
from scipy import special
import math
import shutil
import time
from scipy import stats
```

```
from casa import table as tb

t = time.time()
#Constants defined here


def Find_RMS(Map="",Box=""):
#Finds the RMS of the map from a box specified by Box. This is
    ↪ multiplied by 1.8 as per Hovatta et al. (2012)

    RMS=1.8*numpy.std(Map[(Box[0]-1):(Box[2]-1),(Box[1]-1):(Box[3]-1)])

    return(RMS)

def Error_PANG_Maps(Q="",U="",SigmaQ="",SigmaU="", EVPA_Error ="",N="")
    ↪ :
#Calculates the PANG map errors and their corresponding weights.

    Part1=1/(4*numpy.add(numpy.multiply(Q,Q),numpy.multiply(U,U)))
    Part2=numpy.sqrt(numpy.add(numpy.multiply(numpy.multiply(Q,Q),SigmaU
        ↪ *SigmaU),numpy.multiply(numpy.multiply(U,U),SigmaQ*SigmaQ)))

    Error=numpy.multiply(Part1,Part2)*180/math.pi

    Weight=1/(numpy.multiply(Error,Error))

    return(Error,Weight)

def Read_Maps(Image_Name="",N=""):
#Reads information from cleaned image map.

    tb.open(Image_Name,nomodify=False)
    data=tb.getcol("map")
    PANG=numpy.zeros([N,N])

    PANG[:,:]=data[:,:,0,0,0]

    tb.close()

    return(PANG)
```

```
def Make_Weighted_RM(PANG_Maps="",Weight="",Sigma="",Wave="",No="",
    ↪ Shift="",MaxRM="",MinRM="",NSlice=""):
#Calculates Weighted RM values for given Slice

    Length=NSlice[3]-NSlice[1]
    Width=NSlice[2]-NSlice[0]

    RM=numpy.zeros([Width,Length])
    eRM=numpy.zeros([Width,Length])
    Y=numpy.zeros(No)
    W=numpy.zeros(No)
    S=numpy.zeros(No)
    X=numpy.multiply(Wave,Wave)

    i2=0
    j2=0

    for i in xrange(NSlice[0],NSlice[2]):

        for j in xrange(NSlice[1],NSlice[3]):

            for k in xrange(No):

                Y[k]=PANG_Maps[k][i,j]
                W[k]=Weight[k][i,j]
                S[k]=Sigma[k][i,j]

            RM[i2,j2],eRM[i2,j2]=RM_Shift(X, Y, W, S, No, Shift, MaxRM,
                ↪ MinRM)
            j2=j2+1
        i2=i2+1
        j2=0


    RM=RM*math.pi/180
    eRM=eRM*math.pi/180

    return(RM,eRM)
```

```
def RM_Shift(X="",Y="",W="",S="",No="",Shift="",MaxRM="",MinRM=""):
#Shifts the PANG values due to n*pi ambiguities till a best fit is
    ↪ found. The code shifts based on the array Shift. If this array
    ↪ was [1,2,3] it would shift the first wavelength a maximum of 1 pi
    ↪ , the second a maximum of 2 pi and the third a maximum of 3 pi. A
    ↪  value of n results in 2n+1 checks (for example 2 requires -2,
    ↪ -1, 0, 1 ,2) for each number. Therefore high values can slow down
    ↪  the code a great deal.


    nY=numpy.zeros(No)
    nChi2=1000000000

    nRM=666
    neRM=0
    nSigmaRM=0

    if No==2:
        for a in xrange(-Shift[0],Shift[0]+1):

            nY[0]=Y[0]+a*180

            for b in xrange(-Shift[1],Shift[1]+1):

                nY[1]=Y[1]+b*180

                RM,eRM,Chi2=RM_Calc(X,nY,W,S,No)

                if RM<=MaxRM and RM>=MinRM:
                    if Chi2<nChi2:
                        nRM=RM
                        neRM=eRM
                        nChi2=Chi2


    elif No==3:
        for a in xrange(-Shift[0],Shift[0]+1):

            nY[0]=Y[0]+a*180
```

```
        for b in xrange(-Shift[1],Shift[1]+1):

            nY[1]=Y[1]+b*180

            for c in xrange(-Shift[2],Shift[2]+1):

                nY[2]=Y[2]+c*180

                RM,eRM,Chi2=RM_Calc(X,nY,W,S,No)

                if RM<=MaxRM and RM>=MinRM:
                    if Chi2<nChi2:
                        nRM=RM
                        neRM=eRM
                        nChi2=Chi2

elif No==4:
    for a in xrange(-Shift[0],Shift[0]+1):

        nY[0]=Y[0]+a*180

        for b in xrange(-Shift[1],Shift[1]+1):

            nY[1]=Y[1]+b*180

            for c in xrange(-Shift[2],Shift[2]+1):

                nY[2]=Y[2]+c*180

                for d in xrange(-Shift[3],Shift[3]+1):

                    nY[3]=Y[3]+d*180

                    RM,eRM,Chi2=RM_Calc(X,nY,W,S,No)

                    if RM<=MaxRM and RM>=MinRM:
                        if Chi2<nChi2:
                            nRM=RM
                            neRM=eRM
                            nChi2=Chi2
```

```
elif No==5:
    for a in xrange(-Shift[0],Shift[0]+1):

        nY[0]=Y[0]+a*180

        for b in xrange(-Shift[1],Shift[1]+1):

            nY[1]=Y[1]+b*180

            for c in xrange(-Shift[2],Shift[2]+1):

                nY[2]=Y[2]+c*180

                for d in xrange(-Shift[3],Shift[3]+1):

                    nY[3]=Y[3]+d*180

                    for e in xrange(-Shift[4],Shift[4]+1):

                        nY[4]=Y[4]+e*180

                        RM,eRM,Chi2=RM_Calc(X,nY,W,S,No)

                        if RM<=MaxRM and RM>=MinRM:
                            if Chi2<nChi2:
                                nRM=RM
                                neRM=eRM
                                nChi2=Chi2
elif No==6:
        for a in xrange(-Shift[0],Shift[0]+1):

            nY[0]=Y[0]+a*180

            for b in xrange(-Shift[1],Shift[1]+1):

                nY[1]=Y[1]+b*180

                for c in xrange(-Shift[2],Shift[2]+1):
```

```
                    nY[2]=Y[2]+c*180

                    for d in xrange(-Shift[3],Shift[3]+1):

                        nY[3]=Y[3]+d*180

                        for e in xrange(-Shift[4],Shift[4]+1):

                            nY[4]=Y[4]+e*180

                            for f in xrange(-Shift[5],Shift[5]+1):

                                nY[5]=Y[5]+f*180

                                RM,eRM,Chi2=RM_Calc(X,nY,W,S,No)

                                if RM<=MaxRM and RM>=MinRM:
                                    if Chi2<nChi2:
                                        nRM=RM
                                        neRM=eRM
                                        nChi2=Chi2

elif No==7:
       for a in xrange(-Shift[0],Shift[0]+1):

           nY[0]=Y[0]+a*180

           for b in xrange(-Shift[1],Shift[1]+1):

               nY[1]=Y[1]+b*180

               for c in xrange(-Shift[2],Shift[2]+1):

                   nY[2]=Y[2]+c*180

                   for d in xrange(-Shift[3],Shift[3]+1):

                       nY[3]=Y[3]+d*180

                       for e in xrange(-Shift[4],Shift[4]+1):
```

```
                                nY[4]=Y[4]+e*180

                                for f in xrange(-Shift[5],Shift[5]+1):

                                    nY[5]=Y[5]+f*180

                                    for g in xrange(-Shift[6],Shift[6]+1):

                                        nY[6]=Y[6]+g*180;

                                        RM,eRM,Chi2=RM_Calc(X,nY,W,S,No)

                                        if RM<=MaxRM and RM>=MinRM:
                                            if Chi2<nChi2:
                                                nRM=RM
                                                neRM=eRM
                                                nChi2=Chi2

    return(nRM,neRM)




def RM_Calc(X="",Y="",W="",S="",No=""):
#Calculates the slope of the best fit line (the RM value) using the
    ↪ standard weighted least squares method.

    aW=numpy.sum(W)
    aWxy=numpy.sum(numpy.multiply(numpy.multiply(X,Y),W))
    aWx=numpy.sum(numpy.multiply(X,W))
    aWy=numpy.sum(numpy.multiply(Y,W))
    aWxx=numpy.sum(numpy.multiply(numpy.multiply(X,X),W))

    eRM=0
    SigmaRM=0
    Chi2=0

    D=aW*aWxx-aWx*aWx
```

```
    RM=(aW*aWxy-aWx*aWy)/D

    Int=(aWy*aWxx-aWxy*aWx)/D

    for i in xrange(No):
        Chi2=Chi2+(Y[i]-(RM*X[i]+Int))*(Y[i]-(RM*X[i]+Int))

    for i in xrange(No):
        eRM=eRM+numpy.sqrt(S[i]*S[i]*((aW*W[i]*X[i]-W[i]*aWx)/D)*((aW*W[
            ↪ i]*X[i]-W[i]*aWx)/D))


    return(RM,eRM,Chi2)


def Make_Arrays(Total="",N=""):
#Sets up all arrays together at start rather than when required to
    ↪ decrease code execution time.

    if Total==2:

        Q=numpy.array([numpy.zeros([N,N]),numpy.zeros([N,N])])
        U=numpy.array([numpy.zeros([N,N]),numpy.zeros([N,N])])
        Weight=numpy.array([numpy.zeros([N,N]),numpy.zeros([N,N])])
        Sigma=numpy.array([numpy.zeros([N,N]),numpy.zeros([N,N])])
        PANG=numpy.array([numpy.zeros([N,N]),numpy.zeros([N,N])])
        PPOL=numpy.array([numpy.zeros([N,N]),numpy.zeros([N,N])])



    elif Total==3:

        Q=numpy.array([numpy.zeros([N,N]),numpy.zeros([N,N]),numpy.zeros
            ↪ ([N,N])])
        U=numpy.array([numpy.zeros([N,N]),numpy.zeros([N,N]),numpy.zeros
            ↪ ([N,N])])
        Weight=numpy.array([numpy.zeros([N,N]),numpy.zeros([N,N]),numpy.
            ↪ zeros([N,N])])
        Sigma=numpy.array([numpy.zeros([N,N]),numpy.zeros([N,N]),numpy.
            ↪ zeros([N,N])])
```

```
    PANG=numpy.array([numpy.zeros([N,N]),numpy.zeros([N,N]),numpy.
        ↪ zeros([N,N])])
    PPOL=numpy.array([numpy.zeros([N,N]),numpy.zeros([N,N]),numpy.
        ↪ zeros([N,N])])

elif Total==4:

    Q=numpy.array([numpy.zeros([N,N]),numpy.zeros([N,N]),numpy.zeros
        ↪ ([N,N]),numpy.zeros([N,N])])
    U=numpy.array([numpy.zeros([N,N]),numpy.zeros([N,N]),numpy.zeros
        ↪ ([N,N]),numpy.zeros([N,N])])
    Weight=numpy.array([numpy.zeros([N,N]),numpy.zeros([N,N]),numpy.
        ↪ zeros([N,N]),numpy.zeros([N,N])])
    Sigma=numpy.array([numpy.zeros([N,N]),numpy.zeros([N,N]),numpy.
        ↪ zeros([N,N]),numpy.zeros([N,N])])
    PANG=numpy.array([numpy.zeros([N,N]),numpy.zeros([N,N]),numpy.
        ↪ zeros([N,N]),numpy.zeros([N,N])])
    PPOL=numpy.array([numpy.zeros([N,N]),numpy.zeros([N,N]),numpy.
        ↪ zeros([N,N]),numpy.zeros([N,N])])


elif Total==5:

    Q=numpy.array([numpy.zeros([N,N]),numpy.zeros([N,N]),numpy.zeros
        ↪ ([N,N]),numpy.zeros([N,N]),numpy.zeros([N,N])])
    U=numpy.array([numpy.zeros([N,N]),numpy.zeros([N,N]),numpy.zeros
        ↪ ([N,N]),numpy.zeros([N,N]),numpy.zeros([N,N])])
    Weight=numpy.array([numpy.zeros([N,N]),numpy.zeros([N,N]),numpy.
        ↪ zeros([N,N]),numpy.zeros([N,N]),numpy.zeros([N,N])])
    Sigma=numpy.array([numpy.zeros([N,N]),numpy.zeros([N,N]),numpy.
        ↪ zeros([N,N]),numpy.zeros([N,N]),numpy.zeros([N,N])])
    PANG=numpy.array([numpy.zeros([N,N]),numpy.zeros([N,N]),numpy.
        ↪ zeros([N,N]),numpy.zeros([N,N]),numpy.zeros([N,N])])
    PPOL=numpy.array([numpy.zeros([N,N]),numpy.zeros([N,N]),numpy.
        ↪ zeros([N,N]),numpy.zeros([N,N]),numpy.zeros([N,N])])

elif Total==6:

    Q=numpy.array([numpy.zeros([N,N]),numpy.zeros([N,N]),numpy.zeros
        ↪ ([N,N]),numpy.zeros([N,N]),numpy.zeros([N,N]),numpy.zeros
```

```
        ↪ ([N,N])])
    U=numpy.array([numpy.zeros([N,N]),numpy.zeros([N,N]),numpy.zeros
        ↪ ([N,N]),numpy.zeros([N,N]),numpy.zeros([N,N]),numpy.zeros
        ↪ ([N,N])])
    Weight=numpy.array([numpy.zeros([N,N]),numpy.zeros([N,N]),numpy.
        ↪ zeros([N,N]),numpy.zeros([N,N]),numpy.zeros([N,N]),numpy.
        ↪ zeros([N,N])])
    Sigma=numpy.array([numpy.zeros([N,N]),numpy.zeros([N,N]),numpy.
        ↪ zeros([N,N]),numpy.zeros([N,N]),numpy.zeros([N,N]),numpy.
        ↪ zeros([N,N])])
    PANG=numpy.array([numpy.zeros([N,N]),numpy.zeros([N,N]),numpy.
        ↪ zeros([N,N]),numpy.zeros([N,N]),numpy.zeros([N,N]),numpy.
        ↪ zeros([N,N])])
    PPOL=numpy.array([numpy.zeros([N,N]),numpy.zeros([N,N]),numpy.
        ↪ zeros([N,N]),numpy.zeros([N,N]),numpy.zeros([N,N]),numpy.
        ↪ zeros([N,N])])

elif Total==7:

    Q=numpy.array([numpy.zeros([N,N]),numpy.zeros([N,N]),numpy.zeros
        ↪ ([N,N]),numpy.zeros([N,N]),numpy.zeros([N,N]),numpy.zeros
        ↪ ([N,N]),numpy.zeros([N,N])])
    U=numpy.array([numpy.zeros([N,N]),numpy.zeros([N,N]),numpy.zeros
        ↪ ([N,N]),numpy.zeros([N,N]),numpy.zeros([N,N]),numpy.zeros
        ↪ ([N,N]),numpy.zeros([N,N])])
    Weight=numpy.array([numpy.zeros([N,N]),numpy.zeros([N,N]),numpy.
        ↪ zeros([N,N]),numpy.zeros([N,N]),numpy.zeros([N,N]),numpy.
        ↪ zeros([N,N]),numpy.zeros([N,N])])
    Sigma=numpy.array([numpy.zeros([N,N]),numpy.zeros([N,N]),numpy.
        ↪ zeros([N,N]),numpy.zeros([N,N]),numpy.zeros([N,N]),numpy.
        ↪ zeros([N,N]),numpy.zeros([N,N])])
    PANG=numpy.array([numpy.zeros([N,N]),numpy.zeros([N,N]),numpy.
        ↪ zeros([N,N]),numpy.zeros([N,N]),numpy.zeros([N,N]),numpy.
        ↪ zeros([N,N]),numpy.zeros([N,N])])
    PPOL=numpy.array([numpy.zeros([N,N]),numpy.zeros([N,N]),numpy.
        ↪ zeros([N,N]),numpy.zeros([N,N]),numpy.zeros([N,N]),numpy.
        ↪ zeros([N,N]),numpy.zeros([N,N])])



return(Q,U,Weight,Sigma,PANG,PPOL)
```

```
def Checker(RM='', eRM='', Band='', Slice=''):
#Determines best Sigma value for both bands and also ensures that any
    ↪ spurious gradient is monotonic

    Width=Slice[2]-Slice[0]

    Max_Sigma=numpy.zeros(Width)

    for k in xrange(Width):


        for i in xrange(2*Band+1):

            for j in xrange(2*Band+1):

                Difference=abs(RM[k,i]-RM[k,-(j+1)])
                Sigma_Error=math.sqrt(eRM[k,i]*eRM[k,i]+eRM[k,-(j+1)]*eRM
                    ↪ [k,-(j+1)])

                Sigma_Value=float(Difference/Sigma_Error)

                Delta_RM=numpy.diff(RM[i:(-(j+1))])

                if numpy.all(Delta_RM >= 0) or numpy.all(Delta_RM <= 0):

                if Sigma_Value>Max_Sigma[k]:
                    Max_Sigma[k]=Sigma_Value


    return(numpy.transpose(Max_Sigma))



def Error_Check(Wave="",Shift="",Image_Stem="", Total="", MaxRM="",
    ↪ MinRM=""):
#Checks for any common errors and stops code execution if any are found
    ↪ . Also informs user of those errors.
```

```
    Error=0

    if Total <2:
        print "Too few frequencies. 2 is the minimum number of allowed
            ↪ frequencies."
        Error=1

    if Total >7:
        print "Too many frequencies. 7 is the maximum number of allowed
            ↪ frequencies."
        Error=1

    if MaxRM <= MinRM:
        print "Maximum allowed RM is less than or equal to minimum
            ↪ allowed RM"
        Error=1

    if len(Wave)!=len(Shift):
        print "Wavelength & Shift arrays are of different lengths"
        Error=1

    for i in xrange(Total):
        if os.path.exists(Image_Stem+'Q'+str(i+1)+'.CLEAN.image')==0:
            print Image_Stem+'Q'+str(i+1)+'.CLEAN.image does not exist'
            Error=1
        if os.path.exists(Image_Stem+'U'+str(i+1)+'.CLEAN.image')==0:
            print Image_Stem+'U'+str(i+1)+'.CLEAN.image does not exist'
            Error=1

    return(Error)

def Make_RM(Image_Stem='', Total='' , Wave='' , N='' , Shift='' , Box =
    ↪  '' , Int_RM = '' , Max='' , MaxRM = '' , MinRM = '' , EVPA_Error
    ↪ ='',Slice='', Band=''):

    Error=Error_Check(Wave,Shift,Image_Stem,Total,MaxRM,MinRM)

    if Error==1:
        print "Operation Failed"
```

```
else:

    RM=0
    eRM=0

    Int_RM=Int_RM*180/math.pi
    MaxRM=MaxRM*180/math.pi
    MinRM=MinRM*180/math.pi

    Q,U,Weight,Sigma,PANG,PPOL=Make_Arrays(Total,N)

    NSlice=[Slice[0],Slice[1]-Band,Slice[2],Slice[3]+Band]

    for i in xrange(Total):
        Q[i]=Read_Maps(Image_Stem+'Q'+str(i+1)+'.CLEAN.image',N)
        U[i]=Read_Maps(Image_Stem+'U'+str(i+1)+'.CLEAN.image',N)


    for i in xrange(Total):
        PANG[i]=numpy.multiply(0.5*numpy.arctan2(U[i],Q[i]),180/math
            ↪ .pi)

    for i in xrange(Total):
        SigmaQ=Find_RMS(Q[i],Box)
        SigmaU=Find_RMS(U[i],Box)
        [Sigma[i],Weight[i]]=Error_PANG_Maps(Q[i],U[i],SigmaQ,SigmaU
            ↪ ,EVPA_Error,N)

    for i in xrange(Total):
        PANG[i]=PANG[i]+Int_RM*Wave[i]*Wave[i]+stats.norm.rvs(loc
            ↪ =0.0, scale= EVPA_Error, size=(1,1))


    RM,eRM=Make_Weighted_RM(PANG,Weight,Sigma,Wave,Total,Shift,MaxRM
        ↪ ,MinRM,NSlice)

    return(RM,eRM)

return()
```

```
def Sigma_Check(EVPA_Error="",Band="",Slice="",,Shift="",Box="",Freq=""
    ↪ ,Int_RM="",Npix="",Nmap="",Name=""):


    Image_Stem=""         #Image Stem Name. Code will look for maps in
        ↪ format Image_StemQ1.CLEAN.image
    Total=len[Freq]       #Number of frequencies to use.


    Max=1500          #Maximum Allowed Error
    MaxRM=10000       #Maximum allowed RM (rad/m/m). If no RM in
        ↪ acceptable range is found, RM will equal 0
    MinRM=-10000          #Minimum allowed RM (rad/m/m). If no RM in
        ↪ acceptable range is found, RM will equal 0




    # Code Starts Here

    Total_Sigma=[0,0,0,0,0]
    Max_Sigma=numpy.zeros([(Slice[2]-Slice[0]),Nmap])
    Wave = numpy.divide(constants.c,Freq)

    for i in xrange(Nmap):

        RM,eRM=Make_RM(Image_Stem+str(i+1), Total, Wave, Npix, Shift,
            ↪ Box, Int_RM, Max, MaxRM, MinRM, EVPA_Error, Slice, Band)

        Max_Sigma[:,i]=Checker(RM,eRM,Band,Slice)



    file=open(Name, 'wb')
    file_writer = csv.writer(file)
    for i in xrange((Slice[2]-Slice[0])):
```

```
        file_writer.writerow(Max_Sigma[i,:])

    return(Total_Sigma)
```